SYNTHESIS AND CHARACTERIZATION

OF

MIXED -METAL OXIDES

By

UMESH BABAJI GAWAS

M.Sc.

DEPARTMENT OF CHEMISTRY

GOA UNIVERSITY

TALEIGAO PLATEAU GOA 403206

INDIA

February 2013

SYNTHESIS AND CHARACTERIZATION

OF

MIXED -METAL OXIDES

A Thesis submitted to Goa University for the Award of the

Degree of

DOCTOR OF PHILOSOPHY

IN

CHEMISTRY

By

UMESH BABAJI GAWAS

Research Guide

Dr. V.M.S. Verenkar

DEPARTMENT OF CHEMISTRY

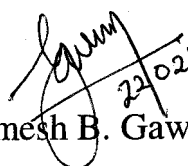GOA UNIVERSITY

GOA 403 206 INDIA

February 2013

DECLARATION

I hereby declare that the matter embodied in this thesis entitled, *"Synthesis and Characterization of Mixed- Metal Oxides"* is the result of investigation carried out by me, in the Department of Chemistry, Goa University, Goa-India, under the supervision of **Dr. V.M.S. Verenkar** and it has not previously formed basis for any other titles.

In keeping with the general practice of reporting scientific observations, due acknowledgement has been made wherever the work described is based on the findings of other investigators.

Goa University   Mr. Umesh B. Gawas

February 2013

CERTIFICATE

This is to certify that the thesis entitled, *"Synthesis and Characterization of Mixed- Metal oxides"* submitted by **Mr. Umesh Babaji Gawas** for the award of Doctor of Philosophy in Chemistry is a record of research done by the candidate during the period of study, under my guidance and that it has not previously formed the basis for award of any degree or other similar titles to the candidate.

Goa University   *Prof. T. Pradeep*   Dr. V. M. S. Verenkar

February 2013   **EXAMINED BY**   22/2/2013

Research Guide

Associate Professor

Department of Chemistry

Goa University, Goa

Corrections suggested by the Examiners were incorporated.

(Umesh B. Gawas)
student

(Research Guide)

ACKNOWLEDGEMENTS

CONTENTS

3   Synthesis and characterization of $Ni_{0.6-x}Mn_xZn_{0.4}Fe_2O_4$ (x = 0.0-0.6) ferrites

3.1   Synthesis and characterisation of hydrazinated mixed nickel manganese zinc
ferrous fumarate precursors, $Ni_{0.6-x}Mn_xZn_{0.4}Fe_2$ $(C_4H_2O_4)_3.6N_2H_4$ (x = 0.0-0.6)

3.2   Characterization of 'as synthesized' $Ni_{0.6-x}Mn_xZn_{0.4}Fe_2O_4$ (x = 0.0-0.6) ferrites   76

LIST OF FIGURES

d) 1250°C / 1h

Chapter 1

Introduction

Chapter 1

Introduction

1.1. History and background

Ferrites are ceramic, homogeneous magnetic materials composed of various oxides with iron oxide as their main constituent. Spinel ferrites are investigated in the recent years for their useful electrical and magnetic properties which find applications in information storage systems, magnetic bulk cores, magnetic fluids, microwave absorbers and medical diagnostics [1]. The most recent reason for upsurge in ferrite interest has been the development of the new, small, efficient power supplies using solid state switching called switch mode power supplies (SMP's). These SMP's are the integral components of modern day electronic equipments such as computers, laptops and entertainment applications. Besides the ease of preparation and low manufacturing cost, the advantage of spinel ferrites is their high magnetic permeability and high electrical resistivity. Also, these materials can be shaped in a variety of different geometries meant for specific applications.

Recently, the nanocrystalline magnetic ferrites have received more attention because of their novel material properties, which are significantly different from those of their bulk counterparts [2]. Some of the phenomena like enhanced coercivity, modified saturation magnetization, superparamagnetism, metastable cation distributions etc. have been observed in various ferrite nanoparticles [3-5].

Spinel-type ferrites have also been investigated for the detection of both oxidizing and reducing gases [6]. In particular, nickel ferrite as p-type semiconducting oxide has been found to be a very good chlorine gas sensor [7]. The semiconductor gas sensors has better

advantages over other gas sensors due to their thermal, physical and chemical stability, low cost and good reliability for real-time control systems [8-9]. Many materials of different types have been studied in the literature for their use as gas and humidity sensors. For better gas sensing, ceramic materials should be in porous form. Thus, controlling porosity and surface activity is of utmost importance as the gas sensitive electrical properties of ceramic material depend on it [10]. Very few spinel ferrites have been reported in the literature as gas sensors. The list of the industrially important ferrites includes among top ten, the Ni-Zn ferrites and Mn-Zn ferrites.

The Ni-Zn ferrites are characterized by high material resistivity suitable for high frequency applications from 1MHz to several hundred megahertzs. Hence, these ferrites find use in microwave devices, power transformer, rod antennas, read / write heads for high speed digital tapes [11] etc. The use of Ni-Zn ferrites is limited due to their low permeability at higher frequencies and increasing cost. Mn-Zn ferrites, on the other hand posses high permeability and saturation magnetization with nearly zero magneto-crystalline anisotropy and magneto-restriction. Hence, it is used in transformer cores, noise filters, recording heads [12] etc. Mn-Zn ferrites also have certain limitations for magnetic applications at high frequencies, because of their low resistivity and hence high eddy current losses. For high frequency magnetic applications, ferrite materials with high permeability as well as high resistivity are more suitable which can reduce eddy current losses. Therefore, an appropriate combination of these two ferrites can result in the material with better properties and will be more suitable for high frequency applications [13].

It is well established fact that, the magnetic and electrical properties of ferrites are sensitive to the cation distributions, which in turn depend on the method of synthesis. Hence,

there is growing interest in the newer and newer synthetic strategies to improve on the properties of ferrite materials. Many authors have reported structural, magnetic, electric and dielectric characteristics of Mn substituted Ni-Zn ferrites, prepared by various synthetic routes like conventional ceramic [14] and non-conventional routes like sol-gel [15], co-precipitation [16] etc.

The magnetism displayed by the spinel ferrites is a value added property which makes them industrially important. The magnetism is one of the earliest known physical phenomena of solid materials. Magnetism emerges from interactions at the smallest measurable scales from the quantum regime, arising from electronic and nuclear interactions. The term magnetism derived from a rock called lodestone (loadstone). The Ancient Greek Philosophers realized the value of the magnetic iron ore, $FeO.Fe_2O_3$ and hypothesized on its origin. Some of the properties of magnets were discovered earlier than 600 BC, although it is only in the twentieth century that Physicists have begun to understand why substance shows magnetism. In 1269, Pierre Pelerin de Maricourt, a French soldier introduced the notion of magnetic poles. He was followed much later by English Physician, William Gilbert, who wrote a book entitled De Magnete in 1600. William Gilbert was the first to apply scientific methods to a systematic exploration of magnetic phenomena. His greatest contribution was the discovery that the earth itself behaves like a giant magnet. In 1750, the English Geologist John Mitchell (1724-1793) invented a balance that he used in the study of magnetic forces. He showed that attraction and repulsion of magnets decreases as the square of the distance from the poles increases. Repeating the experiment of Mitchell, a French Physicists Charles Augustine de Coulomb (1736-1806) demonstrated his famous $1/r^2$ interaction law between magnetic charges by using long magnets. In 1820, the Danish Physicist H. C. Oersted showed that

3

magnetic field could be created by the circulation of an electric current in a conducting wire. In the weeks that followed, Andre Marie Ampere repeated his historic experiment and succeeded in giving elegant formulation. He showed that a current carrying circular coil generates magnetic field identical to that generated by magnetic dipoles. In 1821, the phenomenon of induction was discovered by the English Physicist Michel Faraday who constructed the first dynamo. Pierre Simon de Laplace (1749-1867) established the expression for the force acting on a current carrying conductor in a magnetic field. The equation of electromagnetism deduced by the Scottish Physicist J. C. Maxwell in 1864 is used till today as the analytical basis of magnetism. William Sturgeon built the first electromagnet in 1824 by adding an iron core to the solenoid. Pierre Curie (1859-1906) introduced and clarified the ideas on diamagnetism, paramagnetism and ferromagnetism and the French Physicists Paul Langevin (1872- 1946) dealt with the induced and permanent magnetism and established the classical theory of paramagnetism. Langevin's theory was subsequently expanded by the French Physicist Pierre Ernst Weiss (1865-1940), who postulated the molecular field hypotheses. After Weiss theory, magnetic properties were explored in greater detail by Louis Neel, who was awarded Noble prize in Physics in 1970 for his theory of antiferromagnetism (1936) and ferrimagnetism (1948). In 1900's, Edward M. Purcell and Flix Bloch both American Physicists developed a way to measure the magnetic field of the nuclei. This discovery led to Magnetic Resonance Imaging (MRI). The American Physicists Samuel Goudsmit (1902-1978) and George Uhlenbeck (1900-1988) showed that the electron itself has a spin and behaves like a small bar magnet. At the atomic level, magnetism is measured in terms of magnetic moments. A moment being analogous to a unit of angular momentum in mechanics, except that electric charge is substituted for mass. The German Physicist Werner

4

Heisenberg showed that the strong magnetic interactions responsible for magnetic order were of electrostatic origin and could be interpreted in terms of coupling between two neighboring spins. In 1960's and 1970's scientists developed superconducting magnets. When superconducting magnet is cooled to absolute zero, it can generate magnetic fields up to 200,000 Gauss [17,18].

1.2. Classification of ferrites

Ferrites are the ferrimagnetic ceramic oxides with iron oxides as their main constituent. Ferrimagnetic substances are industrially important because they exhibit a substantial spontaneous magnetization at room temperature. Ferrimagnetic materials have emerged into a distinct class of magnetic materials, which forms the basic components of various energy storing devices from the late 1950s. The increasing research interest in ferrites is not only because of their commercial importance, but also from the point of understanding their fundamental properties. Ferrites are classified mainly into three types on the basis of their crystal structures. They are spinels, garnets and magneto-plumbites. Spinel ferrites have a cubic structure with general formula $AO.Fe_2O_3$, where A is a divalent metal ion like Mn^{2+}, Ni^{2+}, Fe^{2+}, Co^{2+}, Mg^{2+} etc. Garnets have a complex cubic structure having a general formula $A_3Fe_5O_{12}$ where A is the large ion with coordination number eight in a distorted cubic environment. The magneto-plumbites have hexagonal structure with general formula $AO.Fe_{12}O_{18}$, where A is the large divalent metal ion like Ba^{2+}, Pb^{2+} [19,20] etc.

1.3. Crystal structure of spinel ferrites

The structure of spinel ferrites is derived from that of the mineral spinel, $MgAl_2O_4$. The structure consists of eight formula units of MFe_2O_4 in a unit cell, where M is the divalent metal ion. The 32 oxygen anions form a face centered cubic lattice of spinel in which two types of interstitial vacant spaces are present. The one which are surrounded by four oxygen anions are called tetrahedral (A) sites and the other which are surrounded by six oxygen anions are referred to as octahedral [B] sites. There are 64 tetrahedral (A) sites surrounded by 4 oxygen anions and 32 octahedral [B] sites surrounded by 6 oxygen anions in a unit cell of spinels. The metal ions occupy these interstices in the crystal lattice of spinel ferrites. The crystallographic environments of tetrahedral (A) and octahedral [B] sites are therefore distinctly different. The crystal structure of a cubic spinel ferrite with the tetrahedral (A) sites, octahedral [B] sites is represented in Fig. 1.1. The metal ions occupy only one eighth of the tetrahedral (A) sites and one half of the octahedral [B] sites to maintain the overall charge neutrality of the ferrite [21].
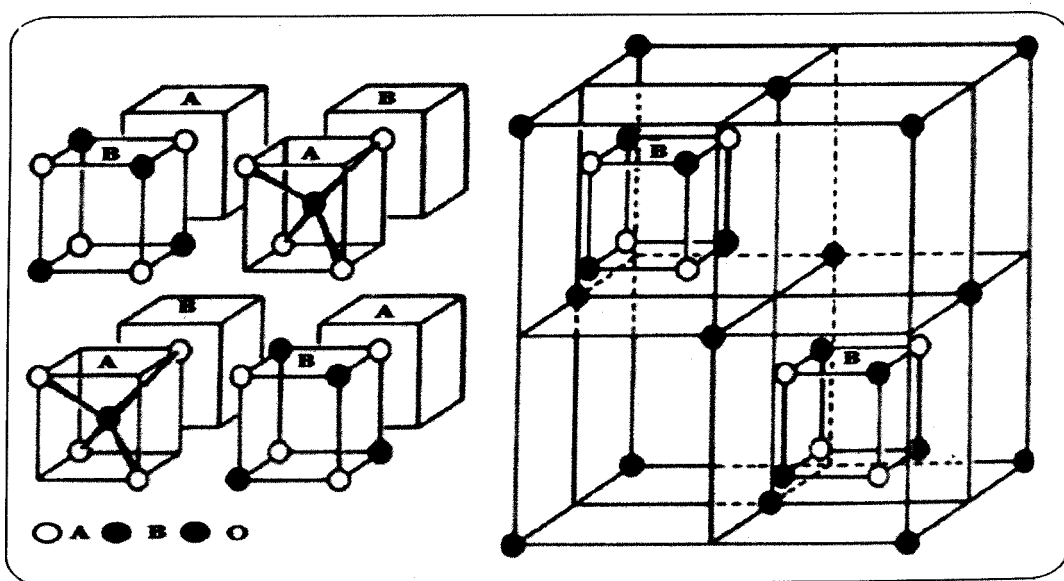
Fig.1.1. Unit cell representation of cubic spinel ferrite

In a chemical formula of spinels, $MO.Fe_2O_3$, if all the M^{2+} ions occupy tetrahedral (A) sites and Fe^{3+} ions are present in the octahedral [B] sites then, this arrangement is referred to as the normal spinel, ex. $ZnFe_2O_4$. When the all the divalent metallic ion M^{2+} ions occupies the octahedral [B] sites and the Fe^{3+} ions are equally divided between tetrahedral (A) and octahedral [B] sites, it results in the configuration which is known as inverse spinel, ex. $NiFe_2O_4$. The normal and inverse spinel structures are the extreme cases, but the experimental studies like X-ray and neutron diffraction have shown that intermediate random configurations can also exist, ex. $MnFe_2O_4$. The factors which determine the cation distribution in tetrahedral (A) and octahedral [B] sites include the cation size, charge and the oxygen position parameter. Besides these, the distribution of the divalent ions can be altered by other factors such as method of preparation, particle size, sintering atmosphere etc. Large divalent ion prefers tetrahedral (A) sites as this is favoured by polarization effects. If the tetrahedral (A) site ions have a lower valency and the octahedral [B] site ions have higher valency then the intermediate O^{2-} ion will become polarized towards octahedral [B] sites. Thus, polarization favours normal spinel configuration. It has been proved that the inverse structure has the lowest lattice energy when oxygen position parameter, $u < 0.379$, where as the normal structure has the lowest energy when oxygen position parameter, $u > 0.379$. These factors alone cannot give consistent picture of the cation distribution observed in spinel ferrites. For ex. $ZnFe_2O_4$ crystallizes in normal spinel structure while $CoFe_2O_4$ is an inverse spinel, although the ionic radii of Zn^{2+} and Co^{2+} ions are very close. These discrepancies can be explained considering the site preference of the individual ions which is the result of their electronic configuration. Two theories have been proposed to explain the site preference of transition metal ions, in various oxides.

7

a. The crystal field theory, which consider the bonding to be purely ionic.

b. The molecular orbital theory which is based on the covalent bonding between oxygen and transition metal atoms or ions.

1.4. Magnetic properties of ferrites

According to the modern theory, magnetism in substance arises from the combined contribution of spin and orbital motion of electrons as well as spin of the nuclei. The spin and orbital motion of electron in an orbital is equivalent to an electric current which produces the magnetic field. When an orbital contains paired electrons, the magnetic moment cancels each other due to opposite spin of electrons. But unpaired electrons posses spin which produces permanent magnetic moments responsible for the magnetism in a substance [22]. The type of magnetic behavior exhibited by a substance depends on the alignment of magnetic moments. The most important parameter which determines the magnetic behavior of atom is the exchange overlap integral of the electronic wave functions on neighboring atoms [23]. This overlap integral depends on distance between the neighboring atoms, which are subject to size effects and crystal lattice parameters. If the atoms are sufficiently close to each other then, the possibility to produce long range order increases. Depending on the interaction of magnetic field with matter, the substances have been grouped under one of the following types of magnetism.

a) Diamagnetism: Diamagnetism arises from the deformation of the electric charge cloud when a substance is placed in a magnetic field but disappears when the field is removed.

b) *Paramagnetism:* Paramagnetism occurs when the atomic, ionic, or molecular constituents possess unpaired electron spins. These spins can be easily aligned by the applied magnetic

field though each electron spin is independent from its neighbors. Removal of the field results in the relaxation of the aligned states back to the random distribution of the moments.

c) *Ferromagnetism:* Ferromagnets are characterized by large spontaneous magnetic moments even in the absence of magnetic field. Long range ordering observed in ferromagnetic materials is a function of the magnetic domains that exists within a sample.

d) *Antiferromagnetism:* Antiferromagnet consists of two interpenetrating sub-lattices such that the atomic or ionic spins of one sublattice are aligned antiparallel to those on other resulting in net zero magnetic moment. This antiparallel alignment in antiferromagnetic material are vulnerable to thermal fluctuations as a result with increasing temperature, the susceptibility increases until it reaches a temperature characteristic of the material where it decreases sharply. The temperature at which this abrupt change in susceptibility occurs is known as the Neel temperature (T_N).

e) *Ferrimagnetism:* Ferrimagnets like, antiferromagnets consists of two interpenetrating sublattices but are known to possess net magnetization even in the absence of magnetic field. The ferrimagnetic materials consist of self saturated domains and exhibit the phenomena of magnetic saturation and hysteresis. The non vanishing net magnetization arises when the two sublattices are occupied by different types of magnetic ions or when the two sublattices corresponds to two different crystallographic sites occupied by same type or different types and number of magnetic ions. Ferrimagnetic materials are characterized by the characteristic temperature known as Curie temperature (T_c). Above the Curie temperature, the spontaneous magnetization is eliminated by thermal energy resulting in paramagnetism.

The spinel ferrites are ceramic mixed metal oxides which display ferrimagnetic behavior due to the unequal number of magnetic ions in two different crystallographic lattice

sites of their cubic structure. The various factors that determine the magnetic properties of the ferrites are the nature of cations, heat treatment, preparative methods, site preference energy of cations and madelung energy. Neel [23] has explained the spontaneous magnetization of ferrites on the basis of Heisenberg's exchange forces. According to this theory the exchange energy between two adjacent atoms having spin angular momentum is given by:

$$E_{ex} = -2J_{ex}.S_i.S_j \qquad \text{---------------------} \{1.1\}$$

Where, E_{ex} is the exchange energy, S_i and S_j are the total spins of adjacent atoms and J_{ex} is the exchange integral which represents the probability of exchange of electron. In spinel ferrites three different types of magnetic interactions are possible between the magnetic ions occupying lattice sites. These interactions occur through the intermediate O^{2-} ions by superexchange mechanism. These are A-A interaction, B-B interaction and A-B interaction. The exchange force acting between the ions on tetrahedral (A) and octahedral [B] site is governed by the equation 1.1 and hence, the interaction will be either ferrimagnetic, ferromagnetic or antiferromagnetic depending on the value of J_{ex}. The interaction energies are found to be negative in case of ferrites and hence, it induces an anti parallel orientation. However, the magnitudes of the A and B sublattice magnetizations are unequal which results in net magnetization in ferrites. In general, the magnitude of the interaction energy between two magnetic ions depends upon the distance of these ions from the oxygen ion and also, the angle (θ) between the magnetic ions (M - O - M'). An angle of 180° will give rise to the greatest exchange energy and the energy decreases very rapidly with increasing distance. Based on the values of the distance and the angle (θ), it may be concluded that, of the three interactions the A-B interaction is of the greatest magnitude and A-A interaction is the weakest. Thus, with only A-B interaction predominating, the spins of the A and B site ions, in

ferrite will be oppositely magnetized in the A and B sublattices, with a resultant magnetic

moment equal to the difference between those of A and B site magnetic ions. In general, the

value of saturation magnetic moment for the B sublattice (M_B) is greater than that of the A

sublattice (M_A) so that the resultant saturation magnetization (M_s) may be written as:

$$M_s = M_B - M_A \qquad\qquad ----------------------\{1.2\}$$

1.4.1. Magnetic domains and superparamagnetism

Ferromagnetic materials exhibit a long-range ordering phenomenon at the atomic level

that causes the unpaired electron spins to line up parallel with each other in a region called a

domain. According to Weiss [24] these domains are aligned in such way that the total

magnetic moment of the material is minimized. Between each domain there exists a boundary

called the domain wall. These domain walls are classified into two types based on the angle of

magnetization that exist between them. The Bloch wall consists of a 180° separation of the

domain magnetization. The magnetization rotates in a plane parallel to the plane of the wall.

The Neel wall consists of a 90° rotation perpendicular to the plane of the wall. Energy is

required to spatially orient spins within a magnetic domain with those in neighboring

domains, however magnetocrystalline anisotropy interactions prevent removing or lowering

domain walls by an external field. This results in a directional dependence of the measured

susceptibility within the material. The magnetocrystalline anisotropy is intrinsic property of

the material, and the saturation value will differ for each crystalline direction which is

commonly referred to as the easy and hard axis. For a ferromagnetic material the magnetic

domains preferentially lie along the easy axis. For a nanocrystalline magnetic system, a

critical dimension exists at which it is so energetically unfavorable for domain walls to exist,

therefore the system is a single domain. This reduction in particle size also allows for the magnetocrystalline anisotropic energy to be influenced by thermal energy, resulting in a superparamagnetic state. Magnetization reversal in a single domain particle can only occur via spin rotation, thus single domain particles generally have a higher coercivity value than multidomain particles simply because it is much more difficult to rotate magnetization than it is to overcome a domain wall. The moment can then freely respond to an applied field. This resembles the normal paramagnetic behavior, but has a large magnetic moment, hence the term superparamagnetism. Particles that exhibit superparamagnetic behavior have a large saturation magnetization but no remanence or coercivity. Hysteresis will appear and superparamagnetism disappears when particles of a certain size are cooled to a particular temperature or when the particle size at a constant temperature increases beyond a particular diameter (D_{SP}).
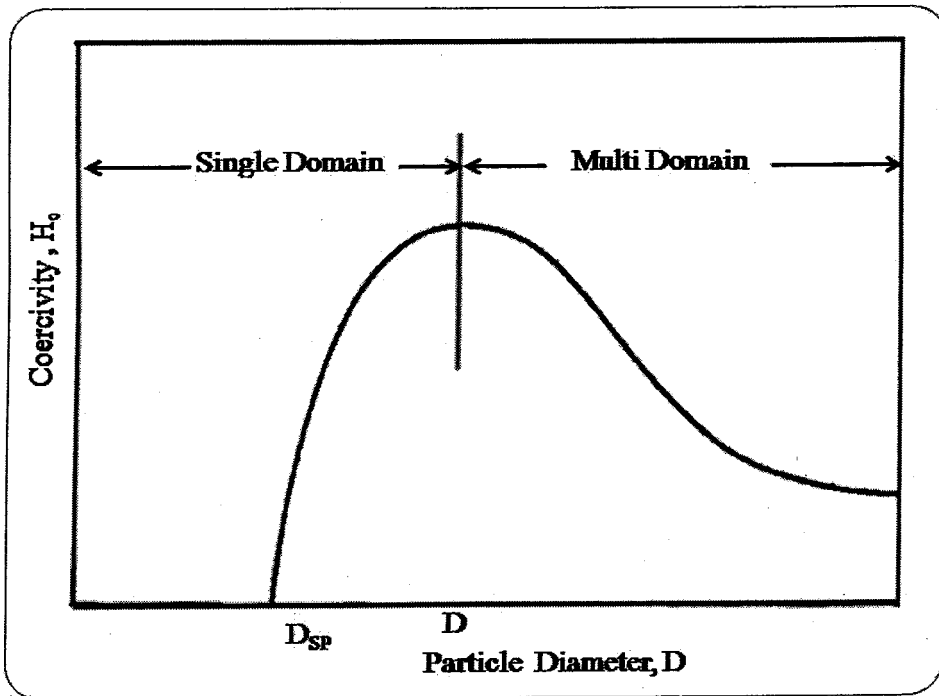
Fig.1.2. Variation of particle coercivity with particle diameter

1.4.2. Magnetic hysteresis

The feature that is commonly used to describe the multidomain properties of magnetic materials is response of the material to an applied field. Hysteresis arises from rearrangement of the domain walls either through displacement, pinning, nucleation or rotation [25]. An ideal hysteresis loop for a multidomain material is shown in Fig. 1.3.
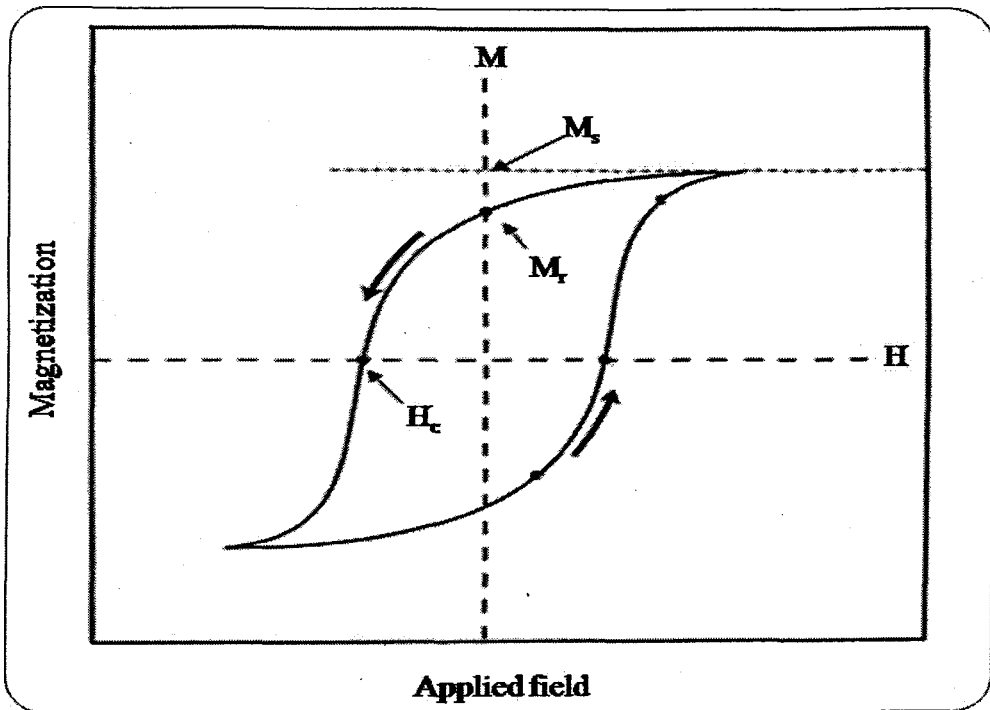
Fig.1.3. Hysteresis loop for a multidomain magnetic material representing saturation magnetization (M_s), coercivity (H_c) and remanent magnetization (M_r)

The remanent magnetization (M_r) and the coercive field or coercivity (H_c) typically defines the hysteresis of a material. The hysteresis or width of the loop results from wall pinning or nucleation or both. A direct measurement of these effects is coercivity (H_c), which is the reverse field necessary to reduce magnetization to zero in the descending loop. Remanent magnetization (M_r) is obtained by applying and removing a large magnetic field

13

and represents the ability of a multidomain material to exhibit spontaneous magnetism. The saturation magnetization is the maximum induced magnetic moment that can be obtained in a magnetic field (M_s), beyond this field no further increase in magnetization occurs. Saturation magnetization (M_s) is an intrinsic property of material which depends on both particle size and temperature. When size is bigger the particles have many domains and magnetic reversal is dominated by domain wall motion resulting in low coercivity (H_c). When a particle size decreases, the coercivity increases until the single domain limit is achieved where the largest values for coercivity occurs and then gradually decrease due to thermal activation over anisotropy barriers [26].

1.5. Electrical properties of spinel ferrites

Spinel ferrites are important than conventional magnetic materials because of their wide range of applications. These ceramic materials have low electrical conductivities as compared to other magnetic materials and hence they find widespread use at microwave frequencies. Spinel ferrites, in general display semiconductor behaviour with conductivities in the range 10^2 and 10^{-11} Ω^{-1} cm^{-1} [27]. The conductivity in ferrites is due to the presence of Fe^{2+} and the metal ions (M^{3+}). The presence of Fe^{2+} results in n-type while, M^{3+} is responsible for p-type semiconducting behaviour. The conductivity originates from the mobility of the extra electron or the positive hole through the crystal lattice. The movement is described by a hopping mechanism, in which the charge carriers jump from one lattice site to the other. In short, one can say that the electrostatic interaction between conduction electron or holes and nearby ions may result in a displacement of the latter and polarization of the surrounding region, so that the carrier is situated at the centre of a polarization potential well. The carrier is

trapped at a lattice site, if this potential well is deep enough. Its transition to a neighbouring site is determined by thermal activation. In such a process the mobility of the jumping electrons or holes are found to be proportional to $e^{-Ea/kT}$ where, E_a is the activation energy, k Boltzman's constant and T is absolute temperature. The conductivity of the ferrites depends on several factors like chemical homogeneity, porosity, grain size, sintering conditions [28] etc.

Spinel ferrites exhibit high dielectric constant and dispersion of dielectric constant varies over the frequency range from a hundred hertz to megahertz. Dielectric properties of ferrites depend on frequency, temperature and surface microstructure. The high resistivity semiconducting behavior of ferrites ensures a practically zero current but the electric field gradient will cause polarization of charges within the lattice. The term polarization refers to the total induced dipole moment per unit volume of the material. The dispersion in the dielectric constant has been explained by Koops phonological model [29].

1.6. Spinel ferrites as gas sensors

The first decade of the 21st century has been labelled as the "Sensor Decade". There is an increasing interest in finding new materials in order to develop high performance solid-state gas sensors. Gas sensors are important in environmental monitoring, home safety and chemical leakages controlling. Spinel-type oxide semiconductors (ferrites) are an alternative for expensive and robust detection systems because of good chemical and thermal stability under operating conditions [30-31]. Multi-functional cubic spinel ferrite materials are nowadays being studied extensively for their magnetic, catalytic, bio-medical and gas sensing applications [32-35]. Some of the spinel ferrites have excellent sensitivity towards reducing gases and some of them are very selective to a specific gas [36-38]. It is known that for

improved gas sensing performance (sensitivity, selectivity, stability, etc.), in addition to the selection of proper semi-conducting oxide material, factors such as their phase purity, charge carrier density and crystallite size also have significant influence. Apart from these factors, the microstructure and porosity of the sensing elements prepared by low temperature sintering of oxide particles, also influence the gas sensing performance [39]. The surface morphology has an essential role in the sensitivity of solid state sensors. The nanosize materials offer new opportunities for enhancing the performance of gas sensors because of their high surface to volume ratios [40-43]. The sensing mechanism is based on the change in electrical resistivity resulting from chemical reaction between gas molecules and the metal oxide surface [44-45]. This change in resistivity is directly related to the concentration of a specific gas present in the environment. The operating conditions must be optimized for both the sensor material and the gas being detected.

Many different semiconducting oxides in bulk ceramic [46-47], thick films [48] and thin films [49-50] form have been studied as the probable candidates of sensor element for gas sensing. Thick film processing would seem to be a suitable method for the production of films with microstructural properties similar to those of porous sintered bodies and for the production of active elements to be used in hybrid integrated devices. This technology has already been used to produce humidity sensitive elements made up of other ceramic oxides [51]. Thick film gas sensors can be easily fabricated by the low cost screen printing technique.

1.7. Literature review

The ferrites belonging to spinel class have been explored widely for their electrical and magnetic properties which find the wide range of applications in the modern electronic

16

industries. Among these, the ferrites containing Ni-Zn ferrites and doped Ni-Zn ferrites are the most frequently encountered systems in the literature and the literature available on these systems is also very vast hence, we have carried out the literature search only of the doped Ni-Zn ferrites.

1.7.1. *Literature review of doped Ni-Zn ferrite systems*

The Ni-Zn ferrites and Mn-Zn ferrites are the most widely studied systems from spinel class ceramic oxides due to their wide range of applications in different fields such as electronics, transformer cores, medical diagnostics, magnetic bubble systems etc.

Sun et al. [52] have studied the effect of Bi_2O_3 additive on the grain growth characteristics of Ni-Zn ferrites prepared by ceramic technique. They observed increase in the diffraction intensity for moderate content of Bi_2O_3 additives, while higher contents were found to reduce the diffraction intensity. Also, the improvement in density, permeability and saturation induction with Bi_2O_3 doping in sintered samples was reported by them. The effect of Be substitution on Mössbauer effect parameters and magnetic properties of polycrystalline Ni-Zn ferrites was reported by *Slama et al.* [53]. They found increase the saturation magnetization and Curie temperature for lower Be contents which was attributed to the modification of A-B sublattice interactions. *El-Nimr et al.* [54] have studied the effect of Li substitution on Ni-Zn ferrite nanoparticles prepared by a chemical co-precipitation method. They have given a comparative account of the d.c. conductivity and magnetic permeability of nano-structured and bulk samples. Also, they observed higher Curie temperature and d.c. resistivity for nanocrystalline samples. They attributed these observations to increase A-B sublattice interactions and to increase in insulating surface on grains and porosity. *Abdullah*

et al. [55] have investigated the impedance characteristics of Li substituted Ni-Zn ferrites in the frequency range of 1 MHz to 10 MHz using a frequency response analyzer. The observed dielectric characteristics were explained by them considering interfacial polarization at lower frequency and orientation polarization in higher frequency region. *Rezlescu et al.* [56] have investigated the effect of the addition of dopants such as CaO, Na_2O, ZrO_2, Sb_2O_3 and K_2O on the densification characteristics of Li-Zn ferrites and Ni-Zn ferrites. They achieved increase in density upto about 98.5 % with above dopants. *Costa et al.* [57] have investigated the effect of Sm additive on the microstructure, relative density and magnetic properties of nanocrystalline Ni-Zn ferrites prepared using combustion method. They achieved increase the relative density upto 98.0 % of the theoretical density with Sm addition while, the hysteresis parameters showed decrease. *Shinde et al.* [58] observed higher values of saturation magnetization for Nd substituted Ni-Zn ferrites prepared using oxalate co-precipitation method. The hyperfine field parameters of rare earth doped Ni-Zn ferrites nanoparticles prepared by the combustion method were studied by *Jacobo et al.* [59]. They observed a small increase in the hyperfine field parameters and a strong decrease of the total resonant area in the rare earth doped Ni-Zn ferrite. The Curie temperature was found to decrease while, the coercive fields showed increase with substitution. *Kumar et al.* [60-61] have studied the electrical and dielectric properties of Gd and Er substituted Ni-Zn ferrites. The electrical conduction in the Gd substituted ferrites was found to be n-type as observed from their thermoemf studies. The dielectric constants showed increasing trend with increase of Er content. *Fu et al.* [62] have prepared WO_3 doped Ni-Zn ferrites by one-step synthesis through the incorporation of WO_3 into the raw powders. The WO_3 doping was found to affect the structural and magnetic properties of Ni-Zn ferrite. The WO_3 doping were found to promote the grain growth causing

18

increase in grain size, density and magnetization at lower concentration but for higher WO_3 content, an uneven abnormal growth, closed pores and decrease in the saturation magnetization were observed. The Curie temperature however, showed increase with increasing amount of WO_3 content. The lower values of dielectric constant and dielectric loss observed for small WO_3 content were found to increase with increasing WO_3 content. *Shen et al.* [63] have developed a simple hydrothermal route with cetyltrimethylammonium bromide for direct synthesis of single crystalline Ni-Zn-Co ferrite at 160°C. They observed increase in the saturation magnetization with Co doping. The dielectric constant of Co substituted Ni-Zn ferrites at higher frequency were found to be very low hence they have suggested the possible application of these compositions in higher frequency range. Similar results were also reported by *Ghodake et al.* [64-65] for nanocrystalline Ni-Co-Zn ferrites prepared using oxalate co-precipitation method. In addition they have observed increase in resistivity with Co doping. *Ahmed et al.* [66] have studied the effect of Cu substitution in Ni-Zn ferrites prepared using ceramic technique while, *Dimri et al.* [67] have used citrate precursor method to prepare Ni-Cu-Zn ferrites. They observed that Cu substitution in Ni-Zn ferrites initiates grain growth but decreases the Curie temperature. They observed very high values of saturation magnetization at lower concentration of Cu in Ni-Zn ferrites. *Hu et al.* [68] have investigated the effect of dopant such as CuO and V_2O_5 on microstuctural, magnetic and permeability characteristics of Ni-Zn ferrites. They observed the optimum additions of CuO and V_2O_5 promotes grain growth and the densification of matrix during the sintering process which decreases the sintering temperatures of Ni-Zn ferrites. The post-sintering density and the initial permeability were found to be strongly affected by the average particle size of raw materials. They have obtained relatively high initial permeability and low relative loss

coefficient at lower sintering temperature of 930°C. *Waje et al.* [69] have synthesized $Co_{0.4}Ni_{0.3}Zn_{0.3}Fe_2O_4$ ferrites material with the crystallite size in the range of 10 nm to 50 nm using mechanical alloying and sintering. They have also measured the initial permeability and permittivity of above composition as the functions of sintering temperatures and the frequency from 10 MHz to 1.8 GHz. The increase in the permeability which they observed with the increasing sintering temperature was attributed to the increased grain growth as a result of the sintering process while, the increase in the permittivity with increasing average grain size, was ascribed to the increase in the Fe^{2+} concentration formed at elevated sintering temperature. The microwave absorption permittivity and permeability characteristics of Ni-Zn ferrite, Cu-doped and Co-doped Ni–Zn ferrites were reported by *Zhao et al.* [70] for samples obtained by conventional ceramic processing method. They found that the samples were good electromagnetic wave absorbers in the microwave frequency range. *Kumar et al.* [71] have studied the effect of Cr doping on d.c. resistivity and magnetic properties of Ni-Zn ferrites. They observed very sharp fall in the initial permeability for lower doping concentration of Cr. *Batoo et al.* [72] have synthesized Zn doped Ni-Cu ferrite nanoparticles using auto-combustion method. In their study the dielectric parameters showed maximum value for 10 % Zn doping. The dielectric constant and loss tangent decreased with increasing frequency of the applied field. These dielectric results were explained on the basis of dielectric polarization. The complex impedance study showed that the conduction process in grown nanoparticles takes place predominantly through grain boundary volume.

The system containing mixed Ni-Zn ferrites and Mn-Zn ferrites compositions have been studied quite recently and not much literature available on this system. The Zn substitution in Ni ferrites have been found to improve their magnetic and electric properties

20

and hence Ni-Zn ferrites system is explored to very large extent all over the world. $Ni_{1-x}Zn_xFe_2O_4$ with composition, $x = 0.4$ and $x = 0.5$ was found to display the optimum magnetic and electric characteristics as reported by many authors [73-79]. The highest saturation magnetization values have been reported for compositions, $x = 0.4$ and $x = 0.5$. This inspired us to select these composition for our study and to further improve on their magnetic properties with substitution of magnetic Mn^{2+} ions for Ni^{2+} ions. Hence, we have used two series of Ni-Zn ferrite compositions i.e. $Ni_{0.5}Zn_{0.5}Fe_2O_4$ and $Ni_{0.6}Zn_{0.4}Fe_2O_4$ to investigate the effect of Mn substitution on structural, Mössbauer, eletric, dielectric and magnetic properties. The oldest report on Ni-Mn-Zn-ferrite system available in the literature was by *Goto et al.* [80]. They have grown the single crystal of Mn-doped Ni-Zn ferrite composition using Bridgman method. They observed that the oxygen pressure required for crystal growth can be lowered by partial substitution of NiO with MnO. They studied the relationship between the amount of MnO substitution and the oxygen pressure required in growing single crystals of Ni-Zn ferrite having about 50 mol % of Fe_2O_3 and found that with increase in MnO content the oxygen pressure was reduced from 100 Kg/cm^2 (6 mol % MnO) to 1 Kg/cm^2 (12 mol% MnO). *Bara et al.* [81] have carried out Mössbauer effect studies of $Mn_xZn_yNi_zFe_2O_4$ (x + y + z = 1) system prepared using double sintering method. They observed that with increase in the concentration of either Zn^{2+} ions or Mn^{2+} ions, affects mainly the hyperfine field of A-sublattice which in turns has effect on B-site hyperfine magnetic field through A-B superexchange interaction. *Dionne et al.* [82] have studied the effect of Mn substitution for Fe in $Ni_{0.65}Zn_{0.35}Fe_{2-x}Mn_xO_4$ (x = 0.0-0.4) on electrical properties. They prepared these ferrites by ceramic method. They observed decrease in the magnetization with increasing Mn substitution for Fe^{3+} ions in Ni-Zn ferrites. The maximum hysteresis loop squareness and

minimum stress sensitivity was observed for sample with composition, $x = 0.2$. Also, the increase in resistivity and low dielectric loss tangent were observed which they have attributed to the very low concentration of Fe^{2+} ions. *Babbar et al.* [83] have developed Ni and Co substituted Mn-Zn ferrites of composition $Mn_{0.6}Zn_{0.4-x}Ni_xFe_2O_4$ ($x = 0.0\text{-}0.4$) and $Mn_{0.6}Zn_{0.4-y}Co_yFe_2O_4$ ($x = 0.0\text{-}0.4$) as high-density magnetic recording materials by hot-pressing technique. They observed improvement in the magnetic properties and resultant materials were found to possess higher hardness, low porosity and small grain size. The initial permeability of the material was increased, whereas the coercive field showed decreased. The Curie temperature was found to increase, whereas the d.c. resistivity showed decreased for a higher concentration of Ni and Co in the ferrite series. *Bhise et al.* [14,84] have investigated the magnetic and electrical properties of $Zn_{0.3}Ni_{0.7+x}Mn_xFe_{2-2x}O_4$ ($x = 0.0\text{-}0.4$) system prepared by conventional method in which Mn and Ni is substituted for Fe. At lower concentration of Mn, Curie temperature and resistivity shows increase, while at higher Mn concentration both, the Curie temperature and resistivity decreases. The resistivity behaviour have been attributed to the hindering of Verwey mechanism at lower temperature and formation of Mn^{3+} clusters at higher temperatures. They also studied the thermoelectric properties of this system and observed n-type conduction at lower temperature and p-type conduction at higher temperature which have been assigned to polaron hopping conduction mechanism. *Rezlescu et al.* [85] have studied the effect of various divalent ions on the physical properties of $Ni_{0.5}Zn_{0.5}Fe_2O_4$ ferrite synthesized using ceramic method. They found that the magnetic and electrical properties of Ni-Zn ferrite changes considerably with the substituent species. The substitution of Cu was found to lower the sintering temperature and increase density while, Mn ions and Co ions substitution was found to increase electrical

resistivity by about two orders of magnitude. They also observed improvement in thermal stability of the initial permeability by substitution of the Ca and Mn in Ni-Zn ferrite. *Singh et al.* [86] have explored the mixed Ni-Mn-Zn ferrite systems in detail for their structural, electric, dielectric and magnetic characteristics by varying the Mn, Ni and Zn content. They used citrate precursor method for preparing mixed Ni-Mn-Zn ferrites. The Mn substitution in $Ni_{0.6-x}Mn_xZn_{0.4}Fe_2O_4$ ($x = 0.0-0.5$) ferrite was found to improve both dielectric and magnetic characteristics. They observed Curie temperatures in the range of $300^\circ C$ to $500^\circ C$ and saturation magnetization in the range 50-65 emu/gm for sintered compositions. The samples showed low permeability and dielectric losses. The effect of Mn substitution on structural, electric, dielectric and magnetic properties of $Ni_{0.5-x}Mn_xZn_{0.5}Fe_2O_4$ ($x = 0.0-0.4$) ferrite compositions was also studied by the group i.e. *Singh et al.* [15, 87-89]. They found that the dielectric constant increases with the increase in Mn substitution with exception for composition, $x = 0.3$. Also, they noted the shift in the resonance frequency towards higher frequency with increasing temperature. The resonance peaks observed in frequency variation of complex initial permeability were assigned by them to domain wall oscillations. They observed Curie temperatures in the range $418^\circ C$ to $488^\circ C$ for sintered $Ni_{0.5-x}Mn_xZn_{0.5}Fe_2O_4$ ($x = 0.0-0.4$) compositions. *Singh et al.* [90] have also reported the effect of Ni substitution on electric, dielectric and magnetic properties of $Mn_{0.4-x}Ni_xZn_{0.6}Fe_2O_4$ ($x = 0.1-0.4$) compositions. They observed increase in the resistivity and decrease in dielectric relaxation intensity with increase in Ni content. Their studies indicated initial rise followed by decrease in the saturation magnetization. They observed increase in Curie temperatures from $370^\circ C$ to $490^\circ C$ with increase in Ni content. The studies carried out by *Singh et al.* [91] on the effect of calcinations and sintering temperature on the lattice parameter and saturation magnetization of

nanocrystalline $Mn_{0.2}Ni_{0.2}Zn_{0.6}Fe_2O_4$ indicated the increase in the saturation magnetization with increasing sintering temperature which was attributed to the increased average grain size with increase in sintering temperature upto 1400°C. The effect of Mn variation on electrical and magnetic properties of $Ni_{0.3}Mn_xZn_{0.7-x}Fe_2O_4$ (x = 0.0-0.5) ferrite compositions was investigated by *Singh et al.* [92]. They observed initial increase followed by decrease in resistivity and saturation magnetization with increase in Mn concentration. Also, a shift in dielectric relaxation peak towards higher frequencies was observed with increase in Mn concentration. Another Ni-Mn-Zn ferrite composition explored by *Singh et al.* [93] was $Ni_{0.8-x}Mn_{0.2}Zn_xFe_2O_4$ (x = 0.2-0.6) where they have studied the effect of variation of Zn content on electrical and magnetic properties. The increase in the resistivity with increasing zinc upto x = 0.5, was explained in terms of hopping and site preference of ions in the lattice. They also reported increase in initial permeability with increase in Zn concentration while, the saturation magnetization increases up to x = 0.4 and then decreasing trend was observed which was explained considering the canting effect for higher Zn concentrations. *Verma et al.* [94] have investigated the electrical and magnetic properties of mixed Mn-Zn ferrites and Ni-Zn ferrite compositions, $Ni_{0.8-x}Mn_{0.2}Zn_xFe_2O_4$ (x = 0.4-0.6) as a function of sintering temperature and Zn content. They reported ferrite formation at temperature as low as 500°C using citrate precursor method and high values of saturation magnetizations were observed for mixed compositions. The Curie temperatures were found to decrease with increase of Zn content, while the permeability and a.c. resistivity showed increase. *Zhong et al.* [95] have investigated the effects of sintering temperature and Mn content on magnetic properties of the Ni-Zn ferrites. They observed increase in initial permeability with the increasing of Mn content at higher sintering temperatures of 1220°C and 1260°C while, at lower sintering temperatures

24

the initial permeability was found to be low. Also, higher quality factor was observed for all Mn substituted ceramic samples sintered at 1220°C. *Sattar et al.* [96-98] have studied the effect of Mn substitution on electrical and magnetic properties of Ni-Zn ferrites prepared by convention solid state method. The increase in the resistivity on Mn substitution was observed which they have attributed to decrease of Fe^{2+} ion concentration. The thermoelectric power studies have shown negative sign indicating n-type conduction. The observed electrical behavior was explained by authors considering the spin polaron model. They have also investigated the effect of Al substitution on the structural, IR spectral and magnetic properties of Mn-Ni-Zn ferrites, wherein marked increase in the values of saturation magnetization, initial permeability, Curie temperature and d.c. resistivity with increasing Al-content were observed. *Bueno et al.* [99] have reported the effect of Mn content on microstructure and magnetic properties of Ni-Zn ferrites synthesized by the nitrate–citrate precursor method. They have observed low coercivity and improvement in density and magnetic characteristics like induction magnetization, remanent magnetization with increasing Mn substitution. Also, the effects of Cu, Mn and Mg substitution on the microwave-absorbing feature, the complex permeability and the complex permittivity of Ni-Zn ferrite system was investigated by *Bueno et al.* [100]. They studied the microwave-absorbing properties as a function of frequency, concentration of substituents and thickness of absorber and observed improvements in the microwave absorption and bandwidth with substitution of Cu and Mn while, the substitution of Mg was found to reduce the microwave absorption in relation to non-substituted Ni-Zn ferrite. *Sun et al.* [101-102] have carried out detailed investigation on microstructural and electromagnetic properties of NiO doped Mn-Zn ferrites prepared by a solid-state reaction method. They observed increase in lattice constant, porosity and electrical resistivity with

increase in NiO doping. The hysteresis loss was found to increase with increasing NiO and the sample doped with 0.10 % NiO showed the lowest losses at 1MHz. *Mathur et al.* [103] have reported the dielectric properties of $Mn_{0.4-x}Ni_xZn_{0.6}Fe_2O_4$ (x = 0.05-0.35) compositions prepared by the citrate precursor method as a function of frequency, temperature, composition, and sintering temperature. The dispersion in the dielectric constant with frequency was observed in the range of 75 Hz to 30 MHz and the resonance peaks were observed for all samples in tan δ versus frequency curve. Also, a shift in the resonance frequency toward higher frequency and increases in peak height was reported with the increase in temperature. *Hossain et al.* [104] have studied the structural and magnetic properties of Mn substituted $Ni_{0.5-x}Mn_xZn_{0.5}Fe_2O_4$ (x = 0.0-0.2) sintered at various temperatures. They observed increase in lattice parameter, average grain size and initial permeability with increase in Mn substitution. The bulk density and initial permeability were found to increase with increasing sintering temperature upto 1300°C. The highest relative quality factor and highest initial permeability was observed for $Ni_{0.3}Mn_{0.2}Zn_{0.5}Fe_2O_4$ composition sintered at 1300°C. Also, they observed the strong dependence of initial permeability on average grain size and intragranular porosity. *Venkatraju et al.* [16,105] have studied the physical characteristics and electrical properties of $Ni_{0.5-x}Mn_xZn_{0.5}Fe_2O_4$ (x = 0.0-0.3) ferrites nano particles synthesized by chemical co-precipitation method. The lattice parameters for nanosize Ni-Mn-Zn ferrites were observed to be lower than the corresponding bulk. They observed decrease in saturation magnetization and Curie temperature with increasing Mn concentration except for composition, x = 0.3, which was justified by them considering the migration of Fe^{3+} ions from A site to B site, causing the canting of spin in the B sublattice. The compositional variation of resistivity

showed increase in its value with increasing Mn content. Some of the researchers [106-108] have reported the effect of Mn substitution on structural and magnetic properties of nanosize $Ni_{0.6-x}Mn_xZn_{0.4}Fe_2O_4$ (x = 0.0-0.6), $Ni_{0.5-x}Mn_xZn_{0.5}Fe_2O_4$ (x = 0.0-0.5) and $Ni_{0.7-x}Mn_x$ $Zn_{0.3}Fe_2O_4$ (x = 0.0-0.7) ferrite compositions. They observed an initial increase in saturation magnetization and initial permeability with increase in Mn content followed by decrease in all compositional series. The Curie temperature however showed decrease with increase in Mn content. The observed magnetic behavior was explained by authors considering cation distribution and sublattice magnetization. *Hua et al.* [109] have investigated the influence of MnO_2 additive on the properties of Ni-Zn ferrites prepared by the conventional powder metallurgy where they observed gradual decrease in the average grain size, sintering density and real permeability with the increase of the MnO_2 content. The d.c. resistivity showed increase, while the saturation magnetization first increases slightly then gradually decreased with increasing MnO_2 mass fraction.

1.7.1. Literature review of metal carboxylate-hydrazinate complexes

Several metal as well as mixed metal carboxylates (mono and di) has been investigated in detail for structure, thermal decomposition and their application as a precursor for synthesis of industrially important ferrites. Recently, the focus has been shifted on the use of hydrazinated metal carboxylates to yield metal oxides at relatively lower temperatures. Although, commercially hydrazine is used as a monopropellant and rocket fuel, it can also serve as very good ligand because of the lone pairs present on nitrogen atoms and hence neutral hydrazine can coordinate to the metal ions as either monodentate ligand or bridging bidentate ligand to form complexes. Neutral hydrazine complexes are thermally more reactive

than mono protonated hydrazine or hydrazinium complexes. Hence, the complexes containing neutral hydrazine molecules such as hydrazinated metal carboxylates are gaining importance, as they can act as a single source precursor to prepare stiochiometrically pure and nanosize mixed metal oxides at relatively lower temperatures and shorter time. Considering the advantages of hydrazinated carbxylate precursor method, we have used this technique for synthesis of preparation of Ni-Mn-Zn ferrites. This section gives the brief literature review of hydrazine / hydrazinated metal carboxylate complexes.

The synthesis of transition metal and mixed metal carboxylate hydrazinate complexes gained momentum in 1983 onwards due to their use as precursors for fine particles metal / mixed metal oxides. K.C. Patil and D. Gajapathy [110-111] reported for the first time the synthesis, spectral, magnetic and thermal characteristics of the hydrazinium oxalates complexes of Mn, Ni, Co and Cu which they have used as precursors to ultrafine metal oxides. The Cu showed square planar geometry while nickel and cobalt formed octahedral complexes.They also synthesized mixed metal oxalate hydrazinates involving metals such as Mn, Co, Ni and Zn from aqueous solution. These mixed metal oxalates hydrazinates were used as precursors in the synthesis of spinel ferrites, MFe_2O_4. These precursors exhibited autocatalytic decomposition behaviour to give ferrites at very low temperatures (130°C to 250°C). *Ravindranathan et al.* [112-115] have prepared metal formate hydrazinates involving Mn, Co, Ni, Zn and Cd and investigated the thermal characteristics of these hydrazinated metal formate precursors. They observed endothermic dehydrazination for all complexes except Ni complex. The decomposition end products were found to be ultrafine metal oxides. They also reported the synthesis of hydrazinium mixed metal hydrazine carboxylate solid solution precursors which were employed in the synthesis of fine-particle cobaltites and Ni-

Zn ferrites at low temperatures. They observed very high sintered densities for Ni-Zn ferrites obtained from above precursors. *Mahesh et al.* [116] have reported the preparation and characterization of metal acetate hydrazinates of Mn, Co, Ni, Zn, and Cd. They reported exothermic thermal decomposition of metal acetate hydrazinates through metal acetate intermediates into their respective ultrafine metal oxides. *K.C. Patil* [117] reported the dependence of thermal reactivity on coordinated anions in metal-hydrazine complexes. The complexes with anions such as sulphate, sulphite, acetate and formate were found to decompose while, the oxalate and hydrazine carboxylates showed deflageration and nitrate and perchlorate complexes were found to detonate. The deflagerating nature of the metal-hydrazine oxalates and hydrazinocarboxylates has been employed by the authors in the combustion synthesis of fine particle of γ-Fe_2O_3, ferrites and cobaltites at low temperature. *Sunder Manoharan et al.* [118] reported the synthesis of copper and chromium hydrazine carboxylate complexes. Their report suggests that the thermal decomposition of copper complex yields mixture of copper metal and copper oxide while, the chromium complexes on thermal decomposition yields Cr_2O_3 as residue. *Moye et al.* [119] have used mixed-metal oxalato hydrazinate precursor prepared by a solution method and the oxalato hydrazinate precursor prepared by under hydrazine method to prepare $Ni_xZn_{1-x}Fe_2O_4$ (x = 0.0-0.1). They investigated the thermal decomposition of the precursors and formation of ferrite by differential thermal analysis, total mass loss studies, infrared, chemical analysis, X-ray diffraction and magnetization measurements. Also, they reported formation of γ-Fe_2O_3 type phase in situ in methods. *Borkar et al.* [120] have reported the preparation of γ-Fe_2O_3 by the thermal decomposition of ferrous oxalate dihydrate and ferrous oxalato hydrazinate precursors. They observed formation of γ-Fe_2O_3 when ferrous oxalate dihydrate decomposed

in the controlled atmosphere, while the autocatalytic decomposition of hydrazinated complexes leads to mixture of γ-Fe_2O_3 and α-Fe_2O_3. *Sekar et al.* [121] have used hydrazine carboxylate precursors to prepare anatase-TiO_2, ZrO_2 and zirconyl titanate. They observed very high surface area for anatase-TiO_2 and very low dielectric loss (4×10^{-4}) for zirconyl titanate. *Sivasankar et al.* [122-126] reported preparation and characterization of bis (hydrazine) complexes of metal malonates and succinates. The hydrazinated complexes were found to be high spin and octahedral. They observed the bidentate bridging nature of hydrazine and monodentate linkages for malonate and succinate moieties in complexes. They also carried out synthesis of hydrazinium complexes of mixed metal malonate dihydrates, which were employed as precursors for the preparation of metal cobaltites. The metal cobaltites, MCo_2O_4 (M = Mg, Mn, Ni, Zn and Cd) were obtained as residue after decomposition of these complexes at 500°C for about 15 minutes. The same group also studied the magnetic and spectral properties of hydrazinium glycinate complexes of metal such as Co, Ni, Zn and anhydrous as well as hydrated rare earth hydrazine acetates involving La, Ce, Pr, Nd and Sm. The decomposition of these complexes were found to be highly exothermic giving metal oxide powder as the final residue in the case of transition metal complexes, while in the case of rare earth complexes the end products were found to be respective metal oxide carbide. *Jiji et al.* [127] have reported the synthesis of ferrous hydrazine acetate complex which was characterized using chemical analysis, magnetic measurements, electronic and IR spectral studies. The autocatalytic decomposition behavior shown by other metal carboxylato hydrazinates was not observed for this complex. They also studied the decomposition kinetics of the complex and observed negative values of activation entropy which were attributed to the more ordered structures of the transition state than the

30

reactants. *Kuppusamy et al.* [128-129] have reported the synthesis of metal hydrazinates of benzoic acid and substituted benzoic acid. They observed the monodentate coordination of carboxylate ion and bidentate bridging coordination of hydrazinium cation in the complexes. The reported magnetic and electronic spectral data indicated the octahedral geometry for Mn, Co and Ni complexes while, the square-planar geometry for Cu complexes. Most of the complexes they studied were found to give metal hydroxybenzoates as intermediates during thermal decomposition. Also, they reported the synthesis of hydrazine benzoate complexes of Mn and Zn, bis(hydrazine) benzoate complexes of Fe, Co, Ni, Zn and Mg, and bis(hydrazinium) nickel benzoate complex in aqueous solution by the reaction of hydrazinium benzoate and the corresponding metal nitrate hydrates. They observed tetrahedral geometries for monohydrazine complexes and octahedral geometries for bis(hydrazine) and bis(hydrazinium) complexes. The thermal studies of complexes indicated both exothermic and endothermic decomposition via metal benzoate or oxalate intermediates. *Yasodhai et al.* [130-133] have explored the chemistry of both hydrazinates and hydrazinium complexes of metals coordinated with carboxylates such as citrate, glutarate, adipate, pimelate, suberate, azelate, sebacate, malate and oxydiacetate. The metal citrate hydrazinates of Co, Ni, Zn and Cd showed monodentate coordination of hydrazine in hydrazinium complexes and bidentate bridging coordination of neutral hydrazine in hydrazinate complexes. The bridging behavior for both, the hydrazine and the long chain dicarboxylate dianion was also observed by them in hydrazinium oxydiacetate salts of Co, Ni, Cd and Zn. The same researchers found that hydrazine complexes of uranium containing above carboxylate moieties shows the uni and bidentate coordination of dicarboxylate anions to uranium depending upon the coordination polyhedra. The end product of decomposition of all the complexes was found to be U_3O_8

formed through their respective uranyl dicarboxylate intermediates. *Rane et al.* [134-135] have reported the synthesis of iron (II) carboxylato-hydrazinates using various carboxylates like oxalate, fumarate, malonate, succinate, maleate, tartrate and malate. These carboxylato-hydrazinates of iron (II) on thermal decomposition in air found to give mostly γ-Fe_2O_3. They later have carried out lithiation of γ-Fe_2O_3 by stirring with n-butyl lithium in inert atmosphere. Also, the electromagnetic properties of magnesium ferrite prepared using γ-Fe_2O_3 obtained from thermal decomposition of above carboxylato-hydrazinates precursor have been reported by them. *Premkumar and others* [136-138] have reported the synthesis of pyrazinecarboxylate hydrazinates of some transition metals obtained by the reaction of respective metal nitrate hydrates with 2-pyrazinecarboxylic acid and hydrazine hydrate. They observed high spin character and octahedral geometry for the Co and Ni complexes. The thermal studies indicated exothermic loss of hydrazine in 2,3-pyrazinedicarboxylate hydrazinate complexes and endothermic loss in 2-pyrazinecarboxylate hydrazinate complexes. Also, they carried out spectral and thermal studies on divalent transition metal 3,5-pyrazoledicarboxylate hydrates, 3,5-pyrazoledicarboxylate hydrazinates and 3,5-pyrazoledicarboxylate hydrazinate hydrate and observed endothermic dehydration for metal carboxylate hydrates and endothermic dehydrazination for metal carboxylate hydrazinates as a first step during thermal decomposition. All the metal complexes were found to give respective metal oxides as the end products except the manganese complex which decomposes to give manganese carbonate. *Vikram et al.* [139-140] have reported the preparation of cobaltites from the thermal decomposition of bis(hydrazine) complexes of mixed metal glyoxylates. The binding nature of hydrazine in these complexes was found to be bidentate bridging. The thermal studies of these complexes indicated multi-step degradation and the final products were found to be the

ultrafine metal cobaltites. They also studied the analytical, spectral and thermal characteristics of hydrazinium complexes of metal (II) ethylenediaminetetraacetates involving Co, Ni, Cu, Mn and Zn. They observed octahedral geometry for all the prepared complexes except Mn and multi-step degradation to give the respective metal oxides as the residue. *Rane et al.* [141] have reported the synthesis of various ceramic materials such as γ-Fe_2O_3, ferrites such as Mn-Zn ferrite and K-doped $CuFe_2O_4$, perovskites like $BaTiO_3$, La-Sr-MnO_3, La-Sr-AlO_3, La-Gd-Ca-Ba-Sr-CoO_3 and anatase TiO_2 by under hydrazine method. The authors observed that the use of hydrazinated carboxylate precursor lowers the decomposition temperature of precursor resulting in ultrafine oxides. *Raju et al.* [142-143] have reported the synthesis and spectral properties of bis(hydrazine) glyoxylate complexes of lanthanide and bis(hydrazine), tris(hydrazine) and hydrazinium pyruvates complexes of transition metals. The thermal studies of metal hydrazine glyoxylates have shown multi-step decomposition resulting into the respective metal oxides. These metal oxide residues were characterized by their metal analysis, infrared spectra and the X-ray powder diffraction patterns. These complexes displayed single step decomposition behavior giving the respective metal carbonate as the end residue. *Verenkar et al.* [144-154] have investigated in detail the thermal behavior of various metal as well as mixed metal carboxylato hydrazinates and explored the possible application of these complexes as precursors in the synthesis of metal oxides like γ-Fe_2O_3 and mixed metal oxides such as manganites, cobaltites, ferrites (simple as well as multi-substituted) using various hydrazinated metal dicarboxylates like malonate, succinate, malate, tartrate, maleate and fumarate. They observed bidentate coordination of hydrazine and monodentate coordination of carboxylate anions to the metal. All the complexes were found to display autocatalytic decomposition behaviour giving ultrafine oxides at relatively lower temperature.

They characterized the decomposition end products using XRD, IR, TG / DSC / DTA, TEM and EDX. The decomposition behavior of these complexes was found to differ markedly depending on the chemical composition of carboxylate anion.

1.8. Aim, objectives and work plan of the present investigation

Nickel zinc ferrite is the most popular composition of soft ferrites and is most versatile ceramic material suitable for high frequency applications in the electronic devices. Due to the high resistivity, low eddy current losses and coercivity, these ferrites are used in radio frequency circuits, high quality filters, rod antennas, transformer cores, read and write heads for high speed digital tapes and operating devices. They are more stable than the other types of ferrites, can be easily manufactured and have excellent magnetic properties. The properties of Ni-Zn ferrite are sensitive to the compositional variability and the microstructure which is governed by the method of preparation. The only disadvantage of this ferrite system is their low permeability at higher frequencies and increasing cost. For high frequency magnetic applications, ferrite materials should possess high permeability as well as high resistivity which can reduce eddy current losses. Therefore, an appropriate doping of manganese in Ni-Zn ferrites can result in the material with enhanced properties, more suitable for high frequency applications.

The nanocrystalline ferrites are the materials of current interest because of their unique electric, dielectric, magnetic and optical properties which make them appealing from theoretical and technological point of view. These nanoparticles find use in biomedical applications like cancer treatment by hyperthermia, MRI contrast agent, drug delivery, DNA hybridization etc.

The properties of ferrite systems are very sensitive to the cation distribution which in turn depends on method of preparation and subsequent heat treatment. Most of the reported studies on Ni-Mn-Zn ferrites involve synthesis by ceramic methods which suffers from drawbacks like low density, large and uneven grain size, non-stoichiometry resulting in deviation in bulk electrical and magnetic properties. It has been well established fact that nanocrystalline ferrites can be easily synthesized using wet chemical methods at relatively lower temperatures. It was therefore proposed to employ carboxylato hydrazinate precursor combustion technique in which precursors not only undergoes autocatalytic decomposition once partially ignited to give as synthesized nanosize ferrites, which can be sintered subsequently but also lowers the ferritization temperature. Hence, we have synthesized Ni-Mn-Zn ferrites using fumarato hydrazinate precursor combustion technique. Since most of the reported studies involve high ferritization temperatures, it was decided to optimize the ferritization temperature, time and atmosphere for bulk Ni-Mn-Zn ferrite systems. The precursor complexes, the 'as synthesized' ferrites and the sintered ferrites were intended to be characterized using various techniques such as FTIR, TG/DTA/DSC, X-ray Diffractometry (XRD), Transmission electron microscopy (TEM), Scanning electron microscopy (SEM), Mössbauer spectroscopy, X-ray photoelectron spectroscopy (XPS). A systematic investigation of effect of manganese doping on structural, electric, dielectric and magnetic properties of both nanosize and bulk Ni-Zn ferrite compositions is also proposed to be carried out.

One of the objectives was to search for some useful commercial applications of these nanocrystalline ferrites. The literature survey revealed that the nanocrystalline spinel ferrites have been explored in recent years as gas sensors for both oxidizing and reducing gases due to their stability and sensing capability over wide range of temperatures. With this goal in mind,

we have studied gas sensing properties of the nanocrystalline ferrite powders for various toxic/nontoxic gases like NH_3, Cl_2, H_2, CO_2, LPG etc.

In summary, the main aim of this research work has been to develop a cost effective preparation technique for industrially important Ni-Mn-Zn ferrite systems and to obtain a material with better and enhanced properties than Ni-Zn ferrites suitable for high frequency magnetic applications. Based on these ideas, systematic investigations were undertaken and the results are presented in the thesis. The thesis is organized into five chapters:

Chapter - I includes the brief introduction of the subject with the aim, objectives and plan of the proposed research work.

Chapter - II describes the details of experimental work and characterization techniques.

Chapter - III deals with synthesis and characterization of hydrazinated precursors of mixed nickel manganese zinc ferrous fumarates, $Ni_{0.6-x}Mn_xZn_{0.4}Fe_2(C_4H_2O_4)_3.6N_2H_4$ ($x = 0.0$-0.6) and solid state studies carried out on $Ni_{0.6-x}Mn_xZn_{0.4}Fe_2O_4$ ($x = 0.0$-0.6) ferrite compositions.

Chapter - IV includes synthesis and characterization of hydrazinated precursors of mixed nickel manganese zinc ferrous fumarates, $Ni_{0.5-x}Mn_xZn_{0.5}Fe_2(C_4H_2O_4)_3.6N_2H_4$ ($x = 0.0$-0.5) and solid state studies carried out on $Ni_{0.5-x}Mn_xZn_{0.5}Fe_2O_4$ ($x = 0.0$-0.5) ferrite compositions.

Chapter - V gives the summary of research work and conclusion drawn on research findings.

A complete list of references has been given towards the end of the thesis. Finally, a concise list of publications in-peer reviewed international journals and national / international conferences related to present research work has been presented at the end.

Chapter 2

Experimental details and characterization techniques

Experimental details and characterization techniques

2.1. Introduction

The synthesis is very important step in a processing of material to obtain desired properties. In case of spinel ferrites the structural and magnetic properties are very sensitive to the preparative conditions. Hence, the properties of ferrites can be tailored by the use of suitable preparative technique. Besides the conventional ceramic methods [14,95,101], various wet chemical methods such as sol-gel [15,99], hydrothermal [155-156], reverse micelle [157], co-precipitation [158-159], precursor [147,160] and combustion method [161-162] were used by researcher to prepare spinel ferrites. There has been considerable interest among researchers in the study of hydrazine derivatives of metal carboxylates, since they can serve as precursors to fine particle oxide materials at relatively lower temperatures. Considering the growing interest in the precursor method particularly for synthesis of nanocrystalline materials, we thought of using this technique to prepare Mn substituted Ni-Zn ferrites.

2.2. Synthesis of hydrazinated mixed nickel manganese zinc ferrous fumarate complexes, $Ni_{0.6-x}Mn_xZn_{0.4}Fe_2(C_4H_2O_4)_3.6N_2H_4$ $(x = 0.0-0.6)$

2.2.1. Materials

All reagents used were of analytical grade. The stoichiometric quantities of chloride salts of Mn (II), Zn (II) and Ni (II) were dissolved in distilled water to achieve the mole ratio

of one. The Fe (II) chloride solution was freshly prepared by dissolving iron powder in concentrated hydrochloric acid under CO_2 atmosphere.

2.2.2. Experimental

The synthesis of Ni-Mn-Zn ferrite precursor was carried out using fumarato hydrazinate precursor method. The stoichiometric mixture of aqueous sodium fumarate and hydrazine hydrate (1:2 ratio) was prepared and stirred continuously for 2h in 3 neck flask under nitrogen atmosphere. The ferrous chloride solution (2M) was freshly prepared by dissolving iron powder in hydrochloric acid under CO_2 atmosphere. The ferrous chloride solution was then added to 1M mixed metal chloride (1M) solution containing zinc chloride, nickel chloride and manganese chloride. The hydrazinated complex of mixed nickel manganese zinc ferrous fumarate was obtained by slow dropwise addition of mixed metal chloride solution to the well stirred stoichiometric mixture of aqueous sodium fumarate and hydrazine hydrate under nitrogen atmosphere. The yellow coloured precipitate of hydrazinated mixed metal fumarate precursor obtained was filtered, washed with ethanol, dried with diethyl ether on suction and stored in vacuum desiccator. The formation of hydrazinated precursor of mixed nickel manganese zinc ferrous fumarate occurs according to following equation:

$$MCl_{2(aq)} + 2FeCl_{2\,aq} + 3C_4O_4H_2Na_{2\,(aq)} + 6N_2H_4.H_2O_{(aq)} \longrightarrow MFe_2(C_4H_2O_4)_3.6N_2H_{4(s)}$$

$$+ 6NaCl_{(aq)} + 6H_2O_{(l)} \quad ----\{2.1\}$$
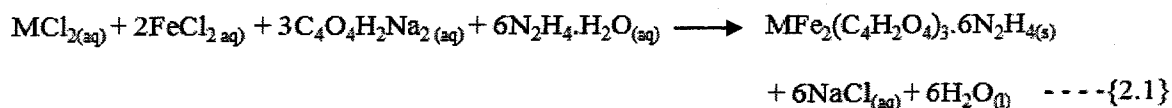
$(M = Mn^{2+}, Ni^{2+} and Zn^{2+})$

The flowsheet (Fig. 2.1) diagram gives the stepwise preparation of the precursor, as synthesized ferrite and sintered Ni-Mn-Zn ferrite.
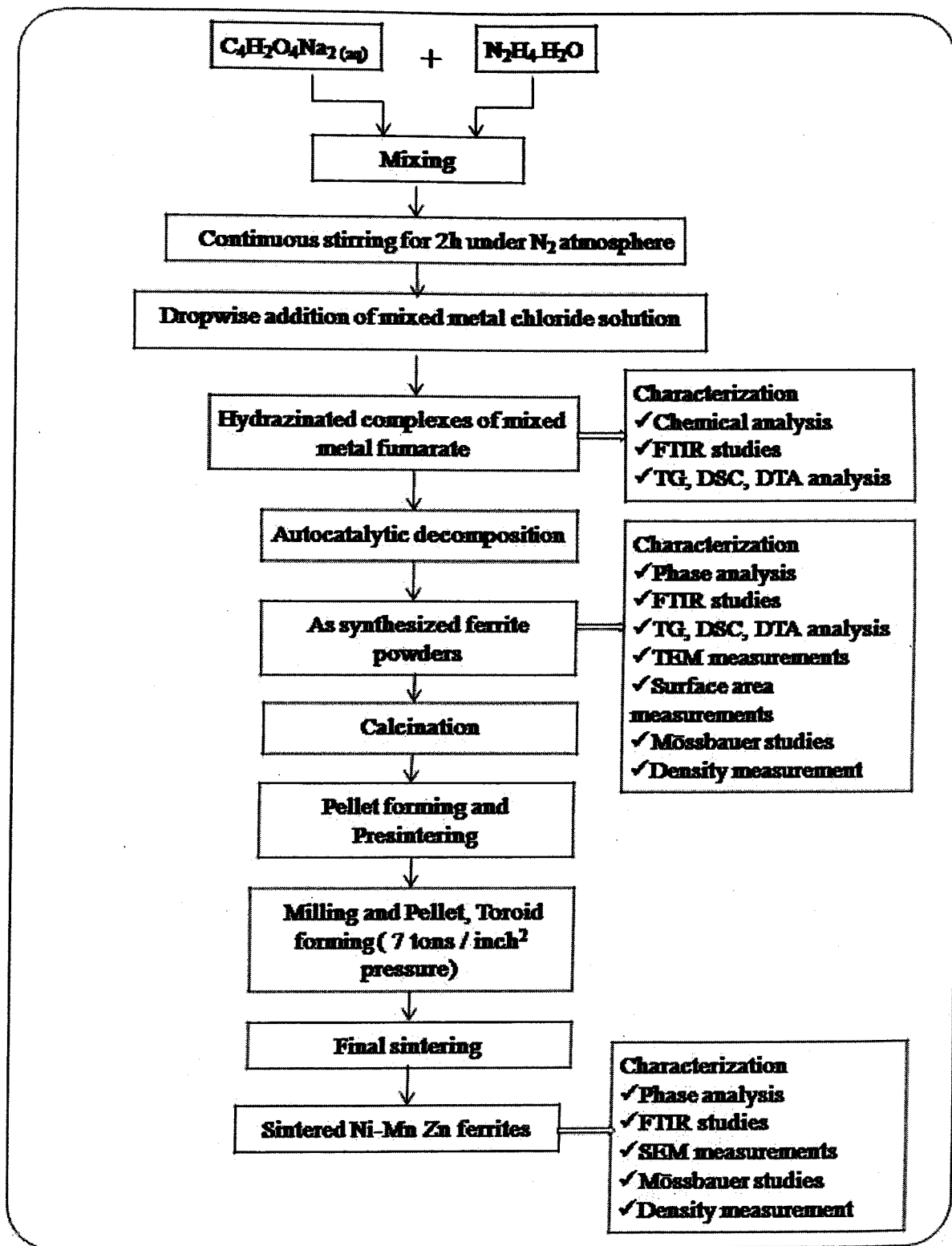
Fig. 2.1. Flowsheet diagram for synthesis of Ni-Mn-Zn ferrites

39

2.2.3. Thermolysis of the hydrazinated mixed nickel manganese zinc ferrous fumarate precursors

The thermal decomposition of precursor complexes in air proceeds according to equation:
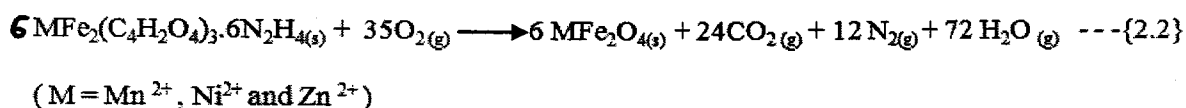
$$6\,MFe_2(C_4H_2O_4)_3.6N_2H_{4(s)} + 35\,O_{2(g)} \longrightarrow 6\,MFe_2O_{4(s)} + 24\,CO_{2(g)} + 12\,N_{2(g)} + 72\,H_2O_{(g)} \quad ---\{2.2\}$$

$(M = Mn^{2+}, Ni^{2+} \text{ and } Zn^{2+})$

The thermal decomposition of hydrazinated precursor of mixed nickel manganese zinc ferrous fumarate precursor was found to self propagating and autocatalytic. For autocatalytic decomposition, the precursors were spread uniformly over a ceramic tile and ignited with a burning splinter at one of the corner. They catch fire and burn without producing flame but forming a red glow which spreads over the entire bulk completing the total decomposition in an ordinary atmosphere. During thermal decomposition of precursor in air, small atomic clusters of nascent metal oxides with proper chemical homogeneity are formed. These clusters react together and forms nanosize ferrites. The exothermicity of the combustion is sufficient enough for complete decomposition of precursor complexes resulting into nanosize spinel oxides without requiring any external supply of heat energy. Also, the evolution of various gases like water vapour, CO_2 and N_2 during decomposition of the precursor helps in the dissipation of the heat of decomposition which prevents the sintering and agglomeration (to some extent) of ultrafine ferrite particles during their formations [163-164].

2.2.4. Calcination

The 'as synthesized' ferrite powders obtained after the autocatalytic thermal decomposition of precursors were found to contain residual carbon as observed in the

thermogram. Further, the thermogram indicates complete oxidation of carbon in the temperature range 400°C to 500°C. Hence, these 'as synthesized' powders were calcined at 500°C for five hours for complete removal of residual carbon.

2.2.5. Presintering and milling

The purpose of presintering in convention method is to start the process of formation of spinel ferrite lattice. In case of ferrites prepared by non conventional methods presintering helps in removing the volatile impurities and homogenization of the powder mixture. Some shrinkage occurs during presintering and hence one advantage of the process is to reduce the shrinkage in the final sintering which allows better control of the final dimension of the sintered pellet or torroid. The calcined 'as synthesized' ferrite powders were pelletized and presintered at 800°C for five hours in muffle furnace. The amount of milling determines the particle size distribution, which in turn influence the homogeneity and microstructure of the pellets or torroids used for the final sintering. These presintered pellets were then made to very fine powders by grinding in agate mortar for 2h.

2.2.6. Pellet and torroid forming

After milling for 2 h, the powders were pressed into pellets of dimension 10 mm diameter and 1mm to 2 mm thickness using a conventional die and applying a pressure of 7 tonnes / inch^2 for 3 minutes using a hydraulic press. The torroids of dimensions, 20 mm outer diameter, 10 mm inner diameter and 2 mm to 3 mm thickness were prepared using torroidal die and applying 7 tonnes / inch^2 pressure for 3 minutes in a hydraulic press.

2.2.7. Final sintering

Sintering is a very important step in processing of ferrite materials. As material synthesis and processing have become crucial in recent years for materials development, the importance of sintering is increasing as a material processing technology. It is a method used to produce density controlled materials and components from ceramic powders by applying thermal energy. Sintering is required for microstructural control which includes the control of grain size, density and distribution of pores. In most cases, the final goal of microstructural control is to prepare a dense material with a uniform grain structure. The two major variables which determine sinterability and the sintered microstructure of a powder are material variables and process variables. The material variables include chemical composition of powder, size, shape, size distribution and degree of powder agglomeration. These variables influence the powder compressibility and sinterability i.e. the densification and grain growth. The process variables involved in sintering are mostly thermodynamic variables, such as temperature, time, atmosphere, pressure, heating and cooling rate. However, in real processing, the effects of sintering atmosphere and pressure are much more complicated. In the present investigation all the presintered pellets and toroids were sintered at four different temperatures from 1100°C to 1250°C at a heating rate 5° / minutes for 1 h in air and furnace cooled.

2.3. Characterization of precursors and Ni-Mn-Zn ferrites

The characterization is required to establish the proper identity of materials. Different characterization technique provides different information related to the chemical identity of a substance and by using the information obtained from different techniques complete chemical

identity can be established. In the present study the chemical composition of precursors, the 'as synthesized' and the 'sintered' Ni-Mn-Zn ferrites were determined using techniques like chemical analysis, XRD, TEM, SEM-EDS, XPS, IR, Mössbauer spectroscopy etc. The studies of physical properties such as density, porosity, phase and structural analysis of 'as synthesized' as well as 'sintered' Ni-Mn-Zn ferrite samples were performed. The electrical and magnetic properties of the sintered pellets and torroids were determined. The nanosize 'as synthesized' Ni-Mn-Zn ferrites were also explored for gas sensing application in the form of thick films. The details of the experimental techniques are as below.

2.3.1. Chemical analysis

The molecular composition of the precursors was determined by chemical analysis. The hydrazine content in the precursors was determined by titrimetric analysis using standard 0.025M KIO_3 solution under Andrew's conditions [165]. The metal contents in the precursors were determined by chemical analysis after decomposing the known amount of precursors with concentrated nitric acid using standard procedures [165]. The iron content was determined gravimetrically as Fe_2O_3, nickel content was determined by gravimetrically as Ni-dimethylglyoximato complex, while manganese and zinc was determined together titrimetrically using suitable masking agent.

2.3.2. FTIR spectral studies

The FTIR spectroscopy has emerge as a very powerful technique for characterization of both organic as well as inorganic compounds. For inorganic crystalline compounds it is very important technique to derive information about the positions of ions in the crystal lattice

through the crystals vibration mode [166]. The spinel ferrites are ceramic oxides which exhibit cubic structure. Both normal and inverse cubic spinel ferrites display two principal absorption bands in the IR spectrum. The occurrence of these two bands (v_1 and v_2) has been attributed to the intrinsic vibrations of tetrahedral and octahedral coordination complexes. Besides these principal absorption bands few weak absorption bands also appears in the lower frequency region of the IR spectrum. These bands arise due to the lattice vibration of oxide ions against the cations [167]. The FTIR spectra of the samples were recorded on a Shimadzu FTIR prestige 21 spectrometer from 4000 cm^{-1} to 300 cm^{-1} in diffuse reflectance mode. The samples were prepared by mixing sample powder with potassium bromide in the ratio of 1:100.

2.3.3. Thermal analysis

Thermal analysis includes a group of techniques in which one (or more) property of a sample is studied while the sample is subjected to a controlled temperature programme. Thermal analysis detects the interatomic and inter / intramolecular interactions which are related to an external change in temperature. The thermogravimetric analysis (TGA) measures the change in mass of materials as a function of temperature and time in a controlled atmosphere. TGA is particularly suitable for study of the volatile content, thermal stability, degradation / decomposition characteristics, sintering behaviour and reaction kinetics of materials. Differential scanning calorimetry (DSC) measures the heat flow associated with physical changes such as phase transition, melting, crystallization, glass transition, curing, adsorption, desorption etc. It is mainly used to determine melting point, crystallinity, heat capacity, crystalline impurities etc. Differential thermal analysis (DTA) measures the

temperature difference of the sample against reference which is caused by thermal event in a material. The information obtained from DTA is similar to DSC. For ferrite materials these techniques provides very essential information related to ferritization temperature, impurities, any metastable secondary phases etc. The simultaneous thermogravimetry and differential scanning calorimetry (TG/DSC) and simultaneous thermogravimetry and differential thermal analysis (TG/DTA) measurements were performed using NETZSCH DSC-DTA-TG STA 409PC setup equipped with control and data acquisition system. The analyses were carried out in air (100 ml / min) at a heating rate of $10^{\circ}C$ /min using 15 mg to 20 mg samples in an alumina crucible with another alumina crucible as the reference material. The thermal analysis was carried out from room temperature to $800^{\circ}C$.

2.3.4. X-ray diffraction

X-ray diffraction (XRD) is a powerful non destructive technique used for characterization of crystalline materials. It is used for structure determination of single crystal as well as polycrystalline materials. The technique provides valuable information of structures, different phases and preferred crystal orientations. Besides this, it also gives reliable information on structural parameters such as average grain size, crystallinity, strain and crystal defects. The applications of XRD technique in the study of materials are many but primararily it is used for:

- Identification and quantification of crystalline phases.

- Measurement of average crystallite size, strain or micro-strain effect

- Phase identification of large variety of bulk as well as thin film samples.

- Detecting crystalline minority phases at concentration above 1%.

- Measuring residual stress in bulk metal and ceramics.

In the X-ray diffraction method peaks are produced by constructive interference of a monochromatic beam of X-ray scattered at specific angles from each set of lattice planes in the sample. The peak intensities are determined by the distribution of atoms or ions within the lattice. Hence, the XRD pattern is the finger print of periodic atomic arrangements in the given crystalline material. A search of the ICDD standard database of XRD pattern enables quick identification of large variety of crystalline samples. The powder X-ray diffraction method is generally used for determination of structure and purity of ferrites. A beam of X-rays is sent into the sample and the way the beam is scattered by the atoms in the path of the X-ray is studied. The constructive interference of scattered X-rays can be looked at using Bragg's Law to determine various characteristics of the crystal as well as polycrystalline material. The interplanar distance 'd' for each 'hkl' plane is calculated using Bragg's equation [168]:

$$n\lambda = 2d\sin\theta \qquad -------------------\{2.3\}$$

Where, d is the interplanar distance, n is the order of interference, λ wavelength of X-ray target used and θ is the angle of diffraction. The lattice parameter 'a' for each plane is calculated using 'd' values obtained from Bragg's Law using the relation [169]:

$$a = d_{hkl}\sqrt{(h^2 + k^2 + l^2)} \qquad ----------------\{2.4\}$$

Where, a is the lattice parameter, d is the spacing between the h, k, l diffraction planes.

The X-ray density can be obtained using equation [170]:

$$\rho_{X-ray} = \frac{8M}{Na^3} \quad --------------------------\{2.5\}$$

Where, M is the molecular weight of the sample, N is the Avogadro's number, a is the lattice parameter. The bulk density is calculated considering the cylindrical shape of the pellet using the relation [170]:

$$\rho_{Exp} = \frac{m}{\pi r^2 h} \quad --------------------------\{2.6\}$$

Where, m is the mass of the pellet, $\pi r^2 h$ represents the volume of the pellet. The porosity of the ferrites is calculated from the X-ray density (ρ_{X-ray}) and bulk density (ρ_{bulk}) density by using the relation [169]:

$$P = 1 - \frac{\rho_{Exp}}{\rho_{X-ray}} \quad --------------------------\{2.7\}$$

The average crystallite size is calculated from most intense XRD peaks using Debye-Scherrer formula [171]:

$$t = \frac{0.89\lambda}{\beta \cos\theta} \quad --------------------------\{2.8\}$$

Where, λ is the wavelength of X-ray used; β is the full width at half maximum; θ is the Bragg's diffraction angle. The distance between the magnetic ions (hopping length) in tetrahedral 'L_A' and octahedral 'L_B' sites in the spinel lattice are calculated by using relation [172-173]:

$$L_A = \frac{a\sqrt{3}}{4} \quad --------------------------\{2.9\}$$

$$L_B = \frac{a\sqrt{2}}{4} \quad --------------------------\{2.10\}$$

The mean ionic radius of the tetrahedral (A) site 'r_A' and octahedral [B] site 'r_B' is calculated from the revised values of ionic radii of metal ions [174] considering the most probable cation distribution using relation [175-176]:

$$r_A = [\, C_{Zn^{2+}}.rZn^{2+} + C_{Mn^{2+}}.rMn^{2+} + C_{Fe^{3+}}.rFe^{3+}\,] \quad --------- \{2.11\}$$

$$r_B = [\, C_{Zn^{2+}}.rZn^{2+} + C_{Mn^{2+}}.rMn^{2+} + C_{Ni^{2+}}.rNi^{2+} + C_{Fe^{3+}}.rFe^{3+}\,] \,/\, 2 \quad --\{2.12\}$$

The theoretical lattice parameter is calculated from mean ionic radii of tetrahedral and octahedral sites using relation [177]:

$$a_{th} = \frac{8}{3\sqrt{3}}[(r_A + R_O) + \sqrt{3}\,(r_B + R_O)] \quad --------------- \{2.13\}$$

The oxygen position parameter 'u' is calculated using the radius of oxygen ion (R_O =1.32 °A) and the mean ionic radii of tetrahedral site 'r_A' in the expression [178]:

$$r_A = \left(u - \frac{1}{4}\right) a\sqrt{3} - R_O \quad ----------------- \{2.14\}$$

The tetrahedral bond length (A-O), octahedral bond length (B-O), tetrahedral edge length (A-E), shared octahedral edge length (B-E shared) and unshared octahedral edge length (B-E unshared) are calculated using the theoretical lattice parameters 'a_{th}' and oxygen position parameter 'u' values in equation [179-180]:

$$d_{A-O} = a_{th}\sqrt{3}\left(u - \frac{1}{4}\right) \quad ------------------- \{2.15\}$$

$$d_{B-O} = a_{th}\sqrt{3u^2 - \left(\frac{11}{4}u\right) + \frac{43}{64}} \quad --------------- \{2.16\}$$

$$d_{A-E} = a_{th}\sqrt{2}\left(2u - \frac{1}{2}\right) \quad ------------------- \{2.17\}$$

$$d_{B-E} = a_{th}\sqrt{2}\,(1 - 2u) \quad ------------------ \{2.18\}$$

$$d_{B-E} = a_{th}\sqrt{2}\,(1 - 2u) \quad ------------------- \{2.18\}$$

$$d_{B-EU} = a_{th} \sqrt{\left(4u^2 - 3u + \frac{11}{16} \right)} \qquad -------------\{2.19\}$$

2.3.5. Transmission electron microscopy (TEM)

Transmission electron microscopy (TEM) has been used as a very important tool in the study of nanocrystalline materials. The advantages of TEM are its high lateral spatial resolution and its capability to provide both image and diffraction information from a single sample. In addition, the highly energetic beam of electrons used in TEM interacts with sample matter to produce characteristic radiation and particles and these signals are often measured to provide materials characterization using EDS. TEM uses electromagnetic lenses to focus the electrons into a very thin beam. The electron beam then travels through the specimen under study. Depending on the density of the material present, some of the electrons are scattered and disappear from the beam. At the bottom of the microscope the unscattered electrons hit a fluorescent screen, which gives rise to a shadow image of the specimen with its different parts displayed in varied darkness according to their density. The image can be studied directly or photographed with a camera. High-Resolution TEM (HRTEM) works on the interference of the electron beam by the sample which gives a higher resolution beneficial when studying nanosize samples. The shape and size of the ferrite nanoparticles was determined using a Philips electron microscope model CM20.

2.3.6. BET surface area

The surface area determination of material is very useful for porous materials like catalyst, adsorbents and non porous materials like filler, metal powders, powdered drugs,

pigments etc. The BET surface area of the samples was determined using micrometric SMART SORB 90/91 adsorption system. The instrument works on the theory proposed by BRUNAUER-EMMET-TELLER known as BET theory. According to this theory, at known partial pressure, amount of N_2 (or any other inert gas) adsorbed by the sample at liquid N_2 temperature can be expressed in the form of mathematical equation, involving physical terms such as partial pressure of gas, volume for monolayer adsorption and volume adsorbed at equilibrium pressure. The mathematical equation for surface area calculation is given as:

$$\frac{P}{V_{ad}}(P_0 - P) = \frac{1}{CV_m} + \left[\left(\frac{C-1}{CV_m}\right)\right] \times \frac{P}{P_0} \qquad - - - - - - - - - - - - - \{2.20\}$$

Where, P is adsorption equilibrium pressure, P_0 standard vapour pressure of the adsorbent, V_{ad} volume at STP occupied by molecules adsorbed at pressure P, V_m volume of adsorbate required for a monolayer coverage, C is the constant related to heat of adsorption.

A plot of P/ V ads (P_0-P) versus (P/P_0) will be straight line usually in the range $0.05 \leq$ P / $P_0 \leq 0.35$. The slope (s) and intercept (i) of the BET plot are

$$S = \frac{(C-1)}{CV_m} \qquad -\{2.21\}$$

$$i = \frac{1}{CV_m} \qquad -\{2.22\}$$

Solving these equations permits the calculation of Vm. Then, the specific surface area of the solid can be calculated as:

$$\text{Specific surface area } (m^2/g) = \left[\frac{(V_m N_a)}{22414} \times W\right] \times A_m \qquad - - - - - - - - - -\{2.23\}$$

Where, A_m is mean cross sectional area occupied by adsorbate molecule (16.2 A^2 for N_2), W weight of the sample, N_a Avogadro number, V_m is monolayer volume in ml at STP [181].

2.3.7. X-ray photoelectron spectroscopy (XPS) measurements

The X-ray photoelectron spectroscopy (XPS) is a surface sensitive analytical technique that uses a high energy electron beam as an excitation source. The excited atom returns to ground state by emitting photons. The kinetic energies of the emitted photons are characteristics of elements present within the top 5 nm to 10 nm of the sample. The electron beam can be scanned over a selected area or it can be focused on a small surface feature of interest. This ability to focus the electron beams to diameter of 10 nm to 20nm makes this technique an extremely useful tool for elemental analysis of surface features. When it is used in combination with ion sputtered sources, it can also perform compositional depth profiling. The XPS data of 'as synthesized' ferrite samples was recorded with the specimen mounted on a specially designed sample holder [182] at a base pressure of 3×10^{-10} mbar. An electron analyzer from SPECS Surface Nano Analysis GmbH, Germany and an Al-Kα laboratory X-ray source have been used for photoelectron spectroscopy measurements.

2.3.8. Mössbauer spectral measurements

Mössbauer spectroscopy is based on the observance of nuclear resonance absorption, which depends upon the recoil free emission and recoil free absorption of gamma rays. Thus, the Mössbauer effect is the recoil free emission of gamma radiation from a solid radioactive material. Since, the gamma emission is recoil free it can be resonantly absorbed by stationary atoms. Resonance absorption occurs at zero velocity only if both the emitting and absorbing species are in the same physical environment. If this is not true then the resonance absorption may occur at a non-zero velocity. This displacement of the resonance from zero velocity is called the chemical or isomer shift (IS). The isomer shift value is a linear function of the s

51

T-604

electron density and for Fe-57 decreases with increasing s-electron density [183]. The electron density at the nucleus is a function of the oxidation state of the absorbing atom and the electronegativity of its nearest neighbours. Hence, the Mössbauer spectra can provide information related to qualitative identification, oxidation states and structural information of the absorbing material. Quadrupole splitting (QS) is the distance between two resonance peaks which result because of interaction of the inhomogeneous electric field at the nucleus with the electric quadrupole moment of the excited nucleus. The doublet occurs because the first nuclear excited level splits into two sublevels. Quadrupole splitting can be related quantitatively to the oxidation state and the nature of the chemical bonding of the absorbing atom. It may also be used as a method of determining the symmetry of crystals. Magnetic hyperfine splitting (MHS) occurs due to interaction of the nuclear magnetic moments with the external or intermolecular magnetic fields which results in six resonance peaks or sextet. Double six line spectra may be obtained when the iron present in the absorber may be in either of two different environments or two different crystal structures where the internal magnetic field is different at each site. A composite of a six line and one or two line spectrum may occur when two, both magnetic and nonmagnetic forms of a material are present in the absorber. Mössbauer spectrum at room temperature was recorded using a Mössbauer spectrometer supplied by Nucleonix Systems Pvt. Ltd., Hyderabad, India, operated in constant acceleration mode in transmission geometry. The source employed was Co-57 in Rh matrix of strength 50 mCi. The calibration of the velocity scale was done by using an enriched α-^{57}Fe metal foil using a value of 330 kOe for the effective nuclear hyperfine field H_{eff} at room temperature. The outer line width of calibration spectra is 0.29 mm / s^{-1}. All the Mössbauer

spectra were fitted by using a Win-Normos fit program. The isomer shift values are relative to α-Fe metal foil.

2.3.9. Gas sensing studies

Nanocrystalline spinel ferrites have been explored in recent years as gas sensors due to their gas sensing capacity over wide range of temperatures. These materials can be used in a tablet form or in the form of thin / thick films. The thick film technology involves low cost as the films can be easily fabricated by casting roll compacting extrusion, screen-printing, spraying and coating. Fabrication of thick films by screen printing technique is the most simple, economic and flexible wherein the films of different shapes and thickness can be easily prepared. In the present work thick films of the 'as synthesized' nanocrystalline ferrites were fabricated using screen printing technique. The thixotropic paste [184] was formulated by mixing ferrites fine powder with a solution of ethyl cellulose (a temporary binder) in a mixture of organic solvents such as butyl cellulose, butyl carbitol acetate and turpineol. The ratio of inorganic to organic part was kept as 75:25 in formulating the paste. The paste was then used to prepare thick films. The thixotropic paste was screen printed on a glass substrate in desired patterns. The films prepared were fired at $500^{\circ}C$ for 24 h. Silver contacts for electrical measurements were made by vacuum evaporation.

2.3.9.1. Details of the gas sensing system

Fig. 2.2 represents the schematic of 'static gas sensing system' used to explore the sensing performance of thick films. The setup has electrical feeds through the base plate. The heater is fixed on the base plate to heat the sample under test up to required operating

temperatures. The current passing through the heating element was monitored using a relay with adjustable ON and OFF time intervals. A Cr-Al thermocouple was used to sense the operating temperature of the sensor. The output of the thermocouple was connected to a digital temperature indicator.
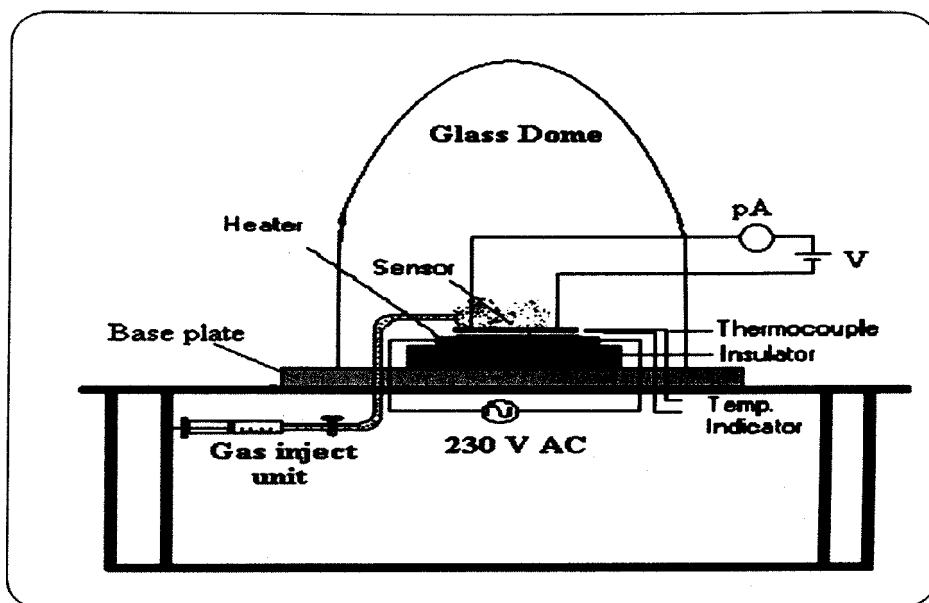
Fig.2.2. Block diagram of static gas sensing system

A gas inlet valve was fitted at one of the ports of the base plate. The required gas concentration inside the static system was achieved by injecting a known volume of test gas using a gas-injecting syringe. A constant voltage was applied to the sensor and current was measured by a digital pico-ammeter. Air was allowed to pass into the glass dome after every exposure cycle of toxic gases such as NH_3, Cl_2, H_2, LPG etc.

2.3.9.2. Gas injection and sensor calibration for different test gas concentrations

The test gas under study was injected into the sensor system inside the glass dome, through the gas inlet (Fig. 2.2) by using calibrated medical practitioner's syringe (Pyrex)

(maximum volume of 5 ml to 50 ml). The required concentration of gas inside the glass dome was achieved by injecting a predefined known volume of the test gas. The volume of the glass dome used was 15 litres. The gas concentration in ppm was determined using relation:

$$\text{Concentration of gas (ppm)} = \frac{\text{Injeted volume of gas(mL)}}{\text{Vloume of glass dome (mL)}} \times 10^6 \qquad ----\{2.24\}$$

2.3.9.3. Measurement of sensor response

The relative response to a target gas was defined as the ratio of the change in conductance of a sample upon exposure to the gas to the original conductance in air. The gas response can be written as:

$$\text{Gas response} = \frac{G_g - G_a}{G_a} = \frac{\Delta G}{G_a} \qquad ---------------\{2.25\}$$

Where, G_a is conductance in air and G_g is conductance in a target gas.

Specificity or selectivity can be defined as the ability of a sensor to respond to a certain gas in the presence of different gases. Response time (RST) was defined as the time required for a sensor to attain the 90 % of the maximum increase in conductance after exposure of the sensor surface to a test gas, while recovery time (RCT) as the time taken to get back 90 % of the maximum conductance [185] in air. The electrical connections from the sensor assembly were brought outside through the feed available with the system. The change in the resistance of the sensor due to the exposure of different gas concentrations was measured applying a d.c. voltage of (30 V) across the sensor, using standard d.c. power supply (Radart P/S, 30 V, 2.5 A). The current output was measured with the help of digital pico-ammeter (pA).

2.3.10. Scanning electron microscopy (SEM)

Scanning electron microscopy (SEM) provides high resolution and long depth of field images of the sample surface and near surface. SEM is one of the most widely used analytical tool due to the extremely detailed images it can quickly provide. It is very useful technique in the study of texture, topography and surface features of solid samples. When it is coupled with an auxillary energy dispersive X-ray spectroscopy (EDS) detector, SEM can offer elemental identification of nearly the entire periodic table. Since, the SEM is recorded under vacuum, the sample must be electrically conductive at the surface. This is achieved by coating a non-conductive sample with gold using RF sputtering which also avoids the charging of surface. The surface topology of the sintered ferrites samples were studied using JEOL scanning electron microscope, model 5800LV.

2.3.11. DC electrical resistivity

The d.c. resistivity studies are one of the useful characterization techniques to understand the conductivity mechanism in ferrite semiconductors. The d.c. resistivity measurement was carried out on the samples by using two probe method. The effect of temperature on conductivity of the material was studied by placing the brass cell containing sample in specially designed tubular furnace. The conductivity measurements were carried out in such a manner that at every temperature, time was allowed for that sample to attain thermal equilibrium. The dimensions of the samples used were approximately 2 mm thickness and 10 mm diameter. The current flow across the sample was measured using Keithley 2010 multimeter. Knowing the current flowing through the circuit and voltage applied across the sample, resistance of the sample can be calculated by using the equation:

$$R = \frac{V}{I} \qquad\qquad - \{2.26\}$$

Where, R is the resistance of the sample, V is the constant voltage applied and I is the current

flowing in the circuit. The resistivity can be calculated using relation [186]:

$$\rho = R\frac{A}{l} \qquad\qquad -\{2.27\}$$

Where, ρ is resistivity, A is the area of cross section of pellet and l is thickness of the pellet.

The d.c. resistivity was measured from room temperature to 773 K. The log resistivity (ρ)

values were then plotted against $10^3 / T$ for all the ferrite samples. The resistivity-temperature

behaviour obeys the relation [186]:

$$\rho = \rho_{o}\exp^{E_a/kT} \qquad\qquad - \{2.28\}$$

Where, ρ is the resistivity at absolute temperature T, E_a the activation energy and k the

Boltzman constant. The activation energy of each sample was determined from the slope of

the linear plots using the relation [186]:

$$Slope = \frac{E_a}{k} \qquad\qquad -\{2.29\}$$

2.3.12. Seebeck coefficient / Thermoelectric power (TEP) measurements

Ferrites having spinel structure are ferrimagnetic and display semiconducting

behaviour. The mechanism of conduction in ferrites involves either n-type or p-type

conductions or both n-type and p-type conduction depending on temperature and majority

charge carriers. The parameters such as thermoelectric power and electrical resistivity are

most convenient to measure and suggest the conduction phenomena. The thermoelectric

power of a material depends on the temperature and crystal structure. Metals show small

thermoelectric power because the contribution of electrons (negative charges) and holes

(positive charges) to the induced thermoelectric voltage is cancelled making it small. However, in semiconductors the concentration of n-type and p-type charge carriers is unequal and thus can have high positive or negative values of the thermoelectric power depending on the concentration of the excess charge carriers. The sign of the thermoemf represents the type of charge carrier's responsible for electric transport in ferrite semiconductors. The Seebeck coefficient 'α' is given by relation [187]:

$$\alpha = \frac{\Delta V}{\Delta T} \qquad --------------------- \{2.30\}$$

Where, ΔV is the voltage developed across the sample and ΔT is the temperature difference across the sample. Seebeck coefficient measurements of ferrites were carried out from 300 K to 800 K using a two probe TEP measurement setup with a temperature difference of 15 K to 20 K across the sample.

2.3.13. AC susceptibility

AC susceptibility measurement is used to study the types of particles viz. multidomain (MD) single domain (SD) and superparamagnetic (SP) responsible for magnetic properties of ferrites [188]. The domain structures and the Curie temperature of the magnetic material can be obtained from the plot of normalized a.c. susceptibility versus temperature. The plots of a.c. magnetic susceptibility against temperature normally shows sharp fall in the susceptibility when the magnetic state of the samples changes from ferrimagnetic to paramagnetic. The a.c. susceptibility measurements were carried out on powdered ferrite samples from 300 K to 800 K using double coil set up described by Likhite et al. [189] and supplied by Magneta, Mumbai, India.

2.3.14. Magnetic hysteresis

Vibrating sample magnetometer (VSM) is very versatile and sensitive technique used to characterize the magnetic properties of materials as a function of magnetic field, temperature and time. It can be used for both weakly and strongly magnetic substances. Some of the properties that VSM can measure include saturation magnetization, remanent magnetization, coercivity, permeability and the dissipated energy. Dissipated energy is the energy necessary to magnetize the sample in the opposite direction. The dissipated energy can be calculated from the area that is included by the hysteresis loop. This technique is based on the flux change in a coil when a magnetized sample is vibrated near it [190]. The sample, commonly a small disk is attached to the end of a nonmagnetic rod, the other end of which is fixed to a kind of mechanical vibrator. The oscillating magnetic field of the moving sample induces an alternating emf in the detection coils, whose magnitude is proportional to the magnetic moment of the sample. The alternating emf is amplified with a lock-in amplifier which is sensitive only to signals at the vibration frequency. Hysteresis loops obtained from VSM can provide a lot of information about the magnetic nature of a sample. By simply looking at the loop one can easily find out whether the sample is diamagnetic, paramagnetic, superparamagnetic, ferrimagnetic or ferromagnetic. Quantitative analysis on hysteresis loop can provide information on the strength and direction of the anisotropy energy. The room temperature VSM measurements were carried out by using a Lakeshore VSM model 7410 and parameters like saturation magnetization (M_s), coercive force (H_c) and remanent magnetization (M_r) were evaluated from the hysteresis loop observed for samples.

2.3.15. Dielectric studies

Every material display unique set of electrical characteristics which are dependent on its dielectric properties. A material is classified as dielectric if it has the ability to store energy when an external electric field is applied. If a d.c. voltage source is placed across a parallel plate capacitor, more charge is stored when the separation between the plates is occupied by a dielectric material. The dielectric material increases the storage capacity of the capacitor by neutralizing charges at the electrodes, which ordinarily would contribute to the external field. If an a.c. sinusoidal voltage source is placed across the capacitor containing dielectric material, the resulting current will be made up of a charging current and a loss current that is related to the dielectric constant. The interaction of material with an electric field is described by the term permittivity. The real part of permittivity (ε'_r) is a measure of how much energy is stored in a material from an external electric field, while the imaginary part of the permittivity (ε''_r) is called the loss factor. The loss factor includes the effects of both dielectric loss and conductivity. The ratio of the imaginary part to real part is called the loss tangent, tan δ. In the present investigation, capacitance of ferrite pellets of dimension, 10 mm diameter and 2 mm thickness was measured at different frequencies from 100 Hz to 10 MHz using WAYNE KERR LCR meter model 6500P. The dielectric measurements were carried out at room temperature as well as at high temperatures upto 250°C. The dielectric constant (ε') and complex dielectric constant (ε'') was calculated using the relation [191]:

$$\varepsilon' = \frac{Cd}{A\,\varepsilon_0} \qquad\qquad\qquad\qquad\qquad\qquad \{2.31\}$$

$$\varepsilon^* = \varepsilon' \tan \delta \qquad\qquad\qquad\qquad\qquad\qquad \{2.32\}$$

Where, C is the capacitance of the specimen in Farad, d is the thickness of the pellet in meters, ε_0 permittivity of free space equals to 8.854×10^{-12} F/m and A is the cross sectional area of the pellet in m^2. The dielectric loss tangent, tan δ was calculated using the relation:

$$\tan \delta = D = \frac{1}{Q} \quad ------------------------\{2.33\}$$

Where, D is the dissipation factor and Q is the quality factor.

2.3.16. Initial permeability

The initial magnetic permeability is a very microstructure sensitive property of ferrites. The study of the thermal variations of initial permeability of polycrystalline ferrites has contributed to significant improvements in understanding the magnetization mechanisms. It can also be used as a quality test in the preparation of ferrite samples. Measurement of initial permeability as a function of temperature is generally performed by measuring the inductance of a torroidal sample. The initial permeability increases with increase in temperature and drops very sharply near Curie point. The verticality of this drop is directly related to the chemical homogeneity of the sample. The initial permeability is defined as:

$$\mu_i = \frac{1}{\mu_0} \times \frac{\Delta B}{\Delta H} \quad --------------------\{2.34\}$$

$$(\Delta H \rightarrow 0)$$

Where, μ_0 is permeability in vacuum, B is the flux density and H is the applied field. The inductance measurements were carried out at fixed frequency of 1 kHz over the temperature range from room temperature to $500^{\circ}C$. Also, the room temperature inductance measurements as a function of frequency were carried out over the frequency range from 100 Hz to 10 MHz

using Wayne Kerr LCR meter model 6500P. The initial permeability was calculated from the low field inductance measurements with a torroidal core of 50 turns using the formula [192]:

$$L = 0.0046\mu_i N^2 h \, \log\frac{d_1}{d_2} \qquad ------------------- \quad \{2.35\}$$

Where, L is the inductance in μH, d_1 is the outer diameter of a torroid, d_2 is the inner diameter of a torroid, μ_i is the initial permeability of the core and h is the height of the core in inches.

Chapter 3

Synthesis and characterization of

$$Ni_{0.6-x}Mn_x Zn_{0.4} Fe_2 O_4$$

$$(x = 0.0, 0.1, 0.2, 0.3, 0.4, 0.5 \text{ \& } 0.6)$$

Synthesis and characterization of $Ni_{0.6-x}Mn_xZn_{0.4}Fe_2O_4$ (x = 0.0-0.6) ferrites

3.1. Synthesis and characterization of hydrazinated mixed nickel manganese zinc ferrous fumarate, $Ni_{0.6-x}Mn_xZn_{0.4}Fe_2(C_4H_2O_4)_3.6N_2H_4$ (x = 0.0-0.6) precursors

3.1.1. Introduction

Nanocrystalline ferrites are the materials of current interest because of their unique electric, dielectric, magnetic and optical properties which make them appealing from theoretical and technological point of view. Recently, the nanocrystalline magnetic ferrites were used in biomedicine and biotechnology as contrast agent in magnetic resonance imaging (MRI) and also as drug carriers in magnetically guided drug delivery systems. The structural as well as magnetic properties of the ferrites are highly sensitive to the cation distribution which in turn depends on the preparative methods. Hence, there is growing interest in the synthetic strategies to improve upon the properties of the ferrites. The wet chemical methods are preferred over conventional ceramic technique since they give better product with small particle size at relatively low temperatures. The product formed is stiochiometrically pure and can be obtained over the wide range of temperatures. Hence, various wet chemical methods like co-precipitation, sol gel, combustion, precursor etc. have been utilised for the synthesis of ferrites. There has been considerable interest among researchers in the study of metal carboxylates and hydrazine derivatives of metal carboxylates, since they can serve as precursors to fine particle oxide materials at relatively lower temperatures. Considering, the

utility of the carboxylato hydrazinate precursor method for synthesis of fine particle oxides in recent years we have adopted this method for preparation of Ni-Mn-Zn ferrites.

3.1.2. Experimental

The details of synthesis of hydrazinated mixed nickel manganese zinc ferrous fumarates are already discussed in the section 2.1. of chapter 2. The hydrazinated carboxylate precursors were characterized by chemical analysis, FTIR spectroscopy, TG and DSC, isothermal mass loss studies and their molecular formulae were fixed accordingly.

3.1.3. Results and discussion

The synthesized hydrazinated mixed nickel manganese zinc ferrous fumarates were characterized by different techniques mentioned in section 3.1.2 and the results of characterization are compiled and discussed in this part of the chapter.

3.1.3.1. Chemical analysis

The chemical analysis results of the hydrazinated mixed nickel manganese zinc ferrous fumarates are given in the Table 3.1. The chemical analysis results were found to be in agreement with the calculated values obtained considering the molecular composition of the precursor complexes as given in the Table 3.1.

Table 3.1. Chemical analysis results of hydrazinated mixed nickel manganese zinc ferrous fumarate precursors,

$Ni_{0.6-x}Mn_xZn_{0.4}Fe_2(C_4H_2O_4)_3.6N_2H_4$ $(x = 0.0\text{-}0.6)$

x	Metal content / %								Hydrazine / %		Proposed molecular formula	Molecular mass
	Fe		Mn		Ni		Zn					
	Obs.	Calc.	Obs.	Calc.	Obs.	Calc.	Obs.	Calc.	Obs.	Calc.		
0.0	15.81	15.79	---		4.68	4.98	3.43	3.70	27.24	27.18	$Ni_{0.6}Zn_{0.4}Fe_2(C_4H_2O_4)_3.6N_2H_4$	707.5
0.1	15.93	15.80	0.784	0.777	4.12	4.15	3.67	3.70	27.44	27.19	$Ni_{0.5}Mn_{0.1}Zn_{0.4}Fe_2(C_4H_2O_4)_3.6N_2H_4$	707.1
0.2	15.78	15.80	1.54	1.56	3.31	3.32	3.68	3.70	27.21	27.21	$Ni_{0.4}Mn_{0.2}Zn_{0.4}Fe_2(C_4H_2O_4)_3.6N_2H_4$	706.8
0.3	15.82	15.81	2.30	2.33	2.45	2.49	3.68	3.70	27.24	27.22	$Ni_{0.3}Mn_{0.3}Zn_{0.4}Fe_2(C_4H_2O_4)_3.6N_2H_4$	706.4
0.4	15.80	15.82	3.09	3.11	1.62	1.66	3.66	3.71	27.49	27.23	$Ni_{0.2}Mn_{0.4}Zn_{0.4}Fe_2(C_4H_2O_4)_3.6N_2H_4$	706.0
0.5	15.81	15.83	3.83	3.89	0.824	0.832	3.69	3.71	27.29	27.25	$Ni_{0.1}Mn_{0.5}Zn_{0.4}Fe_2(C_4H_2O_4)_3.6N_2H_4$	705.6
0.6	15.84	15.84	4.66	4.67	---		3.69	3.71	27.47	27.26	$Mn_{0.6}Zn_{0.4}Fe_2(C_4H_2O_4)_3.6N_2H_4$	705.3

3.1.3.2. FTIR spectral analysis

The FTIR spectra of the synthesized hydrazinated mixed nickel manganese zinc ferrous fumarates are presented in the Fig. 3.1 while, the data of IR absorption frequencies is given in Table 3.2.
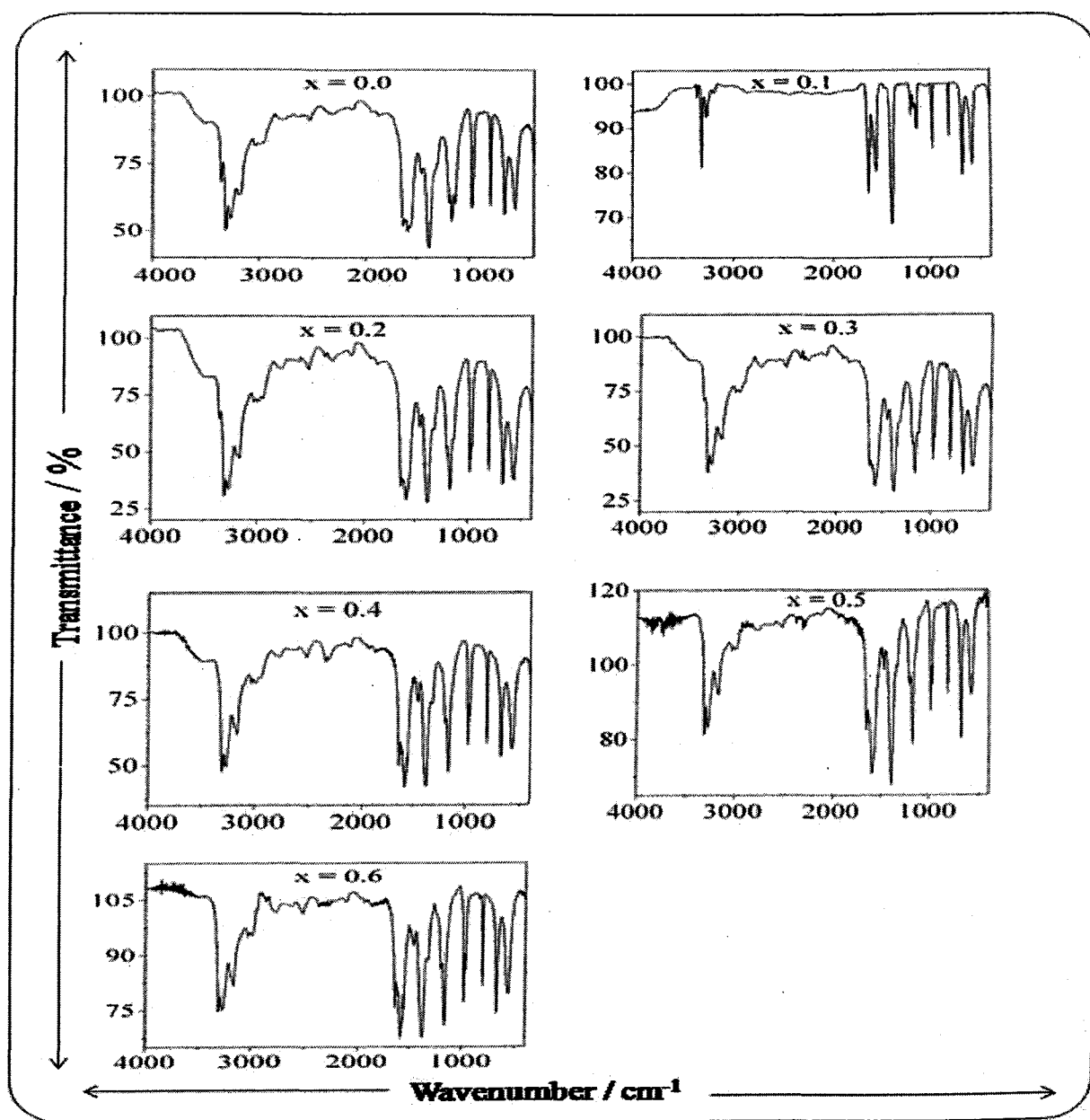
Fig. 3.1. FTIR spectra of $Ni_{0.6-x}Mn_xZn_{0.4}Fe_2(C_4H_2O_4)_3.6N_2H_4$ ($x = 0.0$-0.6) precursors

Table 3.2. FTIR absorption frequencies of hydrazinated mixed nickel manganese zinc ferrous fumarate precursors,

$Ni_{0.6-x}Mn_xZn_{0.4}Fe_2(C_4H_2O_4)_3.6N_2H_4$ $(x = 0.0\text{-}0.6)$

x	FTIR absorptions / cm^{-1}							
	N-H stretching	ν_{asym} COO$^-$ stretching	NH$_2$ deformation	ν_{sym} COO$^-$ stretching	NH$_2$ wagging	N-N stretching	N-N bending	NH$_2$ rocking
0.0	3352-3190	1628	1584	1384	1164	972	802	674
0.1	3352-3192	1627	1550	1390	1131	972	802	674
0.2	3307-3167	1643	1584	1375	1164	977	803	674
0.3	3352-3167	1624	1584	1385	1165	977	802	674
0.4	3304-3169	1643	1584	1382	1165	979	803	674
0.5	3303-3169	1643	1584	1378	1164	979	802	670
0.6	3303-3163	1643	15845	1369	1165	978	803	670

The FTIR spectra display three bands in the region 3352 cm^{-1} to 3163 cm^{-1} [Table 3.2] which have been assigned to the N-H stretching frequencies and the sharp band in the region 1585 cm^{-1} to 1550 cm^{-1} is attributed to NH_2 deformation of hydrazine ligands. The FTIR peak in the region 979 cm^{-1} to 972 cm^{-1} arises due to N-N stretching indicating the bidentate bridging coordination of hydrazine ligands to the central metal ion [193-194]. The asymmetric stretching (v_{asym}) frequencies of the carboxylate ion in the precursors were observed in the range 1643 cm^{-1} to 1624 cm^{-1} while symmetric stretching (v_{sym}) frequencies were observed in the range 1390 cm^{-1}-1369 cm^{-1} [Table 3.2] with Δv (v_{asym} -v_{sym}) separation of 275 cm^{-1} to 237 cm^{-1}, which indicates the monodentate linkage of both carboxylate groups of the fumarate dianion to the central metal ion [195]. Thus, from the above discussion, it can be concluded that the hydrazine ligands are coordinated through bidentate bridge linkage, while fumarate ions exhibit monodentate character which hints towards the polymeric natures of these hydrazinated metal fumarate precursor complexes.

3.1.3.3. Thermal studies

3.1.3.3a. TG and DSC

The TG and DSC profiles of the hydrazinated mixed nickel manganese zinc ferrous fumarate precursors from room temperature to 800°C are shown in Fig. 3.2, while the data gathered from these profiles is represented in Table 3.3. All the synthesized hydrazinated mixed metal fumarate precursors exhibit similar decomposition patterns involving dehydrazination as first step towards decomposition followed by oxidative decarboxylation. The end products of decomposition were found to be ultrafine oxides. The TG profiles of all the precursors show four mass loss regions. The initial mass loss of 1 % - 2.45 % from room

temperature to 75°C observed for all the precursors was due to desorption of adsorbed species including moisture. The mass loss of 2.54 %, 2.33 % and 1.9 % from 75°C to 110°C in precursors with composition, $x = 0.0$, $x = 0.1$ and $x = 0.5$, respectively indicates the beginning of the dehydrazination. The DSC curve shows weak exotherms with a peak temperature of 78.7°C, 87.7°C and 85.9°C respectively in this region. The major mass losses of 26.98 %, 22.62 % and 22.98 % from 110°C to 160°C observed for precursors with above composition corresponds to total dehydrazination with corresponding strong exotherms at 144°C, 152°C and 139°C, respectively. For complexes with composition, $x = 0.2$, 0.4 and 0.6, the major mass losses of 22.94 %, 24.57 % and 25.5 %, respectively corresponding to loss of five hydrazine molecules observed in the temperature range from 75°C to 110°C. The respective strong exotherms in DSC were observed at 91.9°C, 91°C and 96.6°C. The precursor with composition, $x = 0.3$, shows mass loss of 15.85 % from 75°C to 110°C which corresponds to the loss of three and half hydrazine molecules with the peak temperature of 87.2°C in DSC profile. The mass losses from 5.84 % - 10.73 % in the temperature region 160°C to 230°C observed for all the precursors (except composition, $x = 0.3$) were slightly higher side than expected for the loss of one hydrazine which may be due to the beginning of decarboxylation in these precursors, while the precursor with composition, $x = 0.3$, shows mass loss of 15.21 % in the thermogram in this temperature range which corresponds to the loss of two and half hydrazine molecules and beginning of decarboxylation. Thus, the temperature range from 75°C to 230°C represents the region of total dehydrazination (loss of six hydrazine molecules) which has been found to be highly exothermic and this exothermicity initiates the decarboxylation in precursor complexes at relatively lower temperatures.
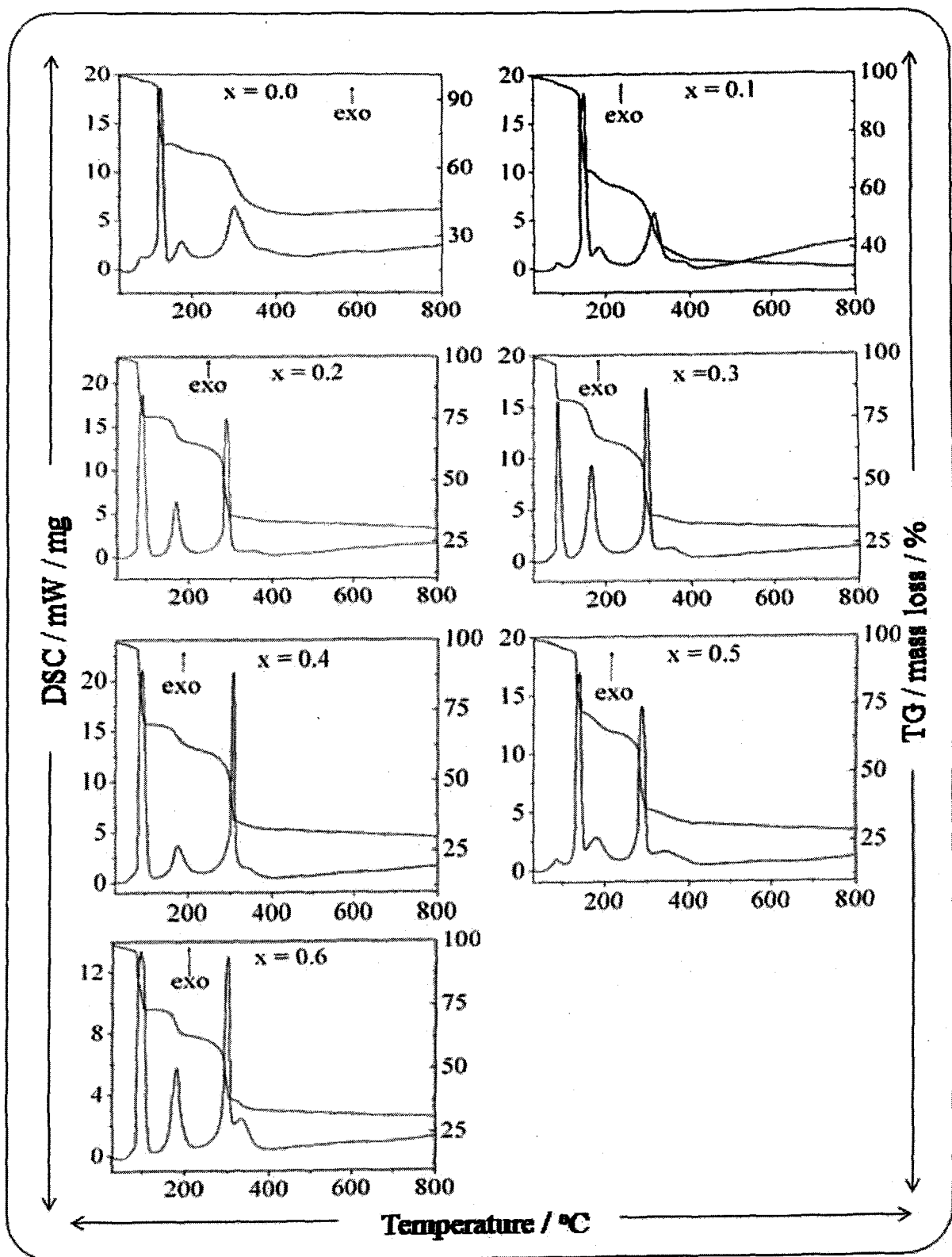
Fig. 3.2. TG and DSC curves of $Ni_{0.6-x}Mn_xZn_{0.4}Fe_2(C_4H_2O_4)_3.6N_2H_4$ ($x = 0.0$-0.6) precursors

70

Table 3.3. TG and DSC data of hydrazinated mixed nickel manganese zinc ferrous fumarate precursors,

$Ni_{0.6-x}Mn_xZn_{0.4}Fe_2(C_4H_2O_4)_3.6N_2H_4$ $(x = 0.0\text{-}0.6)$
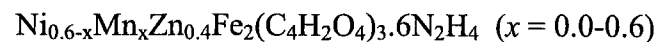
x	Temperature range / °C, mass loss (TG) / % , DSC / °C						
	RT-75	75-110	110-160	160-230	230-330	330-440	RT-440
0.0	2.32	2.54 / 78.7 (exo)	26.98 / 144 (exo)	5.87 / 180 (exo)	22.57 / 306 (exo)	6.82 / 360-390 (broad exo hump)	67.10
0.1	2.26	2.33 / 87.7 (exo)	26.62 / 152 (exo)	5.93 / 185 (exo)	24.42 / 318 (exo)	6.24 / 360-420 (broad exo hump)	67.80
0.2	1.45	22.94 / 91.9 (exo)	----	4.53 / 170 (exo)	35.38/ 289 (exo)	4.50 / 345-390 (broad exo hump)	68.80
0.3	1.48	15.85 / 87.2 (exo)	----	15.21 / 164 (exo)	31.14 / 295 (exo)	3.58 / 340-420 (broad exo hump)	67.22
0.4	2.45	24.57 / 91 (exo)	----	7.56 / 177 (exo)	28.17 / 307 (exo)	3.42 / 340-370 (broad exo hump)	68.69
0.5	2.40	1.9 / 85.9 (exo)	22.98 / 139 (exo)	5.84 / 179 (exo)	28.32 / 286 (exo)	4.74 / 335-360 (broad exo hump)	66.18
0.6	1.0	25.5 / 96.6 (exo)	----	10.73 / 179 (exo)	24.1 / 299 (exo)	6.35 / 340 (exo)	67.67

The next major mass loss region in TG from 230°C to 330°C, with mass losses in the range 22.57 % - 35.38 % results from exothermic oxidative decarboxylation of dehydrazinated precursors. The high exothermicity of decarboxylation is reflected in the DSC profiles, wherein strong exotherms were observed in this temperature region. The mass losses of 3.42 % - 6.82 % from 330°C to 440°C were due to the oxidation of either traces of undecomposed carboxylate or residual carbon formed during the decarboxylation or both as indicated by broad exotherm in DSC in this temperature region.

Besides TG and DSC, the thermal decomposition of the precursors was studied using FTIR spectroscopy by carefully heating the precursors at the rate of 4°C per minute in an electric oven. The FTIR spectrum of the freshly prepared precursor with composition, $x = 0.3$ (Fig. 3.3a) display all the peaks characteristics of the different types of vibrations of hydrazine ligands. When the same precursor was heated carefully to about 170°C, the peaks corresponding to N-H stretching vibration vanishes and a broad band appears in this region (Fig. 3.3b) which is due to the hydration of the precursor during cooling after dehydrazination. There was no change noticed in the position of FTIR bands which belongs to carboxylate groups after hydration of the precursor. On heating further the same precursor to about 380°C, all the FTIR bands corresponding to carboxylate groups disappeared (Fig. 3.3c) and the spectrum shows only two bands in the lower frequency region which is characteristics of metal oxygen (M—O) stretching in oxides. The self propagating autocatalytic behavior was not observed for this dehydrazinated precursor. These observations support the results obtained from TG and DSC as well as isothermal mass loss studies. Hence, it can be concluded that hydrazine coordination is responsible for the low temperature decomposition and self propagating combustion behavior of the precursors.
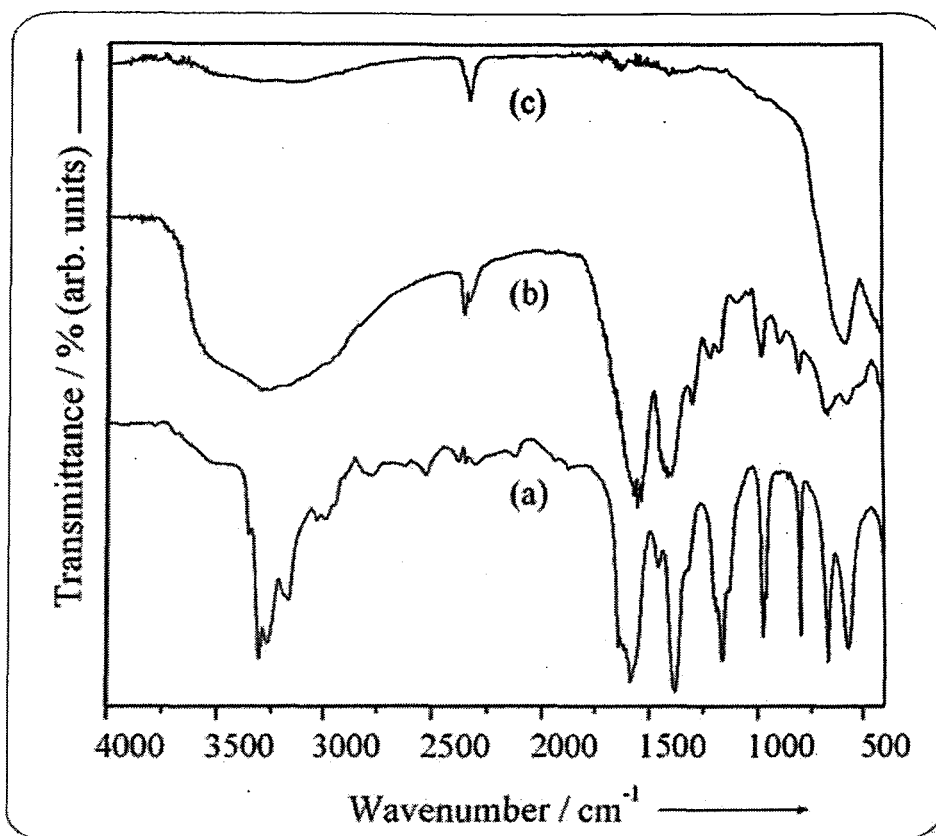
Fig.3.3. FTIR spectrum of $Ni_{0.3}Mn_{0.3}Zn_{0.4}Fe_2(C_4H_2O_4)_3.6N_2H_4$ precursor a) hydrazinated precursor, b) dehydrazinated precursor (heated at 170^0C) and c) decomposed precursor (heated at 380^oC)

3.1.3.3b. Total mass loss studies

The total mass loss studies of the precursors were performed independently by heating the known amount of precursors in silica crucible over burner. The total mass losses of the precursors obtained from thermogravimetric studies and those obtained by pyrolysis in air are found to be in good agreement [Table 3.4] with the calculated values which suggests their formations with assigned stoichiometry.

73

3.1.3.3c. Isothermal mass loss studies and hydrazine analysis

The isothermal mass loss studies of the precursors were carried out in programmable electric oven at various predetermined temperatures from room temperature to 170°C along with titrimetric determination of hydrazine [166] and the results are compiled in the Table 3.4. The isothermal mass loss studies for precursors with composition, x = 0.2, 0.3, 0.4 and 0.6, shows marginal mass losses from 0.26 % - 2.47 % in the temperature range from room temperature to 75°C, however the titrimetric analysis of hydrazine content in these precursors in above mentioned temperature range showed increase in its value which indicated the loss of physisorbed species including moisture and not hydrazine. For precursors with composition, x = 0.2, 0.4 and 0.6, dehydrazination begins above 75°C followed by self propagating autocatalytic decomposition behavior which was observed in the temperature range from 75°C to 100°C. In the precursor with composition, x = 0.0, the dehydrazination begins at about 100°C and after 100°C, the precursor decomposed with self propagating autocatalytic decomposition. Similar thermal events were noticed in case of precursor with composition, x = 0.1, at about 125°C and after 125°C, respectively. In case of precursor with composition, x = 0.5, the mass losses observed from 75°C to 100°C corresponds to the loss of some hydrazine which was confirmed from titrimetric analysis of hydrazine. The precursor was then found to decompose between 100°C to 125°C. For precursor with composition, x = 0.3, stepwise complete dehydrazination was observed from room temperature to 170°C without being decomposed. For this dehydrazinated precursor, the decarboxylation was observed at relatively higher temperature from 380°C to 390°C.

74

Table 3.4. Isothermal mass loss and total mass loss studies of hydrazinated mixed nickel manganese zinc ferrous fumarate precursors,

$Ni_{0.6-x}Mn_xZn_{0.4}Fe_2(C_4H_2O_4)_3.6N_2H_4$ $(x = 0.0\text{-}0.6)$
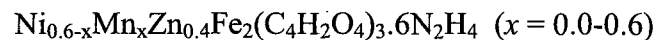
x	Total mass loss / %			Isothermal mass loss / %, Hydrazine analysis / %						
	Obs.		Calc.	RT-75	75-100	RT-100	100-125	RT-125	125-150	150-170
	Pyrolysis in air	TG								
0.0	66.86	67.10	66.49	---	----	4.69 / 23.87	55.44 (complex decomposed)			
0.1	66.63	67.80	66.53	---	----	----	----	4.59 / 23.87	54.45(complex decomposed)	
0.2	67.08	68.80	66.56	2.12 / 27.28	54.34 (complex decomposed)					
0.3	66.66	67.22	66.60	1.42 / 27.26	4.62 / 22.57	---	9.78 /13.42	----	7.52 / 6.45	6.43 / 0.0
0.4	66.67	68.66	66.64	1.47 / 27.56	56.46 (complex decomposed)					
0.5	66.72	66.18	66.67	2.03 / 27. 20	2.35 / 25.40	----	56.75 (complex decomposed)			
0.6	67.11	67.67	66.71	1.47 / 27.48	58.76 (complex decomposed)					

3.2. Characterization of 'as synthesized' $Ni_{0.6-x}Mn_xZn_{0.4}Fe_2O_4$ ($x = 0.0-0.6$) ferrites

The end products obtained by thermolysis of hydrazinated mixed nickel manganese zinc ferrous fumarates (as synthesized ferrites) in air were characterized by X-ray diffraction (XRD), thermal analysis (TG and DSC), FTIR spectroscopy, X-ray photoelectron spectroscopy (XPS), Mössbauer spectroscopic studies and transmission electron microscopy (TEM).

3.2.1. X-ray diffraction studies

The XRD patterns of all the 'as synthesized' $Ni_{0.6-x}Mn_xZn_{0.4}Fe_2O_4$ ($x = 0.0, 0.1, 0.2, 0.3, 0.4, 0.5, 0.6$) ferrites are presented in Fig. 3.4. The X-ray diffractograms displays all the peaks characteristics of the cubic spinel ferrites with no detectable secondary phases which confirm the formation and purity of these ferrite samples. The XRD peaks show broadening which is indicative of the ultrafine (nanocrystalline) nature of all 'as synthesized' $Ni_{0.6-x}Mn_xZn_{0.4}Fe_2O_4$ ($x = 0.0-0.6$) ferrites. The interplanar distance for each diffraction '*hkl*' planes were calculated using Bragg's equation given in the section 2.3.4 of chapter 2. The observed and calculated values of interplanar distances show good agreement. The lattice parameter '*a*' was calculated for each plane using the relation given at 2.4 in section 2.3.4. The Fig. 3.5a represents the variation of lattice parameter '*a*' with Mn substitution '*x*'. It was observed that the lattice parameter increases linearly with increasing Mn substitution in accordance with the Vegard's law [196]. This behavior has been attributed to the replacement of smaller Ni^{2+} ions (0.70 A°) by larger Mn^{2+} ions (0.82 A°) in the crystal lattice. Thus, the introduction of Mn^{2+} ions in lattice causes the expansion of unit cell while preserving the overall cubic symmetry.

The lattice parameters of ferrites calculated from their XRD patterns were found to be in the range 8.3763 A° to 8.4450 A° [Table 3.5] which are in agreement with the reported values for $Ni_{0.6-x}Mn_xZn_{0.4}Fe_2O_4$ (x = 0.0-0.6) ferrites system [97].
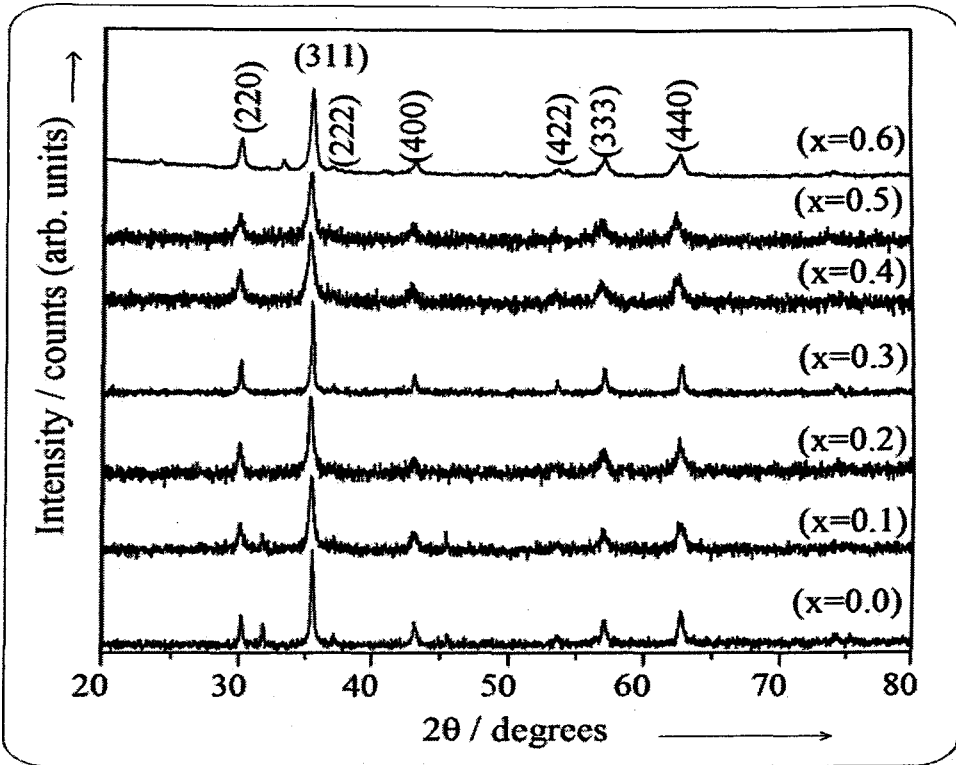
Fig.3.4. XRD pattern of 'as synthesized' $Ni_{0.6-x}Mn_xZn_{0.4}Fe_2O_4$ (x = 0.0-0.6) ferrites

The X-ray density was obtained using equation number 2.5 given in the section 2.3.4, while the bulk density was calculated considering the cylindrical shape of the pellet using the relation number 2.6 given in the same section. The porosity of the ferrites was calculated from the X-ray (ρ_{X-ray}) and bulk (ρ_{bulk}) density as per the relation number 2.7 from section 2.3.4. It was observed that both X-ray and bulk density decreases, while the porosity increases with increasing Mn substitution (Fig. 3.5b). This density behavior is attributed to the replacement of heavier NiO (6.72 g / cc) by the lighter MnO (5.37 g / cc) in the spinel lattice

while, the increase in the porosity is due to the combine effect of decreasing density and particle size. The average crystallite size was calculated from most intense XRD peaks using Debye-Scherrer equation 2.8 given in the section 2.3.4. The average crystallite size was observed in the range 14 nm to 30 nm suggesting the nanocrystalline nature of these 'as synthesized' ferrites [Table 3.5]. The surface area of 'as synthesized' $Ni_{0.6-x}Mn_xZn_{0.4}Fe_2O_4$ (x = 0.0-0.6) obtained from BET measurement was found to be in the range of 29.5 m^2 / gm to 61.0 m^2 / gm. These high values of surface area are due to the combine effect of decrease in the particle size and increase in porosity with increasing Mn content. The very high value of surface area observed for composition, x = 0.5, may be due to its very small crystallite size. The unit cell of cubic spinel ferrites is known to contain 64 tetrahedral sites and 32 octahedral sites. The metal ions occupy only 8 tetrahedral sites and 16 octahedral sites. The distance between the magnetic ions (hopping length) in tetrahedral 'L_A' and octahedral 'L_B' sites in the spinel lattice were calculated by using equation number 2.9 and 2.10 given in the chapter 2. The variation of hopping lengths (L_A, L_B) with composition is represented in Fig. 3.5(c). Both the hopping length (L_A and L_B) increases with increasing Mn content, which is attributed to the increase of lattice parameter. The mean ionic radius of the tetrahedral 'r_A' sites and octahedral 'r_B' sites was calculated from the revised values of ionic radii of metal ions [174] using equation number 2.11 and 2.12, respectively mentioned in the section 2.3.4. These calculations are based on the cation distributions given in the Table 3.6. The mean ionic radius of tetrahedral 'r_A' sites increases sharply with increasing Mn content, while that of octahedral 'r_B' sites displays marginal increase (Fig. 3.5d). This behavior can be explained considering the preference of metal ions for tetrahedral and octahedral sites in spinel lattice. The Fe^{3+} ions and Mn^{2+} ions exist at both tetrahedral (A) and octahedral [B] sites, but Mn^{2+}

ions prefer tetrahedral (A) sites than Fe^{3+} ions, while for octahedral [B] site Fe^{3+} ions have more preference than Mn^{2+}ions.
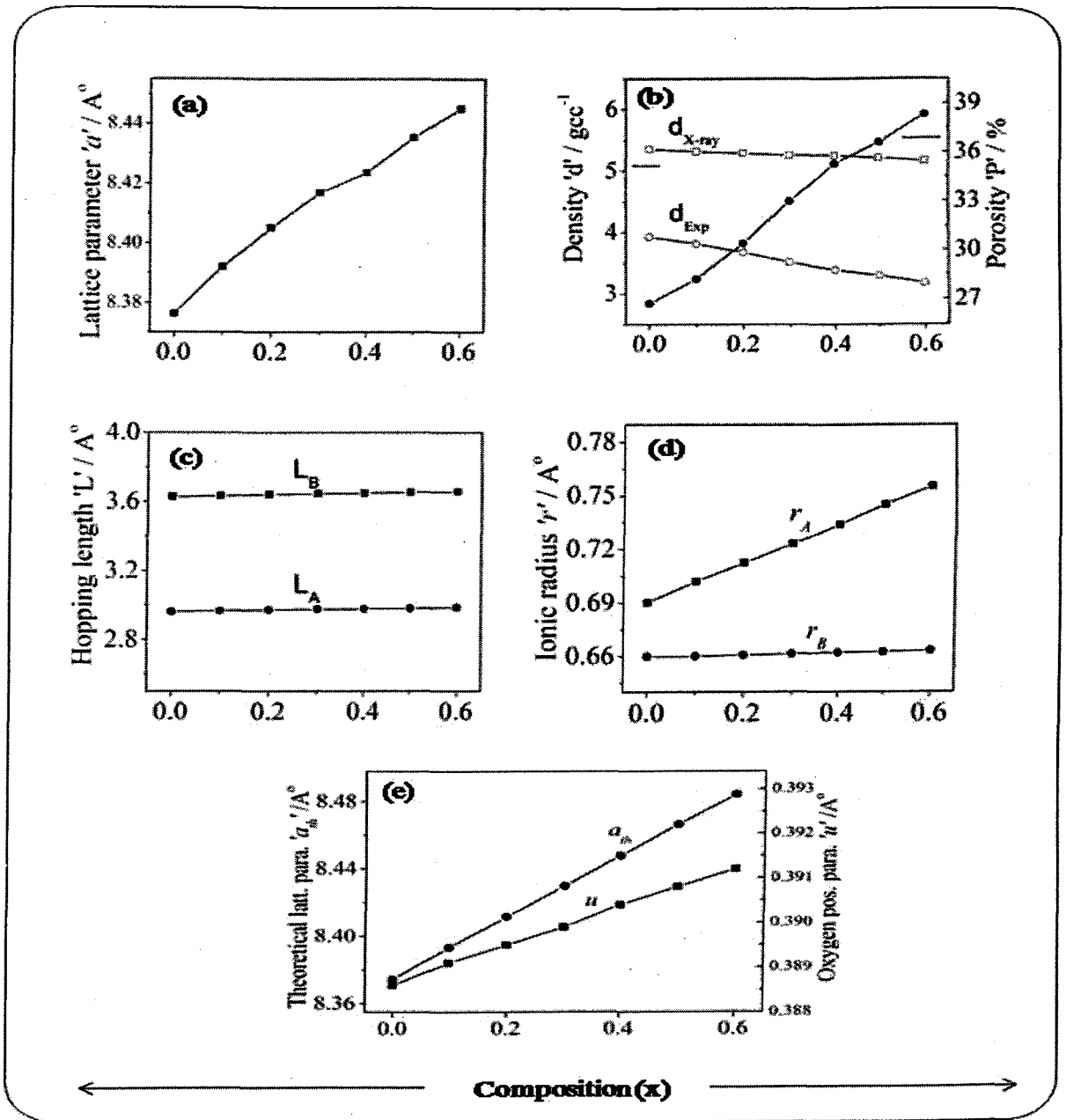
Fig.3.5. Variation of a) lattice parameter, b) density and porosity, c) hopping length, d) ionic radius, e) theoretical lattice parameter and oxygen position parameter with composition of 'as synthesized' $Ni_{0.6-x}Mn_xZn_{0.4}Fe_2O_4$ (x = 0.0-0.6) ferrites

Table 3.5. Lattice constant 'a', density 'd', porosity 'P', particle size 't', surface area 'SA', hopping lengths in tetrahedral 'L_A' and octahedral 'L_B' site of 'as synthesized' $Ni_{0.6x}Mn_xZn_{0.4}Fe_2O_4$ ($x = 0.0$-0.6) ferrites

x	a /A°	d / gcc^{-1}		P / %	t / nm		SA / m^2	L_A / A°	L_B / A°
		X-ray	bulk		XRD	TEM			
0.0	8.3763	5.36	3.93	26.7	30	12-35	29.5	3.627	2.962
0.1	8.3920	5.32	3.82	28.2	19	16-31	32.7	3.634	2.967
0.2	8.4051	5.29	3.68	30.4	21	11-23	33.5	3.640	2.972
0.3	8.4150	5.26	3.52	33.1	23	10-25	34.6	3.645	2.976
0.4	8.4236	5.25	3.39	35.3	17	8-23	49.5	3.648	2.978
0.5	8.4354	5.21	3.30	36.6	14	8-17	61.0	3.653	2.982
0.6	8.4450	5.16	3.18	38.3	22	9-26	37.4	3.657	2.986

It is estimated that nearly about 80 % of Mn^{2+} ions occupy tetrahedral (A) sites, while remaining 20 % goes to octahedral [B] sites [197]. It is also known that Zn^{2+} and Ni^{2+} ions has strong preference for tetrahedral (A) and octahedral [B] sites, respectively in bulk ferrite materials. However, in ultrafine state considerable concentrations of Zn^{2+} ions occupy octahedral [B] sites and Ni^{2+} ions occupy tetrahedral (A) sites, which is against their site preferences [198]. When Mn^{2+} ions are substituted for Ni^{2+} ions in the spinel lattice, it forces the Fe^{3+} ions and Ni^{2+} ions from tetrahedral (A) sites to octahedral [B] sites, at the same time Zn^{2+} ions from octahedral [B] sites are transferred to tetrahedral (A) sites. The net result of this displacement is sharp increase in radius of tetrahedral 'r_A' site and marginal rise in radius of octahedral 'r_B' sites. The theoretical lattice parameter 'a_{th}' was calculated from mean ionic

radii of tetrahedral and octahedral sites using equation 2.13 given in the chapter 2. The oxygen position parameter 'u', which is a quantitative measure of the displacement of an oxygen ion due to substitution of a metal cation in tetrahedral site was calculated using the radius of oxygen ion (R_O = 1.32 °A) and the mean ionic radii of tetrahedral ' r_A' sites in the expression number 2.14 given in the section 2.3.4. The Fig. 3.5(e) represents the variation of theoretical lattice parameter 'a_{th}' and oxygen position parameter 'u' with increasing Mn substitution. The theoretical lattice parameter 'a_{th}' increases from 8.3744 A° (x = 0.0) to 8.4842 A° (x = 0.6) which follows the same trend as lattice parameter 'a' obtained from XRD patterns of the ferrites. The oxygen position parameter 'u' increases from 0.3886 A° to 0.3912 A° with increasing Mn content. In an ideal face centre cubic structure, the oxygen position parameter, u =3/8=0.375. But in practice this ideal arrangement is slightly deformed. In most of the substituted spinel ferrites higher values of oxygen position parameters are reported [199-200].The high values of oxygen position parameter 'u' suggests that the oxygen ions are displaced in such a way that in the A-B interaction, the distance between A and O ions is increased while that between B and O is decreased. This leads to a decrease in the A-A interaction and an increase in the B-B interaction. Increase in the concentration of the Mn^{2+} ions into the A sub-lattice makes it expand to accommodate these ions. This expansion creates oxygen vacancies in the A-sites, which increases the trigonal distortion of the B-site oxygen coordination resulting in high values observed for oxygen position parameter 'u'. The tetrahedral bond length 'A-O', octahedral bond length 'B-O', tetrahedral edge length 'A-E',

Table 3.6. Theoretical lattice constant 'a_{th}', ionic radii at tetrahedral site 'r_A', ionic radii at octahedral site 'r_B', tetrahedral bond '$A\text{-}O$', octahedral bond '$B\text{-}O$', tetrahedral edge '$A\text{-}E$', octahedral edge '$B\text{-}E$' (shared), octahedral edge '$B\text{-}E$' (unshared), cation distribution and oxygen position parameter 'u' of 'as synthesized' $Ni_{0.6-x}Mn_xZn_{0.4}Fe_2O_4$ ($x = 0.0\text{-}0.6$) ferrites

x	$a_{th}/$ A°	$r_A/$ A°	$r_B/$ A°	$d_{A\text{-}O}/$ A°	$d_{B\text{-}O}/$ A°	$d_{A\text{-}E}/$ A°	$d_{B\text{-}E}/$ A°		$u/$ A°	cation distribution	
							shared	unshared		(A-site)	[B-site]
0.0	8.3744	0.6902	0.6599	2.004	1.987	3.283	2.639	2.970	0.3886	$(Zn_{0.369}Ni_{0.118}Fe_{0.513})$	$[Zn_{0.031}Ni_{0.482}Fe_{1.487}]O_4$
0.1	8.3932	0.7019	0.6601	2.022	1.988	3.302	2.633	2.977	0.3891	$(Mn_{0.073}Zn_{0.384}Ni_{0.088}Fe_{0.465})$	$[Mn_{0.027}Zn_{0.026}Ni_{0.412}Fe_{1.535}]O_4$
0.2	8.4114	0.7125	0.6608	2.032	1.989	3.319	2.629	2.984	0.3895	$(Mn_{0.139}Zn_{0.379}Ni_{0.061}Fe_{0.421})$	$[Mn_{0.061}Zn_{0.021}Ni_{0.339}Fe_{1.579}]O_4$
0.3	8.4297	0.7233	0.6614	2.043	1.990	3.336	2.625	2.991	0.3899	$(Mn_{0.205}Zn_{0.385}Ni_{0.036}Fe_{0.374})$	$[Mn_{0.095}Zn_{0.015}Ni_{0.264}Fe_{1.626}]O_4$
0.4	8.4478	0.7340	0.6620	2.054	1.991	3.355	2.619	2.998	0.3904	$(Mn_{0.270}Zn_{0.388}Ni_{0.019}Fe_{0.323})$	$[Mn_{0.130}Zn_{0.012}Ni_{0.181}Fe_{1.677}]O_4$
0.5	8.4663	0.7452	0.6625	2.065	1.992	3.372	2.615	3.005	0.3908	$(Mn_{0.354}Zn_{0.391}Ni_{0.011}Fe_{0.264})$	$[Mn_{0.166}Zn_{0.009}Ni_{0.089}Fe_{1.736}]O_4$
0.6	8.4842	0.7554	0.6633	2.075	1.994	3.388	2.611	3.012	0.3912	$(Mn_{0.393}Zn_{0.396}Fe_{0.211})$	$[Mn_{0.207}Zn_{0.004}Fe_{1.789}]O_4$

octahedral edge length '*B-E*' (shared) and octahedral edge length '*B-E*' (unshared) were calculated using the theoretical lattice parameters 'a_{th}' and oxygen position parameter '*u*' values in equation number 2.15, 2.16, 2.17, 2.18 and 2.19, respectively given section 2.3.4 chapter 2. The increase in tetrahedral bond length '*A-O*', octahedral bond length '*B-O*' tetrahedral edge length '*A-E*' and octahedral edge length '*B-E*' (unshared) with increasing Mn substitution can be directly related to increase of mean ionic radii (r_A and r_B) of both tetrahedral and octahedral interstices in 'as synthesized' nanocrystalline $Ni_{0.6-x}Mn_xZn_{0.4}Fe_2O_4$ (*x* = 0.0-0.6) ferrite lattice.

3.2.2. FTIR spectral analysis

The infrared spectroscopy is a very important technique to derive information about the positions of ions in the crystal lattice through the crystal's vibration modes [166]. The IR bands in the region 700 cm^{-1} to 300 cm^{-1} are assigned to the fundamental vibrations of the ions of the crystal lattice. The FTIR spectra of all 'as synthesized' $Ni_{0.6-x}Mn_xZn_{0.4}Fe_2O_4$ (*x* = 0.0-0.6) ferrites were represented in the Fig. 3.6 while, the absorption frequencies are given in the Table. 3.7. All the ferrite samples display two principal absorption bands in the frequency region from 1000 cm^{-1} to 340 cm^{-1}. The high frequency band (v_1) in the region 593 cm^{-1} to 563 cm^{-1} results from stretching vibration of the tetrahedral Fe^{3+}--O^{2-} bond, while low frequency band (v_2) in the region 404 cm^{-1} to 390 cm^{-1} arises due to Fe^{3+}--O^{2-} stretching vibration in octahedral sites [167]. The difference in the positions and intensities of v_1 and v_2 band are due to the different Fe^{3+}--O^{2-} distances for the tetrahedral and octahedral sites, since the vibrational frequencies depend on cation mass, M^{n+}--O^{2-} distance and the bonding force [201]. The relatively weak shoulder (v'_1) which slowly appears in the region ~730 cm^{-1} with

increasing Mn^{2+} ion concentration has been attributed to the stretching vibration of $Mn^{2+}\text{--}O^{2-}$ in tetrahedral sites [202].
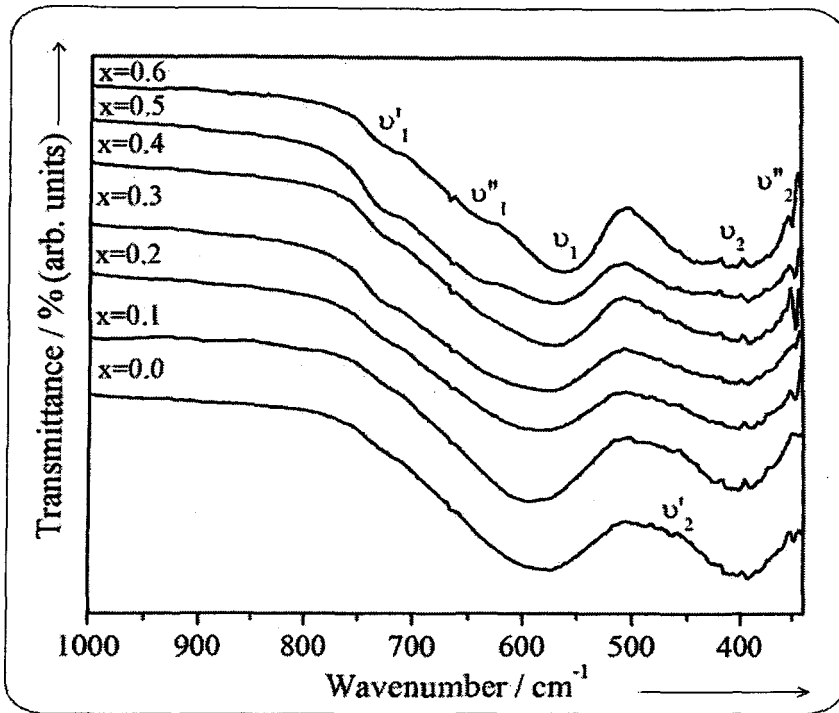
Fig.3.6. FTIR spectra of 'as synthesized' $Ni_{0.6-x}Mn_xZn_{0.4}Fe_2O_4$ (x = 0.0-0.6) ferrites

Another weak shoulder (v''_1) observed in the range 600 cm^{-1} to 650 cm^{-1} have been assigned to stretching vibration of tetrahedral $Zn^{2+}\text{--}O^{2-}$ bond. At lower concentration of Mn^{2+} ions, the concentration of Fe^{3+} ions at tetrahedral sites is relatively high as a result the band (v''_1) due to $Zn^{2+}\text{--}O^{2-}$ tetrahedral complexes was merged with v_1 band and was not visible in the samples with composition, x = 0.0 and 0.1. As the Mn^{2+} ions concentration increases at tetrahedral (A) sites, it pushes the Fe^{3+} ions on to octahedral [B] sites thereby decreasing their concentration at tetrahedral (A) sites. This causes the decrease in the intensity of v_1 band as a result of which the v''_1 shoulder starts appearing slowly from composition, x = 0.2. Mohammad *et al.* [203] have observed similar shoulder in the IR spectra of Mg-Zn ferrites

84

and Deraz [204] have reported similar results for the alumina-doped zinc ferrites. They have assigned this shoulder to both Fe^{2+}--O^2 and Zn^{2+}--O^{2-} tetrahedral complexes. Since, the Mössbauer spectral results of 'as synthesized' $Ni_{0.6-x}Mn_xZn_{0.4}Fe_2O_4$ ($x = 0.2, 0.3$) rules out the possibility Fe^{2+} ion formation, this shoulder can be been assigned to stretching vibrations of tetrahedral Zn^{2+}--O^{2-} bonds. A very weak (v'_2) band in the region ~ 465cm^{-1} was observed for all the composition except for composition, $x = 0.6$, have been assigned to the stretching vibrations of Ni^{2+}--O^{2-} bond in octahedral sites, since the concentration of Ni^{2+} ions in the octahedral sites is very high [107]. The IR peak (v''_2) observed in the region 349 cm^{-1} to 337 cm^{-1} can be assigned to Zn^{2+}--O^{2-} stretching vibrations. Srinivasan et al. [205] have reported similar peak at about 338 cm^{-1} for zinc ferrite, while Josyulu et al. [206] have observed the same peak at 325 cm^{-1}. Shirsath et al. [107] have also reported peak in this region in the FTIR spectra of Mn substituted Ni-Zn ferrites. The slight deviations in the positions of peaks are mainly due to the factors like amount of dopant, synthesis technique, grain size and density [207-209]. The absorption frequency and intensity of v_1 band decreases as the Mn^{2+} ions concentration is increased, whereas the intensity of v_2 band increases, but there is hardly any change in its absorption frequency. These observations can be explained considering the site preference and distribution of cations in tetrahedral and octahedral sites When Mn^{2+} ions ($r = 0.82$ A°) are introduced for Ni^{2+} ions ($r = 0.70$ A°) in spinel lattice it displaces Fe^{3+} ions ($r = 0.645$ A°) from tetrahedral to octahedral sites, since Mn^{2+} ions prefers tetrahedral sites over Fe^{3+} ions. This results in decrease in the concentration of Fe^{3+} ions in tetrahedral sites and sharp increase in mean ionic radius 'r_A' of tetrahedral sites. As a result the absorption frequencies and intensities of v_1 band decreases.

Table 3.7. FTIR absorption bands of 'as synthesized' $Ni_{0.6-x}Mn_xZn_{0.4}Fe_2O_4$ ($x = 0.0-0.6$) ferrites

Sites	Bands	FTIR absorption frequencies of 'as synthesized' $Ni_{0.6-x}Mn_xZn_{0.4}Fe_2O_4$ ($x = 0.0-0.6$) ferrites / cm^{-1}							
		0.0	0.1	0.2	0.3	0.4	0.5	0.6	M^{n+}---O^{2-}
Tetrahedral	v_1	585	594	586	580	579	572	563	Fe^{3+}---O^{2-}
	v'_1	---	--	~730	~730	~730	~730	~730	Mn^{2+}---O^{2-}
	v''_1	---	---	~640	~640	~640	~640	~640	Zn^{2+}---O^{2-}
Octahedral	v_2	404	404	404	404	404	404	402	Fe^{3+}---O^{2-}
		393	393	394	394	392	394	390	
	v'_2	465	464	468	465	464	465	---	Ni^{2+}---O^{2-}
	v''_2	349	345	347	337	347	347	349	Zn^{2+}---O^{2-}

For v_2 band, the substitution of Mn^{2+} ions do not affect much the ionic radius of octahedral 'r_B' sites as a result of which there is hardly any change in its absorption frequency, but its intensity increases due to increase of Fe^{3+} ions concentration at octahedral sites. Considering, the IR results and above discussion, it can be concluded that the expansion of tetrahedral site is greater than that of octahedral site. The increase observed in the cell dimensions is in accordance with the results obtained from X-ray diffraction and Mössbauer spectroscopic studies.

3.2.3. TG and DSC studies

The TG and DSC profiles of 'as synthesized' ferrite samples (Fig. 3.7) shows two mass loss regions. The marginal mass loss observed upto 100°C was due to the loss of physisorbed moisture on these samples.
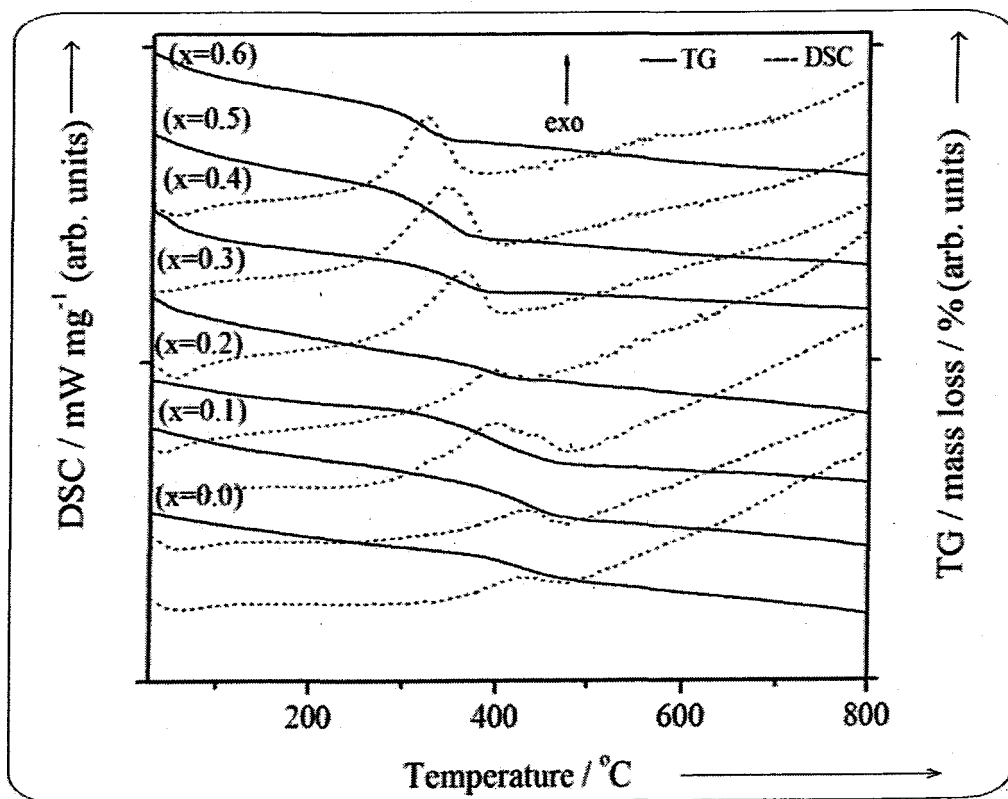
Fig.3.7. TG and DSC profiles of 'as synthesized' $Ni_{0.6-x}Mn_xZn_{0.4}Fe_2O_4$ ($x = 0.0-0.6$) ferrites

The next region of mass loss was observed from 330°C to 440°C, this mass loss has been attributed to the oxidation of residual carbon as indicated by broad exotherm in DSC in this region. It was observed that with increase in Mn concentration, the oxidation temperature decreases which may be due the increased catalytic activity of the Ni-Mn-Zn ferrites with increased in Mn content. In addition, the stable regions in TG and DSC above 400°C confirms absence of any metastable phases and hence the purity of 'as synthesized' $Ni_{0.6-x}Mn_xZn_{0.4}Fe_2O_4$ ($x = 0.0$-0.6) ferrites.

3.2.3. TEM measurements

The TEM was used to investigate into the size and shape and to confirm the nanocrystalline nature of the 'as synthesized' $Ni_{0.6-x}Mn_xZn_{0.4}Fe_2O_4$ ($x = 0.0$-0.6) ferrites. The Fig. 3.8 represents the TEM micrographs of the 'as synthesized' samples of above mentioned ferrite compositions. It has been observed from the TEM images that the particle size of all the ferrite samples lies in the range 8 nm to 35 nm. The ferrite nanoparticles were polydispersed and nearly spherical in shape. These nanoparticles display low tendency towards agglomeration and hence occur as loose agglomerates. It has been reported that Mn^{2+} ions substitution in ferrites accelerates grain growth [108]. Hence, it was expected that with increasing Mn concentration particle size should increase linearly. But no such effect on particle size was observed in our samples prepared using hydrazinated carboxylate precursor technique, which suggests that the decomposition exothermicity plays dominant role in determining the particle sizes than the Mn concentration. The particles size calculated using Scherrer method from XRD measurements matches with those obtained from TEM micrographs [Table 3.5]. The selective area electron diffraction (SAED) pattern images of 'as synthesized' ferrites nanoparticles are shown in the Fig. 3.9. The SAED images indicates the nanoparticles of

'as synthesized' $Ni_{0.6-x}Mn_xZn_{0.4}Fe_2O_4$ (x = 0.0-0.6) ferrites are highly crystalline in nature, since the distinct rings were observed in the images.
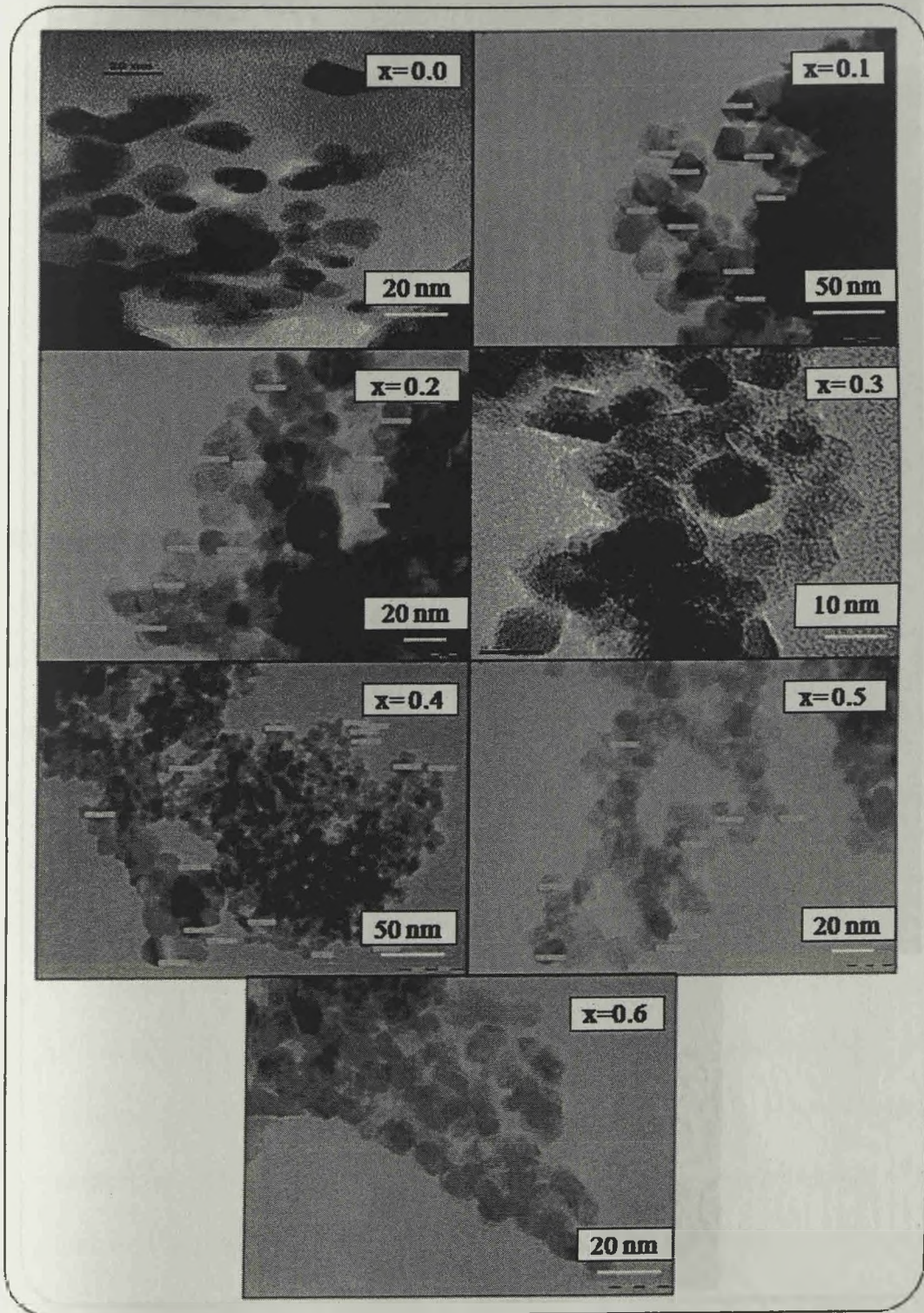
Fig.3.8. TEM micrographs of 'as synthesized' $Ni_{0.6-x}Mn_xZn_{0.4}Fe_2O_4$ (x = 0.0-0.6) ferrites
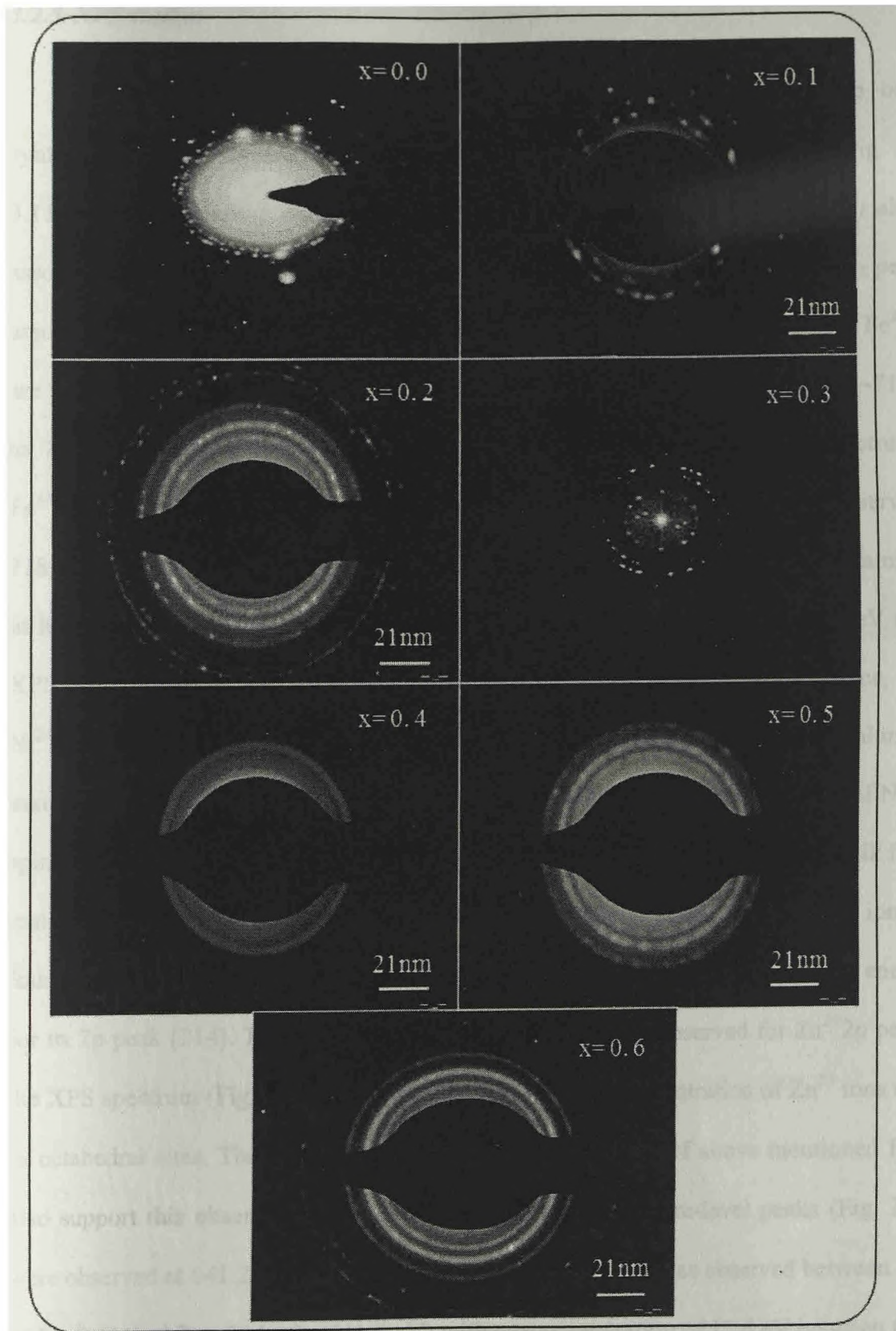
Fig.3.9. SAED patterns of 'as synthesized' $Ni_{0.6-x}Mn_xZn_{0.4}Fe_2O_4$ ($x = 0.0\text{-}0.6$) ferrites

3.2.5. XPS studies

The XPS core level spectra of $Fe^{2+}2p$, $Mn^{2+}2p$, $Ni^{2+}2p$ and $Zn^{2+}2p$ of 'as synthesized' $Ni_{0.6-x}Mn_xZn_{0.4}Fe_2O_4$ ($x = 0.2$ and 0.3) ferrites are shown in the Fig. 3.10-3.11, while their binding energies are given in the Table 3.8. The $Fe^{3+}2p_{3/2}$ peak is always associated with a satellite peak at 8.0 eV above the main peak, while Fe^{2+} $2p_{3/2}$ peak is associated with a satellite peak at 6.0 eV above the main peak. If, both Fe^{3+} and Fe^{2+} ion are present in the material, then it results in a broad background over the region ~710 eV to 720 eV, due to overlapping of satellite peaks of both ions. The XPS spectrum of $Fe^{3+}2p_{3/2}$ (Fig. 3.10c) shows a main peak at 710.6 eV and a satellite peak was observed at 718.8 eV, which indicates that, the surface of the $Ni_{0.4}Mn_{0.2}Zn_{0.4}Fe_2O_4$ ferrite contains iron in its trivalent oxidation state only [210]. The $Ni^{2+}2p_{3/2}$ peak observed at 855.2 eV in the XPS spectrum (Fig. 3.10d) is characteristics of Ni^{2+} ions in spinel ferrite lattice, since $Ni^{2+}2p_{3/2}$ peak in NiO is always associated with a satellite peak at 1 eV to 2 eV along the main peak, but no such satellite peak was observed which suggests the presence of Ni^{2+} in spinel lattice [211]. The Zn^{2+} ions prefers tetrahedral sites in spinel structure in bulk ferrite material, while in the nanocrystalline state, considerable concentration of Zn^{+2} ions are found to occur at octahedral [B] sites, which can results in slightly higher binding energies for its 2p peak [214]. Thus, the binding energy of 1021.7 eV observed for $Zn^{2+}2p$ peak in the XPS spectrum (Fig. 3.10e) suggests that considerable concentration of Zn^{2+} ions exists in octahedral sites. The FTIR and Mössbauer spectral results of above mentioned ferrite also support this observation. The $Mn^{2+}2p_{3/2}$ and $Mn^{2+}2p_{1/2}$ core-level peaks (Fig. 3.10f) were observed at 641.2 eV and 652.8 eV. The $Mn^{2+}2p_{3/2}$ peak was observed between those of MnO (641 eV) and Mn_2O_3 (641.6 eV) with energy separation of 11.6 eV between them, which suggests that the product has been formed that most closely resembles the stoichiometric ferrites [198, 213].
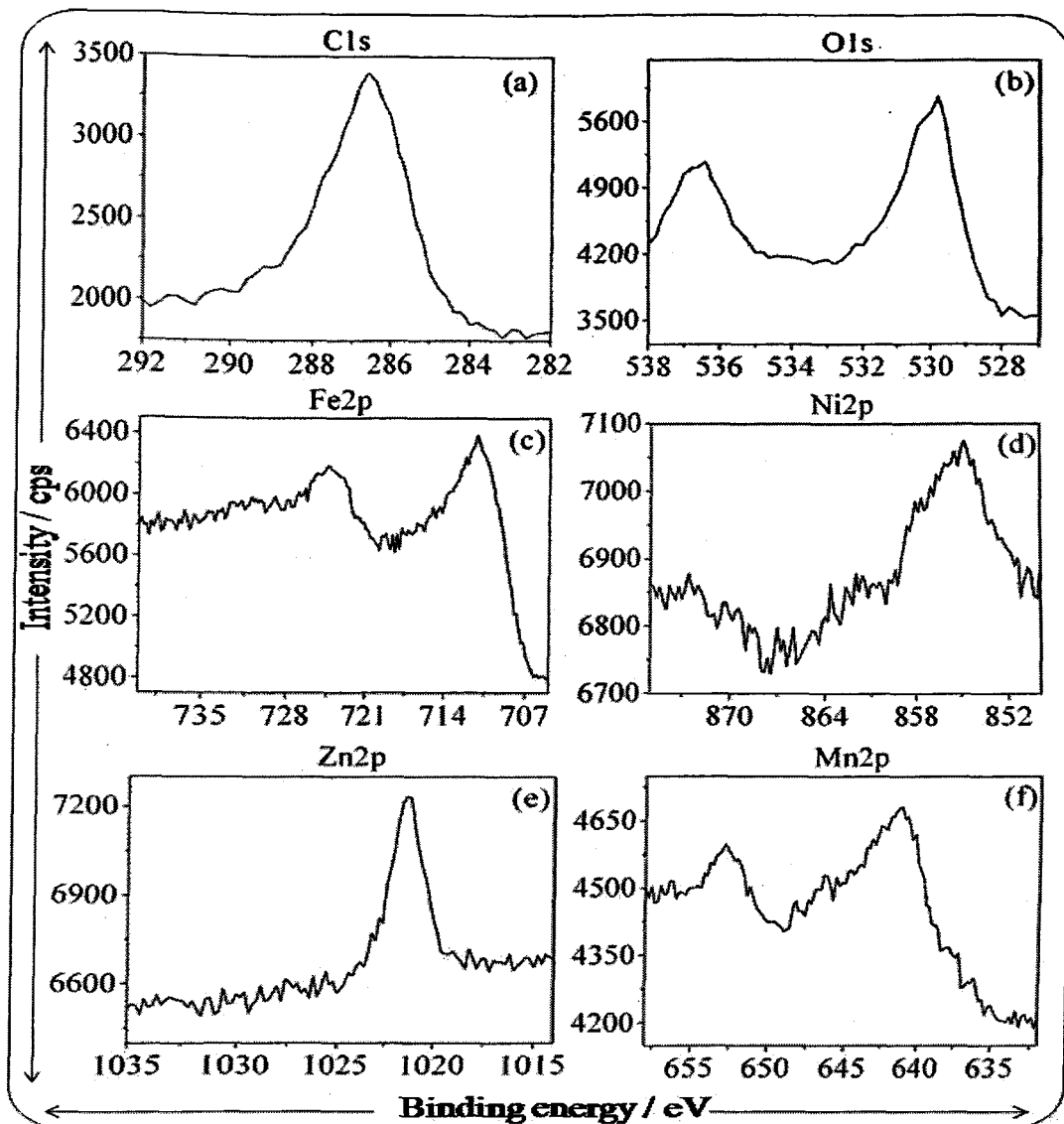
Fig.3.10. XPS spectra of 'as synthesized' $Ni_{0.6-x}Mn_xZn_{0.4}Fe_2O_4$ ($x = 0.2$)

Table 3.8. Binding energies of the metal ions obtained from XPS measurements of 'as synthesized' $Ni_{0.6-x}Mn_xZn_{0.4}Fe_2O_4$ ($x = 0.2$ and $x = 0.3$) ferrites

x	Binding energies / eV						
	Fe2p		Ni2p	Zn2p	Mn2p		O1s
0.2	710.6	718.8	855.2	1021.7	641.2	652.8	530.3
0.3	711.2	719.2	854.8	1021.4	641.4	652.9	529.9

Also, since the valence of other cations present in the sample is not changed during the formation of ferrite, manganese should be present in divalent state [214-215]. Similar results were observed in the XPS spectra of 'as synthesized' $Ni_{0.3}Mn_{0.3}Zn_{0.4}Fe_2O_4$ ferrite (Fig. 3.11). The binding energy corresponding to the $Fe^{3+}2p_{3/2}$ peak (Fig. 3.11c) shows slight increase [Table 3.8] which may be due to the transfer of Fe^{3+} ions from tetrahedral (A) site to octahedral [B] sites with the introduction of Mn^{2+} ions at tetrahedral (A) sites and presence of satellite at 8.0 eV above the main peak hints towards its trivalent oxidation state [216].
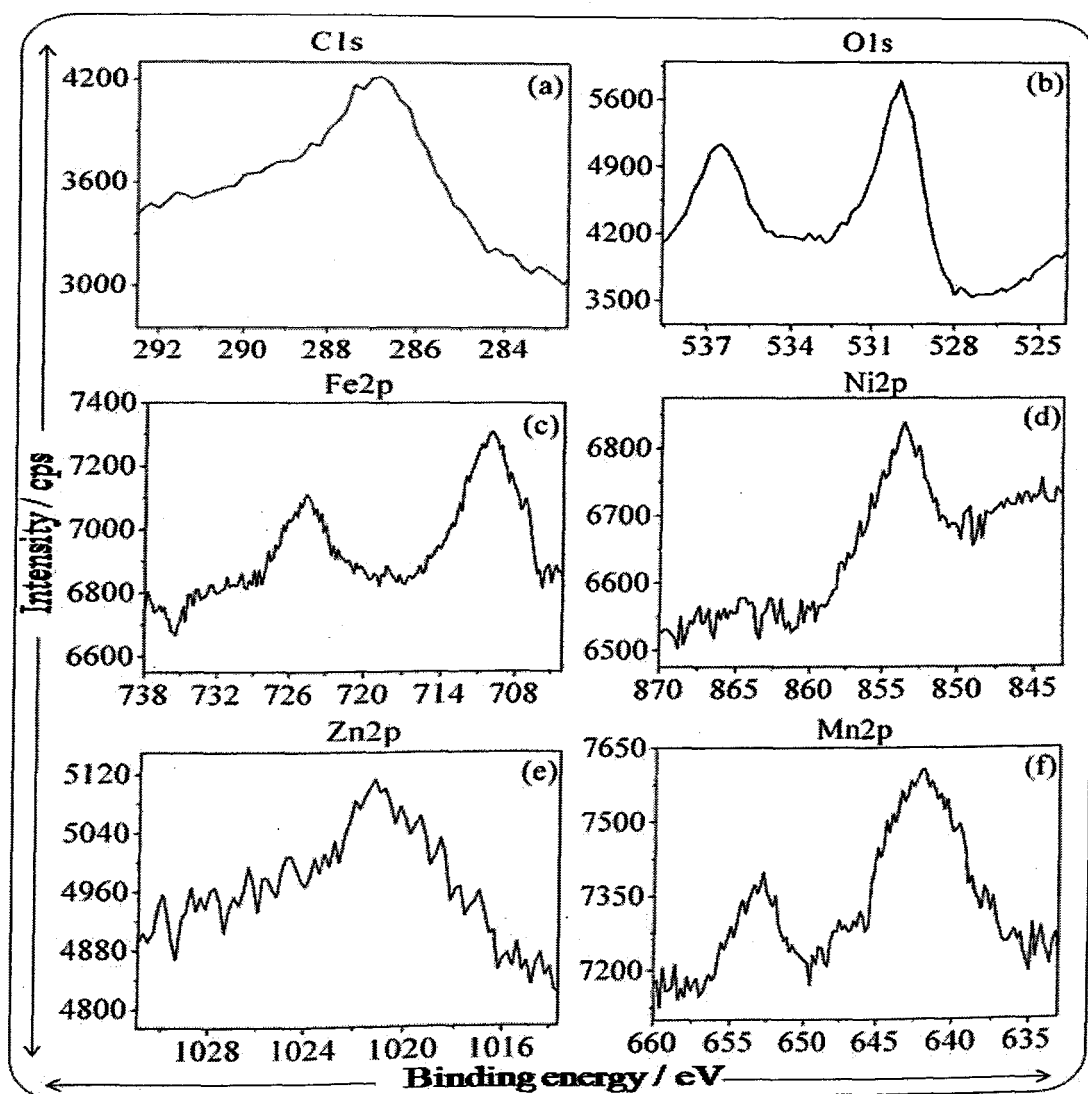
Fig.3.11. XPS spectra of 'as synthesized' $Ni_{0.6-x}Mn_xZn_{0.4}Fe_2O_4$ ($x = 0.3$)

The decrease in the binding energy observed for $Ni^{2+}2p_{3/2}$ peak is attributed to the change in surroundings of Ni^{2+} ions due to different cationic distribution in tetrahedral (A) and octahedral [B] sites, but the nature of the spectrum indicates that Ni^{2+} ions are present in spinel lattice only [211]. The binding energy for $Zn^{2+}2p_{3/2}$ peak (Fig. 3.11e) observed at 1021.4 eV in XPS spectrum is lower than that observed for composition, $x = 0.2$.

This lowering of binding energy may be due to transfer of Zn^{2+} ions occupying octahedral [B] sites to tetrahedral (A) sites with increasing Mn substitution in the spinel lattice [212]. The binding energies for $Mn^{2+}2p_{3/2}$ peak was observed at 641.4 eV and that for $Mn^{2+}2p_{1/2}$ peak was observed at 652.9 eV with energy separation of 11.5 eV between them indicates the formation of ferrite with proper stoichiometry [198, 213]. The binding energy for O1s peak was observed at 530.3 eV for composition, $x = 0.2$ (Fig. 3.10a) and 529.9 eV for composition, $x = 0.3$ (Fig. 3.11a) are in agreement with the reported values for the O1s peak in the spinel lattice [214]. Hence, it can be concluded that all the metal ions are present in their proper valence in the crystal lattice of 'as synthesized' $Ni_{0.6-x}Mn_xZn_{0.4}Fe_2O_4$ ($x = 0.2$ and $x = 0.3$) ferrites.

3.2.6. Mössbauer spectral studies

The Mössbauer spectra of 'as synthesized' $Ni_{0.6-x}Mn_xZn_{0.4}Fe_2O_4$ ($x = 0.0$-0.6) ferrites are given in the Fig. 3.12. The various Mössbauer effect parameters such as magnetic hyperfine field 'H_{hf}' values, isomer shift 'δ', quadrupole splitting 'Δ', linewidth 'Γ' and relative areas 'R_A' of tetrahedral and octahedral sites of iron ions are summarized in Table 3.9. In the mixed Ni-Mn-Zn-ferrites, Zn^{2+} ions have strong preference for the tetrahedral (A) sites, while Ni^{2+} ions have strong preference for the octahedral [B] sites. Mn^{2+} ions also occupy octahedral [B] sites albeit with small preference. The Mössbauer spectra of 'as synthesized' Mn substituted Ni-Zn ferrite samples exhibits a superposition

of three zeeman sextets due to ferromagnetic particles and a doublet due to superparamagnetic behaviour of nano-sized particles [217-218]. In general, a system of magnetic nanoparticles becomes single-domain below a critical size. In the single-domain state, these nanoparticles become superparamagnetic with a blocking temperature 'T_B'. Below T_B, the magnetization of such superparamagnetic nanoparticles fluctuates spontaneously with a relaxation time (τ) $\leq 10^{-9}$ sec. As a result, in the Mössbauer spectrum, magnetic splitting disappears resulting in a superparamagnetic doublet, as observed for 'as synthesized' $Ni_{0.6-x}Mn_xZn_{0.4}Fe_2O_4$ ($x = 0.0$-0.6) ferrites [218-219]. In nanoferrites, the H_{hf} values for both tetrahedral (A) and octahedral [B and B_1] sites are close to each other at higher Mn substitution ($x = 0.6$). This is because, the tetrahedral (A) and octahedral [B and B_1] sublattices are magnetically coupled and hence the spins at these sites fluctuate in unison [220].
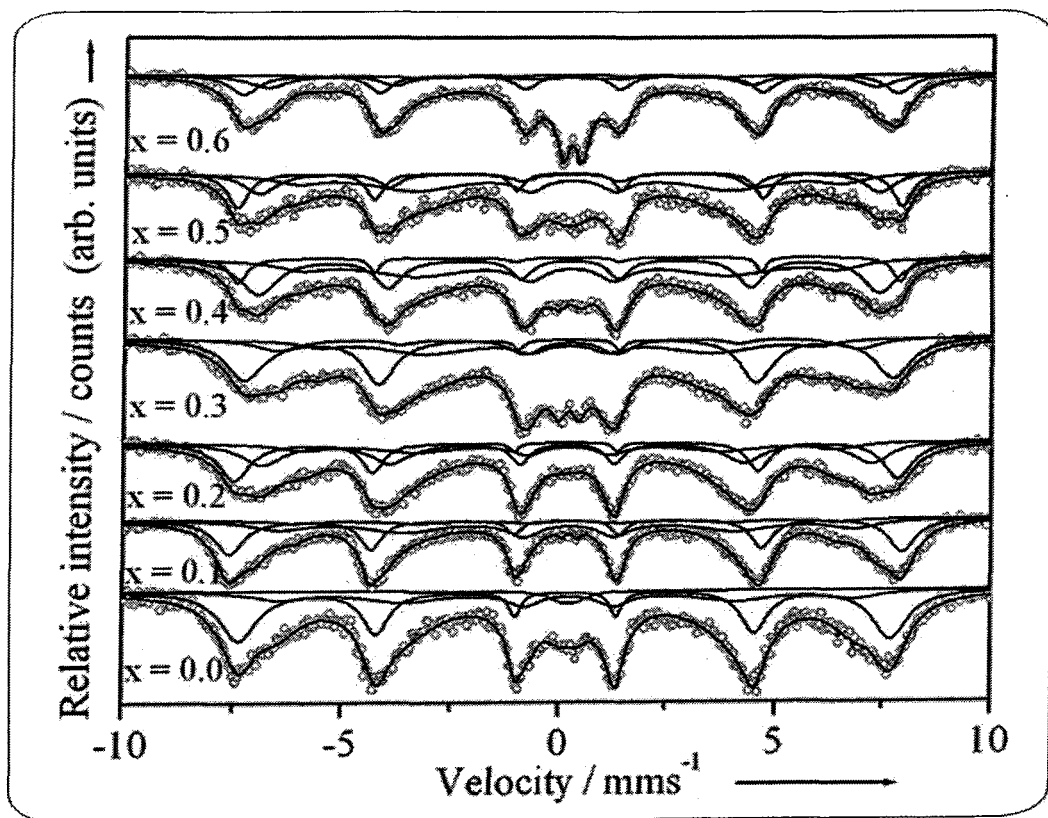
Fig.3.12. Room temperature Mössbauer spectra of 'as synthesized' $Ni_{0.6-x}Mn_xZn_{0.4}Fe_2O_4$ ($x = 0.0$-0.6) ferrites

Table 3.9. Room temperature Mössbauer effect parameters: isomer shift 'δ', quadrupole splitting 'Δ', hyperfine field 'H_{hf}', relative Area 'R_A' and inner line width 'Γ' of 'as synthesized' $Ni_{0.6-x}Mn_xZn_{0.4}Fe_2O_4$ (x = 0.0-0.6) ferrites

Sample	Site	*δ / mms^{-1}	Δ / mms^{-1}	H_{hf} / Tesla	R_A / %	Γ / mms^{-1}
0.0	Sextet 1, (A)	0.321	-0.054	41.19	56.52	0.911
	Sextet 2, [B]	0.279	-0.006	46.67	40.92	0.333
	Doublet	0.341	0.414	---	2.52	0.659
0.1	Sextet 1, (A)	0.292	-0.028	44.56	35.17	0.531
	Sextet 2, [B]	0.287	-0.001	48.24	39.68	0.389
	Sextet 2, [B$_1$]	0.321	-0.146	38.91	24.83	1.05
	Doublet	0.348	0.356	----	0.32	0.171
0.2	Sextet 1, (A)	0.332	0.004	38.13	42.2	0.834
	Sextet 2, [B]	0.273	0.0245	47.59	16.9	0.243
	Sextet 2, [B$_1$]	0.294	0.012	43.65	39.3	0.517
	Doublet	0.243	0.342	----	1.6	0.999
0.3	Sextet 1, (A)	0.319	0.035	46.2	29.4	0.882
	Sextet 2, [B]	0.313	-0.01	36.3	58.2	0.243
	Sextet 2, [B$_1$]	0.316	0.021	41.5	9.6	0.867
	Doublet	0.307	0.480	----	2.8	0.499
0.4	Sextet 1, (A)	0.332	-0.030	38.41	57.67	0.921
	Sextet 2, [B]	0.288	0.05	47.56	5.16	0.373
	Sextet 2, [B$_1$]	0.309	-0.003	44.57	34.64	0.592
	Doublet	0.31	0.528	-----	2.53	0.589
0.5	Sextet 1, (A)	0.329	-0.69	38.99	81.60	0.822
	Sextet 2, [B]	0.303	0.051	47.71	0.22	0.382
	Sextet 2, [B$_1$]	0.313	-0.007	44.45	34.03	0.694
	Doublet	0.316	0.421	-----	6.51	0.938
0.6	Sextet 1, (A)	0.349	0.141	36.01	30.16	1.396
	Sextet 2, [B]	0.307	0.011	46.97	27.42	0.488
	Sextet 2, [B$_1$]	0.338	-0.005	43.65	36.22	0.591
	Doublet	0.338	0.45	-----	6.2	0.398

*Isomer shift values are relative to α-Fe metal foil (δ = 0.0 mm/s), (): tetrahedral, []: octahedral

But, the H_{hf} values at the octahedral [B and B$_1$] site are much lower as compared to tetrahedral (A) at lower Mn substitution (x ≤0.5), which is due to a much faster relaxation

process. The isomer shift 'δ' values for all the samples in the range 0.285 mm/s to 0.312 mm/s for tetrahedral (A), 0.287 mm/s to 0.339 mm/s for octahedral [B] and 0.292 mm/s to 0.324 mm/s for octahedral [B_1] with respect to α-Fe metal foil ($\delta = 0.00$ mm/s) were observed. It indicates that, iron is present in its Fe^{3+} high spin ionic state [221]. The observed values of isomer shift are comparatively less than the expected value of 0.8 mm/s for the Fe^{2+} ion, which indicates that the formation of Fe^{2+} ion do not occurs during ferritization [222-224]. Hence, the sample maintains stiochiometry during their formations. The isomer shift 'δ' value of sextet A and sextet B is increases with Mn substitution, Fig. 3.13 (a). This is showing that bond length (Fe^{3+}-- O^{2-}) of tetrahedral and octahedral site is increases with Mn substitutions. Except for the superparamagnetic (SP) doublets ($\Delta_D = 0.388$ mm/s to 0.528 mm/s, $\delta_D = 0.305$ mm/s to 0.341mm/s and $R_A = 0.75$ % - 7.4 %), the quadrupole splitting 'Δ' values were nearly 0.0 mm/s, suggesting that Fe^{3+} ions show cubic symmetry of polyhedron. The variation in the quadrupole splitting 'Δ' with Mn substitution of different Fe^{3+} ion sites is shown in Fig. 3.13 (b). The comparatively higher value of quadrupole splitting 'Δ' for doublet was attributed to an increase in the asymmetry around the iron ions. Fig. 3.13 (c) represents the variation in relative area 'R_A' with Mn substitution of different Fe^{3+} ion sites. The relative area of sextet B and SP doublet were found to increase whereas the relative area of sextet A and sextet B_1 decreases with Mn substitutions. The isomer shift 'δ' values of SP doublet are between 0.305 mm/s to 0.341 mm/s. These values are consistent with iron ions in trivalent state (octahedral). The final relative area of tetrahedral (A) site (sextet A) and octahedral B site (sextet B + sextet B_1 + SP doublet) is shown in the Fig. 3.13d. It is clear from the Fig. 3.13d that relative area of tetrahedral (A) site (R_A- A site) decreases (from 48.6 % -11.9 %) whereas, the relative area of octahedral [B] site (R_A- B site) increases (from 51.4 % - 88.1 %) with increasing Mn substitutions.
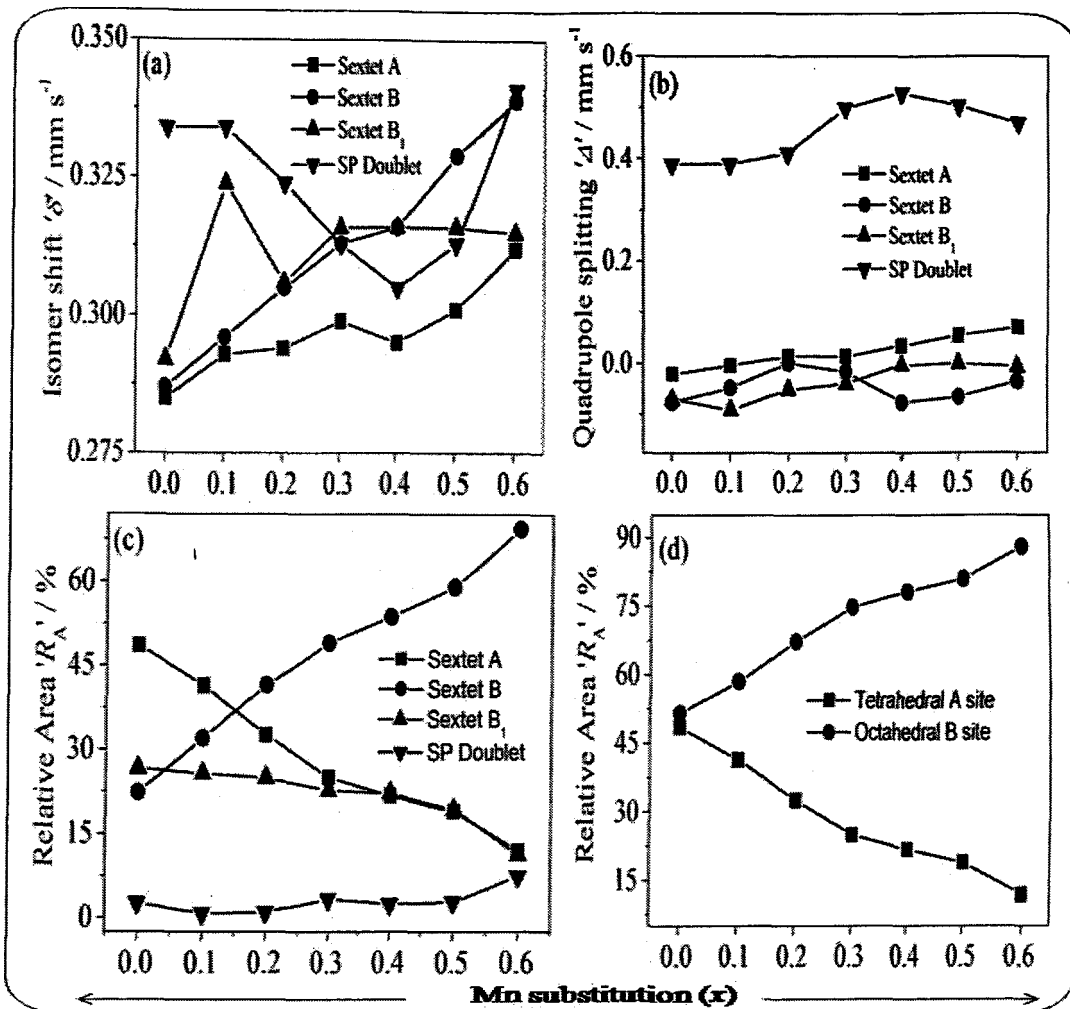
Fig.3.13. Variation of room temperature Mössbauer effect parameters, a) isomer shift 'δ',

b) quadrupole splitting 'Δ', c) relative area 'R_A' (sextet *A, B, B_1* and *SP* doublet) and d)

relative area 'R_A' (tetrahedral 'A' and octahedral 'B' site) with Mn substitution (x) of 'as

synthesized' $Ni_{0.6-x}Mn_xZn0_.4Fe_2O_4$ (x = 0.0-0.6) ferrites

3.3. Solid state properties of 'as synthesized' $Ni_{0.6-x}Mn_xZn_{0.4}Fe_2O_4$ (x = 0.0-0.6) ferrites

Spinel ferrites find wide range of applications in different fields such as electronics

and mass communication, memory devices etc. because of their unique electrical and

magnetic properties. Recently, the ferrite nanoparticles were being investigated for their

magnetic behavior which is particularly suitable for biomedical applications like MRI,

magnetic drug delivery system etc. This inspired us to study the electrical and magnetic characteristics of nanocrystalline 'as synthesized' $Ni_{0.6-x}Mn_xZn_{0.4}Fe_2O_4$ (x = 0.0-0.6) ferrites.

3.3.1. DC resistivity measurements

Spinel ferrites are known to exhibit semiconducting behaviour, though the mechanism of conduction is different. The mechanism of electrical conductivity in ferrites involves hopping of electrons between cations of same metal present in different oxidation states as explained by the Verwey model [225]. According to this model, in close-packed lattice formed by oxygen (anions), the metal ions occupy tetrahedral (A) sites and the octahedral [B] sites. The cations at these A and B sites can be treated as isolated from each other. The electron hopping at between two tetrahedral sites (A-A) does not take place since distance between two tetrahedral sites is larger than the distance between two octahedral sites [B-B], hence the hopping between the Fe^{2+} and Fe^{3+} ions occupying the octahedral [B] sites is primararily responsible for conduction [225-226]. Besides electron hopping, other factors such as particle size, grain boundaries, nature and concentration of other substituents present are known to affect the conductivities of ferrites [227-228]. In case of nanocrystalline ferrite materials, their resistivity was found to be affected by moisture content which results from their high porosity and low green density. The temperature dependence of the dc resistivity (log ρ) for the 'as synthesized' $Ni_{0.6-x}Mn_xZn_{0.4}Fe_2O_4$ (x = 0.0-0.6) ferrite nanoparticles is shown in Fig. 3.14. The plot (Fig. 3.14a) displays two distinct regions of conductivity. In the first region from room temperature to 393 K to 403 K (Fig. 3.14a) resistivities of the order of 10^5 Ωcm to 10^7 Ωcm were observed depending upon the composition of the nanosize ferrites. With

increase in temperature in this region, the resistivity increases and reaches maximum in the temperature range 373 K to 388 K.
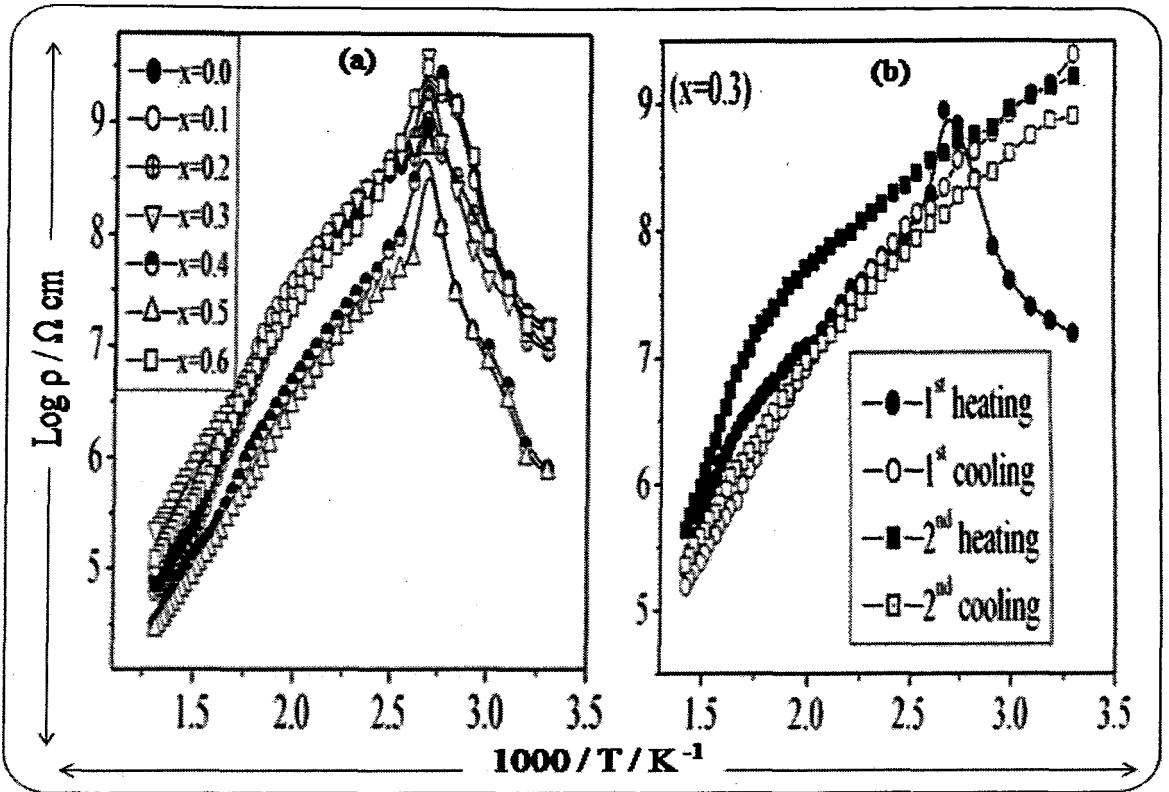
Fig.3.14. Plot of a) log resistivity against $10^3 / T$ 'as synthesized' $Ni_{0.6-x}Mn_xZn_{0.4}Fe_2O_4$ (x = 0.0-0.6) ferrites during heating and b) log resistivity (ρ) against $10^3 / T$ representing heating and cooling cycles for 'as synthesized' $Ni_{0.3}Mn_{0.3}Zn_{0.4}Fe_2O_4$

This behaviour is attributed to the presence of open porosity, loose agglomeration and entrapped moisture inside the pores of the powders [229-230]. The heating from room temperature upto ~383K causes total evaporation of moisture from the samples and therefore, maximum resistivities ($\rho = 10^8$ Ωcm to 10^9 Ωcm) were observed in the temperature region 373 K to 388 K. To obtained a fair idea about the conduction in this temperature region, the resistivity studies were carried out in heating and cooling cycles on a representative ferrite sample with composition, $x = 0.3$ and the plot of the same is shown in Fig. 3.14b. It was found that low resistivity behavior at room temperature was

100

observed only during the first heating. Also, the resistivity do not follow same trend during first heating and cooling cycle instead an hysteresis in the resistivity plots was observed, which clearly indicates that the mechanism of conduction during first heating and cooling cycle is different. The low resistivity at room temperature is resultant of protonic conductivity due to entrapped moisture [231-232], hence during the subsequent heating and cooling cycles the sample shows normal semiconducting behavior. Similar hysteresis behaviour is also reported in the literature for γ-Fe_2O_3 with high moisture contents [134]. In the second region above 393 K (Fig. 3.14a), the samples exhibits typical negative temperature coefficient of resistance (NTC) behaviour of ferrites [233] and linear plots were obtained. The plots were straight lines of two different slopes indicating that the samples change their magnetic behaviour at Curie temperature (T_c). The resistivity-temperature behavior obeys the equation 2.28 given in the section 2.3.11 of chapter 2. The activation energy of each sample was determined from the slope of the linear plots using the equation number 2.29 describe in section 2.3.11 of chapter 2. In low temperature (ferrimagnetic) region, the activation energies in the range 0.246 eV to 0.311 eV were observed, while in the high temperature (paramagnetic) region the activation energies were found to be in the range 0.382 eV to 0.587 eV [Table 3.10]. In mixed ferrite system like Ni-Mn-Zn ferrites, the activation energy is decided by the hopping probability of electrons and holes among $Fe^{3+} \leftrightarrow Fe^{2+}$, $Mn^{3+} \leftrightarrow Mn^{2+}$ and $Ni^{3+} \leftrightarrow Ni^{2+}$ pairs. The activation energy required for conduction due to electron hopping in ferrites is found to be of the order of 0.4 eV [234]. For hole hopping on the other hand still much energy is needed as compared to electron hopping. The observed values of activation energy suggests, the electronic conduction in the ferrimagnetic region, while the conduction in paramagnetic region is due to polaron hoping as it requires higher activation energies (> 0.4 eV). The effect of Mn substitution on room temperature dc resistivity is not clearly seen for 'as

synthesized' ferrites indicating that the effect of particle size, porosity and moisture content is more predominant on the resistivity than Mn substitution.

Table 3.10. Activation energies and Curie temperatures of 'as synthesized' $Ni_{0.6-x}Mn_xZn_{0.4}$ Fe_2O_4 $(x = 0.0-0.6)$ ferrites

x	Activation energy (E_a) / eV		Curie temperature (T_c) / K
	Low temperature region / E_f	High temperature region / E_p	
0.0	0.301	0.547	669
0.1	0.295	0.469	693
0.2	0.270	0.466	657
0.3	0.285	0.488	588
0.4	0.246	0.450	643
0.5	0.255	0.384	637
0.6	0.311	0.420	633

3.3.2. Thermoemf / Seebeck coefficient measurements

The thermoemf measurements were carried out on 'as synthesized' $Ni_{0.6-x}Mn_xZn_{0.4}Fe_2O_4$ $(x = 0.0-0.6)$ ferrites from 313 K to 723 K. The plots of four representative samples are shown in Fig. 3.15. The Seebeck coefficient was calculated using equation 2.30 given in the section 2.3.12 of chapter 2. The negative value of Seebeck coefficient suggests n-type charge carriers and positive values are attributed to p-type charge carriers. The most probable mechanism for n-type conduction is electron

hopping between Fe^{3+} and Fe^{2+} ions [225, 235]. The hole exchange between Ni^{3+} and Ni^{2+} as well as between Mn^{3+} and Mn^{2+} ions is responsible for p-type charge carriers [225].
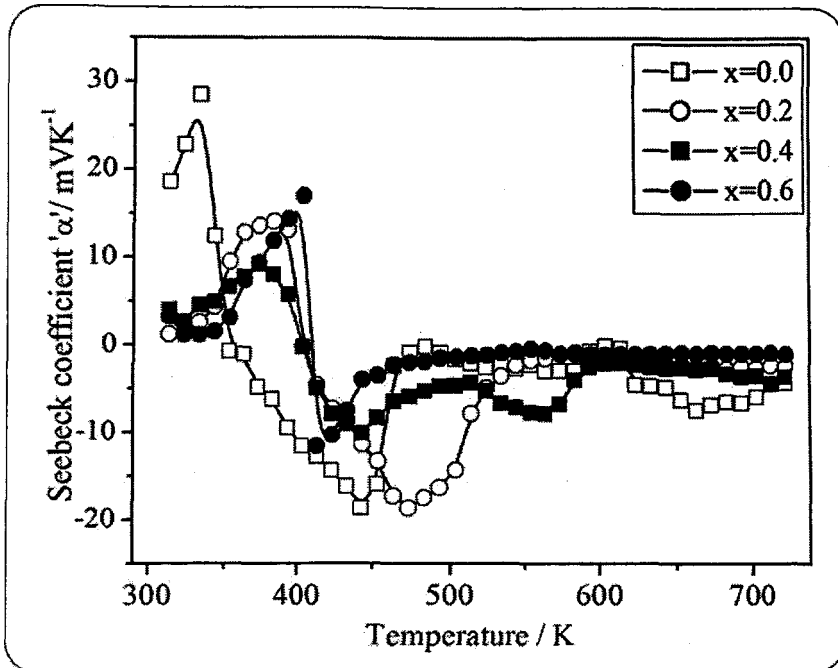
Fig.3.15. Variation of Seebeck coefficient with temperature of some representative of 'as synthesized' $Ni_{0.6-x}Mn_xZn_{0.4}Fe_2O_4$ (x = 0.0, 0.2, 0.4 and 0.6) ferrites

It is clear from Fig. 3.15 that all the samples are degenerate semiconductors [236]. All the samples show a p-type to n-type transition in the temperature region 373 K to 393 K suggesting the change in the conduction mechanism. In general, a small value of Seebeck coefficient ($\leq 30\ \mu V\ K^{-1}$) indicates that the electronic state is metallic, while large values of Seebeck coefficient ($\geq 100\ \mu V\ K^{-1}$) are related to localized electronic states for the oxide ceramics [237]. The values of Seebeck coefficient obtained for 'as synthesized' $Ni_{0.6-x}Mn_xZn_{0.4}Fe_2O_4$ (x = 0.0-0.6) ferrites are much greater than 100 $\mu V\ K^{-1}$, indicating polaron hopping type of conduction. The change in the conduction mechanism in the temperature range 373 K to 393 K may be due to the protonic conductivity at lower temperature which is also observed in the dc resistivity plots.

3.3.3. Dielectric measurements

The dielectric properties of 'as synthesized' $Ni_{0.6-x}Mn_xZn_{0.4}Fe_2O_4$ ($x = 0.0$-0.6) ferrites were studied in a frequency range from 100 Hz to 10 MHz at room temperature as well as at higher temperature upto 250°C. The dielectric constant, complex dielectric constant and dielectric loss tangent were calculated using equation number 2.31, 2.32 and 2.33 respectively, given in the section 2.3.15 of chapter 2.

3.3.3.1. Frequency variation of dielectric properties

The frequency variation of dielectric constant and complex dielectric constant at room temperature, of 'as synthesized' $Ni_{0.6-x}Mn_xZn_{0.4}Fe_2O_4$ ($x = 0.0$-0.6) ferrites in the frequency range of 100 Hz to 10 MHz is presented in Fig.3.16 (a-b). The dielectric constant (ε') and complex dielectric constant (ε'') shows sharp decrease upto 1 kHz, followed by a gradual decrease from 1 kHz to 10 kHz, and is nearly independent of frequency from 10 kHz to 10 MHz. The decrease in dielectric constant with increasing frequency is a normal behaviour observed in most of the ferromagnetic materials. The dielectric constant of any material, in general, is due to dipolar, electronic, ionic and interfacial polarizations [238]. In a lower frequency region, surface polarization contributes predominantly than electronic or ionic polarization in determining the dielectric properties of ferrite materials [239]. The dispersion in dielectric constant observed in lower frequency region is due to Maxwell-Wagner interfacial type of polarization [239,240] which is well in agreement with Koop's phenomenological theory of dielectrics [29]. According to this model, the dielectric structure is assumed to be composed of two layers; the first layer is composed of well conducting grains separated by thin layer which is composed of relatively poor conducting grain boundaries. This creates inhomogeniety in the dielectric material which results in local accumulation of charge

under the influence of an electric field. The electrons reach the grain boundary through hopping and if the grain boundary resistance is high enough, the electrons pile up at the grain boundaries and produce polarization. However, as the frequency of the applied field is increased, the electrons reverse their direction of motion more often. This decreases the probability of electrons reaching the grain boundary and as a result the polarization decreases.

Fig.3.16. Frequency variation of ; a) dielectric constant (ε'), b) complex dielectric constant (ε''), c) dielectric loss tangent (tan δ) at room temperature and temperature variation of ; d) dielectric constant (ε'), e) complex dielectric constant (ε''), f) dielectric loss tangent (tan δ) at 100 Hz of 'as synthesized' $Ni_{0.6-x}Mn_xZn_{0.4}Fe_2O_4$ ($x = 0.0-0.6$) ferrites

Therefore, the dielectric constant decreases with increasing frequency of the applied field. The dielectric constant values are quite low and are in the range of 0.05 to 380 at room temperature [Table 3.11] which are about 10^3 times lower than those reported for samples prepared using conventional ceramic method [29,241]. These low dielectric constant values are attributed to homogeneity, better symmetry and small grain size [242]. Small grains have large surface boundaries which act as scattering centres for the flow of electrons thus reducing the interfacial polarization [89]. The variation of dielectric loss (tan δ) with frequency at room temperature is depicted in the Fig. 3.16c. It was observed that dielectric loss decreases initially with frequency followed by an increase for the composition, $x = 0.1$ and 0.2. The dielectric loss in ferrite materials depend on a number of factors such as stoichoimetry, Fe^{2+} concentration and structural homogeneity which in turn depend on the composition and method of preparation. The dielectric loss gives the loss of energy from the applied field into the sample. This is caused by domain wall resonance. At higher frequencies, the losses are found to be low, since domain wall motion is inhibited and magnetization is forced to change rotation. The initial decreased can be understood from Koop's phenomenological model [29]. The appearance of a resonance peak (Debye relaxation peaks) for the compositions $x = 0.3$, 0.4 and 0.5 can be explained on the basis of the position exchange of ions, where the ions have more than one equilibrium positions of the same potential energy separated by a potential barrier. If the natural frequency of ion exchange between positions of equal potential is the same as the frequency of the externally applied alternating field, then maximum energy is transferred to the oscillating ions and the loss tangent shoots up, thereby resulting in a resonance [89]. Further, the position of the resonance peak shifted toward the lower frequency as the Mn concentration was increased. In the present work the loss tangent peak, for the composition, $x = 0.3$, 0.4 and 0.5 at room temperature was observed at frequencies below 50 kHz.

Table 3.11. Room temperature dielectric characteristics of 'as synthesized' $Ni_{0.6-x}Mn_x$ $Zn_{0.4}Fe_2O_4$ ($x = 0.0$-0.6) ferrites

Dielectric		x						
characteristics		0.0	0.1	0.2	0.3	0.4	0.5	0.6
Dielectric	100Hz	300.9	0.12	0.32	383.5	38.9	9.31	26.98
constant	1kHz	14.2	0.069	0.129	60.3	1.02	0.334	0.931
($\acute{\varepsilon}$)	10kHz	1.46	0.057	0.093	20.7	0.123	0.081	0.114
	1MHz	0.205	0.052	0.079	3.70	0.027	0.059	0.061
Complex	100Hz	1272	0.071	0.282	652	226	75.6	91.0
dielectric	1kHz	90.12	0.014	0.043	123	7.50	4.41	5.65
constant	10kHz	11.90	0.004	0.013	16.04	0.992	0.830	1.33
(ε")	1MHz	0.708	0.0009	0.074	4.522	0.035	0.059	0.21
Dielectric	100Hz	4.23	0.588	0.875	3.27	5.81	8.12	3.37
loss	1kHz	6.37	0.203	0.335	5.39	7.36	13.21	6.07
tangent	10kHz	8.17	0.075	0.143	7.55	8.046	10.30	11.67
($\tan \delta$)	1MHz	3.45	0.017	0.95	1.28	1.29	0.992	3.343

3.3.3.2. Temperature variation of dielectric properties

The temperature variation of dielectric constant (ε') and complex dielectric constant (ε") of 'as synthesized' $Ni_{0.6-x}Mn_xZn_{0.4}Fe_2O_4$ ($x = 0.0$-0.6) ferrites in the frequency range from 100 Hz to 10 MHz was studied and a representative study at 100 Hz is shown in Fig.3.16 (d-e). The dielectric constant (ε') and complex dielectric constant (ε") increases with temperature at all frequencies. It was observed in the present study that the increase in dielectric constant is rapid at lower frequencies than at higher frequencies. The

107

dielectric constant of ferrite materials is due to the contribution of four types of polarizations, namely, interfacial, dipolar, electronic and ionic [239]. At lower frequencies, the dipolar and interfacial polarizations are known to play the dominant role. Both these polarizations are strongly temperature dependent. The interfacial polarization increases with temperature due to creation of crystal defects, dipolar polarization decreases with increase in temperature. The rapid increase in the dielectric constant with increase in temperature at low frequencies suggests that the effect of temperature is more pronounced on the interfacial than on the dipolar polarization [243]. At high frequencies, electronic and ionic polarizations are the main contributor and their temperature dependence is insignificant. Hence, it results in constant value of dielectric constant at higher frequencies.

The temperature variation studies of the dielectric loss tangent of 'as synthesized' $Ni_{0.6-x}Mn_xZn_{0.4}Fe_2O_4$ (x = 0.0-0.6) ferrites at 100 Hz Fig.3.16 (f) shows increase with temperature which is also observed for all frequencies. The energy losses in the dielectric materials are due to the electric conductivity of the materials and the relaxation effect related to the dipole orientation. With increase in temperature, losses due to dipole orientations decreases, while those due to electric conductivity increases [239]. In the case of 'as synthesized' $Ni_{0.6-x}Mn_xZn_{0.4}Fe_2O_4$ (x = 0.0-0.6) ferrites, an increase in the dielectric loss was observed with temperature hence, it follows that losses due to electrical conductivity dominate over those due to relaxation effects. The effect of Mn substitution on the dielectric properties do not follows any regular trend suggesting that the factors such as particle size, porosity and density are predominant over Mn substitution in determining the dielectric properties of 'as synthesized' $Ni_{0.6-x}Mn_xZn_{0.4}Fe_2O_4$ (x = 0.0-0.6) ferrites.

3.3.4. Magnetic measurements

The magnetic measurements of 'as synthesized' $Ni_{0.6-x}Mn_xZn_{0.4}Fe_2O_4$ (x = 0.0-0.6) ferrites were carried out at room temperature using vibrating sample magnetometer (VSM) with field upto 2 tesla.

3.3.4.1. Magnetization

The magnetic hysteresis loops of 'as synthesized' $Ni_{0.6-x}Mn_xZn_{0.4}Fe_2O_4$ (x = 0.0-0.6) ferrite samples are presented in the Fig. 3.17 and values of various magnetic parameter are listed in the Table 3.12. The compositional variation of saturation magnetization and coercivity is given in the Fig. 3.18. The saturation magnetization values increases upto concentration, x = 0.2, and then decrease further with increase in Mn content with exception of x = 0.5. Similar variations were observed by other authors [107, 244]. The increasing trend suggests that the variation in saturation magnetization can be explained on the basis of Neel two sublattice model [245]. The decreasing trend is due to the nonzero Yafet-Kittel (Y-K) angles in the sample which cannot be explained on the basis of Neel theory sublattices. Thus, for the samples (x > 0.2) the Y-K angles are nonzero which suggests triangular type spin arrangements on B sites that weakens the A-B interactions. In the spinel system containing mixed Ni-Zn ferrites and Mn-Zn ferrites, the Fe^{3+} ions and Mn^{2+} ions exist at both tetrahedral (A) and octahedral [B] sites, although Mn^{2+} ions prefer tetrahedral (A) sites than Fe^{3+} ions, while for octahedral [B] sites, Fe^{3+} ions have more preference than Mn^{2+} ions. The Zn^{2+} ions on the other hand have strong preference for the tetrahedral (A) sites while, the Ni^{2+} ions strongly prefers the octahedral [B] sites. When Mn^{2+} ions are introduced at the cost of Ni^{2+} ions, some of the Fe^{3+} ions migrate from tetrahedral (A) sites to the octahedral [B] sites.

Fig.3.17. Hysteresis loops of 'as synthesized' $Ni_{0.6-x}Mn_xZn_{0.4}Fe_2O_4$ (x = 0.0-0.6) ferrites

110

Table 3.12. Hysteresis parameters of 'as synthesized'$Ni_{0.6-x}Mn_xZn_{0.4}Fe_2O_4$ (x = 0.0-0.6) ferrites

x	M_s / A m^2 kg^{-1}	M_r / A m^2 kg^{-1}	H_c x 10^{-3} / Tesla	Curie temp. 'T_c' / K
0.0	40.02	13.69	392.6	671
0.1	53.28	15.96	381.7	690
0.2	64.95	20.37	363.9	652
0.3	53.91	16.54	348.1	585
0.4	33.78	11.39	331.4	639
0.5	45.17	1.56	30.84	633
0.6	32.87	2.03	49.44	628

This will increase the concentration of Fe^{3+} ion at octahedral [B] sites, which results in increase of magnetic moment of B sublattice and hence the increase in total magnetization for lower Mn^{2+} ions content upto x = 0.2 [Table 3.12]. However, as Mn^{2+} ions concentration increases further, the Fe^{3+} ions left at tetrahedral (A) sites being small in number, the A-B sublattice interaction experienced by octahedral [B] site Fe^{3+} ions decreases. Also, the increase of Fe^{3+} ions concentration at octahedral [B] site increases the B-B interaction, which results in the canting of spins [246] and hence, the magnetization of B sublattice decreases. Although the magnetic moment of Mn^{2+}ions and Fe^{3+} ions is same (5 μB), the exchange interaction between Mn^{2+}ions and Fe^{3+} ions at tetrahedral (A) sites being small, there will be canting of spins at the tetrahedral (A) site. The increase in the Mn concentration in the ferrite therefore decreases the magnetic moment of the A sublattice and hence the overall decrease (Fig. 3.18). The low values of magnetization observed for 'as synthesized' $Ni_{0.6-x}Mn_xZn_{0.4}Fe_2O_4$ (x = 0.0-0.6) nanocrystalline ferrites as compared with the bulk may be due to the surface disorder and modified cationic

distribution [247-249]. In addition, formation of dead layer on the surface, existence of random canting of particle's surface spins, non-saturation effects due to random distribution of cations, have been reported for the reduction in magnetic properties of ferrite nanoparticles [250].

3.3.4.2. Coercivity (Hc)

The coercivity is the most fundamental hysteresis loop parameter which affects the shape of hysteresis loop. The coercivity is influenced by factors such as magnetocrystalline anisotropy, micro-strain, magnetic particle morphology, size distribution, shape anisotropy and magnetic domain size. Fig. 3.18 shows the variation of coercivity (Hc) with Mn substitution. The magnitude of coercivity decreases with increase in Mn content. It is known that the coercivity has a direct relation with the anisotropy constant of the sample.
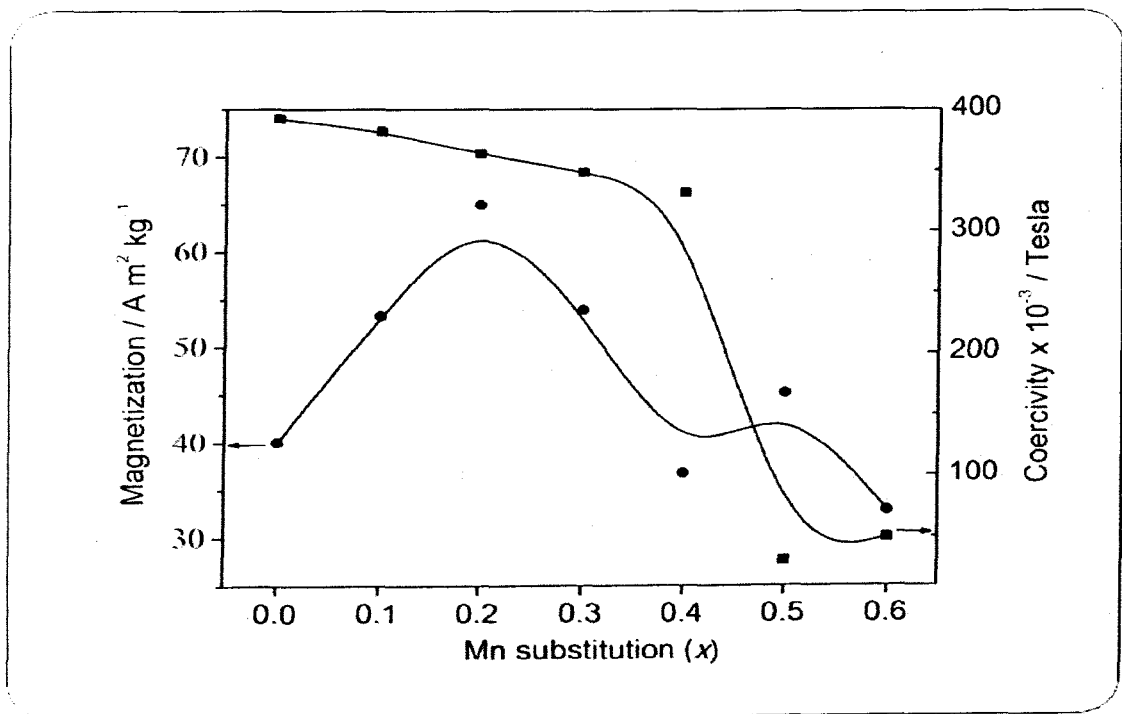
Fig.3.18. Variation of saturation magnetization and coercivity with Mn substitution (x) in 'as synthesized' $Ni_{0.6-x}Mn_xZn_{0.4}Fe_2O_4$ ($x = 0.0$-0.6) ferrites

The anisotropy constant of Ni-Zn ferrites is greater than the Mn-Zn ferrites and hence the decrease in coercivity can be related to the decreasing concentration of Ni^{2+} ions [251]. This means that the anisotropy constant decreases with increase in Mn^{2+} ions content and consequently, the magnitude of coercivity decreases. The very high values of coercivity observed for the compositions, $x = 0.0, 0.1, 0.2, 0.3$ and 0.4 [Table 3.12], are due to the significant percentage of single domain particles, while for composition $x = 0.5$ and 0.6, the low values of coercivity suggests that the samples contains predominantly superparamagnetic particles.

3.3.5. AC susceptibility studies

The magnetic properties of materials are determined by the types of particles which includes, single domain (SD), multidomain (MD) and superparamagnetic (SP) particles. The ac susceptibility measurements can be used to find out the types of particles responsible for magnetic properties. Hopkinson was the first person to study the variation in ac susceptibility with temperature in an iron sample and observed that, ac susceptibility reaches a peak value and rapidly becomes zero near Curie temperature. Later on many researchers have reported the variation in ac susceptibility (χ_T/χ_{RT}) with temperature (T) for ferromagnetic materials [252-253]. The plot obtained by these researchers gives an idea about the Curie temperature and domain structure. Below the Curie temperature ferrites have ferromagnetic nature and above Curie temperature they are paramagnetic in nature. The Hopkinson effect is observed in nanocrystalline single domain particles where the size of the particles is neither very small to be superparmagnetic nor very large to be multidomain in nature. According to Bean [254], the susceptibility is inversely proportional to the coercive force. The existence of a coercive force clearly indicates that the 'as synthesized'$Ni_{0.6-x}Mn_xZn_{0.4}Fe_2O_4$ ($x = 0.0$-0.6) ferrite samples contain clusters of

different sizes. For single domain particles, coercive force is large whereas it tends towards zero for superparamagnetic particles [254]. The variation of normalized ac susceptibility against temperature of 'as synthesized' $Ni_{0.6-x}Mn_xZn_{0.4}Fe_2O_4$ ($x = 0.0$-0.6) ferrites is shown in Fig. 3.19 (a). These graphs show normal ferrimagnetic behavior and the susceptibility suddenly drops to zero at certain temperature, this temperature is called Curie temperature (T_c). The nature of plots indicates that, the sample contains clusters of both single domain and superparamagnetic particles and the superparamagnetic character increases with increase in Mn^{2+} ions substitution. The Curie temperature determined for all samples are listed in Table 3.12. The variation of Curie temperature with composition of the ferrite series under study is shown in the Fig. 3.19 (b) which can be correlated with the Mn^{2+} ions concentration and A-B interactions except for composition, $x = 0.3$, where sudden drop in the Curie temperature was observed.
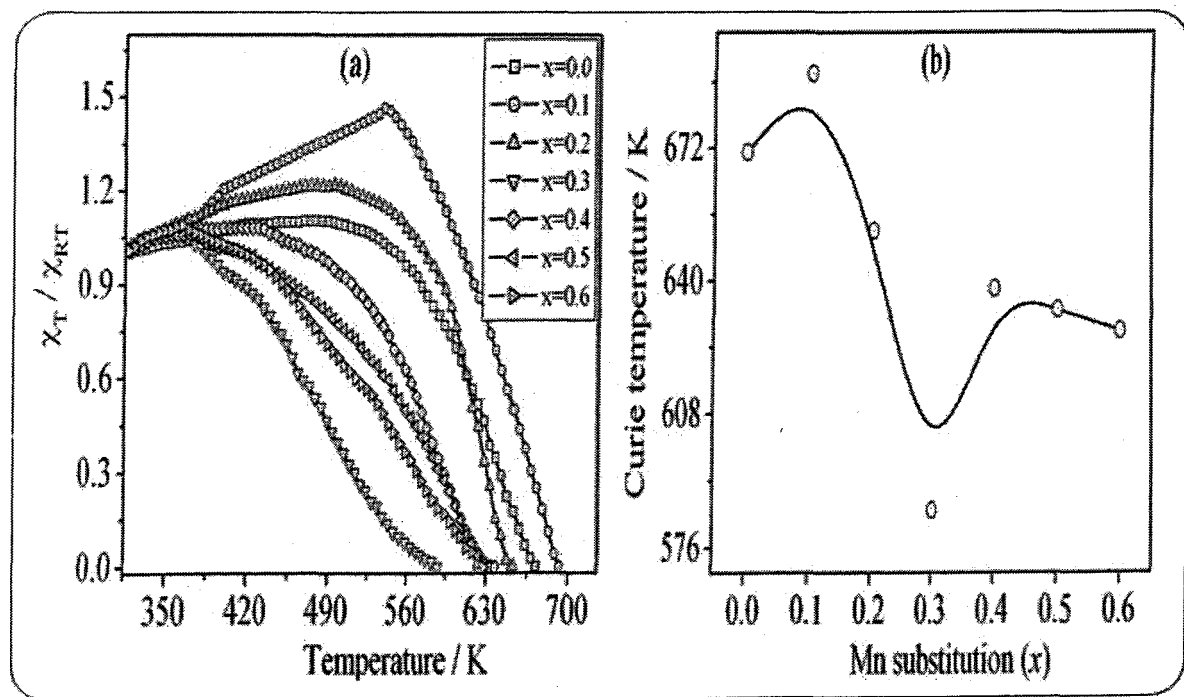
Fig.3.19. The plots of a) normalized a.c. susceptibility 'χ_T/χ_{RT}' against temperature, b) variation of Curie temperature 'T_c' with Mn substitution in 'as synthesized' $Ni_{0.6-x}Mn_xZn_{0.4}Fe_2O_4$ ($x = 0.0$-0.6) ferrites

This initial increase in Curie temperature is due to the increased of the A-B interaction and can be attributed to the increase in the distance between the moments of A and B sites which is confirmed by the increase in the lattice parameter with increasing Mn substitution. The decrease in Curie temperature, with increasing Mn content ($x > 0.1$) can be attributed to the decreasing B-B interaction resulting from canting of spins at B sites.

3.4. Gas sensing studies of 'as synthesized' $Ni_{0.6-x}Mn_xZn_{0.4}Fe_2O_4$ ($x = 0.0- 0.6$) ferrites

The gas sensing performance of the Ni-Mn-Zn ferrites is being reported for the first time. Gas sensing studies were carried out using the thick films resistors prepared from 'as synthesized' ferrite nanopowders. The details of gas sensing set up used are discussed in section 2.3.9 of chapter 2. Also, the detailed characterization of 'as synthesized' ferrite nanopowders is covered in section 3.2.1 to 3.2.6 of chapter 3. The sensing response and selectivity was found to vary with the composition of the present ferrite material. The sensor response was studied for various gases like H_2, CO_2, NH_3, H_2S, Cl_2, LPG, ethanol etc. from room temperature to 400°C. The sensor response of samples with composition, $x = 0.0$, 0.1 and 0.6 being very weak is not discussed here. The sensor response of thick film of composition, $x = 0.2$ with temperature is presented is Fig. 3.20 (a). The sample shows quite good sensitivity for gases like H_2 and CO_2 at room temperature. With increasing temperature the sensitivity was found to decrease sharply and the negligible response was observed for all the test gases at higher temperatures. For composition, $x = 0.4$, Fig. 3.20 (b) mixed response for test gases was observed over a range of temperatures. At room temperature, the sample shows comparatively high response for ethanol and NH_3 which, decreases sharply with increasing temperature. The response for CO_2 gas was observed at about 100°C which increases with increasing temperature upto 250°C and then decrease with further increase in temperature, while for

gases like H_2 and H_2S, the sensor shows increase in response with temperature. The sensor prepared from composition, $x = 0.5$, Fig. 3.20 (c) shows good response to H_2S at room temperature, which shows continuous increase with temperature upto 400°C. The highest response however at room temperature was shown by the sample for NH_3 gas which decreases sharply with increasing temperature.
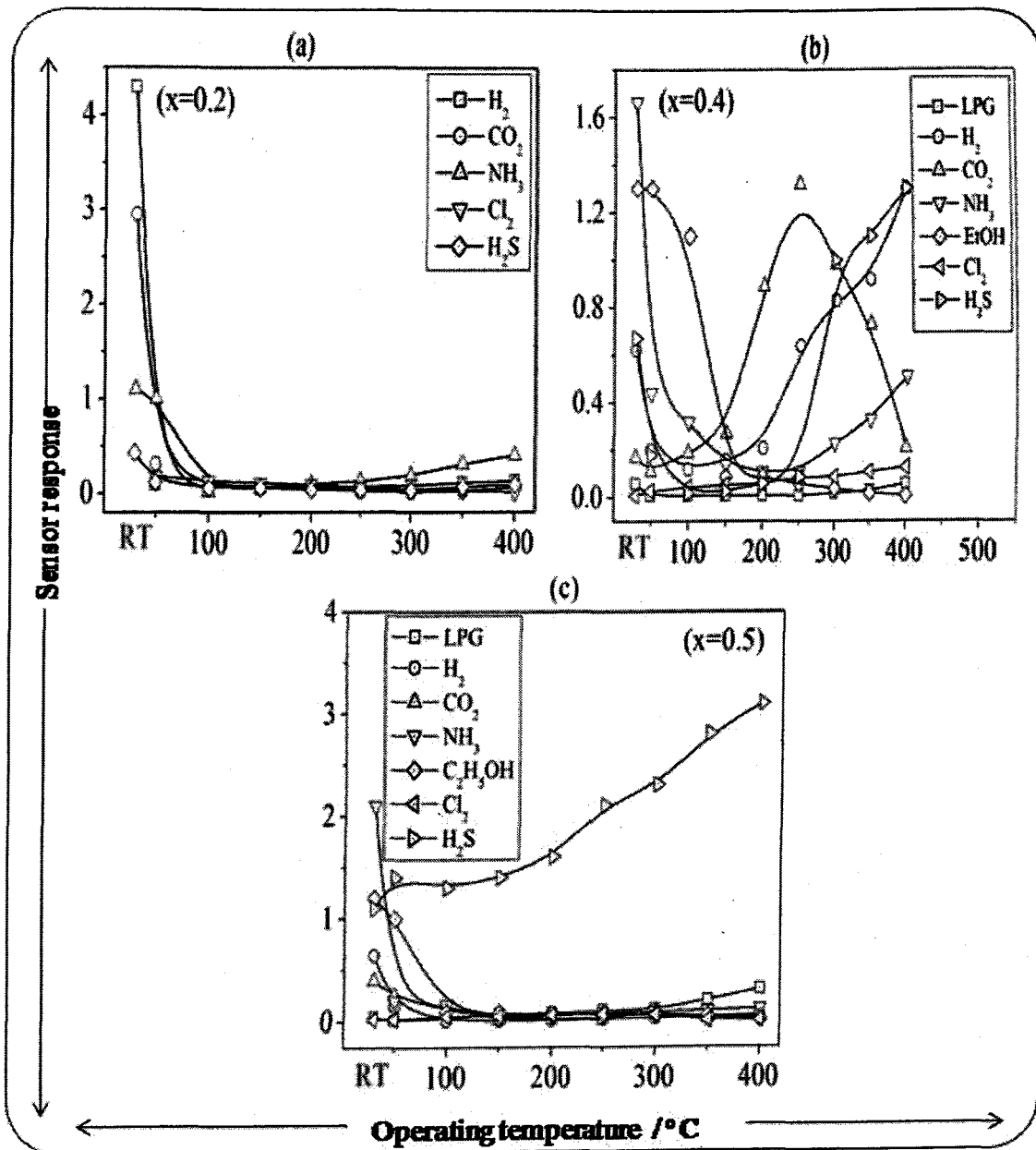
Fig.3.20. Variation of gas response with operating temperature of 'as synthesized' $Ni_{0.6-x}Mn_xZn_{0.4}Fe_2O_4$ ($x = 0.2$, 0.4 and 0.5) ferrites

Gas sensing mechanism for H_2S gas at higher temperatures is generally explained in terms of change in conductance either by adsorption of atmospheric oxygen on the surface and its subsequent reaction with the test gas and / or by direct reaction of lattice oxygen or interstitial oxygen with the gas. In the former case, the atmospheric oxygen adsorbs on the surface by extracting electrons from the conduction band to form superoxides or peroxides, which are mainly responsible for the detection of the test gases. The details of sensing mechanism for H_2S gas is described in the section 4.5. of chapter 4.

3.4.1. Gas sensing performance of thick film of 'as synthesized' $Mn_{0.3}Ni_{0.3}Zn_{0.4}Fe_2O_4$

The sample with composition, $x = 0.3$ displayed very good sensing response for NH_3 gas at room temperature hence, the sensing performance of thick film prepared from this sample have been investigated in detail.

3.4.1.1. SEM micrograph of thick film of 'as synthesized' $Mn_{0.3}Ni_{0.3}Zn_{0.4}Fe_2O_4$

Fig. 3.21 depicts the micrograph of $Mn_{0.3}Ni_{0.3}Zn_{0.4}Fe_2O_4$ sample under test. All particles were observed to be distributed randomly.
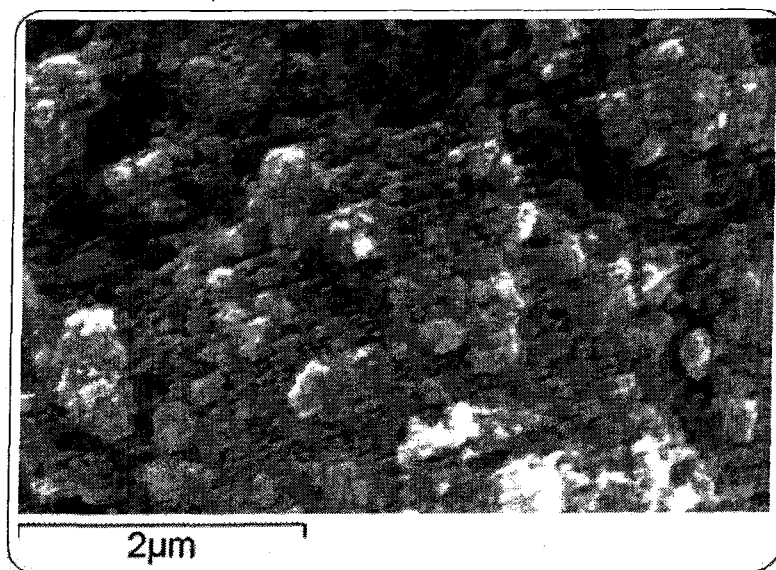
Fig.3.21. SEM image of thick film of 'as synthesized' $Mn_{0.3}Ni_{0.3}Zn_{0.4}Fe_2O_4$ sensor

The film was observed to be porous. Porosity increases the effective surface area of the film. As the gas sensing phenomenon is the surface phenomenon, the gas sensing performance was enhanced by such porous films. The maximum ammonia gas molecules may reach to interstitials of the films, which enhance the ammonia sensing even at room temperature. The thicknesses of the films were observed to be in the range from 17 μm to 22 μm. The reproducibility of the film thickness was achieved by maintaining the proper rheology and thixotropy of the paste.

3.4.1.2. Electrical conductivity of the sensor

The variation of log conductivity with reciprocal temperature of the $Mn_{0.3}Ni_{0.3}Zn_{0.4}Fe_2O_4$ film is shown in Fig. 3.22. The conductivity values of this ferrite sample increase with operating temperature. It is nearly linear to 1 / T in the range from 75°C to 400°C. The increase in conductivity with increasing temperature could be attributed to the negative temperature coefficient of resistance and semiconducting nature of the $Mn_{0.3}Ni_{0.3}Zn_{0.4}Fe_2O_4$ film.
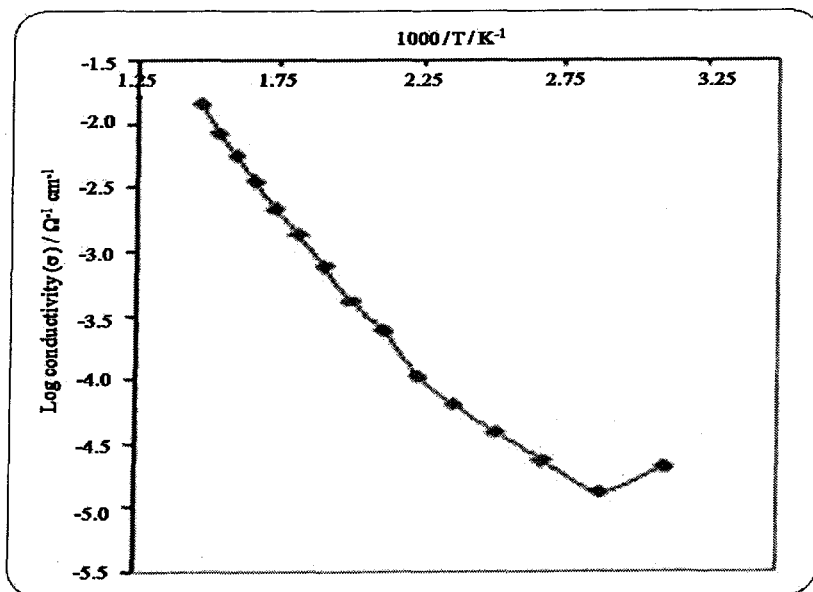
Fig.3.22. Conductivity-temperature profile of $Mn_{0.3}Ni_{0.3}Zn_{0.4}Fe_2O_4$ sensor

3.4.1.3. Effect of operating temperature

Fig. 3.23 depicts the variation of response to NH_3 gas (10 ppm) with operating temperature of $Mn_{0.3}Ni_{0.3}Zn_{0.4}Fe_2O_4$ ferrite thick film. The largest response of $Mn_{0.3}Ni_{0.3}Zn_{0.4}Fe_2O_4$ was observed to be 16.4 at room temperature. The ammonia response at room temperature is expected to be monitored by adsorption of moisture on the film. The cumulative effect would decrease the film resistance, giving a response to ammonia gas at room temperature. At room temperature, there would be no oxygen adsorption on the film surface. Therefore the oxygen adsorption-desorption mechanism is not employed to sense the NH_3 gas. When raising temperature above room temperature, the moisture from the film surface evaporates and hence the response would decrease further.
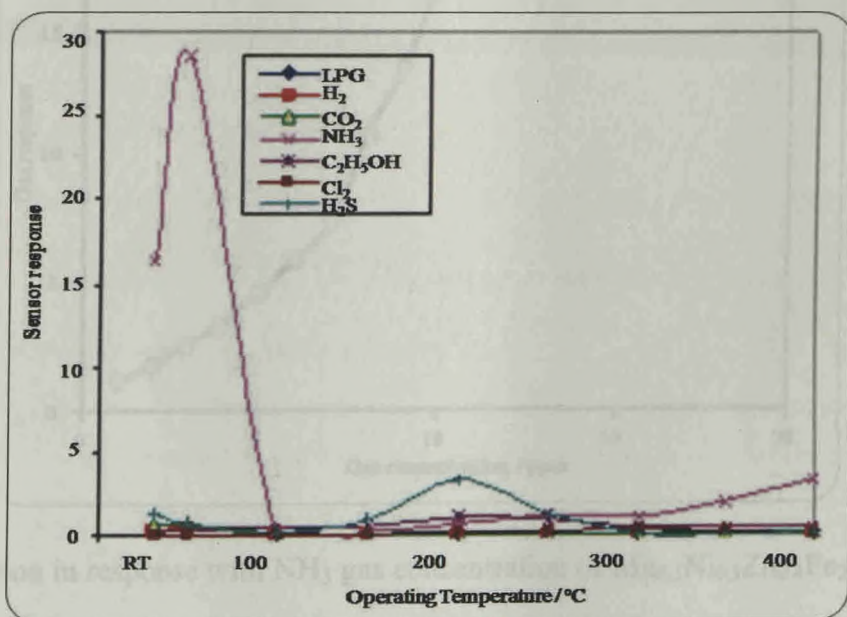
Fig.3.23. Variation of gas response with operating temperature of $Mn_{0.3}Ni_{0.3}Zn_{0.4}Fe_2O_4$ sensor

3.4.1.4. Active region of the sensor

The variation of gas response of the $Mn_{0.3}Ni_{0.3}Zn_{0.4}Fe_2O_4$ sample with NH_3 gas concentration at room temperature is represented in Fig. 3.24. This film was exposed to

varying concentrations of NH_3. For the $Mn_{0.3}Ni_{0.3}Zn_{0.4}Fe_2O_4$ sample, the response values were observed to increase continuously with increasing the gas concentration up to 10 ppm at room temperature. The rate of increase in response was relatively larger up to 10 ppm, but smaller during 10 ppm and 20 ppm. Thus, the active region of the sensor would be up to 10 ppm. At lower gas concentrations, the unimolecular layer of gas molecules would be formed on the surface of the sensor which could interact more actively giving larger response. The multilayers of gas molecules on the sensor surface, at the higher gas concentrations, would result into saturation in response beyond 10 ppm gas.
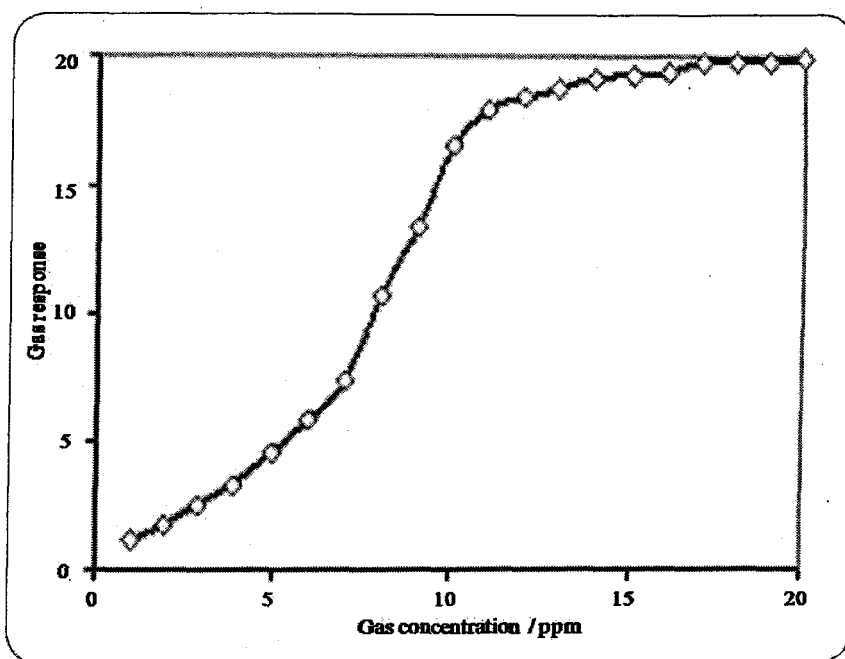
Fig.3.24. Variation in response with NH_3 gas concentration of $Mn_{0.3}Ni_{0.3}Zn_{0.4}Fe_2O_4$ sensor

3.4.1.5. Selective nature of the sensor

Fig. 3.25 depicts the selectivity of $Mn_{0.3}Ni_{0.3}Zn_{0.4}Fe_2O_4$ sensor for NH_3 (10 ppm) gas at room temperature. The sensor showed high selectivity to NH_3 against LPG, CO_2, C_2H_5OH, H_2, H_2S and Cl_2 gases.
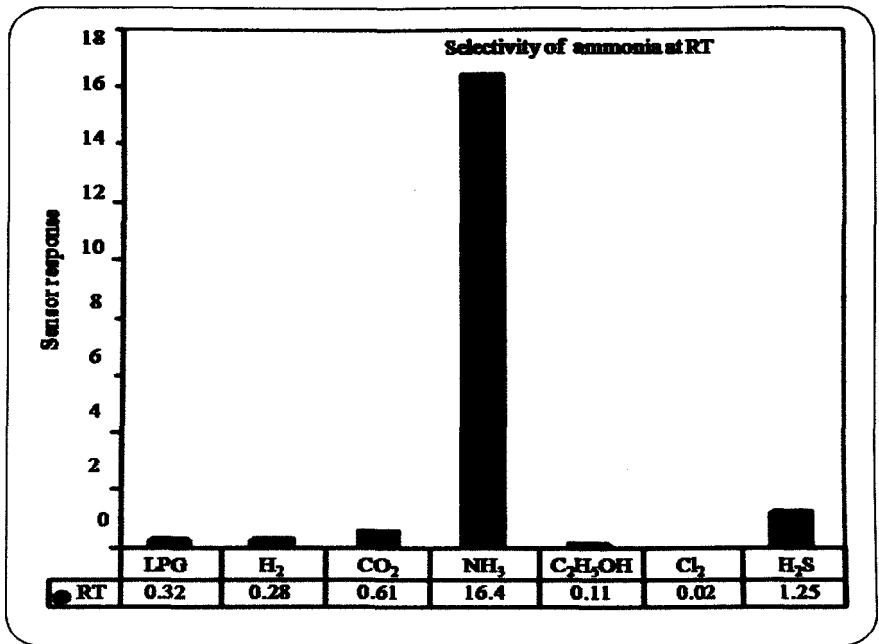
Fig 3.25. Selectivity of $Mn_{0.3}Ni_{0.3}Zn_{0.4}Fe_2O_4$ sensor for NH_3 gas at room temperature

3.4.1.6. Response and recovery of the sensor

The response and recovery profiles of $Mn_{0.3}Ni_{0.3}Zn_{0.4}Fe_2O_4$ sensor at room temperature are represented in Fig. 3.26. The response was quick (~ 13 s) to 10 ppm of NH_3, while the recovery was considerably fast (~ 22 s).
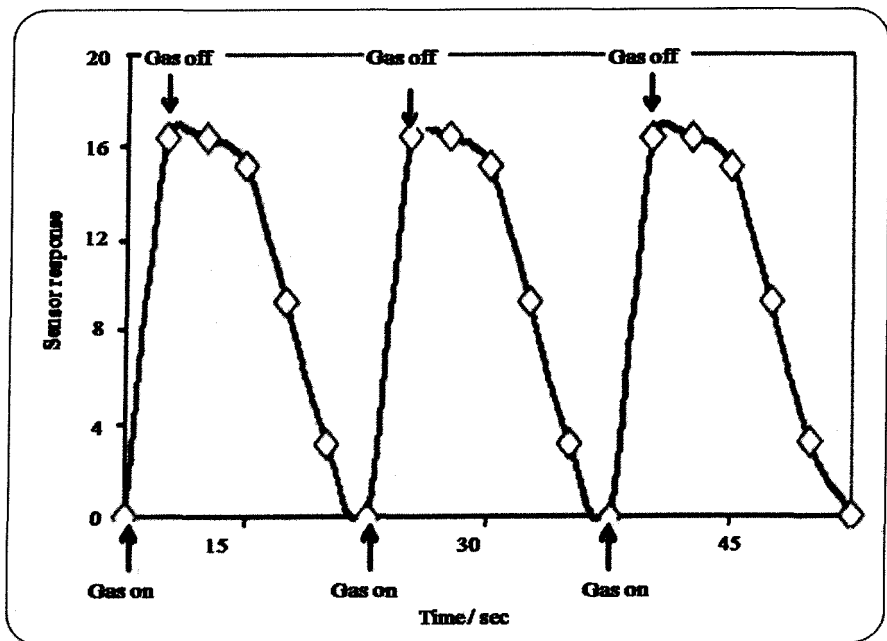
Fig.3.26. Response-recovery profile of the of $Mn_{0.3}Ni_{0.3}Zn_{0.4}Fe_2O_4$ sensor

121

A negligible quantity of the surface reaction product and its high volatility explain its quick response to ammonia and fast recovery to its initial chemical status.

3.4.1.7. Mechanism of gas sensing

The selective ammonia response of the sensor at room temperature can be explained by the surface reaction processes. Few moles of H_2O from air (moisture) could be expected to adsorb on the surface of the film at room temperature. Upon exposure to ammonia (Fig. 3.27), a remarkable decrease in the resistance of the sensor was observed, which may be due to the surface reaction of ammonia with physisorbed H_2O or by proton conductivity via NH_4^+ cations [255]. The solid acidity on the sensor surface would form NH_4^+ cations, which constitutes the proton conductivity leading to a crucial decrease of the resistance. This would decrease the barrier height among the $Mn_{0.3}Ni_{0.3}Zn_{0.4}Fe_2O_4$ grains.

$$NH_{3(g)} + H_2O_{(Surface)} \xrightarrow{RT} NH_4OH_{(g)} \quad ------------- \{2.36\}$$

Ammonium hydroxide NH_4OH produced during the surface reaction is volatile in nature. The high volatility of NH_4OH explains the quick response and fast recovery of the sensor.
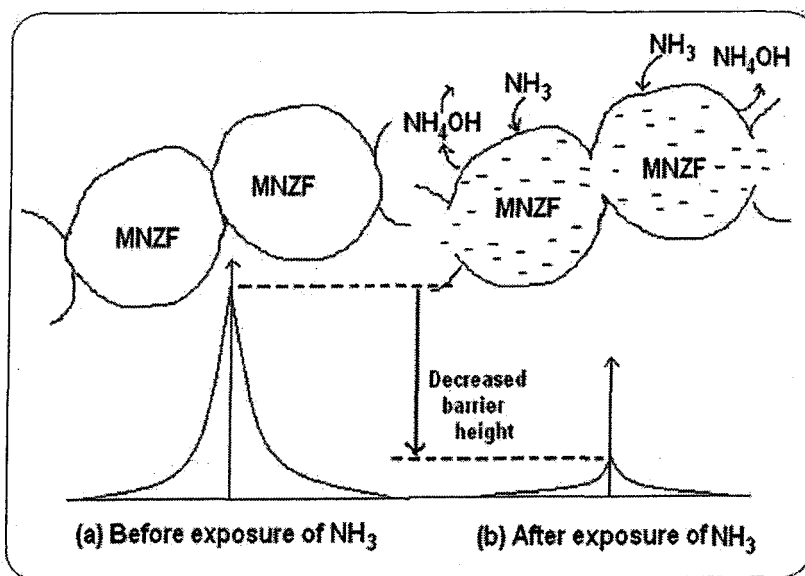
Fig.3.27. Ammonia sensing mechanism of the of $Mn_{0.3}Ni_{0.3}Zn_{0.4}Fe_2O_4$ sensor

3.5. Characterization of sintered $Ni_{0.6-x}Mn_xZn_{0.4}Fe_2O_4$ ($x = 0.0$-0.6) ferrites

The detail procedure followed for sintering has been already discussed in the section 2.2.4 to 2.2.7 of chapter 2. The samples were sintered at four different temperatures starting from 1100°C to 1250°C in air at constant time of 1h and furnace cooled to room temperature. The sintering temperature of 1100°C was fixed by carrying out optimization of sintering temperature for complete spinel phase formation using X-ray diffraction technique. The sintered $Ni_{0.6-x}Mn_xZn_{0.4}Fe_2O_4$ ($x = 0.0$-0.6) ferrites samples were then characterized by XRD, FTIR, SEM-EDS and Mössbauer spectroscopy.

3.5.1. Optimization of sintering temperature

Most of the reported studies on Ni-Mn-Zn ferrite systems involves either very high sintering temperatures (>1200°C) or sintering under inert atmospheres wherein precise control of many parameters such as heating rate, cooling rate, partial pressures of gases is required. Few authors [87-91] have reported sintering in air for this system hence, we thought of optimizing the sintering temperature for Ni-Mn-Zn ferrites system and sample from middle of the series ($x = 0.3$) was chosen for optimization. The X-ray diffraction (XRD) patterns of the samples sintered at different temperatures from 600°C to 1100°C are given in the Fig.3.28. It was observed that, the ferrite sample decomposes into Fe_2O_3 and Mn_2O_3, when sintered at 600°C and above in the air atmosphere, a prominent impurity peak, corresponding to α-Fe_2O_3, appears in the XRD patterns of samples sintered at or above 600°C, whose intensity goes on increasing as the sintering temperature was increased upto 900°C as can be seen in Fig. 3.28 (a-d).). However, when the same sample was sintered above 900°C, the intensity of impurity peaks decreases and completely disappears at 1100°C, as can be seen in Fig.3.28 (g), due to the dissolution of α-Fe_2O_3 and Mn_2O_3 to give single phase spinel ferrite.
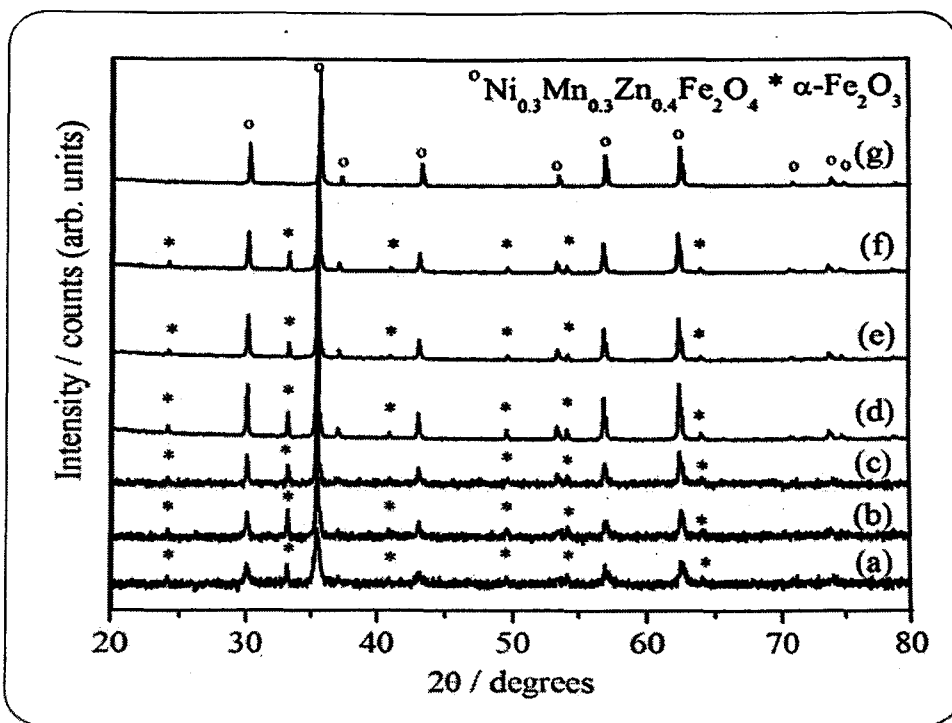
Fig.3.28. XRD patterns of 'as synthesized' $Ni_{0.3}Mn_{0.3}Zn_{0.4}Fe_2O_4$ annealed at different temperatures a) 600°C / 5h, b) 700°C / 5h, c) 800°C / 5h, d) 900°C / 5h, e) 1000°C / 5h, f) 1050°C / 5h and g) 1100°C / 1h

Thus, the minimum sintering temperature require for total ferritization was optimized and all the samples were then sintered from 1100°C to 1250°C at constant sintering time of 1h with interval of 50°C

3.5.2. X-ray diffraction studies

The phase analysis of sintered $Ni_{0.6-x}Mn_xZn_{0.4}Fe_2O_4$ (x = 0.0-0.6) ferrites were carried out using X-ray diffraction technique. The X-ray diffraction patterns of ferrites sintered at 1100°C, 1150°C, 1200°C and 1250°C for 1h are shown in the Fig. 3.29. The X-ray diffraction patterns for all the composition (except for the composition, x = 0.6, sintered at 1100°C and 1150°C) clearly indicate the formation of single phase spinel type cubic structure. For composition, x = 0.6, single phase formation occurs when sintered at

124

1200°C and above. The complete analysis of XRD patterns revealed that the 2θ positions of the peaks match with the reported values [98]. The measured lattice parameter, density and porosity of samples sintered at different temperature are given in the Table 3.12. It was observed that lattice parameters increases with increasing Mn substitution. The increase of the lattice parameter with increasing Mn content can be explained in terms of ionic radii [175] as already discussed in the section 3.2.1.
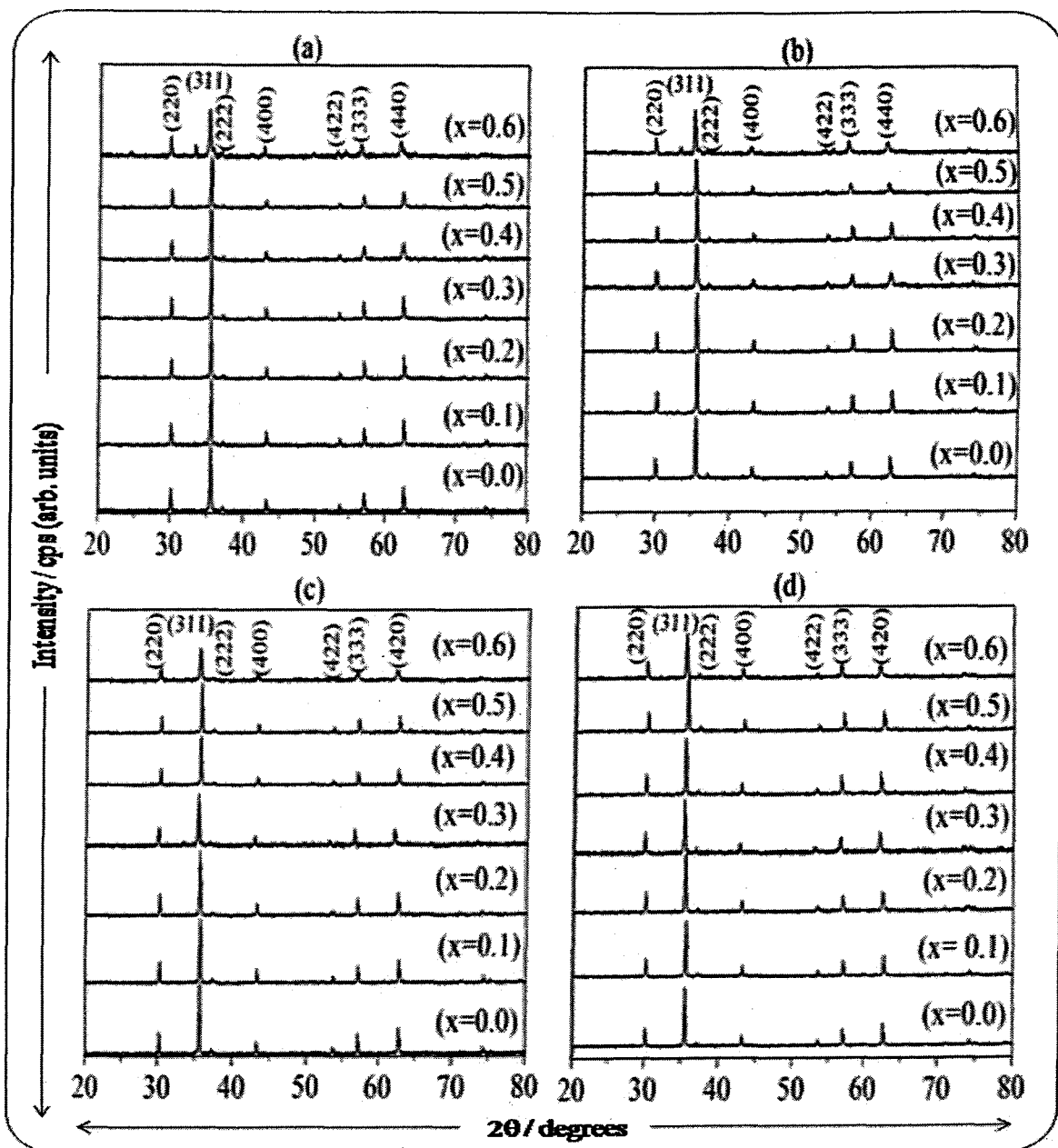
Fig.3.29. XRD patterns of $Ni_{0.6-x}Mn_xZn_{0.4}Fe_2O_4$ (x = 0.0-0.6) ferrites sintered at

a) 1100°C / 1h, b) 1150°C / 1h, c) 1200°C / 1h and d) 1250°C /1h

125

Table 3.13. Lattice constant '*a*', density '*d*', porosity '*P*' and grain diameter of sintered $Ni_{0.6-x}Mn_xZn_{0.4}Fe_2O_4$ (x = 0.0-0.6) ferrite samples

Property	Sintering temp. / °C	x 0.0	0.1	0.2	0.3	0.4	0.5	0.6
Lattice parameter '*a*' / A°	1100°C / 1h	8.3757	8.3858	8.3915	8.4124	8.4263	8.4335	---
	1150°C / 1h	8.3751	8.3884	8.3960	8.4194	8.4263	8.4360	----
	1200°C / 1h	8.3746	8.3867	8.3959	8.4177	8.4257	8.4332	8.4432
	1250°C / 1h	8.3747	8.3851	8.4007	8.4160	8.4260	8.4335	8.4435
Density '*d*' (X-ray / Exp) / gcc^{-1}	1100°C / 1h	5.36 / 4.16	5.33 / 4.08	5.31 / 3.92	5.26 / 3.88	5.23 / 3.74	5.21 / 3.63	---
	1150°C / 1h	5.36 / 4.49	5.33 / 4.41	5.30 / 4.29	5.25 / 4.14	5.23 / 3.98	5.20 / 3.89	---
	1200°C / 1h	5.36 / 4.96	5.33 / 4.93	5.30 / 4.89	5.25 / 4.87	5.23 / 4.82	5.21 / 4.69	5.16 / 4.58
	1250°C / 1h	5.36 / 5.01	5.33 / 4.96	5.29 / 4.92	5.26 / 4.90	5.23 / 4.85	5.21 / 4.76	5.16 / 4.68
Porosity '*P*' / %	1100°C / 1h	22.39	23.45	26.18	26.24	28.49	30.33	---
	1150°C / 1h	13.06	15.95	19.06	21.14	23.90	25.19	---
	1200°C / 1h	7.46	7.51	7.74	7.24	7.84	9.98	11.24
	1250°C / 1h	6.53	6.94	6.99	6.84	7.27	8.64	9.30

With increasing sintering temperature hardly any variation in the lattice parameter was observed. It was observed that density decreases with increasing Mn substitution. This behaviour is explained considering the atomic weight of Ni (58.69amu) which is greater than that of Mn (54.94amu) [256]. The variation of bulk density and porosity with sintering temperature of sintered $Ni_{0.6-x}Mn_xZn_{0.4}Fe_2O_4$ (x = 0.0-0.6) ferrites is represented in Fig. 3.30. It was noticed that the density of samples increases with increasing sintering temperature from 1100°C to 1250°C, while porosity decreases with increasing sintering temperatures. The increase of density with increasing temperature is expected because during sintering process, the thermal energy generates the force that drives the grain boundaries to grow over pores thereby decreasing the pore volume.
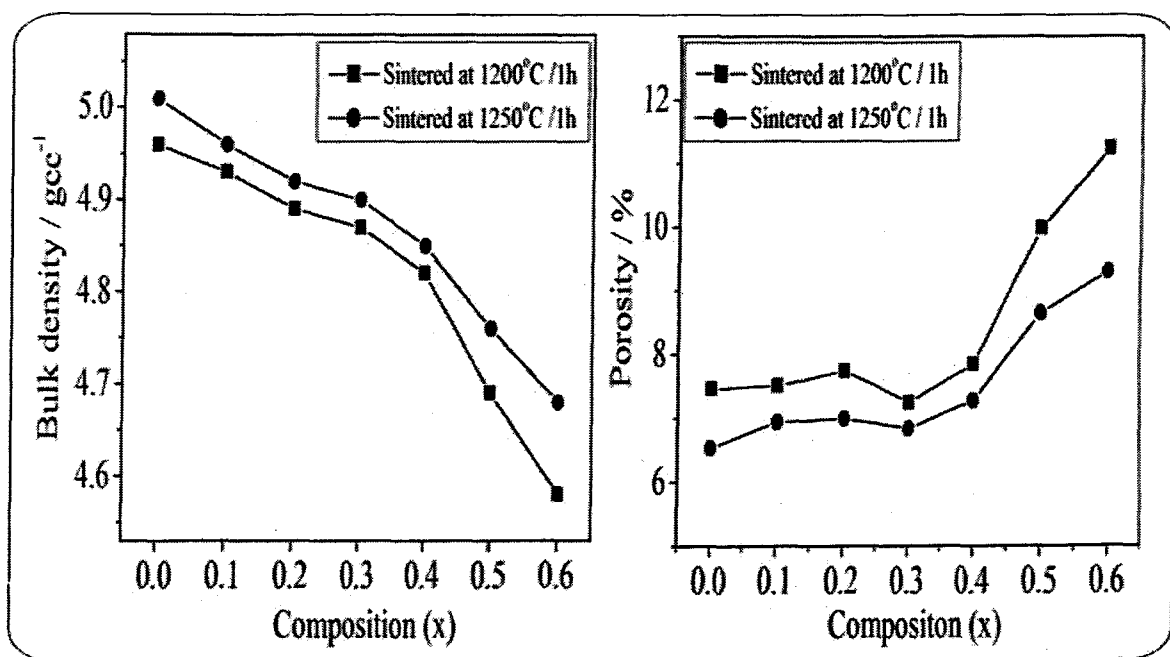
Fig.3.30. Variation of bulk density and porosity against composition (x) of sintered $Ni_{0.6-x}Mn_xZn_{0.4}Fe_2O_4$ (x = 0.0-0.6) ferrites

3.5.3. FTIR spectral studies

The FTIR spectra of $Ni_{0.6-x}Mn_xZn_{0.4}Fe_2O_4$ (x = 0.0-0.6) ferrites sintered at different sintering temperature are shown in the Fig. 3.31 and the absorption frequency values are

127

given in the Table 3.14. The spectra shows two principal absorption bands in the frequency range 750 cm^{-1} to 340 cm^{-1}. The high frequency (v_1) band was observed in the range 604 cm^{-1} to 561 cm^{-1} and the lower frequency (v_2) band was observed in the range 418 cm^{-1} to 397 cm^{-1}. The high frequency (v_1) band is related to the intrinsic vibrations of Fe^{3+}---O^{2-} bond in tetrahedral sites, while the lower frequency (v_2) band is due to the stretching vibrations of Fe^{3+}---O^{2-} groups occupying octahedral sites [166-167].
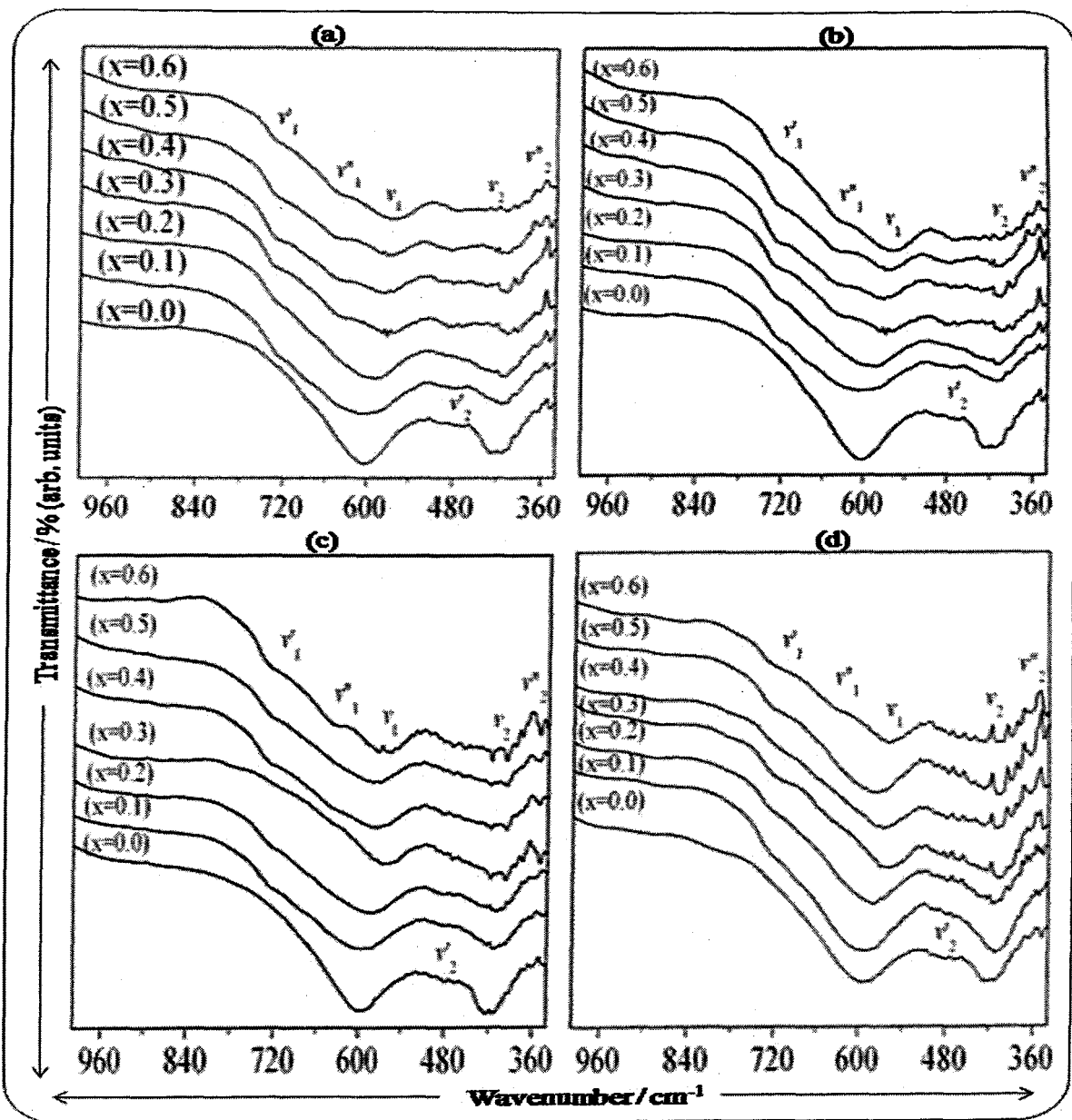
Fig.3.31. FTIR spectra of $Ni_{0.6-x}Mn_xZn_{0.4}Fe_2O_4$ (x = 0.0-0.6) ferrites sintered at

a) 1100°C / 1h, b) 1150°C / 1h, c) 1200°C / 1h and d) 1250°C / 1h

Table 3.14. Position of absorption bands of FTIR spectra of sintered $Ni_{0.6-x}Mn_xZn_{0.4}Fe_2O_4$ ($x = 0.0-0.6$) ferrites

FTIR bands	Temp. / °C	x 0.0	0.1	0.2	0.3	0.4	0.5	0.6
v_1 / v_2	1100°C / 1h	604 / 412	603 / 414	587 / 408	571 / 405	574 / 407	571 / 418	561 / 409
	1150°C / 1h	604 / 414	607 / 414	590 / 411	571 / 405	574 / 406	571 / 417	563 / 408
	1200°C / 1h	597 / 417	596 / 412	583 / 411	564 / 397	575 / 397	570 / 397	561 / 397
	1250°C / 1h	597 / 412	592 / 412	579 / 417	562 / 404	567 / 411	574 / 408	561 / 408
v'_1 / v'_2	1100°C / 1h	--- / 468	--- / 470	726 / 467	730 / 468	727 / 468	726 / 462	727 / ---
	1150°C / 1h	--- / 463	726 / 467	727 / 463	727 / 468	727 / 468	728 / 462	731 / ---
	1200°C / 1h	--- / 466	726 / 468	727 / 468	726 / 471	729 / 468	729 / 471	729 / ---
	1250°C / 1h	--- / 468	726 / 470	--- / 463	--- / 463	--- / 464	726 / 464	727 / ---
v''_1 / v''_2	1100°C / 1h	--- / 347	--- / 348	--- / 348	630 / 347	631 / 347	631 / 347	627 / 349
	1150°C / 1h	--- / 347	--- / 348	--- / 348	631 / 347	631 / 347	631 / 347	627 / 348
	1200°C / 1h	--- / 337	--- / 345	--- / 342	--- / 351	--- / 351	--- / 351	634 / 352
	1250°C / 1h	--- / 349	--- / 355	--- / 347	--- / 347	--- / 338	--- / 347	631 / 342

Besides these main absorption bands, few weak bands were also observed in the FTIR spectra which were assigned considering the site preference of metal ions for tetrahedral and octahedral sites in the mixed $Ni_{0.6-x}Mn_xZn_{0.4}Fe_2O_4$ (x = 0.0-0.6) ferrite system. The relatively weak shoulder (v'_1) which appears with increasing Mn content in the region ~ 730 cm^{-1} has been attributed to the stretching vibration of Mn^{2+}--O^{2-} in tetrahedral sites as reported in the literature [202]. Another weak shoulder (v''_1) observed in the range 634 cm^{-1} to 624 cm^{-1} with increasing Mn content has been assigned to the tetrahedral Zn^{2+}--O^{2-} stretching. An very weak band (v'_2) around 470 cm^{-1} to 463 cm-1 observed for all the composition (except for, x = 0.6) have been assigned to the stretching vibrations of Ni^{2+}-- O^{2-} bond in octahedral sites [107]. The IR peak (v''_2) observed in the region 355 cm^{-1} to 337 cm^{-1} can be assigned to Zn^{2+}--O^{2-} stretching vibrations [107]. The appearance of these weak absorption bands in the FTIR spectra is discussed in details in section 3.2.2 The sintering temperature does not seem to affect the positions of absorption bands, while their intensity was found to increase with increasing sintering temperature which may be due to the effect of increase in the grain size.

3.5.4. SEM microstructures of sintered $Ni_{0.6-x}Mn_xZn_{0.4}Fe_2O_4$ (x = 0.0-0.6) ferrites

The SEM microstructures of $Ni_{0.6-x}Mn_xZn_{0.4}Fe_2O_4$ (x = 0.0-0.6) ferrite samples sintered at different temperatures from 1100°C to 1250°C are presented in the Fig. 3.32 (a-b) and 3.33 (a-b). The average grain sizes (grain diameter) of the samples were determined from optical micrographs by linear intercept method [257] and are given in the Table 3.14. The grain size significantly depends on the Mn concentration in Ni-Zn ferrite. In general, the average grain size increases with increasing Mn content which is also reported in the literature [258]. This is due to the lower melting point of Mn as compared to Ni [104]. The samples sintered at 1100°C reveal porous microstructure with fine grains less than 2.5 μm

in diameter as can be seen in Fig. 3.32 (a). The samples sintered at 1150°C and 1200°C presented a homogeneous microstructure with narrow grain distribution and average grain diameter in the range 0.62 μm to 1.45 μm.
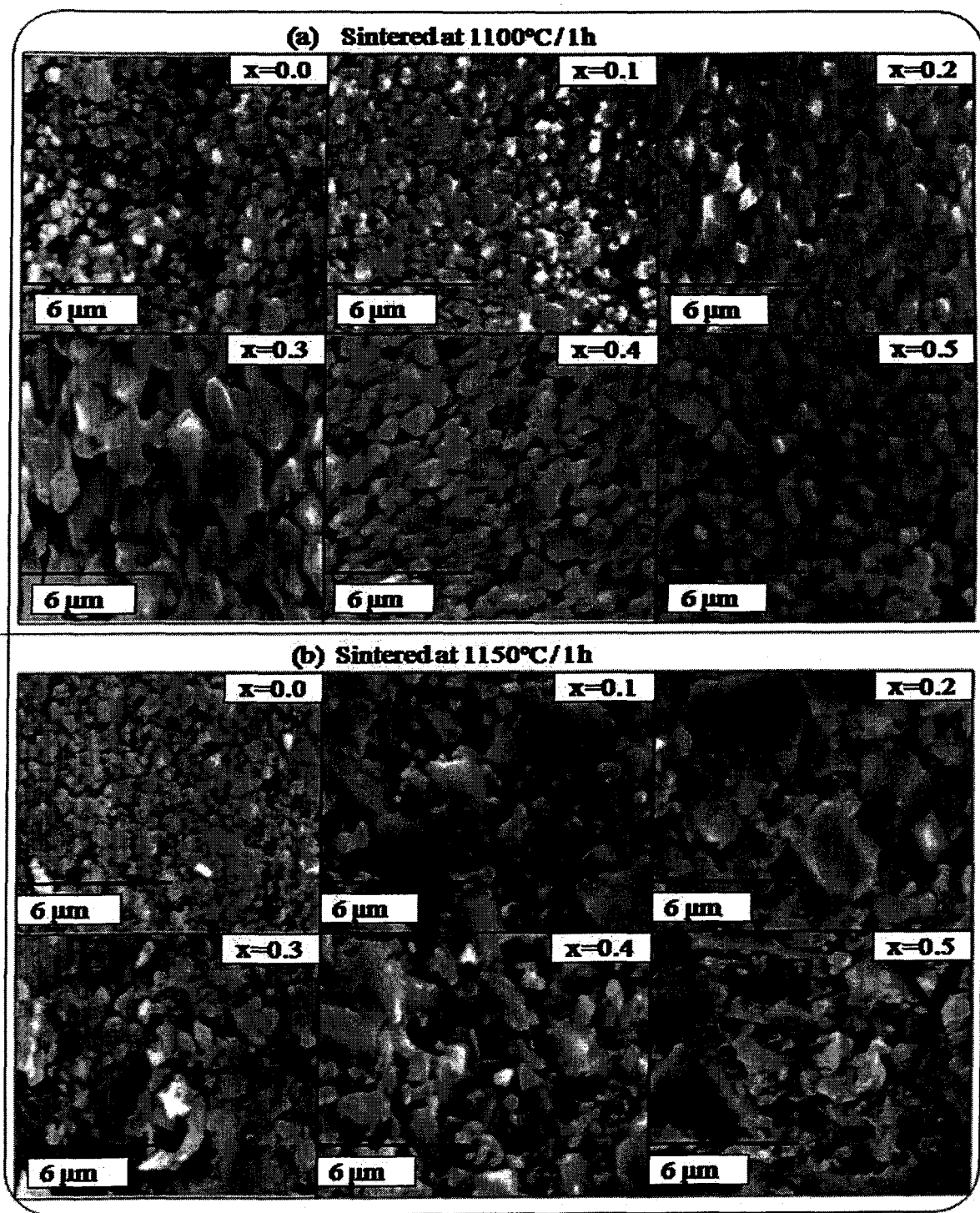
Fig.3.32. SEM of $Ni_{0.6-x}Mn_xZn_{0.4}Fe_2O_4$ (x = 0.0-0.5) ferrites sintered at (a) 1100°C / 1h and (b) 1150°C / 1h

Further increase in sintering temperature (1250°C) results in discontinuous grain growth for higher Mn content (x = 0.5 and 0.6) while compositions with lower Mn content ($x \leq 0.4$) shows uniform microstructure. The intragranular porosity was found to be very low in all the sintered compositions.
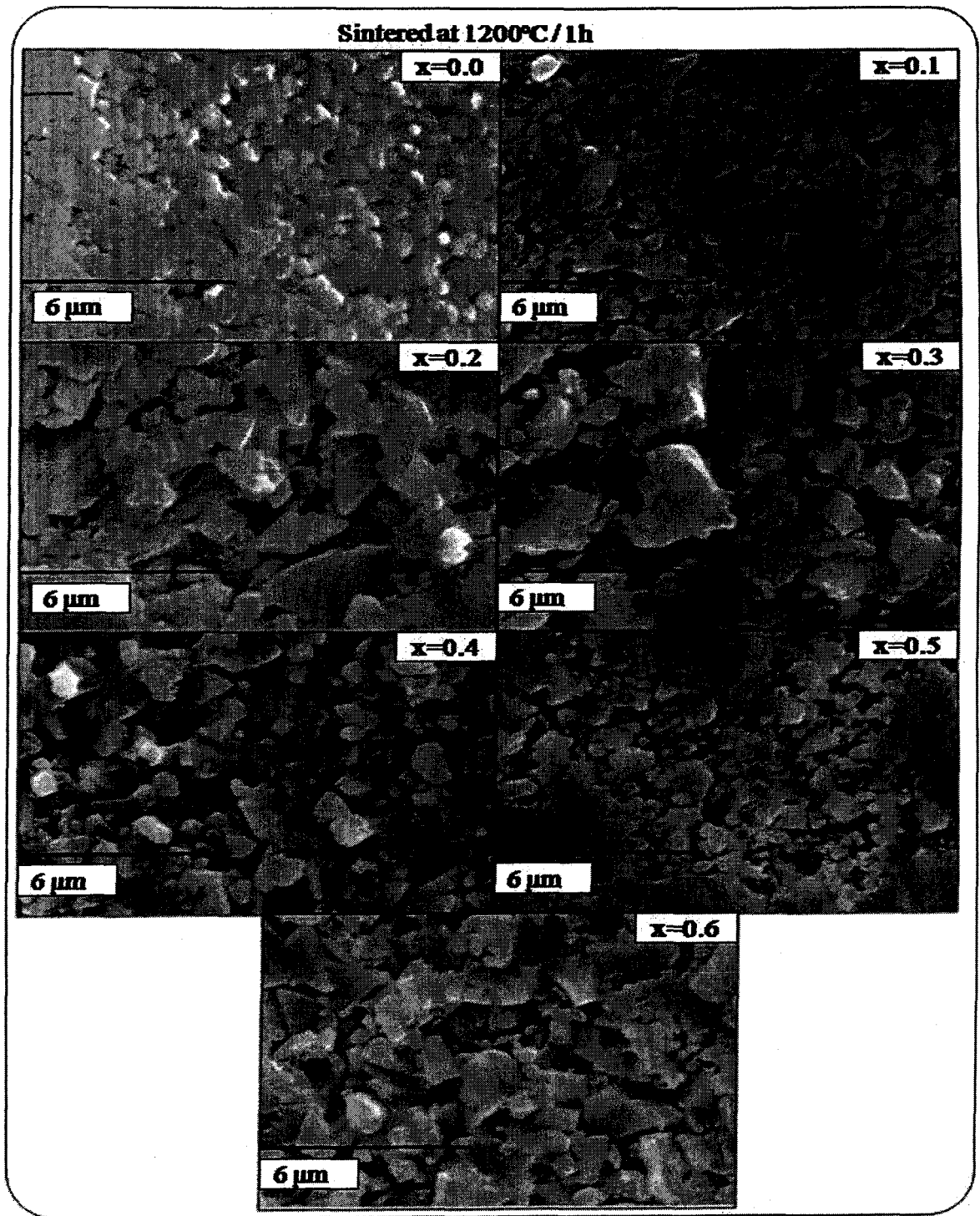
Fig.3.33a. SEM of $Ni_{0.6-x}Mn_xZn_{0.4}Fe_2O_4$ (x = 0.0-0.6) ferrites sintered at 1200°C / 1h
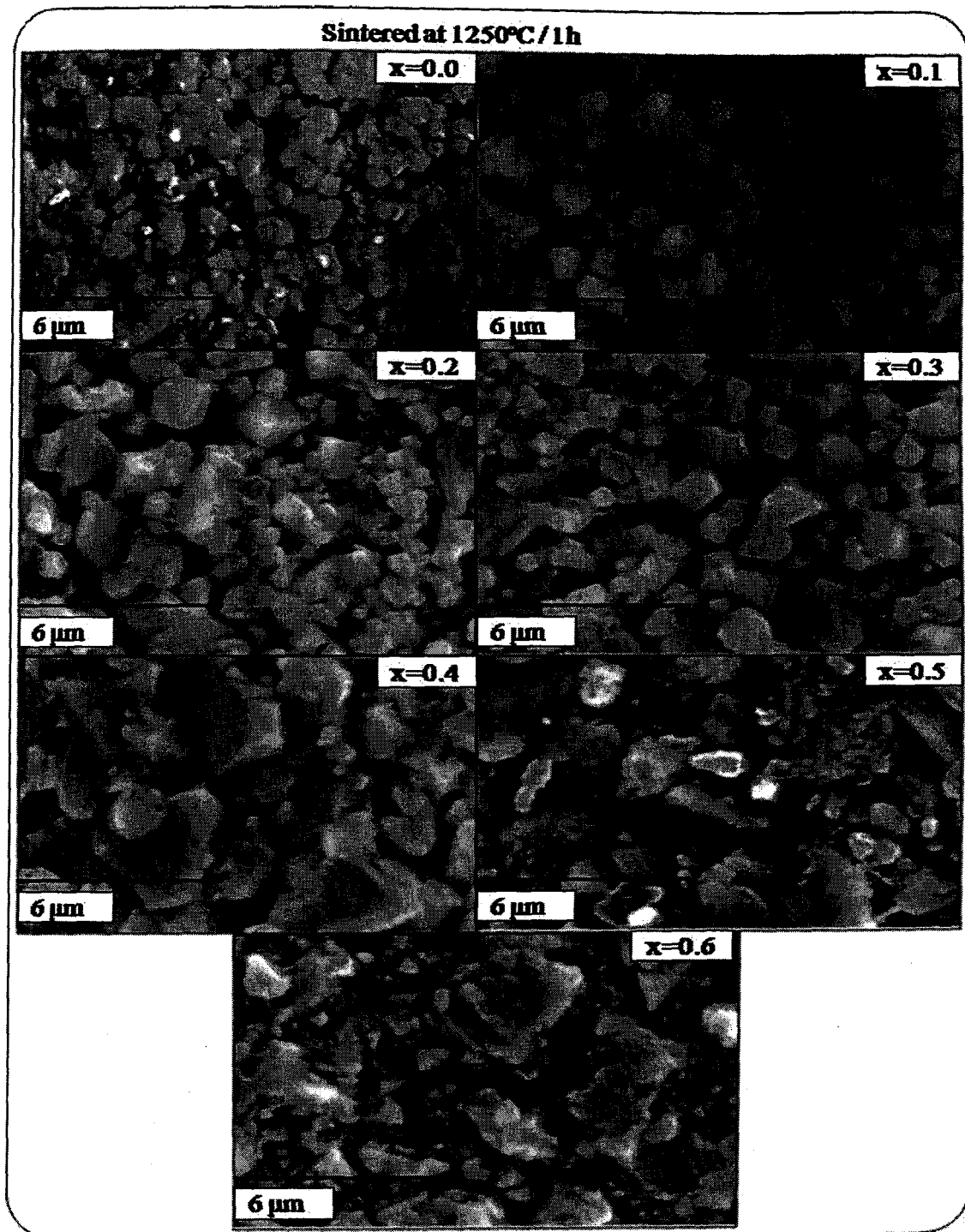
Fig.3.33b. SEM of $Ni_{0.6-x}Mn_xZn_{0.4}Fe_2O_4$ (x = 0.0-0.6) ferrites sintered at $1250^{\circ}C$ / 1h

The average grain diameter increases and largest particle diameter of 4.3 μm was observed for composition, x = 0.4, sintered at $1250^{\circ}C$ which is much lower than reported for sintered ferrites prepared by conventional method [82,259].

Table 3.15. Average grain diameter and diameter range of $Ni_{0.6-x}Mn_xZn_{0.4}Fe_2O_4$ (x = 0.0-0.6) ferrites sintered at different temperatures

Composition (x)	Average grain diameter (diameter range) / μm			
	1100°C / 1h	1150°C / 1h	1200°C / 1h	1250°C / 1h
0.0	0.59	0.62	0.81	0.84
	(0.21 - 0.87)	(0.22 - 0.89)	(0.34 - 1.31)	(0.66 - 1.38)
0.1	0.74	0.79	0.91	1.02
	(0.21 -1.52)	(0.33 - 2.73)	(0.41 - 3.11)	(0.55 - 3.32)
0.2	0.86	1.30	1.45	1.49
	(0.33 - 1.31)	(0.44 - 3.16)	(0.44 - 3.38)	(0.55 – 3.93)
0.3	1.20	0.82	1.29	1.34
	(0.76 - 2.4)	(0.33 - 1.32)	(0.44 - 3.28)	(0.66 - 3.76)
0.4	0.73	1.0	1.43	1.62
	(0.44 - 1.1)	(0.33 - 2.18)	(0.46 - 2.21)	(0.55 – 4.21)
0.5	0.78	1.06	1.24	1.51
	(0.55 - 1.96)	(0.33 - 2.73)	(0.36 - 2.06)	(0.44 - 2.95)
0.6	---	---	1.12	1.24
			(0.44 - 2.4)	(0.44 - 3.27)

3.5.5. EDS analysis

The EDS spectra of ferrite samples sintered at 1200°C for 1h is represented in the Fig. 3.34 and 3.34a. The EDS spectra reveals the presence of all the components of $Ni_{0.6-x}Mn_xZn_{0.4}Fe_2O_4$ (x = 0.0-0.6) ferrites in proper proportion thus confirming their identity. No additional peaks corresponding to any impurity were observed in the spectra.
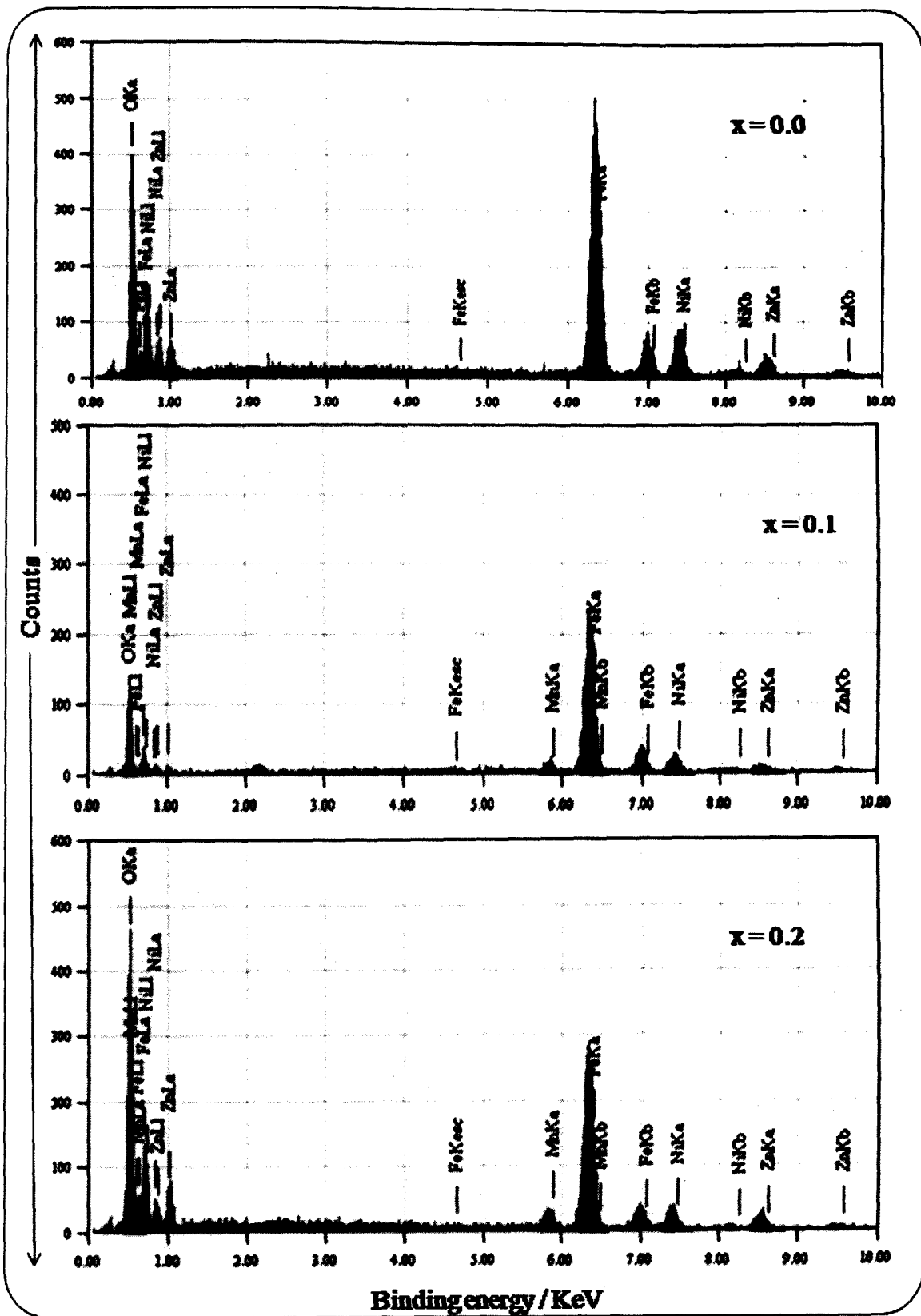
Fig.3.34. EDS spectra of $Ni_{0.6-x}Mn_xZn_{0.4}Fe_2O_4$ (x = 0.0, 0.1 and 0.2) ferrites sintered at
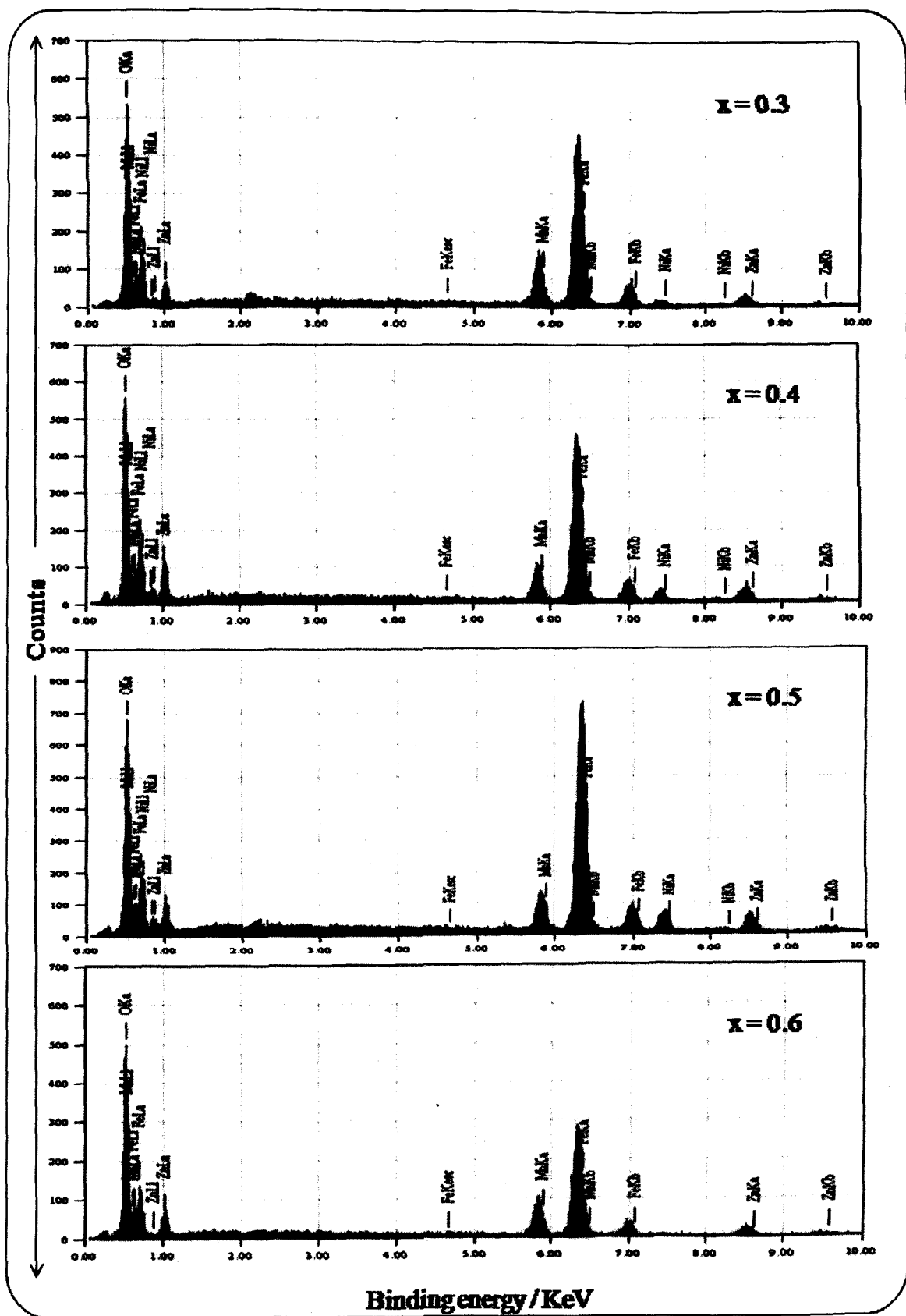
1200°C / 1h

Fig.3.34a. EDS spectra of $Ni_{0.6-x}Mn_xZn_{0.4}Fe_2O_4$ (x = 0.3, 0.4, 0.5 and 0.6) ferrites sintered

at 1200^oC / 1h

3.5.6. Mössbauer spectral analysis

The Mössbauer spectra of mixed Ni-Mn-Zn ferrites, $Ni_{0.6-x}Mn_xZn_{0.4}Fe_2O_4$ ($x = 0.0$-0.6) sintered at 1200°C / 1h recorded at room temperature are displayed in Fig. 3.34.
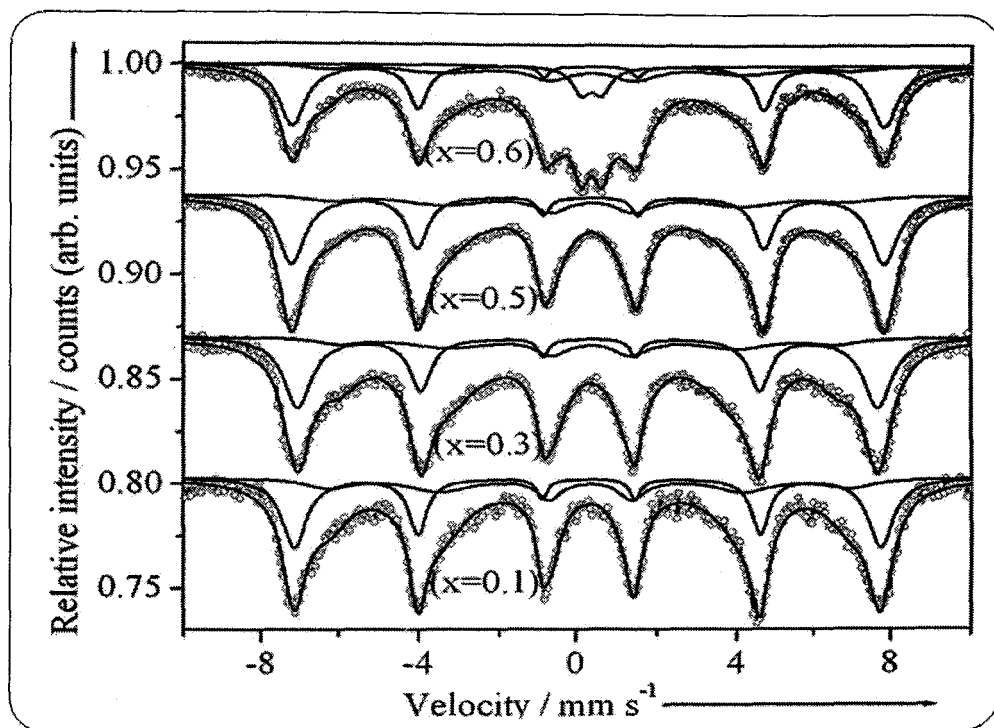
Fig.3.35. Room temperature Mössbauer spectra of representative $Ni_{0.6-x}Mn_xZn_{0.4}Fe_2O_4$ ($x = 0.1, 0.3, 0.5$ and 0.6) ferrites sintered at 1200°C / 1h

Each spectrum (except composition, $x = 0.6$) exhibits a superposition of two Zeeman sextets, one sextet corrosponding to a higher magnetic field was attributed to Fe^{3+} ions on the B site and the other sextet corrosponding to lower magnetic field was attributed to Fe^{3+} ions on A site. The Mössbauer spectrum of composition, $x = 0.6$ consists of two Zeeman sextet and single quadrupole doublet which indicate that the sample has ferromagnetic and paramagnetic natures simultaneously. The central doublet can be attributed to the magnetically isolated Fe^{3+} ions which do not participate in the long range magnetic ordering due to a large number of nonmagnetic nearest neighbours. The refined values of the hyperfine parameters computed from the Mössbauer spectra are listed in

Table 3.16. In the mixed Ni-Mn-Zn ferrites system, with increasing Mn substitution, it was observed that the values of isomer shift 'δ' of tetrahedral (A) sites increases indicating that Mn^{2+} ions predominatly occupy A sites in spinel lattice [197].

Table 3.16. Room temperature Mössbauer effect parameters: isomer shift 'δ', quadrupole splitting 'Δ', hyperfine field 'H_{hf}', relative Area 'R_A' and inner line width 'Γ' of $Ni_{0.6-x}Mn_xZn_{0.4}Fe_2O_4$ ($x = 0.0$-0.6) ferrites sintered at 1200°C / 1h

Sample	Site	*δ / mms^{-1}	Δ / mms^{-1}	H_{hf} / Tesla	R_A / %	Γ / mms^{-1}
0.0	Sextet 1, (A)	0.278	0.005	44.66	53.20	0.358
	Sextet 2, [B]	0.287	0.014	41.28	46.80	0.726
0.1	Sextet 1, (A)	0.288	0.004	48.05	61.98	0.416
	Sextet 2, [B]	0.381	-0.015	43.91	38.02	0.583
0.2	Sextet 1, (A)	0.291	0.013	38.13	46.05	0.317
	Sextet 2, [B]	0.341	0.003	40.83	56.95	0.753
0.3	Sextet 1, (A)	0.287	0.016	45.62	44.75	0.427
	Sextet 2, [B]	0.353	0.005	40.02	55.25	0.937
0.4	Sextet 1, (A)	0.299	0.002	45.56	41.93	0.314
	Sextet 2, [B]	0.334	-0.019	38.95	58.07	0.373
0.5	Sextet 1, (A)	0.313	-0.000	46.58	46.90	0.361
	Sextet 2, [B]	0.344	-0.012	40.41	53.10	0.982
0.6	Sextet 1, (A)	0.319	-0.004	46.46	34.12	0.305
	Sextet 2, [B]	0.335	-0.028	41.20	60.42	1.189
	Doublet	0.363	0.509	---	5.45	0.556

*Isomer shift values are relative to α-Fe metal foil (δ = 0.0 mm/s), (): tetrahedral, []: octahedral

The isomer shift at room temperature for A and B site were found to be in the range 0.278 mm/s to 0.319 mm/s and 0.287 mm/s to 0.381 mm/s, respectively, relative to the α-Fe metal foil which are consistent with the high spin Fe^{3+} ionic state [221]. Furthermore, the observed isomer shift values are significantly lower than the expected value , 0.8 mm/s for Fe^{2+} ions, hence the formation of Fe^{2+} ions during sintering is ruled out in the present ferrite system [222-224]. Except for the paramagnetic doublet for composition, $x = 0.6$ ($\Delta = 0.509$ mm/s, $\delta = 0.363$ mm/s and $R_A = 5.45$ %), the quadrupole splitting 'Δ' values were nearly 0.0 mm/s, suggesting that Fe^{3+} ions show cubic symmetry of polyhedron.

3.6. Studies on solid state properties of sintered $Ni_{0.6-x}Mn_xZn_{0.4}Fe_2O_4$ ($x = 0.0$-0.6) ferrites

The sintered $Ni_{0.6-x}Mn_xZn_{0.4}Fe_2O_4$ ($x = 0.0$-0.6) ferrites were analyzed for their solid state properties such as dc resistivity, dielectric properties, ac susceptibility, hysteresis characteristics and magnetic permeability measurements.

3.6.1. DC resistivity studies on sintered $Ni_{0.6-x}Mn_xZn_{0.4}Fe_2O_4$ ($x = 0.0$-0.6) ferrites

The dc resistivity measurements were carried out on the silver coated pellets of sintered ferrite samples using two probe method. The details of resistivity measurement are discussed in the section 2.3.11. of chapter 2. The resistivity values were calculated using expression 2.27 given in the same section.

3.6.1.1. Thermal variation of dc resistivity

The thermal variation of log resistivity 'log ρ' of sintered $Ni_{0.6-x}Mn_xZn_{0.4}Fe_2O_4$ ($x = 0.0$-0.6) ferrites is represented in the Fig. 3.36 while the room temperature d.c. resistivity and

activation energy values are given in the Table 3.17. The sintered $Ni_{0.6-x}Mn_xZn_{0.4}Fe_2O_4$ (x = 0.0-0.6) ferrites shows decrease in the resistivity with increasing temperature displaying a typical semiconducting (NTC) behaviour. The log ρ versus 10^3 / T (K^{-1}) graph for each sample can be divided into three linear regions.
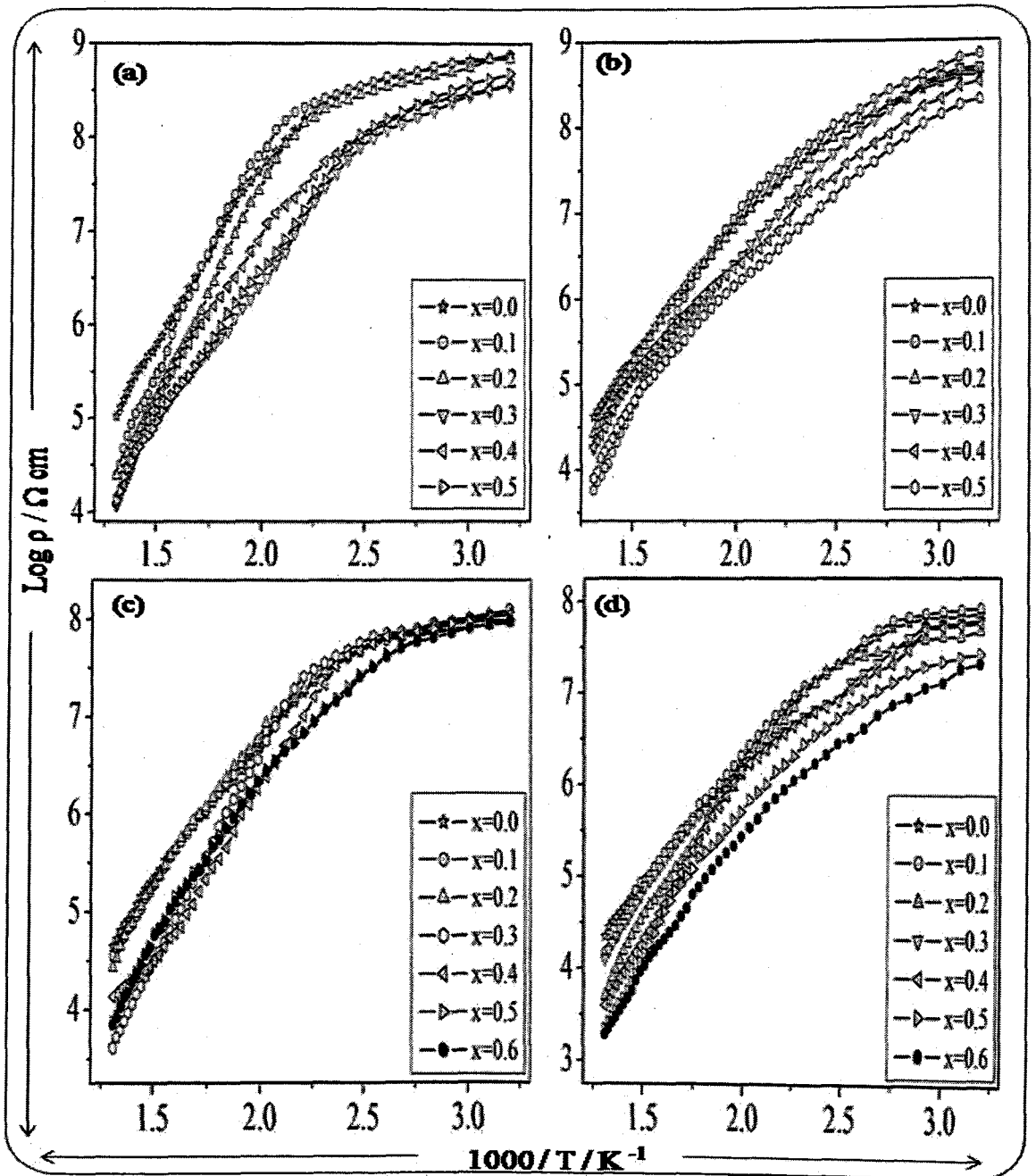
Fig.3.36. Variation of log d.c. resistivity with 10^3 / T of $Ni_{0.6-x}Mn_xZn_{0.4}Fe_2O_4$ (x = 0.0-0.6) ferrites sintered at a) 1100°C / 1h, b) 1150°C / 1h, c) 1200°C / 1h and d) 1250°C / 1h

Table 3.17. Room temperature d.c. resistivity and activation energy data of the sintered $Ni_{0.6-x}Mn_xZn_{0.4}Fe_2O_4$ ($x = 0.0$-0.6) ferrites

| x | RT dc resisitivity ' ρ ' x 10^7 / Ω cm | | | | Activation energy 'Ea' / eV | | | | | | | |
| | 1100°C | 1150°C | 1200°C | 1250°C | 1100°C | | 1150°C | | 1200°C | | 1250°C | |
					E_f	E_p	E_f	E_p	E_f	E_p	E_f	E_p
0.0	89	71	67	6.7	0.427	0.456	0.418	0.442	0.396	0.406	0.385	0.384
0.1	84	74	60	3.6	0.436	0.542	0.424	0.478	0.397	0.429	0.388	0.396
0.2	69	61	32	1.6	0.419	0.533	0.410	0.495	0.375	0.415	0.380	0.393
0.3	53	47	18	1.4	0.382	0.661	0.369	0.561	0.343	0.453	0.313	0.402
0.4	46	42	8.8	1.5	0.368	0.513	0.353	0.438	0.331	0.409	0.324	0.383
0.5	48	39	4.9	1.5	0.362	0.492	0.365	0.451	0.385	0.412	0.381	0.394
0.6	---	---	6.5	1.3	---	---	---	---	0.345	0.435	0.322	0.419

The first region extends upto 390 K where change in the slope was observed. This region was found to be almost independent of Mn substitution and hence the conduction in this region can be attributed to the impurities as reported [260-262]. The second region of slope change was found to depend on the Mn content and hence, the transition in this region can be attributed to the magnetic phase changes from ferrimagnetic to paramagnetic state or the Curie temperature. The third region represents the conductivity in paramagnetic region. The activation energy 'E_a' corresponding to ferrimagnetic and paramagnetic region was calculated using the formula 2.28 given in the section 2.3.11. The activation energy values for sintered ferrites are given in the Table 3.17.

In the low temperature (ferrimagnetic) region the activation energies were observed in the range 0.313 eV to 0.436 eV. At higher temperatures, the concentration of Fe^{2+} and Mn^{3+} is known to increase by the process [263]:

$$Ni^{2+} + Fe^{3+} \leftrightarrow Ni^{3+} + Fe^{2+} \qquad ----------------\{2.40\}$$

$$Fe^{3+} + Mn^{2+} \leftrightarrow Fe^{2+} + Mn^{3+} \qquad ---------------\{2.41\}$$
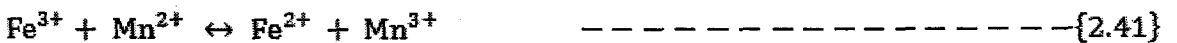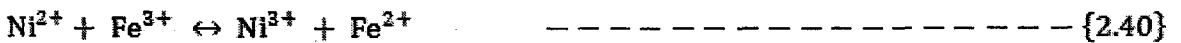
The increased concentration of Fe^{2+} and Mn^{3+} ions increases the hopping and thereby increases the conductivity at higher temperatures. It has been reported that [178,264] the activation energy associated with the above processes is in the range of 0.3 eV to 0.5 eV. The observed values in the range 0.383 eV to 0.661 eV for sintered $Ni_{0.6-x}Mn_xZn_{0.4}Fe_2O_4$ ($x = 0.0$-0.6) ferrites suggest the polaron hopping conduction mechanism.

3.6.1.2. Compositional variation of dc resistivity

The dc resistivity values of sintered ferrites at room temperature are given in Table 3.17. The resistivity values were found to be in the range 10^8 to 10^7 Ωcm. In general, the the resistivity decreases with increasing Mn substitution except for composition, $x = 0.1$ sintered at 1150°C. The observed variation in the resistivity can be explained considering

the distribution of cations in tetrahedral (*A*) and octahedral [*B*] sites in spinel lattice. It is well known fact that iron goes in ferrite systems primarily as Fe^{3+}, while manganese goes primarily as Mn^{2+}. There is also a small probability of finding Fe and Mn in +2 and +3 states, respectively. The introduction of any small amount of Mn^{3+} at the cost of Ni^{2+} creates charge imbalance in the lattice. In order to maintain charge neutrality, Fe^{3+} ions get converted to Fe^{2+} and as a result the conductivity increases due to increase in hopping between Mn^{3+} and Mn^{2+} and between Fe^{2+} and Fe^{3+} ions.

3.6.1.3. Effect of sintering temperature on dc resistivity

The dc resistivity values of the sintered $Ni_{0.6-x}Mn_xZn_{0.4}Fe_2O_4$ (x = 0.0-0.6) ferrites have been summarised in the Table 3.17. These values are much higher than the reported [178,265-266]. It was observed that the resistivity decreases with increase in sintering temperature. During sintering the grains coalesce to reduce total surface energy of the system. The grain size, therefore, increases with increase in sintering temperature. The average grain sizes of the sintered ferrites are presented in Table 3.15. The average grain sizes increases from 0.59 μm to 1.62 μm with increasing sintering temperature from 1100°C to 1250°C. The decrease in resistivity with increase in sintering temperature can be attributed to increase in average grain size. The resistivity of polycrystalline materials, in general, increases with decrease in grain size [267] because smaller grains has larger number of grain boundaries which acts as scattering centres to the flow of electrons thereby increasing the grain boundary resistance and also the resistivity. Also, with small grain size the oxidation of Fe^{2+} advances faster due to larger surface to volume ratio [268]. Therefore, in smaller grains re-conversion of any Fe^{2+} formed during the sintering process, back to Fe^{3+} takes place readily. At lower sintering temperature (≤ 1200°C) the probability of the existence of Fe^{2+} ions is relatively low. And, also the conduction in ferrites being

primarily due to hopping of electrons between ions of the same element but of different valencies, present at equivalent sites [225], one can assume that samples sintered at lower temperature ($\leq 1200^{\circ}$C) will have high resistivity. The relatively lower values of resistivity of the samples sintered at 1250°C [Table 3.17] are due to the fact that at higher sintering temperatures there is bound to be some Zn loss by increased volatilization [269]. This Zn loss causes unsaturated oxygen bonds which tend to saturate by bonding with the surrounding Fe^{3+} ions, at least in part, reducing latter to Fe^{2+}, which increases the Fe^{2+} ion concentration, resulting in increased hopping. Non-uniform grain sizes obtained for samples sintered at 1250°C may also contribute to their lower resistivity.

3.6.2. Thermoemf / Seebeck coefficient measurements

The plots of Seebeck coefficient 'α' with temperature for $Ni_{0.6-x}Mn_xZn_{0.4}Fe_2O_4$ ($x =$ 0.0-0.6) ferrites sintered at 1200°C and 1250°C are represented in the Fig. 3.37. Similar plots were observed for sample sintered at 1100°C and 1150°C. The values of Seebeck coefficient 'α' were found to be negative throughout the temperature range from 393 K to 720 K. The negative value of Seebeck coefficient 'α' indicates that the samples are n-type semiconductors with electron as dominant charge carriers. From the thermal variation it was observed that the absolute value of Seebeck coefficient 'α' in the paramagnetic (after Curie temperature) region is greater than ferrimagnetic (before Curie temperature) region which can be interpreted in terms of spin polaron formation where after Curie temperature the moving electron will tend to polarise the ion spins near to it, in ferromagnetic sense. Hence, if the band is sufficiently narrow the electron will be trapped in the ferromagnetic spin cluster [270]. Therefore the number of electron in the conduction process reduces and hence, the absolute value of thermoelectric power increases [271]. Thus, these results support polaron hopping conduction mechanism.

Fig.3.37. Variation of Seebeck coefficient 'α' with temperature of $Ni_{0.6-x}Mn_xZn_{0.4}Fe_2O_4$
(*x* = 0.0-0.6) ferrites sintered at a) 1200°C / 1h and b) 1250°C / 1h

3.6.3. Dielectric properties of sintered $Ni_{0.6-x}Mn_xZn_{0.4}Fe_2O_4$ (x = 0.0-0.6) ferrites

The dielectric constant and dielectric loss studies of sintered $Ni_{0.6-x}Mn_xZn_{0.4}Fe_2O_4$
(*x* = 0.0-0.6) ferrites were carried out with respect to the frequency as well as temperature.

3.6.3.1. Frequency variation of dielectric constant and dielectric loss

The frequency variation of the dielectric constant of the samples has been studied
from room temperature to 250°C. Each sintered $Ni_{0.6-x}Mn_xZn_{0.4}Fe_2O_4$ (*x* = 0.0-0.6) ferrites
exhibits normal dielectric behavior wherein the dielectric constant decreases rapidly up to
1 kHz, followed by a slow decrease from 1 kHz to 100 kHz, and was nearly independent
of frequency above 100 kHz. The room temperature frequency variation of dielectric
constant of ferrites sintered at different temperatures is depicted in the Fig. 3.38.

145
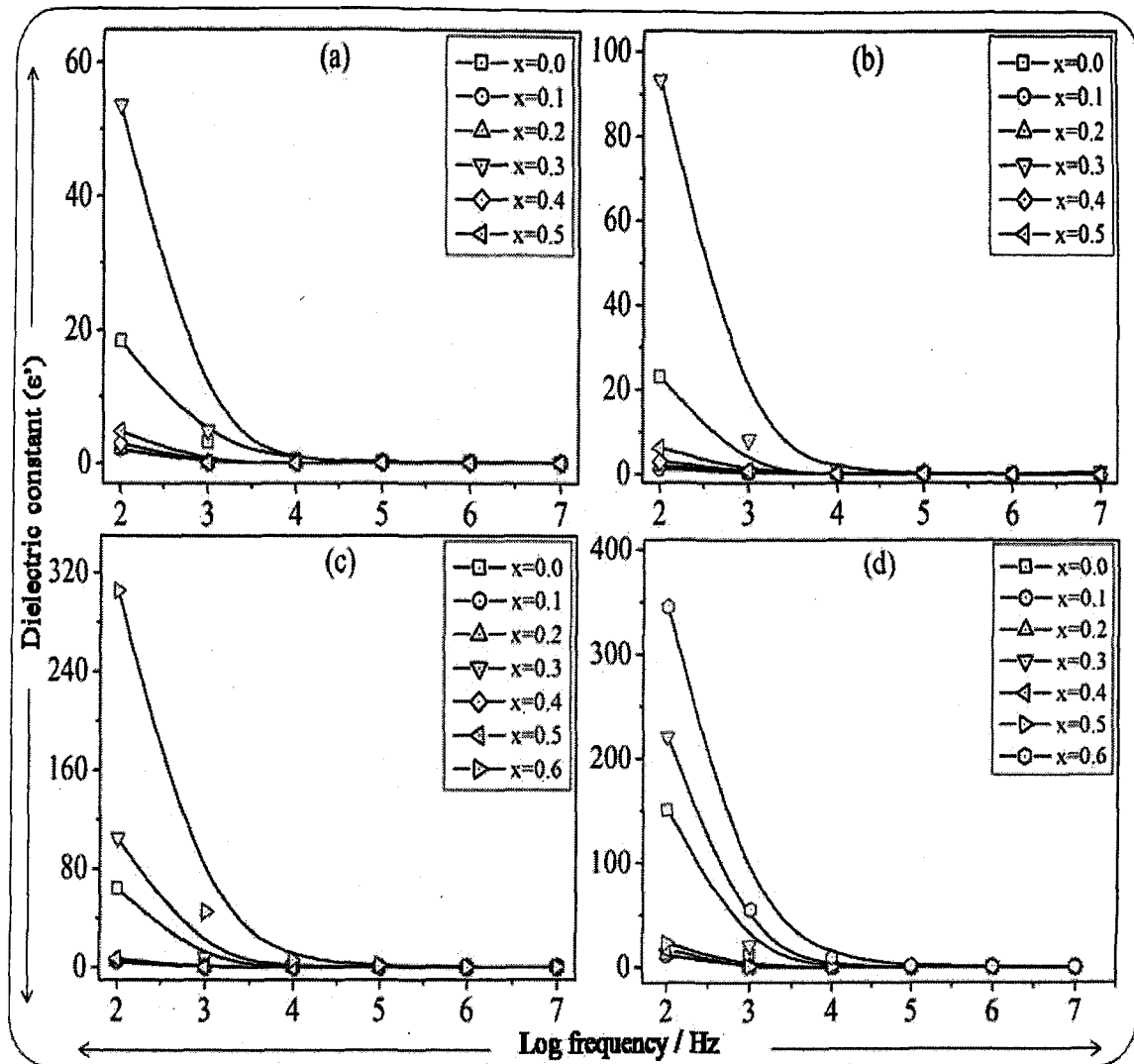
Fig.3.38. Room temperature frequency variation of dielectric constant at room temperature of $Ni_{0.6-x}Mn_xZn_{0.4}Fe_2O_4$ ($x = 0.0$-0.6) ferrites sintered at a) 1100°C / 1h, b) 1150°C / 1h, c) 1200°C / 1h and d) 1250°C / 1h

As observed in Fig. 3.38, the dielectric constant values are quite low at room temperature, which is also observed by other group who prepared the similar ferrites series by citrate method [87]. However, the groups [29,241] who prepared the similar ferrites by ceramic method reported about 10^3 times higher values. The lower values of dielectric constant is due to the fact that wet chemical methods like precursor method forms homogeneous ferrites with low Zn losses unlike in ferrite prepared by ceramic method

146

which are generally inhomogeneous with higher Zn losses and hence higher dielectric constant values. The observed results of dielectric constant versus variable frequency can be explained on the basis of space charge polarization which is a result of the presence of higher conductivity phases (grains) in the insulating matrix (grain boundaries) of dielectrics, causing localized accumulation of charge under the influence of an electric field [29]. The electrons reach the grain boundaries through hopping and if the resistance of the grain boundary is high enough, electrons pile up at the grain boundaries and produce polarization. However, as the frequency of the applied field is increased, there is phase lag between the moving electrons and applied field making the electrons to reverse the direction of motion. This decreases the probability of electron reaching the grain boundaries and as a result, the polarization decreases. Therefore, the dielectric constant decreases with an increasing frequency of the applied field [29].

The frequency variation of dielectric loss tangent 'tan δ' at room temperature of ferrites sintered at different temperatures is represented in the Fig. 3.39. The loss tangent decreases initially with increasing frequency, followed by the appearance of a resonance peak in the frequency range from 100 kHz to 1MHz. The value of the loss tangent obtained for all the sintered ferrites are in the range 10^{-2} to 25 in a frequency range from a 100 Hz to 1 MHz. These values of the loss tangent are lower than those reported for ferrites prepared by the conventional ceramic method [29,241,272]. The initial decrease of loss tangent with an increase in frequency is explained on the basis of Koops' theory [29] while, the appearance of a resonance peak is due to the matching of the time period of the applied electric field with that of the corresponding relaxation phenomena and the resonance is due to the jump of ion between more than one of its equilibrium positions. If an ion has more than one equilibrium position, say two positions X and Y of equal potential energies, separated by the potential barrier, the probabilities of jumping of ions

147

from X to Y and from Y to X are the same. Depending upon this probability, the ion exchanges position between the two states with some frequency, called the natural frequency of jump between the two positions. When an external alternating electric field of same frequency is applied, maximum electrical energy is transferred to the oscillating ions and power loss shoots up, thereby resulting in resonance.

Fig.3.39. Room temperature frequency variation of dielectric loss tangent at room temperature of $Ni_{0.6-x}Mn_xZn_{0.4}Fe_2O_4$ (x = 0.0-0.6) ferrites sintered at a) 1100°C / 1h, b) 1150°C / 1h, c) 1200°C / 1h and d) 1250°C / 1h

Since Mn^{2+} ($r = 0.82$ A°) ion has higher ionic radius than that of Zn^{2+} ($r = 0.75$ A°) ion, the Mn^{2+} ion pushes the neighbouring ions and that results in the separation between the equilibrium positions of the next neighbouring ions. Consequently, the jump probability between the two next neighbouring positions increases. This results in an increase in the jump frequency and therefore a shift in the resonance peak towards higher frequency. This behavior is also observed by Singh *et al.* [87].

3.6.3.2. Temperature variation of dielectric constant and dielectric loss

The temperature variation of dielectric constant $Ni_{0.6-x}Mn_xZn_{0.4}Fe_2O_4$ ($x = 0.0-0.6$) ferrites at 100 Hz is shown in the Fig. 3.40. The dielectric constant increases with temperature at all the frequencies. The increase in the value of the dielectric constant is very large at lower frequencies (100 Hz), while at higher frequencies (10 MHz) the increase is very small. The dielectric constant of any material, in general, is due to dipolar, electronic, ionic and interfacial polarizations [238]. At low frequencies, dipolar and interfacial polarizations are known to play the most important role. Both these polarizations are strongly temperature dependent. The interfacial polarization increases with temperature due to creation of crystal defects whereas, the dipolar polarization decreases with an increase in the temperature. The rapid increase in the dielectric constant with an increase in the temperature at low frequencies suggests that the effect of temperature is more pronounced on the interfacial than on the dipolar polarization. At higher frequencies, electronic and ionic polarizations are the main contributors [238] and their temperature dependence is insignificant therefore it results in a constant and low value of the dielectric constant at higher frequencies. The temperature variation of dielectric loss tangent of $Ni_{0.6-x}Mn_xZn_{0.4}Fe_2O_4$ ($x = 0.0-0.6$) ferrites at frequency of 100 Hz is shown in the Fig. 3.41
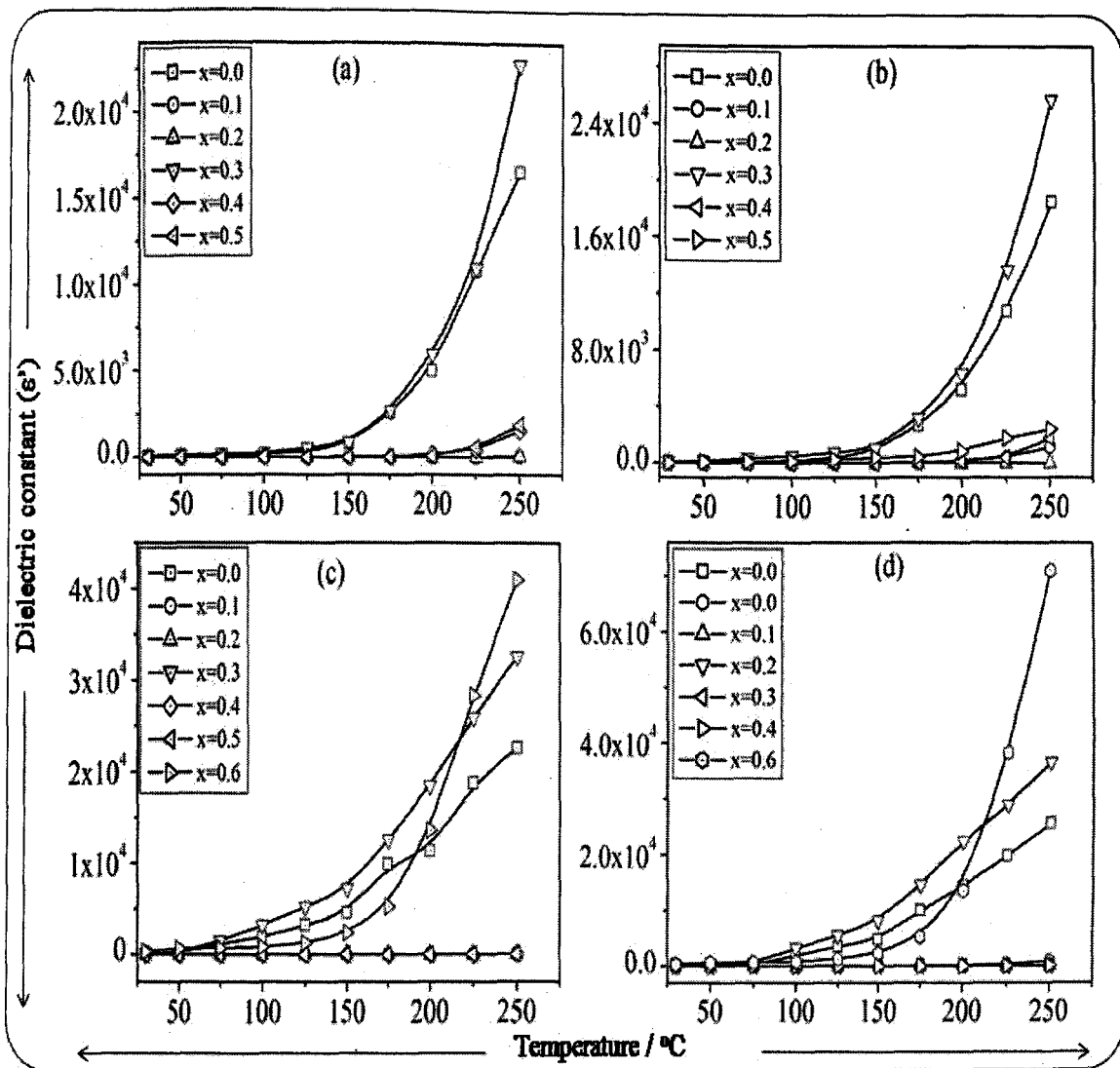
Fig.3.40. Temperature variation of dielectric constant at 100 Hz of $Ni_{0.6-x}Mn_xZn_{0.4}Fe_2O_4$

($x = 0.0$-0.6) ferrites sintered at a) 1100°C / 1h, b) 1150°C / 1h, c) 1200°C / 1h and

d) 1250°C / 1h

The dielectric loss tangent increases with increasing temperature. This increased is high at lower frequency while at higher frequency region the increase is very small. The increase in the dielectric loss can be explained on the similar lines considering the increase in interfacial polarization with increasing temperature. The energy losses in the dielectrics are due to the electric conductivity of the materials and the relaxation effect related to the dipole orientation.

150
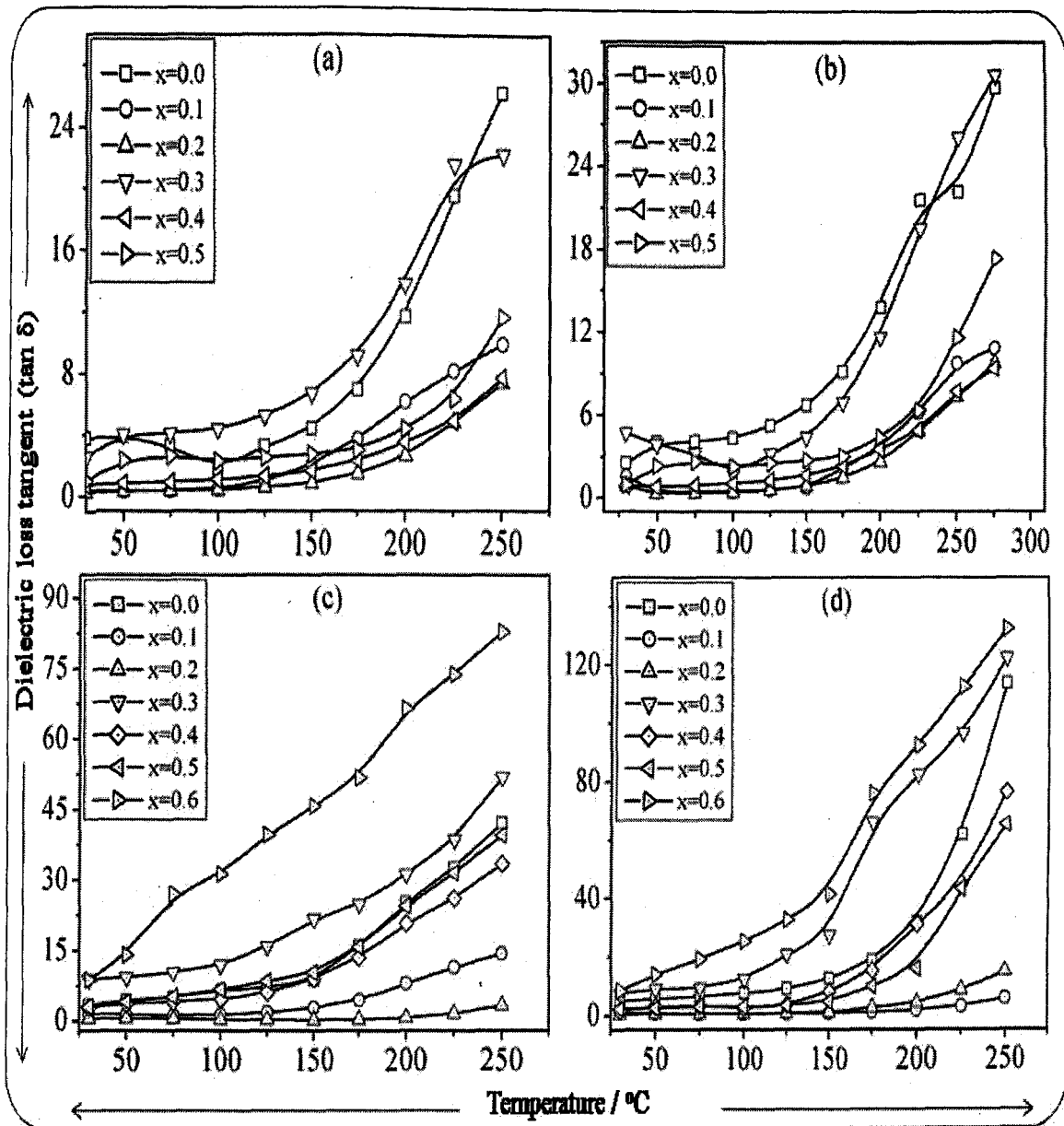
Fig.3.41. Temperature variation of dielectric loss tangent of $Ni_{0.6-x}Mn_xZn_{0.4}Fe_2O_4$

(x = 0.0-0.6) ferrites sintered at a) 1100°C / 1h, b) 1150°C / 1h, c) 1200°C / 1h and

d) 1250°C / 1h

With increase in temperature the losses due to dipole orientation decreases while those due to electric conductivity increases [238]. The increase in dielectric loss was observed for the sintered ferrites with increasing temperature suggest that the losses due to electrical conductivity dominate over losses due to relaxation effects

151

3.6.3.3. Compositional variation of dielectric constant

The room temperature values of dielectric constant ($\acute{\varepsilon}$) and dielectric loss (tan δ) at 1 kHz for all the sintered ferrites are given in the Table 3.18.

Table 3.18. Dielectric constant and dielectric loss of sintered $Ni_{0.6-x}Mn_xZn_{0.4}Fe_2O_4$ (x = 0.0-0.6) ferrites

x	Dielectric constant ($\acute{\varepsilon}$) / dielectric loss (tan δ) at 1kHz frequency							
	1100°C / 1h		1150°C / 1h		1200°C / 1h		1250°C / 1h	
	$\acute{\varepsilon}$	tan δ	$\acute{\varepsilon}$	tan δ	$\acute{\varepsilon}$	tan δ	$\acute{\varepsilon}$	tan δ
0.0	3.204	2.002	3.497	2.633	8.89	3.30	11.70	4.15
0.1	1.673	0.148	1.731	0.155	10.89	1.17	3.03	2.17
0.2	1.748	0.159	1.848	0.216	2.28	1.19	3.38	2.21
0.3	4.956	1.581	6.23	1.811	8.69	3.44	21.1	4.19
0.4	1.993	0.421	2.13	0.771	2.66	1.28	4.21	2.33
0.5	2.111	0.969	2.71	1.408	3.56	1.91	5.63	2.51
0.6	---	---	---	---	13.97	2.35	55.31	6.13

It was observed that the dielectric constant increases with an increase in Mn concentration except for composition, x = 0.3, where it shows a sudden rise. The exceptional behavior for composition, x = 0.3 is also reported by others [87,265]. In mixed spinel system such as Mn-Ni-Zn ferrites, Zn and Ni ions occupy tetrahedral (*A*) and octahedral [*B*] sites, respectively [178,273]. Both Mn and Fe ions, which exists in 2+ and 3+ states, are known to exist at both A and B sites [273-274]. When Mn^{2+} is added in place of Ni^{2+} and if it changes partly to Mn^{3+} in the system then, it will reduce some of the Fe^{3+} to Fe^{2+} so as to maintain the charge balance. This increased concentration of Fe^{2+} will

increase the hopping between Fe^{3+} and Fe^{2+} ions, thereby decreasing the resistance of the grain as a result the probability of the electrons reaching the grain boundary increases causing increase in polarization and hence the increase in dielectric constant as observed.

3.6.3.4. Effect of sintering temperature on dielectric properties

The dielectric constant and dielectric loss values increases with sintering temperatures. The sintering of the ferrites at higher temperatures can results in the loss of Zn due to volatilization [268]. As a result of Zn loss, the associated oxygen bonds become unsaturated. These unsaturated bonds get associated with the neighboring Fe^{3+} ions and convert later to Fe^{2+} ions. The Zn loss increases with the increase in sintering temperature and as a result, the Fe^{2+} concentration increases. Since, the Fe^{2+} ions are easily polarizable as compared to Fe^{3+} ions, the dielectric constant increases with the increasing sintering temperature. The lower values of dielectric constant and dielectric loss suggest the better homogeneity and lower Zn losses in the samples prepared by fumarato hydrazinate precursor method.

3.6.4. Magnetization studies

The magnetic properties such as saturation magnetization, coercivity, remanence were studied at room temperature for sintered $Ni_{0.6-x}Mn_xZn_{0.4}Fe_2O_4$ ($x = 0.0-0.6$) ferrites.

3.6.4.1. Compositional variation of magnetic properties

The magnetic hysteresis loops of some representative $Ni_{0.6-x}Mn_xZn_{0.4}Fe_2O_4$ ($x = 0.0, 0.1, 0.4$ and 0.6) ferrites sintered at 1200°C / 1h are shown in the Fig. 3.42 and the values of various magnetic parameters are listed in the Table 3.19.
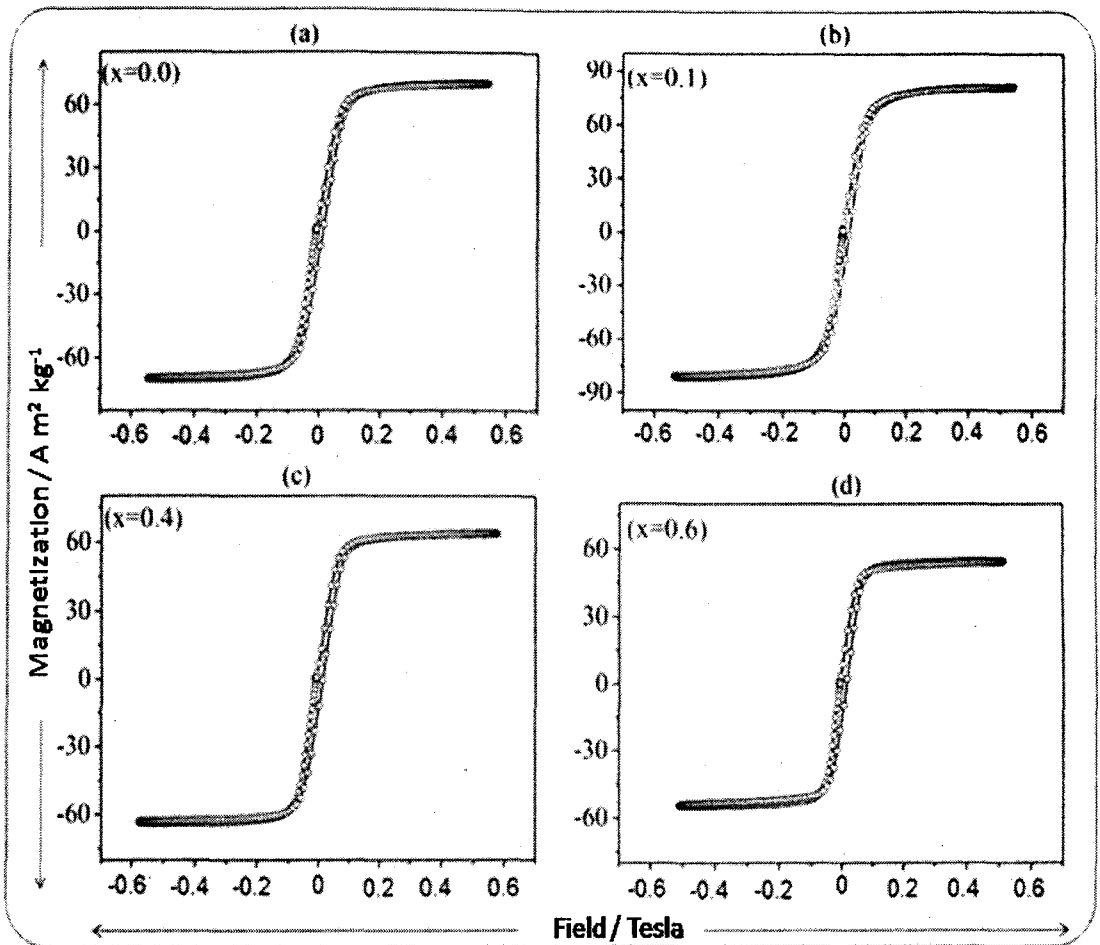
Fig.3.42. Hysteresis loops of $Ni_{0.6-x}Mn_xZn_{0.4}Fe_2O_4$ (x = 0.0-0.6) ferrites sintered at 1200°C / 1h

The observed variations can be explained on the basis of cation distributions and exchange interaction between Fe^{3+} and Mn^{2+} ions at tetrahedral (*A*) and octahedral [*B*] sites. It is known [178] that Zn^{2+} and Ni^{2+} ions occupy A and B sites, respectively. Although Fe^{3+} and Mn^{2+} ions exist at both A and B sites, they have preference for the B and the A sites, respectively [178]. In ferrites, the saturation magnetization is the difference between the magnetization of B and A sublattices. The effect of composition on the saturation magnetization can be due to the redistribution of ions in A and B sites which can directly affect the net magnetization. When Mn^{2+} ions are substituted for Ni^{2+} ions,

some of the Fe^{3+} ions migrate from A to the B sites in view of their site preference. This increases the Fe^{3+} ion concentration at B sites. As a result, the magnetic moment of B sublattice increases for small Mn^{2+} concentrations (upto, $x = 0.2$) as explained on the basis of Neel two sublattice model [245]. However, as Mn^{2+} concentration increases ($x > 0.2$), the Fe^{3+} ions left at A site being small in number, the A-B interaction experienced by B site Fe^{3+} ions decreases. Also, the increased number of Fe^{3+} ions at the B site increases the B-B interaction, resulting in spin canting [247-249,275]. Consequently, the magnetizations of B sublattice decreases. Similar variations of saturation magnetization are also reported in the literature [15,107]. The observed values of saturation magnetization in the present study [Table 3.19] are higher than those reported for sintered $Ni_{0.6-x}Mn_xZn_{0.4}Fe_2O_4$ ($x = 0.0$-0.6) ferrites system [86].

The coercivity was found to increase initially and then decreases with increasing Mn substitution which may be due to the decrease in the anisotropy constant with increasing Mn substitution. The results can also be justified from the fact that the anisotropy constant of Mn-Zn ferrites is less than Ni-Zn ferrites [251].

3.6.4.2. Effect of sintering temperature on magnetic properties

The saturation magnetization values of sintered $Ni_{0.6-x}Mn_xZn_{0.4}Fe_2O_4$ ($x = 0.0$-0.6) ferrites listed in the Table 3.19 shows that the saturation magnetization increases with increase in the sintering temperature upto $1200^{\circ}C$. The increase in saturation magnetization is expected, since the saturation magnetization is directly related to the density and grain size [276-277] which increases with increasing sintering temperature and inversely to the magnetocrystalline anisotropy which decreases with increasing Mn substitution.

Table 3.19. Magnetic hysteresis data of $Ni_{0.6-x}Mn_xZn_{0.4}Fe_2O_4$ ($x = 0.0-0.6$) ferrites sintered at different temperatures

Magnetic characteristics	Sintering temp. / °C	x						
		0.0	0.1	0.2	0.3	0.4	0.5	0.6
Saturation magnetization (M_s) / A m^2 kg^{-1}	1100°C / 1h	74.9	82.8	79.1	73.3	69.9	65.1	--
	1150°C / 1h	78.9	83.3	81.0	76.2	72.1	68.2	--
	1200°C / 1h	85.5	89.1	86.8	81.6	78.9	72.7	61.6
	1250°C / 1h	84.2	87.9	85.6	80.2	76.3	71.1	58.2
Remanent magnetization (M_r) / A m^2 kg^{-1}	1100°C / 1h	11.2	14.2	11.95	11.35	9.78	8.35	--
	1150°C / 1h	7.23	10.56	11.8	9.30	4.82	5.37	--
	1200°C / 1h	5.85	6.47	7.69	5.74	3.15	3.37	11.6
	1250°C / 1h	2.85	2.10	3.07	2.0	1.03	1.09	3.67
Coercivity (H_c) x 10^{-3} / Tesla	1100°C / 1h	124.3	127.8	128.6	130.2	129.5	122.3	--
	1150°C / 1h	117.5	121.3	121.4	123.8	120.1	116.2	--
	1200°C / 1h	115.0	118.8	119.2	116.7	106.7	113.8	118.2
	1250°C / 1h	114.5	112.5	107.9	111.7	103.2	105.3	105.6

The decrease in the saturation magnetization in the samples sintered at 1250°C may be due to the zinc loss due to volatilization at higher temperatures (< 1200°C) which reduces Fe^{3+} ions to Fe^{2+} ions to maintained charge neutrality. This results in an increase in anisotropy [268] and decrease in the magnetic moment thereby decreasing the magnetization. This behavior was also observed by Verma *et al.* [94] for Zn substituted Mn-Ni ferrites. The coercivity was found to decrease with increase in the sintering temperature [Table 3.19]. It is known that coercivity varies directly with porosity and anisotropy constant and inversely with grain size [278]. With increasing sintering temperature grain size increases while porosity and anisotropy constant decreases and the overall effect of these factors results in decrease of coercivity.

3.6.5. Initial permeability measurements

The magnetic permeability may be considered to be measure of efficiency of magnetic materials. The inductance measurements were carried out by winding 50 turns of 30 SWG enamelled copper wire on toroids as function of frequency (100 Hz to 10 MHz) as well as temperature from room temperature to 723 K. The initial permeability was calculated using relation 2.35 given in the section 2.3.16 of chapter 2.

3.6.5.1. Frequency variation of initial permeability 'μ_i' and tan δ

The observed initial permeability 'μ_i' as a function of frequency at room temperature for sintered $Ni_{0.6-x}Mn_xZn_{0.4}Fe_2O_4$ ($x = 0.0\text{-}0.6$) ferrites is shown in Fig. 3.43. It was observed that initial permeability decreases very slowly with frequency up to about 6 MHz and shows an increase at higher frequencies upto 10 MHz, the frequency limit upto which the measurements carried out. This increase is attributed to the onset of resonance which is also reported in the literature [94,279-280]. The initial permeability in ferrites is

due to domain wall displacement. The decrease in initial permeability with frequency is due to phase lag between the applied field and the domain wall displacement.
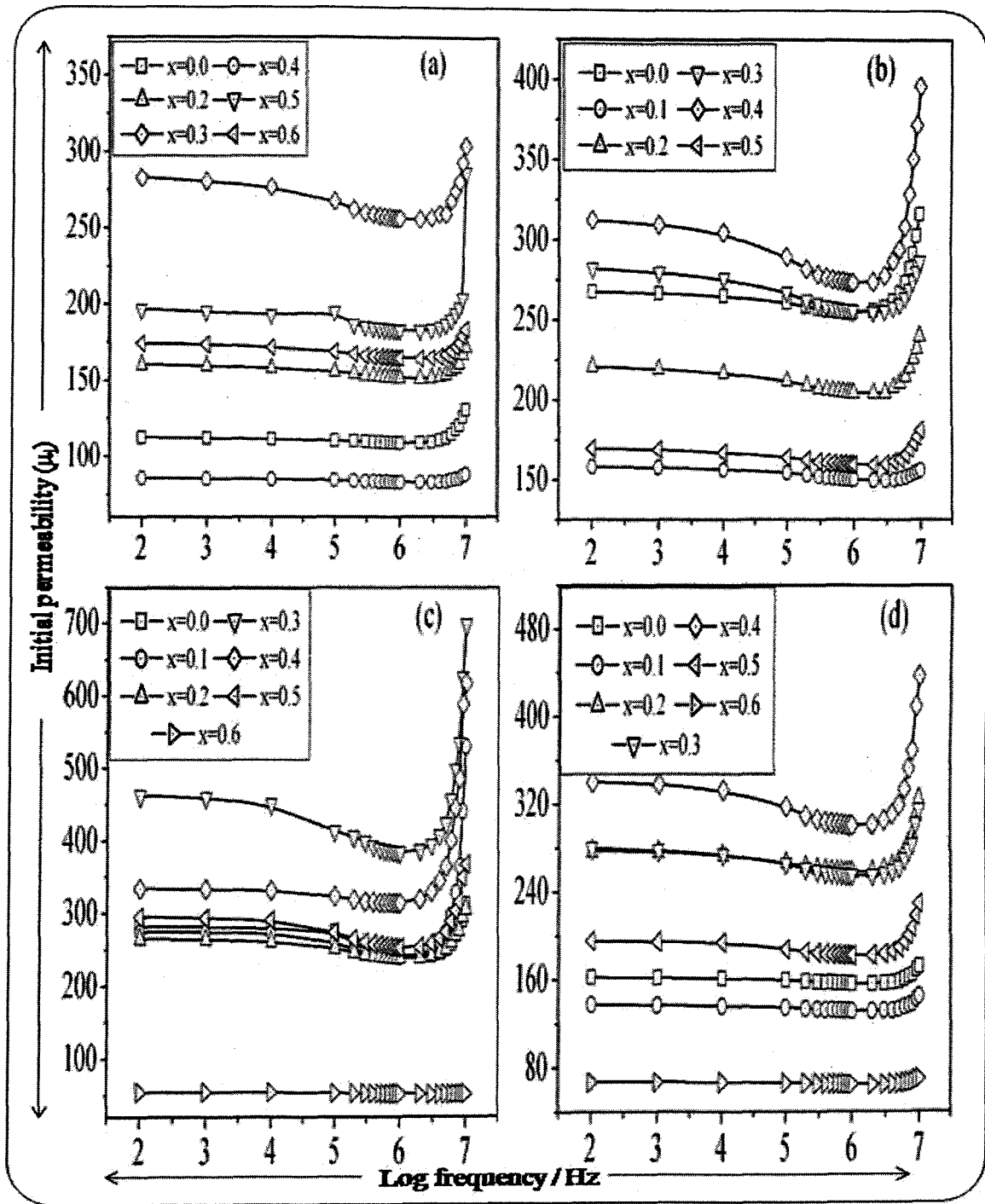
Fig.3.43. Room temperature frequency variation of initial permeability 'μᵢ' of

$Ni_{0.6-x}Mn_xZn_{0.4}Fe_2O_4$ (x = 0.0-0.6) ferrites sintered at a) 1100°C / 1h, b) 1150°C / 1h, c) 1200°C / 1h and d) 1250°C / 1h

158

In general, the resonance peak in ferrites is observed due to domain wall oscillations [280-281] at lower frequencies (1MHz to100 MHz) and another at higher frequencies (~1 GHz) due to Larmor precession of electron spins [279]. The initial permeability values at 1 kHz are found to be in the range 48 to 463 for all sintered $Ni_{0.6-x}Mn_xZn_{0.4}Fe_2O_4$ (x = 0.0-0.6) ferrites. These values are higher than those reported in the literature [97].

Table 3.20. Initial permeability 'μ_i' and loss factor of $Ni_{0.6-x}Mn_xZn_{0.4}Fe_2O_4$ (x = 0.0-0.6) ferrites sintered at different temperatures

x	Initial permeability 'μ_i' / loss factor at 1 kHz							
	1100°C / 1h		1150°C / 1h		1200°C / 1h		1250°C / 1h	
	μ_i	loss factor	μ_i	loss factor	μ_i	loss factor	μ_i	loss factor
0.0	112.3	0.875	267	0.91	328.8	2.22	161.8	1.79
0.1	85.63	0.855	158.1	0.92	289.3	3.04	137.2	1.92
0.2	160.3	0.87	220.8	1.09	280.2	2.45	277.1	3.07
0.3	196.5	1.11	282.2	2.13	462.4	1.12	279.7	0.976
0.4	273.7	0.873	282.9	0.871	340.1	0.873	312.3	0.93
0.5	169.3	0.865	174.3	0.861	220.0	1.29	195.2	1.12
0.6	---	---	---	---	66.86	3.89	48.57	4.32

The variation of tan δ with frequency for all ferrite samples sintered at different temperatures has been studied from 100 Hz to 10 MHz is shown in Fig. 3.44. The tan δ values are found to be in the range 44 to 10^{-3} in the frequency range 100 Hz to 10 MHz. These values are low as compare to those reported for ferrites by other workers [178,280-

281]. The loss is due to lag of motion of domain walls with respect to the applied alternating magnetic field and is attributed to imperfections in the lattice [282].
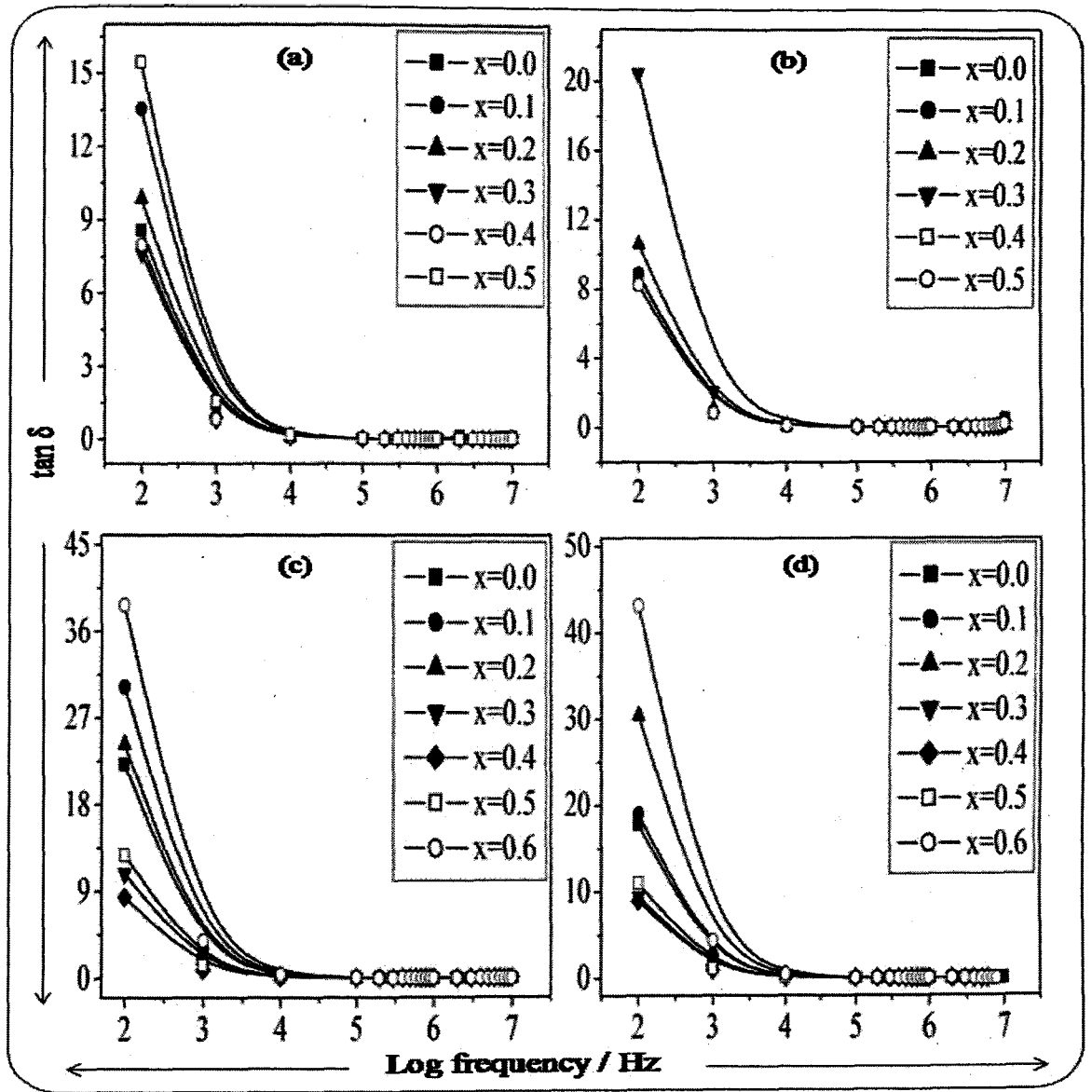
Fig.3.44. Room temperature frequency variation of tan δ at room temperature of $Ni_{0.6-x}Mn_xZn_{0.4}Fe_2O_4$ (x = 0.0-0.6) ferrites sintered at a) 1100°C / 1h, b) 1150°C / 1h, c) 1200°C / 1h and d) 1250°C / 1h

3.6.5.2. Temperature variation of initial permeability 'μ$_i$' and tan δ

In order to study the temperature dependence of initial permeability 'μi', the permeability was determined and plotted as a function of temperature. The initial

permeability-temperature 'μi - T' curves for all the ferrites sintered at different temperatures are shown in the Fig. 3.45.
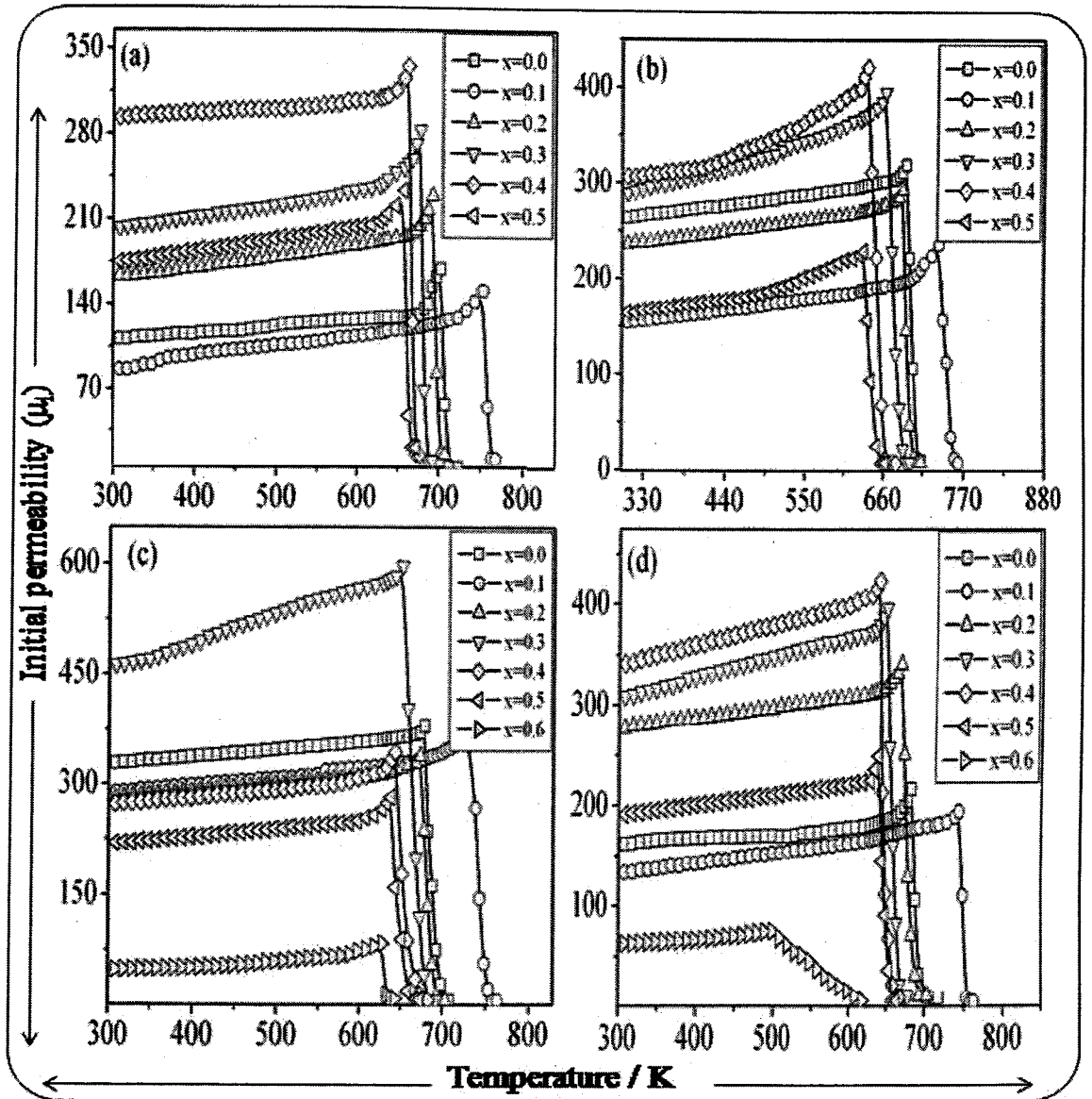
Fig.3.45. Temperature variation of initial permeability 'μ$_i$' of sintered

Ni$_{0.6-x}$Mn$_x$Zn$_{0.4}$Fe$_2$O$_4$ (x = 0.0-0.6) ferrites sintered at a) 1100°C / 1h, b) 1150°C / 1h, c) 1200°C / 1h and d) 1250°C / 1h

This sharp drop in initial permeability 'μ$_i$' supports the single phase formation of the compositions and homogeneity of the sample [283]. The Curie temperatures were determined by drawing tangent to the μ$_i$ -T plots at a point of sharp fall in initial

permeability. The profiles also shows a Hopkinson's peak near the Curie temperature which is a typical behavior exhibited by cubic structures [284].

The variation of tan δ with temperature of all the ferrite samples sintered at different temperatures is shown in the Fig. 3.46. The tan δ is almost constant in the temperature range from room temperature to near Curie temperature, while above Curie temperature it increases exponentially.
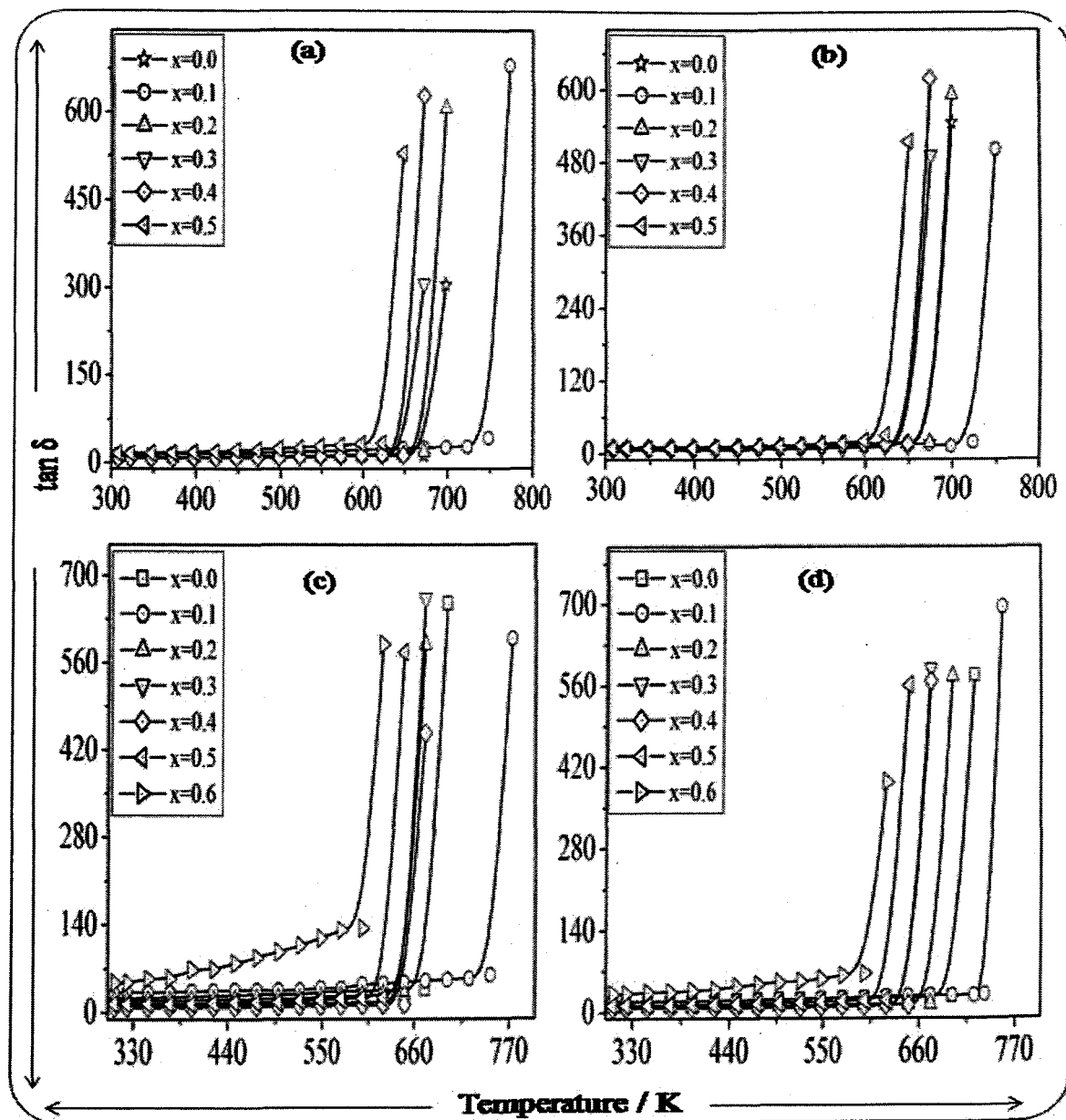
Fig.3.46. Temperature variation of tan δ of sintered $Ni_{0.6-x}Mn_xZn_{0.4}Fe_2O_4$ (x = 0.0-0.6) ferrites sintered at a) 1100°C / 1h, b) 1150°C / 1h, c) 1200°C / 1h and d) 1250°C / 1h

3.6.5.3. Compositional variation of initial permeability 'μ_i'

The initial permeability and loss factor values of the sintered $Ni_{0.6-x}Mn_xZn_{0.4}Fe_2O_4$ ($x = 0.0$-0.6) ferrites at room temperature and 1 kHz frequency are listed in the Table 3.20. It is clear from the Table 3.20 that initial permeability increases upto $x = 0.4$ and then decreases. The initial permeability is dependent on many parameters such as stoichiometry, grain structure, composition, impurity contents, crystal anisotropy, and porosity. The value of initial permeability increases with the increase in grain size and stoichiometry [280,285] and decreases with the increase in porosity and decrease in the magnetocrystalline anisotropy [280, 286-287]. It has a major contribution from domain wall motion, but a smaller effect due to spin rotation [280]. The initial increase in initial permeability suggests that the effect of stoichiometry and magnetocrystalline anisotropy play a dominant role at lower Mn substitution ($x \leq 0.4$). This means that as the Mn concentration increases, the anisotropy constant (K_1) decreases, and thus the initial permeability increases at lower Mn substitution. Also, as the particle size increases, porosity decreases with the increase in sintering temperature. It therefore follows that the effect of particle size and porosity would increase the value of initial permeability for compositions, $x \leq 0.4$. Since saturation magnetization and permeability being interdependent, their variations with Mn substitution are self consistent. The Curie temperatures [Table 3.21] has been observed to increase initially ($x = 0.1$) and then decrease with the increase in the Mn substitution. The variation of Curie temperature can be explained on the basis of strength of the exchange interactions. In the case of $Ni_{0.6-x}Mn_xZn_{0.4}Fe_2O_4$ ($x = 0.0$-0.6) ferrites, the ferromagnetic Fe^{3+} ions are replaced by the diamagnetic Mn^{2+} ions with every step of substitution. Therefore, a decrease in the density of magnetic ions and the magnetic moment of the sublattices is expected. This weakens the A-B exchange interactions.

Table 3.21. Curie temperatures determined from d.c. resistivity, a.c. susceptibility and initial permeability studies of sintered of $Ni_{0.6-x}Mn_xZn_{0.4}Fe_2O_4$ ($x = 0.0-0.6$) ferrites

Curie Temperature / K	Sintering temp. / °C	x						
		0.0	0.1	0.2	0.3	0.4	0.5	0.6
DC resistivity	1100°C / 1h	702	731	704	666	653	647	--
($\log \rho - 10^3 / T$)	1150°C / 1h	705	738	690	670	661	649	--
plots	1200°C / 1h	693	743	699	673	667	654	603
	1250°C / 1h	690	723	686	661	643	632	583
AC susceptibility	1100°C / 1h	700	751	692	675	667	658	--
($\chi_T / \chi_{RT} - T$)	1150°C / 1h	699	753	691	673	665	657	--
plot	1200°C / 1h	701	756	690	672	661	653	624
	1250°C / 1h	700	750	691	676	661	654	623
Initial	1100°C / 1h	707	753	698	680	663	655	--
permeability	1150°C / 1h	701	756	693	676	664	659	--
(μ_i -T) plot	1200°C / 1h	704	758	696	678	665	658	627
	1250°C / 1h	702	755	692	673	663	656	620

Since, the Curie temperature is determined by an overall strength of the A-B exchange interactions, the weakening of the $Fe^{3+}_{(A)}-O^{2-}-Fe^{3+}_{(B)}$ interaction results in a decrease in the Curie temperature, when the concentration of Mn increases. Also, exchange integral 'J' between Fe^{3+} ions and Ni^{2+}ions (J = -24 K) is greater than that between Fe^{3+} ions and Mn^{2+} ions (J = -19.1 K) which causes the decrease in A-B interactions [288] and hence the Curie temperature.

3.6.5.4. Effect of sintering temperature on initial permeability 'μ_i' and tan δ

It has been observed that initial permeability increases with the increase in sintering temperature upto 1200°C but decreases with further increase in sintering temperature. This increase in initial permeability can be attributed to the increase in density and grain size, which increases with sintering temperature [289]. Increase in grain size results in an increase in the number of domain walls in each grain. As the movement of walls determines the initial permeability, any increase in the number of domain walls would result in an increase in initial permeability. At higher sintering temperatures (>1200°C) there is increase in the intragranular pores that are trapped in the grains. These pores act as pinning centers for the domain wall movement. Consequently, domain wall movement is restricted and this limits the rate of growth of initial permeability. Further, magnetocrystalline anisotropy decreases with the increase in sintering temperature and therefore enhances the initial permeability [290].

The tan δ was also observed to increase with increase in sintering temperature [Table 3.20]. The increase in the sintering temperature results in Zn loss in the samples thereby creating defects in the lattice which gives rise to magnetic loss.

3.6.6. AC susceptibility studies

The plots of normalized a.c. susceptibility against temperature for all the ferrites sintered at different temperatures are shown in the Fig. 3.47.
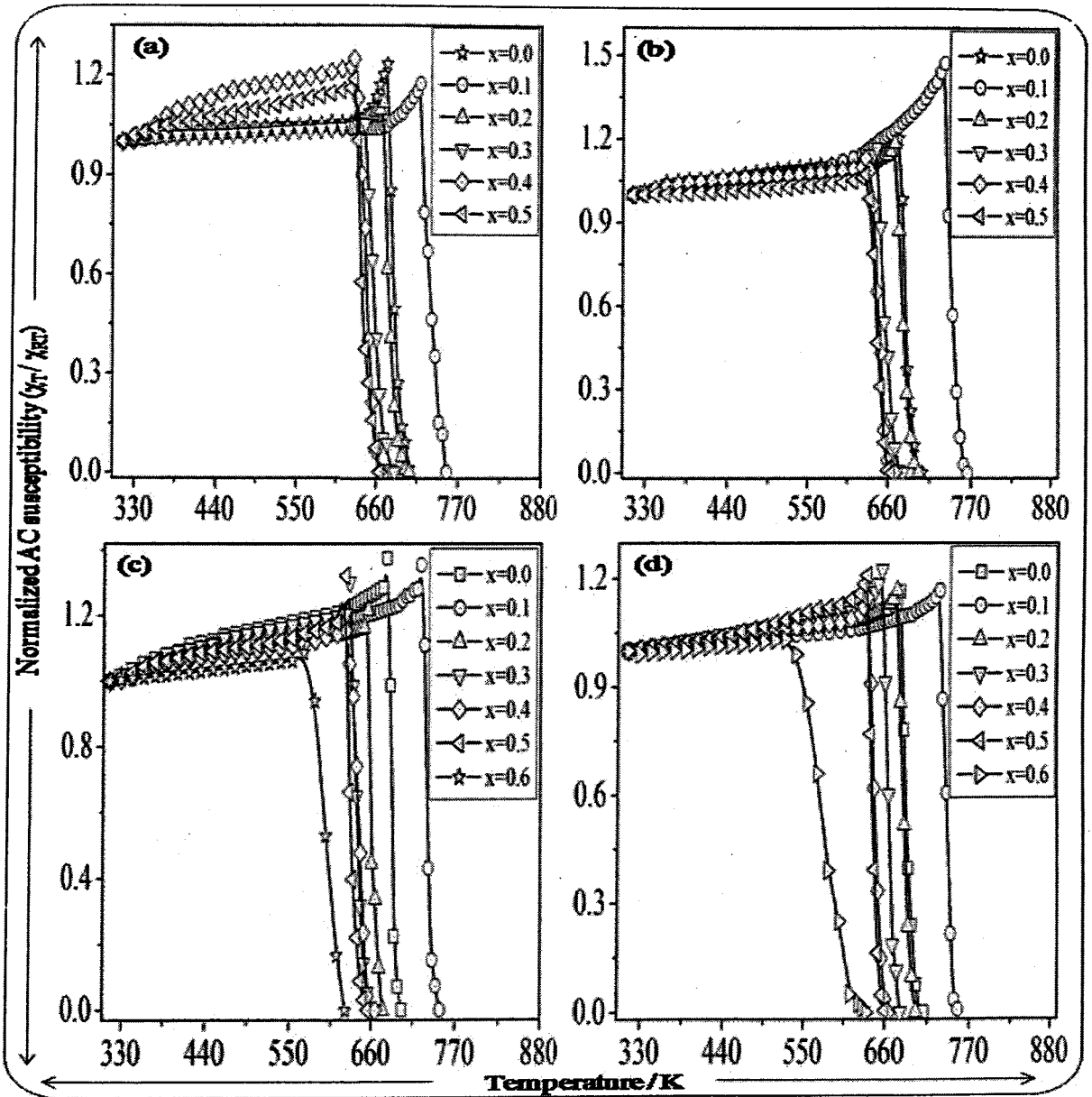
Fig.3.47. The plot of normalized ac susceptibility against temperature of $Ni_{0.6-x}Mn_xZn_{0.4}Fe_2O_4$ (x = 0.0-0.6) ferrites sintered at a) 1100°C / 1h, b) 1150°C / 1h, c) 1200°C / 1h and d) 1250°C / 1h

The sintered samples exhibit normal ferromagnetic behavior. The Curie temperature determined from the ac susceptibility measurement is given in the Table 3.21. According to Neel's model [245] the A-B interaction is most dominant in ferrites and therefore the Curie temperatures are determined from the overall strength of A-B interaction. The strength of A-B interaction is a function of number of Fe^{3+}_A - O^{2-} -Fe^{3+}_B linkage [291] which in turn depend upon the number of Fe^{3+} ions in the formula unit and their distribution amongst tetrahedral (A) and octahedral [B] sites. The observed variation of Curie temperature with Mn substitution can be explained considering the distribution of Mn^{2+} ions in tetrahedral (A) and octahedral [B] sites. The initial increase in Curie temperature (upto concentration, $x = 0.1$) is due to the strengthening of A-B interaction due to the transfer of Fe^{3+} ions from tetrahedral (A) and octahedral [B] sites, while decrease in Curie temperature at higher Mn substitution is because of spin canting due to excess Fe^{3+} ions in octahedral [B] sites.

3.7. Summary

The spinel system having mixed Ni-Zn ferrites and Mn-Zn ferrites [$Ni_{0.6-x}Mn_xZn_{0.4}Fe_2O_4$ ($x = 0.0-0.6$)] have been successfully synthesized by low temperature self propagating autocatalytic decomposition of hydrazinated mixed metal fumarate precursors prepared from mixed metal chlorides and hydrazine hydrate-sodium fumarate aqueous solution. The precursor formula was fixed as $Ni_{0.6-x}Mn_xZn_{0.4}Fe_2(C_4H_2O_4)_3.6N_2H_4$ ($x = 0.0-0.6$), based on chemical analysis, total mass loss, FTIR and thermal studies. The precursor decomposed autocatalytically to nanosize $Ni_{0.6-x}Mn_xZn_{0.4}Fe_2O_4$ ($x = 0.0-0.6$) ferrites ('as synthesized'). The nanosize nature of 'as synthesized' $Ni_{0.6-x}Mn_xZn_{0.4}Fe_2O_4$ ($x = 0.0-0.6$) ferrites was confirmed by TEM. The XRD analysis reveals the formation of single phase cubic spinel structure. The

lattice parameter increases while, the X-ray as well as bulk density decrease with increase in Mn concentration. The FTIR spectra of the studied ferrite samples display two principal absorption bands characteristics of intrinsic M—O vibrations in two different crystallographic sites in spinel ferrite lattice. The absorption frequency of high frequency band was found to decrease with increasing Mn substitution. The Mössbauer studies of 'as synthesized' $Ni_{0.6-x}Mn_xZn_{0.4}Fe_2O_4$ (x = 0.0-0.6) ferrites indicated their superparamagnetic and ferromagnetic nature while, the sintered $Ni_{0.6-x}Mn_xZn_{0.4}Fe_2O_4$ (x = 0.0-0.6) ferrites showed ferromagnetic nature (except for, x = 0.6). The ac susceptibility studies reveals presence of clusters of both superparamagnetic and single domain particles in 'as synthesized' $Ni_{0.6-x}Mn_xZn_{0.4}Fe_2O_4$ (x = 0.0-0.6) ferrites. The saturation magnetization shows initial increase followed by decrease with increasing Mn substitution attributed to the Fe^{3+} ions transfer leading to spin canting. The reduction of magnetic moment of nanocrystalline $Ni_{0.6-x}Mn_xZn_{0.4}Fe_2O_4$ (x = 0.0-0.6) ferrites was attributed to both the anisotropy constant and canted spin structure at the surface of the particles and the high value of coercivity to strong interparticle interactions. The lattice parameter and average grain size increases with increasing Mn substitution in sintered Ni-Zn ferrites. The microstructural studies show that the grain size increases with sintering temperature. The dc resistivity was found to decrease with Mn substitution and sintering temperature. The Seebeck coefficient measurement shows negative values indicating n-type conduction and high values of Seebeck coefficient suggests polaron hopping mechanism. The dielectric constant and dielectric loss were found to be comparatively low and were found to increase with sintering temperature. The dispersion observed in the dielectric constant is explained on the basis of the double layer dielectric structure and the relaxation peaks observed in the variation of dielectric loss tangent is due to the matching of hopping

frequency of electrons with that of the electric field. The frequency variation of complex initial permeability indicates that the resonance peak due to domain wall oscillation is at a frequency above 10MHz. The sharp decrease in the initial permeability at Curie temperature indicates high homogeneity for sintered ferrite samples. The initial permeability was found to increase with increase in Mn content upto $x = 0.4$, followed by decrease. The saturation magnetization and initial permeability increases with increasing sintering temperature upto 1200°C and shows decrease thereafter. The Curie temperature of the samples determined by permeability studies, dc resistivity measurements and those obtained from ac susceptibilty studies matches closely. The gas sensing studies carried out on the thick films of 'as synthesized' $Ni_{0.6-x}Mn_xZn_{0.4}Fe_2O_4$ ($x = 0.0-0.6$) ferrite samples indicated high sensitivity towards H_2S and NH_3 among all the test gases. One of the sample ($x = 0.3$) shows good gas sensing activity at room temperature and low gas concentration for ammonia. Also, the response was very fast and recovery time was very quick for this composition. The thick film of composition, $x = 0.5$ showed quite good response for H_2S gas at higher temperatures.

Chapter 4

Synthesis and characterization of

$$Ni_{0.5-x}Mn_xZn_{0.5}Fe_2O_4$$
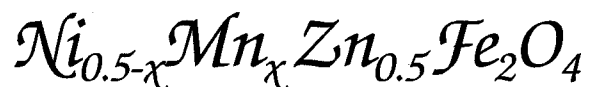
$$(x = 0.0,\ 0.1,\ 0.2,\ 0.3,\ 0.4\ \&\ 0.5)$$

Synthesis and characterization of $Ni_{0.5-x}Mn_xZn_{0.5}Fe_2O_4$ (x = 0.0-0.5) ferrites

4.1. Synthesis and characterization of hydrazinated mixed nickel manganese zinc ferrous fumarate, $Ni_{0.5-x}Mn_xZn_{0.5}Fe_2(C_4H_2O_4)_3.6N_2H_4$ (x = 0.0-0.5) precursors

4.1.1. Experimental

The detail of the synthesis procedure of hydrazinated mixed nickel manganese zinc ferrous fumarates is already discussed in the section 2.2. in chapter 2. The precursors were characterized by chemical analysis, FTIR spectroscopy, TG and DTA, isothermal mass loss studies and their molecular formulae were fixed accordingly.

4.1.2. Results and discussion

The synthesized hydrazinated mixed nickel manganese zinc ferrous fumarates were characterized by various techniques mentioned in section 3.1.2 and the results of characterization are compiled and discussed in this part of the chapter.

4.1.2.1. Chemical analysis

The chemical analysis was carried out to establish the molecular stoichiometry of the precursors. The chemical analysis results of the hydrazinated mixed nickel manganese zinc ferrous fumarates are given in the Table 4.1. The chemical analysis results were found to be in agreement with the calculated values obtained considering the molecular composition of the precursor complexes as given in the Table 4.1.

Table 4.1. Chemical analysis results of hydrazinated mixed nickel manganese zinc ferrous fumarate complexes,

$Ni_{0.5-x}Mn_xZn_{0.5}Fe_2(C_4H_2O_4)_3.6N_2H_4$ (x = 0.0-0.5)

x	Metal content / %								Hydrazine / %		Proposed molecular formula	Molecular mass
	Fe		Mn		Ni		Zn					
	Obs.	Calc.	Obs.	Calc.	Obs.	Calc.	Obs.	Calc.	Obs.	Calc.		
0.0	15.75	15.77	-----		4.11	4.15	4.59	4.61	27.12	27.16	$Ni_{0.5}Zn_{0.5}Fe_2(C_4H_2O_4)_3.6N_2H_4$	708.2
0.1	15.77	15.78	0.76	0.77	3.30	3.32	4.58	4.62	27.29	27.17	$Ni_{0.4}Mn_{0.1}Zn_{0.5}Fe_2(C_4H_2O_4)_3.6N_2H_4$	707.8
0.2	15.80	15.79	1.51	1.56	2.48	2.49	4.60	4.62	27.39	27.18	$Ni_{0.3}Mn_{0.2}Zn_{0.5}Fe_2(C_4H_2O_4)_3.6N_2H_4$	707.4
0.3	15.81	15.80	2.30	2.33	1.63	1.66	4.57	4.62	27.24	27.20	$Ni_{0.2}Mn_{0.3}Zn_{0.5}Fe_2(C_4H_2O_4)_3.6N_2H_4$	707.1
0.4	15.83	15.81	3.08	3.11	0.826	0.832	4.61	4.62	27.49	27.21	$Ni_{0.1}Mn_{0.4}Zn_{0.5}Fe_2(C_4H_2O_4)_3.6N_2H_4$	706.7
0.5	15.80	15.82	3.86	3.89	-----		4.55	4.63	27.16	27.22	$Mn_{0.5}Zn_{0.5}Fe_2(C_4H_2O_4)_3.6N_2H_4$	706.3

4.1.2.2. FTIR spectral analysis

The FTIR spectra of $Ni_{0.5-x}Mn_xZn_{0.5}Fe_2(C_4H_2O_4)_3.6N_2H_4$ (x = 0.0-0.5) precursors are presented in the Fig. 4.1 and the corresponding IR absorption frequencies are listed in the Table 4.2.
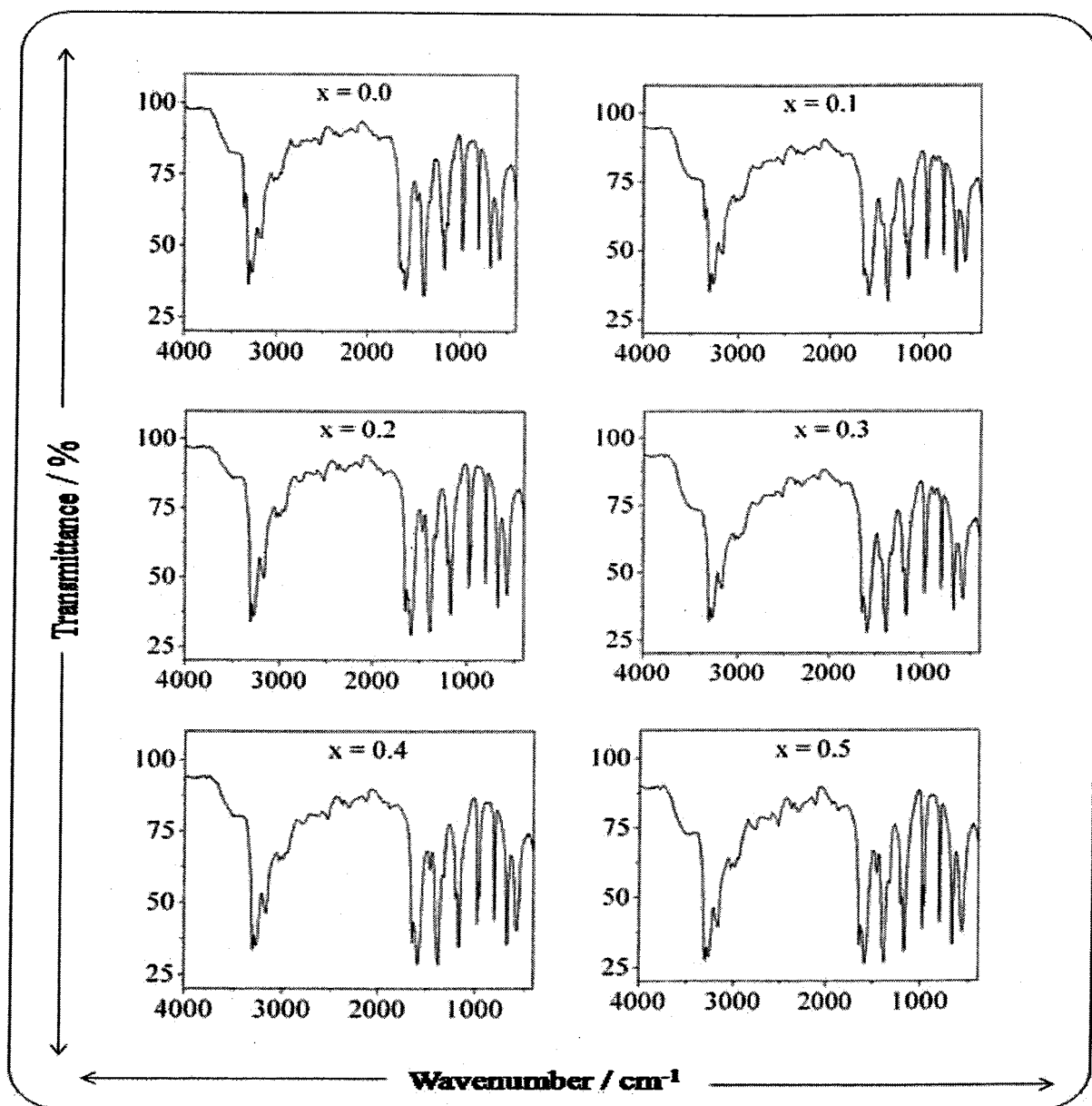
Fig.4.1. FTIR spectra of $Ni_{0.5-x}Mn_xZn_{0.5}Fe_2(C_4H_2O_4)_3.6N_2H_4$ (x = 0.0-0.5) precursors

Table 4.2. FTIR absorption frequencies of hydrazinated mixed nickel manganese zinc ferrous fumarate precursors,

$Ni_{0.5-x}Mn_xZn_{0.5}Fe_2(C_4H_2O_4)_3.6N_2H_4$ ($x = 0.0-0.5$)

x	FTIR absorptions / cm^{-1}							
	N-H stretching	ν_{asym} COO$^-$ stretching	NH$_2$ deformation	ν_{sym} COO$^-$ stretching	NH$_2$ wagging	N-N stretching	N-N bending	NH$_2$ rocking
0.0	3355-3167	1644	1585	1380	1164	980	802	674
0.1	3355-3167	1644	1584	1380	1164	980	802	670
0.2	3304-3167	1644	1581	1380	1165	980	803	674
0.3	3304-3167	1644	1581	1380	1165	980	803	670
0.4	3304-3167	1644	1581	1380	1165	980	803	670
0.5	3304-3167	1644	1581	1380	1165	980	803	670

173

The IR peaks characteristics of N-H stretching vibrations of hydrazine in the precursors were observed in the region 3304 cm^{-1} to 3167 cm^{-1} [Table 4.2], while peak due NH$_2$ deformation was observed in the range 1585 cm^{-1} to 1581 cm^{-1}. The N-N stretching frequencies observed at 980 cm^{-1} are characteristics of bidentate bridging linkage of hydrazine ligands in the precursors [193,194]. The asymmetric stretching vibration (ν_{asym}) frequencies of the fumarate ion was observed at 1644 cm^{-1} and symmetric stretching vibration (ν_{sym}) frequencies which appeared at 1380 cm^{-1} [Table 4.2], gives a separation $\Delta\nu$ (ν_{asym} -ν_{sym}) of 264 cm^{-1} which confirms the monodentate linkage behavior of both carboxylate groups in the fumarate dianions [195]. Thus, the FTIR analysis points towards the bidentate bridging nature of neutral hydrazine ligands and monodentate linkage of fumarate dianions and hence the polymeric nature of hydrazinated mixed nickel manganese zinc ferrous fumarate precursors.

4.1.2.3. Thermal studies

4.1.2.3a. TG and DTA analysis

The TG and DTA profiles of all the synthesized precursors are shown in the Fig. 4.2 and the thermal analysis data is presented in Table 4.3 The thermal decomposition of all the Ni$_{0.5-x}$Mn$_x$Zn$_{0.5}$Fe$_2$(C$_4$H$_2$O$_4$)$_3$.6N$_2$H$_4$ (x = 0.0-0.5) precursors occur in three steps. The initial mass losses of 10.19%, 10.22%, 10.46% and 9.95% in precursors with composition, x = 0.0, 0.1, 0.3 and 0.4, respectively, from room temperature to 110°C are due to the loss of adsorbed species including moisture (desorption) and beginning of the dehydrazination.
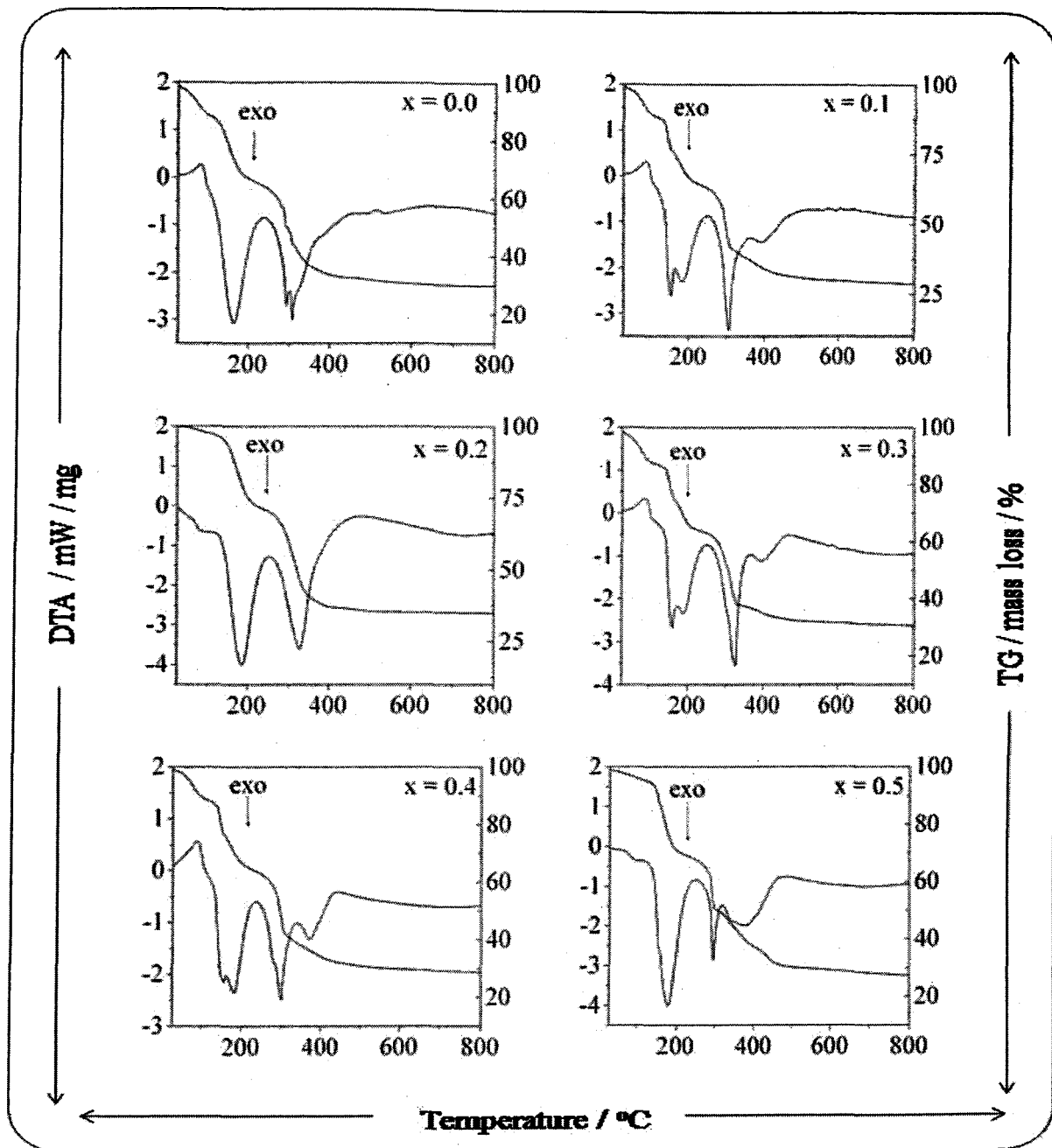
Fig.4.2. TG and DTA curves of $Ni_{0.5-x}Mn_xZn_{0.5}Fe_2(C_4H_2O_4)_3.6N_2H_4$ ($x = 0.0$-0.5) precursors

This desorption of adsorbed species was indicated by a weak endotherm in the temperature range 80°C to 90°C, while the hydrazine loss was indicated by weak exotherm in the DTA curve in the region from 90°C to 110°C. The mass loss of 3.10 % and 3.05 %

observed in precursors with composition, $x = 0.2$ and 0.5, respectively, indicates very low moisture contents. Infact, the DTA curve display only a weak exotherm which marks the beginning of dehydrazination from room temperature to 110°C. The mass loss of 17.86 %, 16.85 % and 17.79 % observed in precursors with composition, $x = 0.1$, 0.3 and 0.4 respectively, in the region 110°C to 170°C corresponds to the loss of four hydrazine molecules. The DTA profile displays strong exotherm with peak temperature of 153.8°C, 161.7°C and 156.9°C corresponding to this dehydrazination and, the mass loss of 5.4 %, 5.6 % and 5.04 % observed from 170°C to 210°C is due to the complete dehydrazination of these complexes. The exothermic peaks in DTA were observed at 181.7°C, 188.9°C and 182.4°C for composition, $x = 0.1$, 0.3 and 0.4, respectively. In the complexes with composition, $x = 0.0$, 0.2 and 0.5, this dehydrazination was found to occur in one step with mass losses of 22.21 %, 23.74 % and 26.04 %, respectively, in the temperature region from 110°C to 210°C. The single step dehydrazination was indicated by strong exothermic peak at 164.8°C, 186.8°C and 180.7°C, respectively, in the DTA profiles. The mass loss region, from 210°C to 360°C with mass losses of 27.81 % - 33.68 % results from the oxidative decarboxylation of dehydrazinated precursors with corresponding strong exotherms in DTA in this region. The high exothermicity of dehydrazination acts as a driving force for low temperature decarboxylation of dehydrazinated precursors. The marginal mass loss region (3.58 % - 8.41 % mass loss) with broad exotherm in DTA from 330°C to 460°C results from mainly the oxidation of the residual carbon formed during decarboxylation or due to the oxidation of trace of undecomposed carboxylate.

Table 4.3. TG and DTA analysis data of hydrazinated mixed nickel manganese zinc ferrous fumarate complexes,

$Ni_{0.5-x}Mn_xZn_{0.5}Fe_2(C_4H_2O_4)_3.6N_2H_4$ ($x = 0.0\text{-}0.5$)
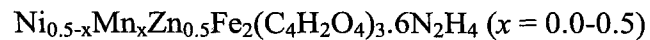
x	TG (mass loss / %) / DTA (mW mg^{-1} / °C)						
	RT - 110	110 - 170	170 - 210	110 - 210	210 - 360	360 - 460	RT - 460
0.0	10.19 / 84.4 (endo)	---	---	22.21 /164.8 (exo)	29.85 / 292, 307 (exo)	3.58 / ~386 (exo hump)	65.83
0.1	10.22/ 89.2 (endo)	17.86 / 153.8 (exo)	5.4 / 181.7 (exo)	---	28.33 / 306 (exo)	5.08 / 391.2 (exo)	66.89
0.2	3.10 / 89.8 (exo)	---	---	23.74 / 186.8 (exo)	33.68 / 327.3 (exo)	3.58 / ~386 (exo hump)	65.36
0.3	10.46 / 89 (endo)	16.85/ 161.7 (exo)	5.6 / 188.9 (exo)	---	27.81 / 327.3 (exo)	5.62 / 396 (exo)	66.33
0.4	9.95 / 89.7 (endo)	17.79 / 156.9 (exo)	5.04 /182.4 (exo)	---	28.84 / 300.6 (exo)	5.36 / 370.8 (exo)	66.98
0.5	3.05 / 98.6 (exo)	---	---	26.04 / 180.7 (exo)	30.13 / 293.4 (exo)	8.41 / 373.2 (exo)	67.63

4.1.2.3b. Total mass loss studies

The total mass losses obtained from thermogravimetric measurement [Table 4.3] and those obtained from pyrolysis of precursors in air [Table 4.4] were found to be slightly higher than the calculated values considering the stoichiometric molecular composition [Table 4.1] assigned to the precursors. The difference observed is due to high concentration of adsorbed species like moisture on these precursors. The presence of adsorbed moisture was also reflected in the FTIR spectra of precursors wherein weak band due to O--H stretching was observed in the region 3550 cm^{-1} to 3460 cm^{-1}. Besides this, the initial increase in the hydrazine content observed upto 75°C during isothermal mass loss studies [Table 4.4] also supports the above observations.

4.1.2.3c. Isothermal moss loss and hydrazine analysis

The isothermal mass loss studies were carried out at various predetermined temperatures along with the hydrazine analysis at every temperature in programmable electric oven. For complexes with composition, x = 0.0, 0.1, 0.3 and 0.4, the mass loss of 3.56 % - 4.44 % was observed from room temperature to 75°C, but hydrazine analysis showed increase in the hydrazine content [Table 4.4] which indicated the loss of volatile adsorbed species including moisture, while for complexes with composition, x = 0.2 and 0.5, the mass loss observed upto 75°C was comparatively smaller which indicated low concentration of adsorbed species. When these precursors were heated to 100°C, the mass loss observed corresponds to loss of about one hydrazine as can be seen from decrease in hydrazine content [Table 4.4].

Table 4.4. Total mass loss and isothermal mass loss studies data of hydrazinated mixed nickel manganese zinc ferrous fumarate complexes, $Ni_{0.5-x}Mn_xZn_{0.5}Fe_2(C_4H_2O_4)_3.6N_2H_4$ ($x = 0.0\text{-}0.5$)

x	Total mass loss / %		Isothermal mass loss studies / %, hydrazine content / %			
	Pyrolysis in air (Obs.)	Calc.	RT - 75 / °C	75 - 100 / °C	100 - 125 / °C	125 - 150 / °C
0.0	67.41	66.44	4.21 / 28.75	5.26 / 23.78	1.60 / 20.66	56.76 / complex decomposed
0.1	66.99	66.47	4.44 / 28.21	5.53 / 23.40	1.65 / 23.76	53.51 / complex decomposed
0.2	67.26	66.50	2.26 / 27.23	5.15 / 24.43	1.10 / 23.60	58.41 / complex decomposed
0.3	67.53	66.54	3.56 / 28.13	4.67 / 22.70	1.51 / 21.56	54.93 / complex decomposed
0.4	66.99	66.57	4.32 / 28.32	5.12 / 24.45	1.72 / 18.40	57.91 / complex decomposed
0.5	67.15	66.68	2.44 / 27.85	4.63 / 22.46	1.53 / 20.54	56.75 / complex decomposed

On further heating these precursors upto temperature of 125°C, a marginal mass loss was observed along with the decrease of hydrazine content indicating continuous dehydrazination but when the temperature was slowly raised above 125°C, the complexes were found to undergo combustion which was self propagating and autocatalytic.

4.2. Characterization of 'as synthesized' $Ni_{0.5-x}Mn_xZn_{0.5}Fe_2O_4$ ($x = 0.0$-0.5) ferrites

The end products (as synthesized ferrites) obtained by thermolysis of hydrazinates of mixed nickel manganese zinc ferrous fumarate precursors in air were characterized by X-ray diffraction, thermal analysis, FTIR spectroscopy, Mössbauer spectroscopic studies and TEM measurements.

4.2.1. X-ray diffraction studies

The X-ray powder diffraction patterns of the 'as synthesized' ferrite powders are represented in the Fig. 4.3. The XRD patterns do not show any additional peaks corresponding to secondary phases but a small peak around 32° observed in few patterns is due to the unburned carbon which decomposes on heating at 500°C. The broadening observed for the peaks is indicative of their nanosize nature. The interplanar distance for each lattice '*hkl*' planes were calculated using Bragg's equation given in the section 2.3.4. The observed and calculated values of interplanar distances show good agreement. The lattice parameter '*a*' was calculated for each plane using the relation 2.4 given in section 2.3.4. The Fig. 4.4a represents the variation of lattice parameter '*a*' with Mn substitution. The lattice parameter shows linear increase with increasing Mn substitution which is in accordance with the

Vegard's law [198]. This behavior has been attributed to the replacement of smaller Ni^{2+} ions (0.70 A°) by larger Mn^{2+} ions (0.82 A°) in the crystal lattice of spinel ferrite.
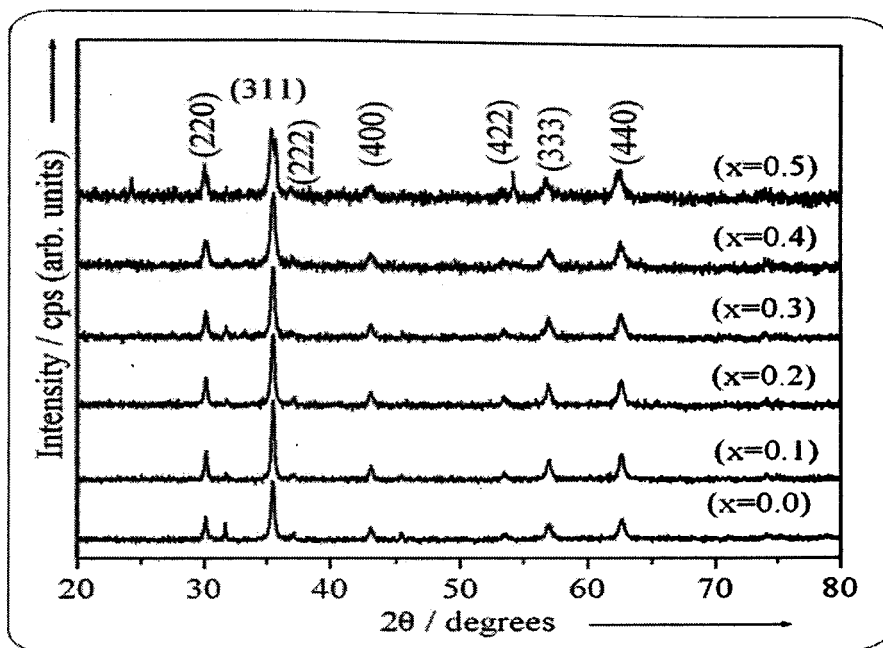
Fig.4.3. XRD pattern of 'as synthesized' $Ni_{0.5-x}Mn_xZn_{0.5}Fe_2O_4$ (x = 0.0-0.5) ferrites

Thus, the introduction of Mn^{2+} ions in lattice causes the expansion of unit cell while preserving the overall cubic symmetry. The lattice parameters obtained from X-ray diffraction measurements were found to be in the range 8.3850 A° to 8.4404 A° [Table 4.5] which matches closely with the reported values for $Ni_{0.5-x}Mn_xZn_{0.5}Fe_2O_4$ (x = 0.0-0.5) ferrites system [107]. The X-ray density was obtained using equation number 2.5 given in the section 2.3.4, while the bulk density was calculated considering the cylindrical shape of the pellet using the relation number 2.6 given in the same section. The percentage porosity of the ferrites was calculated using the X-ray (ρ_{X-ray}) and bulk densities (ρ_{X-exp}) as per the relation number 2.7 from section 2.3.4. It was observed that both X-ray and bulk density decreases (Fig. 4.4b), while the porosity increases with increasing Mn substitution. The decrease in the density is

181

attributed to the substitution of heavier NiO (6.72 g/cc) by the lighter MnO (5.37 g/cc) in the spinel lattice and the increase in porosity is due to the effect of decrease in both X-ray and bulk density.
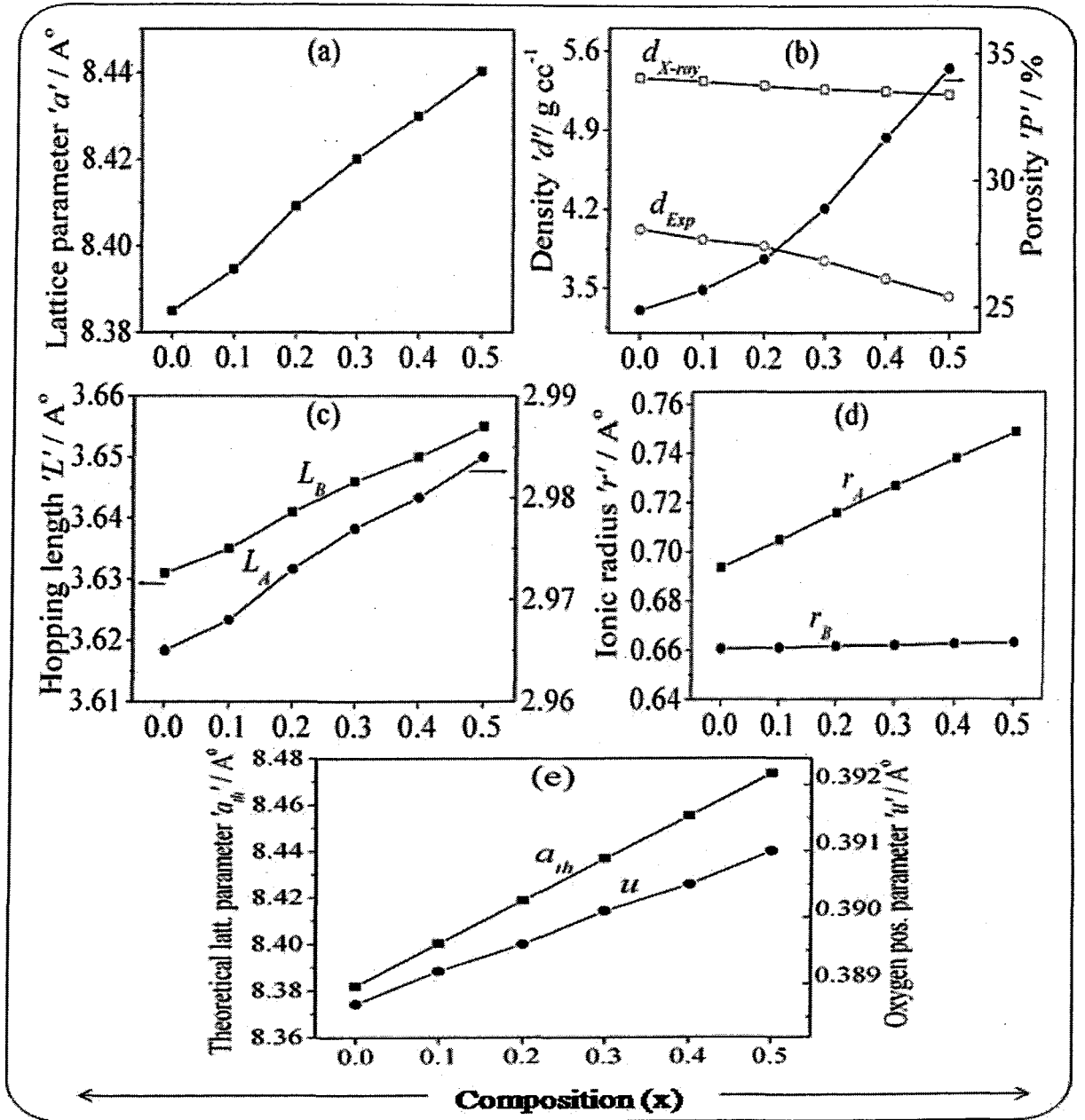
Fig.4.4. Variation of (a) lattice parameter, (b) density and porosity, (c) hopping length, (d) ionic radius, (e) theoretical lattice parameter and oxygen position parameter with Mn substitution of 'as synthesized' $Ni_{0.5-x}Mn_xZn_{0.5}Fe_2O_4$ (x = 0.0-0.5) ferrites.

The crystallite size was calculated from most intense XRD peaks using Debye-Scherrer equation 2.8 given in the section 2.3.4. The average crystallite size was observed in the range 19 nm to 28 nm [Table 4.5] which points towards the nanocrystalline nature of these 'as synthesized' $Ni_{0.5-x}Mn_xZn_{0.5}Fe_2O_4$ (x = 0.0-0.5) ferrites. The surface area of 'as synthesized' $Ni_{0.5-x}Mn_xZn_{0.5}Fe_2O_4$ (x = 0.0-0.5) obtained from BET measurement was found to be in the range of 28.6 m^2 to 47.5 m^2. These high values of surface area are due to the combine effect of decrease in the particle size and increase in porosity with increasing Mn content.

Table 4.5. Lattice constant 'a', density 'd', porosity 'P', particle size 't', surface area 'SA', hopping lengths in tetrahedral 'L_A' and octahedral 'L_B' site of 'as synthesized' $Ni_{0.5-x}Mn_xZn_{0.5}Fe_2O_4$ (x = 0.0-0.5) ferrite samples

x	a / A°	d / gcc^{-1}		P / %	t / nm		SA / m^2	L_A / A°	L_B / A°
		X-ray	bulk		XRD	TEM			
0.0	8.3850	5.36	4.02	24.9	28.1	15-30	28.6	3.631	2.965
0.1	8.3946	5.33	3.93	25.7	27.6	15-40	33.4	3.635	2.968
0.2	8.4091	5.29	3.87	26.9	26.4	12-40	43.7	3.641	2.973
0.3	8.4201	5.26	3.74	28.9	24.0	16-50	47.5	3.646	2.977
0.4	8.4299	5.24	3.58	31.7	19.4	10-27	44.5	3.650	2.980
0.5	8.4404	5.21	3.42	34.4	24.0	12-42	44.8	3.655	2.984

The unit cell of cubic spinel ferrites is known to contain 64 tetrahedral sites and 32 octahedral sites. The metal ions occupy only 8 tetrahedral sites and 16 octahedral sites. The

distance between the magnetic ions (hopping length) in tetrahedral 'L_A' and octahedral 'L_B' sites in the spinel lattice were calculated by using equation number 2.9 and 2.10 given in the section 2.3.4 of chapter 2. The variation of hopping lengths (L_A, L_B) with Mn substitution is represented in Fig. 4.4c. Both L_A and L_B increases with increasing Mn content [Table 4.5], which is attributed to the increase in lattice parameter. The mean ionic radius of the tetrahedral site 'r_A' and octahedral site 'r_B' was calculated from the revised values of ionic radii of metal ions [174] using equation number 2.11 and 2.12, respectively mentioned in the section 2.3.4. These calculations were based on the cation distributions given in the Table 4.6. The mean ionic radius of tetrahedral sites 'r_A' increases sharply with increasing Mn substitution while, the mean ionic radius of octahedral site 'r_B' displays marginal increase (Fig. 4.4d). This behavior can be explained considering the preference of metal cations for tetrahedral (A) and octahedral [B] sites in spinel lattice. The Fe^{3+} ions and Mn^{2+} ions exist at both tetrahedral (A) and octahedral [B] sites, but Mn^{2+} ions prefer tetrahedral (A) sites while Fe^{3+} ions shows more preference for octahedral [B] sites. It is estimated that nearly about 80 % of Mn^{2+} ions occupy tetrahedral (A) sites, while remaining 20 % goes to octahedral [B] sites [197]. It is also known that Zn^{2+} and Ni^{2+} ions has strong preference for tetrahedral (A) and octahedral [B] sites respectively, in bulk ferrite materials. However, in ultrafine state considerable Zn^{2+} ions concentrations exists in octahedral [B] and Ni^{2+} ions in tetrahedral (A) sites which is against their site preferences [198]. When Mn^{2+} ions are substituted for Ni^{2+} ions in the spinel lattice, it forces the Fe^{3+} ions from tetrahedral (A) sites to octahedral [B] sites at the same time Zn^{2+} ions from octahedral [B] sites are transferred to tetrahedral (A) sites. The outcome of this rearrangement is sharp increase in tetrahedral site ionic radius 'r_A' and marginal increase in octahedral site ionic radius 'r_B'.

Table 4.6. Theoretical lattice constant 'a_{th}', ionic radii at tetrahedral site 'r_A', ionic radii at octahedral site 'r_B', tetrahedral bond 'A-O', octahedral bond 'B-O', tetrahedral edge 'A-E', octahedral edge 'B-E'(shared), octahedral edge 'B-E' (unshared), cation distribution and oxygen position parameter 'u' of 'as synthesized' $Ni_{0.5-x}Mn_xZn_{0.5}Fe_2O_4$ (x = 0.0-0.5) ferrite samples

x	a_{th} /A°	r_A / A°	r_B / A°	d_{A-O} / A°	d_{B-O}/ A°	d_{A-E} / A°	d_{B-E} / A°		u / A°	cation distribution	
							shared	unshared		(A-site)	[B-site]
0.0	8.3820	0.6936	0.6607	2.014	1.988	3.288	2.639	2.972	0.3887	$(Zn_{0.418}Ni_{0.086}Fe_{0.512})$	$[Zn_{0.082}Ni_{0.414}Fe_{1.504}]O_4$
0.1	8.4004	0.7048	0.6611	2.025	1.988	3.307	2.633	2.980	0.3892	$(Mn_{0.067}Zn_{0.422}Ni_{0.068}Fe_{0.443})$	$[Mn_{0.033}Zn_{0.078}Ni_{0.322}Fe_{1.557}]O_4$
0.2	8.4188	0.7159	0.6616	2.036	1.990	3.324	2.629	2.987	0.3896	$(Mn_{0.125}Zn_{0.431}Ni_{0.056}Fe_{0.389})$	$[Mn_{0.075}Zn_{0.069}Ni_{0.244}Fe_{1.611}]O_4$
0.3	8.4369	0.7269	0.6620	2.047	1.991	3.343	2.623	2.994	0.3901	$(Mn_{0.185}Zn_{0.450}Ni_{0.042}Fe_{0.323})$	$[Mn_{0.115}Zn_{0.050}Ni_{0.158}Fe_{1.677}]O_4$
0.4	8.4452	0.7380	0.6625	2.058	1.992	3.360	2.619	3.001	0.3905	$(Mn_{0.244}Zn_{0.472}Ni_{0.013}Fe_{0.271})$	$[Mn_{0.156}Zn_{0.028}Ni_{0.087}Fe_{1.729}]O_4$
0.5	8.4736	0.7489	0.6631	2.069	1.993	3.379	2.612	3.008	0.3910	$(Mn_{0.306}Zn_{0.479}Fe_{0.215})$	$[Mn_{0.194}Zn_{0.021}Fe_{1.785}]O_4$

The theoretical lattice parameter 'a_{th}' was calculated from mean ionic radii of tetrahedral (A) and octahedral [B] sites using equation 2.13 given in the section 2.3.4 of chapter 2. The oxygen position parameter 'u' was calculated using the radius of oxygen ion (R_O =1.32 A°) and the mean ionic radii of tetrahedral site 'r_A' in the expression number 2.14 given in the section 2.3.4. The Fig. 4.4e represents the variation of theoretical lattice parameter 'a_{th}' and oxygen position parameter 'u' with increasing Mn substitution. The theoretical lattice parameter 'a_{th}' increases from 8.3820 A° (x = 0.0) to 8.4736 A° (x = 0.5) which is in fair agreement with the lattice parameter 'a' obtained from XRD powder pattern of the ferrites. The oxygen position parameter 'u' shows increase from 0.3887 A° to 0.3910 A° with increasing Mn content. The higher values of oxygen position parameter 'u' have been reported in most of the substituted spinel ferrites [199-200] which suggests that the oxygen ions are displaced in such a way that in the A-B interaction, the distance between A and O ions is increased, while that between B and O is decreased leading to a decrease in the A–A interaction and an increase in the B-B interactions. Increased concentration of the Mn^{2+} ions into the A sub-lattice makes it to expand to accommodate these ions which creates oxygen vacancies in the tetrahedral (A) sites, thereby increasing the trigonal distortion of the octahedral [B] site oxygen coordination resulting in high values for oxygen position parameter 'u'.

The tetrahedral bond length 'A-O', octahedral bond length 'B-O', tetrahedral edge length 'A-E', octahedral edge length 'B-E' (shared) and octahedral edge length 'B-E' (unshared) were calculated using the theoretical lattice parameters 'a_{th}' and oxygen position parameter 'u' values in equation number 2.15, 2.16, 2.17, 2.18 and 2.19, respectively, given in section 2.3.4 of chapter 2. The increase in tetrahedral bond length 'A-O', octahedral bond

186

length '*B-O*' tetrahedral edge length '*A-E*' and octahedral edge length '*B-E*' (unshared) with increasing Mn substitution can be directly related to increase of mean ionic radii (r_A and r_B) of both tetrahedral (*A*) and octahedral [B] interstices in 'as synthesized' $Ni_{0.5-x}Mn_xZn_{0.5}Fe_2O_4$ (x = 0.0-0.5) ferrites lattice.

4.2.2. FTIR spectral analysis

The FTIR spectra of 'as synthesized' $Ni_{0.5-x}Mn_xZn_{0.5}Fe_2O_4$ (x = 0.0-0.5) ferrites are represented in the Fig. 4.5.
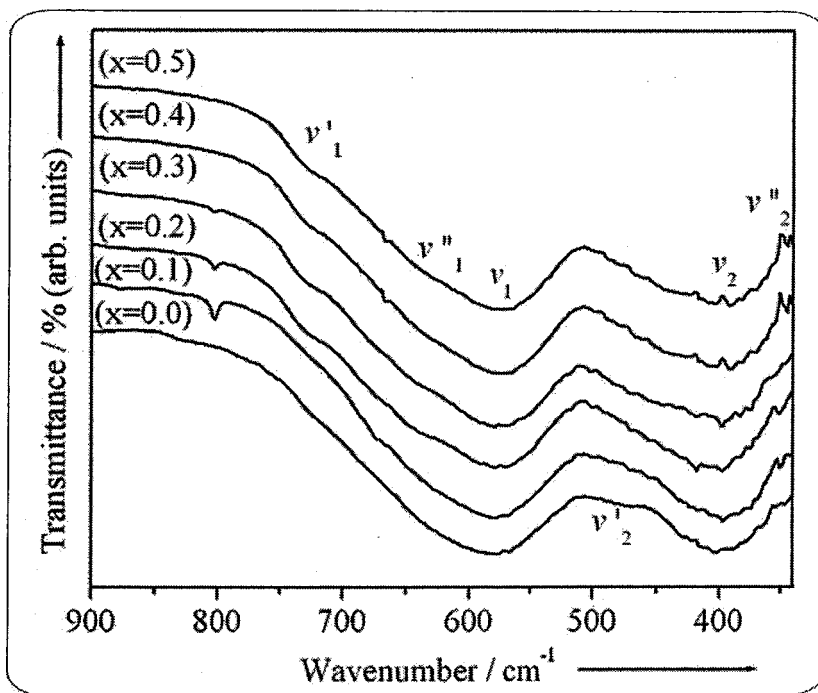
Fig.4.5. FTIR spectra of 'as synthesized' $Ni_{0.5-x}Mn_xZn_{0.5}Fe_2O_4$ (x = 0.0-0.5) ferrites

Two principal absorption bands were observed in the frequency region from 1000 cm^{-1} to 340 cm^{-1} for all the 'as synthesized' $Ni_{0.5-x}Mn_xZn_{0.5}Fe_2O_4$ (x = 0.0-0.5) ferrites.

Table 4.7. FTIR absorption bands of 'as synthesized' $Ni_{0.5-x}Mn_xZn_{0.5}Fe_2O_4$ ($x = 0.0$-0.5) ferrites

Sites	Bands	FTIR absorption frequencies of 'as synthesized' $Ni_{0.5-x}Mn_xZn_{0.5}Fe_2O_4$ ferrites / cm^{-1}						
		0.0	0.1	0.2	0.3	0.4	0.5	M^{n+}---O^{2-}
Tetrahedral	v_1	582	579	579	572	566	561	Fe^{3+}---O^{2-}
	v'_1	---	---	~730	~730	~730	~730	Mn^{2+}---O^{2-}
	v''_1	---	---	~640	~640	~640	~640	Zn^{2+}---O^{2-}
Octahedral	v_2	402		418	418	404	404	Fe^{3+}---O^{2-}
			396	398	398	397	397	
	v'_2	470	471	470	469	469	---	Ni^{2+}---O^{2-}
	v''_2	345	349	351	345	346	346	Zn^{2+}---O^{2-}

188

The high frequency band (v_1) in the region 582 cm^{-1} to 561 cm^{-1} [Table 4.7] has been assigned to the Fe^{3+}---O^{2-} stretching vibration in tetrahedral sites and low frequency band (v_2) in the region 418 cm^{-1} to 396 cm^{-1} assigned to Fe^{3+}---O^{2-} stretching vibrations of octahedral groups [167]. The difference in the positions and intensities of v_1 and v_2 band was expected because of different Fe^{3+}--O^{2-} bond distances in the tetrahedral (A) and octahedral [B] interstices, as the vibrational frequencies varies with the cation mass, M^{n+}–O^{2-} distance and the bond strength [201]. Besides, these two principal absorption bands few weak bands, are also observed in the IR spectra of these 'as synthesized' ferrites. The relatively weak shoulder (v'_1) which appears at ~ 730 cm^{-1} with increasing Mn substitution has been assigned to the vibration of Mn^{2+}--O^{2-} tetrahedral bonds [202]. Another weak shoulder (v''_1) observed at about ~ 640 cm^{-1} has been attributed to Zn^{2+}--O^{2-} tetrahedral groups. The increase in the intensity observed for this shoulder with increasing Mn substitution can be explained considering the redistribution of cations between the tetrahedral (A) and octahedral [B] interstices. At lower content of Mn ($x < 0.2$) , relatively high concentration of Fe^{3+} ions exists at tetrahedral (A) sites as a result, the band due to Zn^{2+}--O^{2-} tetrahedral groups (v''_1) merges with main absorption (v_1) band and is not clearly visible for the compositions, $x < 0.3$. With increase in Mn substitution, the concentration of Mn^{2+} ions at tetrahedral (A) sites increases thereby pushing the Fe^{3+} ions into octahedral [B] sites. This causes the decrease in the intensity of v_1 band as a result of which the weak v''_1 shoulder starts appearing slowly for higher Mn substitutions ($x > 0.3$). Mohammad *et al.* [203] have observed similar shoulder in the IR spectra of Mg-Zn ferrites while, Deraz [204] have reported similar results for the alumina-doped zinc ferrites. They have assigned this shoulder to both Fe^{2+}--O^{2-} and Zn^{2+}--O^{2-} tetrahedral bonds. Since, the Mössbauer spectral results of 'as synthesized' Ni$_{0.5}$-

$_x$Mn$_x$Zn$_{0.5}$Fe$_2$O$_4$ (x = 0.0-0.5) confirmed the absence of Fe^{2+} ion, this shoulder can be been assigned to Zn^{2+}--O^{2-} tetrahedral groups. A weak band at about ~ 470 cm^{-1} was observed for all the composition (except for composition, x = 0.5) can be assigned to the Ni^{2+}-- O^{2-} octahedral groups [107]. The IR peak observed in the region 351 cm^{-1} to 345 cm^{-1} have been assigned to Zn^{2+}--O^{2-} stretching vibrations [107, 205-206]. The slight deviations observed in the peak position are mainly due to the factors like concentration of dopant, synthetic technique, grain size and density [207-209]. The absorption frequency and intensity of v_1 band decreases as the Mn^{2+} ions concentration is increased, whereas the intensity of v_2 band increases, but there is hardly any change observed in its absorption frequency. These observations are explained considering the site preference and distribution of cations between tetrahedral and octahedral sites. The substitution of Mn^{2+} ions (r = 0.82 A$^{\circ}$) for Ni^{2+} ions (r = 0.70 A$^{\circ}$) in spinel lattice displaces Fe^{3+} ions (r = 0.645 A$^{\circ}$) from tetrahedral to octahedral sites as per their site preferences. The net result of this displacement is increase in mean ionic radius 'r_A' and decrease in the concentration of Fe^{3+} ions at tetrahedral (A) sites, which results in the decrease in the absorption frequencies and intensities of v_1 band. For v_2 band since, the substitution of Mn^{2+} ions do not affect much the ionic radius of octahedral 'r_B' site, there was hardly any change in absorption frequency of v_2 band but its intensity increases due to increase of Fe^{3+} ions concentration at octahedral [B] sites. Considering the IR results and above discussion, it can be concluded that the expansion of tetrahedral (A) site is larger than that of octahedral [B] site. Thus, the increase observed in the cell dimensions is in accordance with the results obtained from X-ray diffraction and Mössbauer spectroscopic studies.

4.2.3. TG and DTA measurements

The TG and DTA curves of 'as synthesized' ferrites (Fig. 4.6) display two mass loss regions. The initial mass loss region observed upto 100°C was due to the loss of physisorbed species including moisture on these samples. It is indicated by endotherms in the corresponding DTA profiles. The high adsorption tendency of the 'as synthesized' spinel ferrite samples is justified by their high porosity, nanocrystalline nature and high surface area. The next region of marginal mass loss was from 400°C to 500°C is attributed to oxidation of residual carbon as indicated by broad exotherm in DTA profiles in this region. Thus, the stable regions in TG and DTA above 500°C confirms absence of any metastable phases and hence the purity of 'as synthesized' $Ni_{0.5-x}Mn_xZn_{0.5}Fe_2O_4$ ($x = 0.0$-0.5) ferrites.
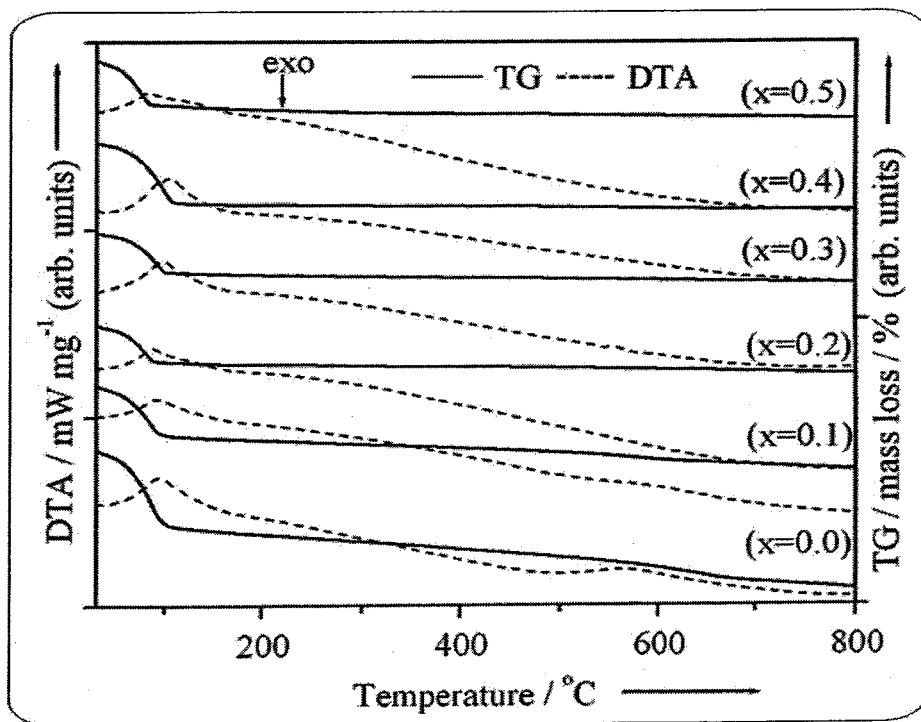
Fig.4.6. TG and DTA profiles of 'as synthesized' $Ni_{0.5-x}Mn_xZn_{0.5}Fe_2O_4$ ($x = 0.0$-0.5) ferrites

4.2.4. TEM measurements

The TEM micrographs of the 'as synthesized' $Ni_{0.5-x}Mn_xZn_{0.5}Fe_2O_4$ (x = 0.0-0.5) ferrites are presented in the Fig. 4.7. It is clear from the TEM images that all the 'as synthesized' spinel ferrites are nanocrystalline in nature with particle size in the range 10 nm to 50 nm. The ferrite nanoparticles are polydispersed and display low tendency towards agglomeration, hence occur as loose agglomerates.
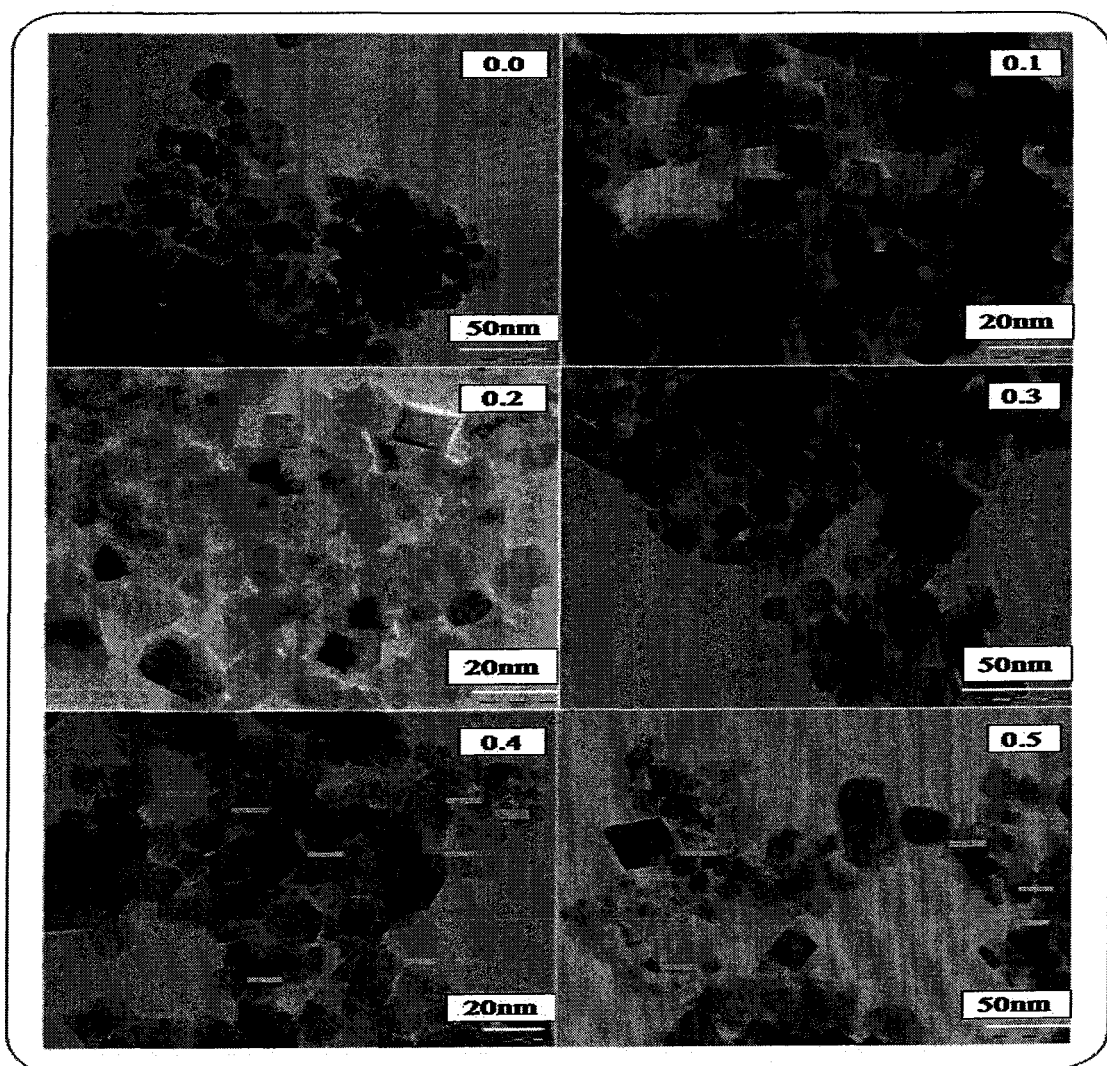
Fig.4.7. TEM micrograph of 'as synthesized' $Ni_{0.5-x}Mn_xZn_{0.5}Fe_2O_4$ (x = 0.0-0.5) ferrites

The effect of Mn substitution on grain growth in ferrites, as reported [107] is not observed in our samples prepared using metal carboxylate hydrazinate precursor technique. This may be due to the fact that the exothermicity generated during autocatalytic decomposition has dominating effect on particle size of these ferrites than Mn substitution. The particle size determined using Scherrer method from XRD measurements are in the range with those obtained from TEM micrographs [Table 4.5]. The selective area electron diffraction (SAED) patterns images of 'as synthesized' $Ni_{0.5-x}Mn_xZn_{0.5}Fe_2O_4$ (x = 0.0-0.5) ferrite nanoparticles are presented in the Fig. 4.8. The SAED pattern indicates good crystallinity of 'as synthesized' $Ni_{0.5-x}Mn_xZn_{0.5}Fe_2O_4$ (x = 0.0-0.5) ferrite nanoparticles, since the pattern exhibit distinct rings.
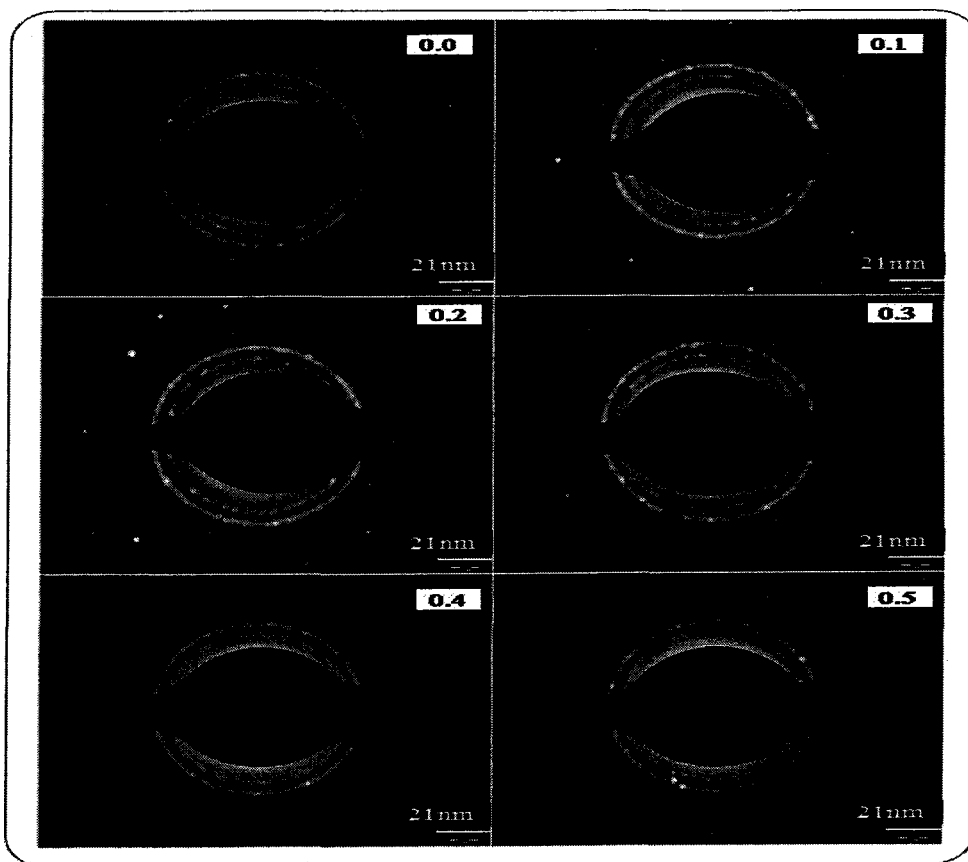
Fig.4.8. SAED pattern of 'as synthesized' $Ni_{0.5-x}Mn_xZn_{0.5}Fe_2O_4$ (x = 0.0-0.5) ferrites

4.2.5. Mössbauer spectral studies

The Mössbauer spectra of 'as synthesized' $Ni_{0.5-x}Mn_xZn_{0.5}Fe_2O_4(x = 0.0-0.5)$ ferrites is

represented in Fig. 4.7. The various Mössbauer effect parameters such as magnetic hyperfine

field values 'H_{hf}', isomer shift 'δ', quadrupole splitting 'Δ', linewidth 'Γ' and relative areas

'R_A' of tetrahedral and octahedral sites of Fe ions are summarized in Table 4.8. In the mixed

Ni-Mn-Zn-ferrites, Zn^{2+} ions have strong preference for the tetrahedral (A) sites, while Ni^{2+}

ions have strong preference for the octahedral [B] sites. The Mn^{2+} ions also occupy octahedral

[B] sites albeit with small preference. The Mössbauer spectra of 'as synthesized' Mn

substituted Ni-Zn ferrites exhibit a superposition of three zeeman sextets due to ferromagnetic

particles and a doublet due to superparamagnetic behaviour of nano-sized particles [217-218].
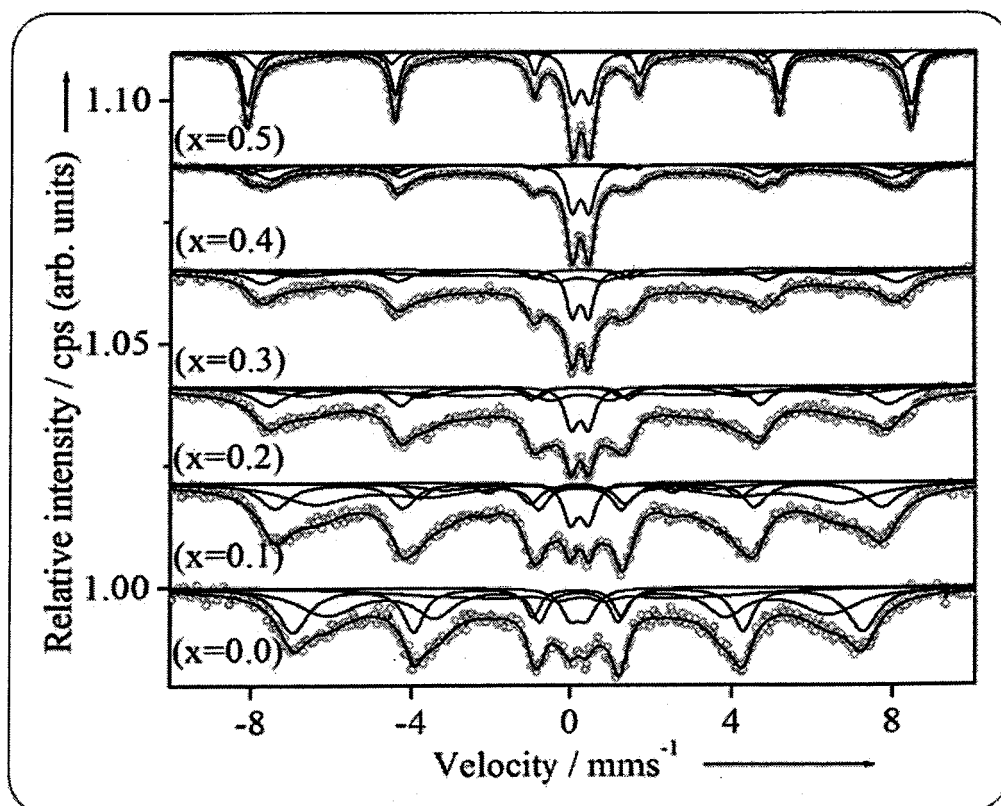
Fig.4.9. Room temperature Mössbauer spectra of 'as synthesized' $Ni_{0.5-x}Mn_x Zn_{0.5}Fe_2 O_4$

($x = 0.0-0.5$) ferrites

Table 4.8. Room temperature Mössbauer effect parameters: isomer shift 'δ', quadrupole splitting 'Δ', hyperfine field 'H_{hf}' relative are 'R_A' and inner line width 'Γ' of 'as synthesized' $Ni_{0.5-x}Mn_xZn_{0.5}Fe_2O_4$ ($x = 0.0$-0.5) ferrites samples

Sample	Site	*δ / mms^{-1}	Δ / mms^{-1}	H_{hf}/ Tesla	R_A / %	Γ/mms^{-1}
0.0	Sextet 1, (A)	0.306	-0.014	38.87	38.15	0.481
	Sextet 2, [B]	0.281	0.011	44.04	30.79	0.456
	Sextet 2, [B_1]	0.357	-0.067	22.55	27.49	0.810
	Doublet	0.319	0.418	---	3.57	0.560
0.1	Sextet 1, (A)	0.293	0.030	40.27	24.85	1.79
	Sextet 2, [B]	0.289	-0.004	46.67	28.07	0.491
	Sextet 2, [B_1]	0.364	-0.156	36.53	44.59	0.750
	Doublet	0.354	0.455	---	2.49	0.422
0.2	Sextet 1, (A)	0.319	-0.006	42.06	23.45	0.522
	Sextet 2, [B]	0.306	-0.033	47.92	22.46	0.455
	Sextet 2, [B_1]	0.397	0.101	28.88	49.92	0.813
	Doublet	0.341	0.431	---	4.17	0.393
0.3	Sextet 1, (A)	0.274	-0.022	21.93	17.14	0.382
	Sextet 2, [B]	0.329	-0.045	49.01	20.27	0.479
	Sextet 2, [B_1]	0.333	0.011	21.92	52.17	0.763
	Doublet	0.343	0.406	---	5.42	0.334
0.4	Sextet 1, (A)	0.375	-0.197	50.83	7.604	0.201
	Sextet 2, [B]	0.309	0.033	50.00	31.23	0.268
	Sextet 2, [B_1]	0.317	-0.057	40.45	47.04	1.514
	Doublet	0.346	0.421	---	14.12	0.342
0.5	Sextet 1, (A)	0.254	0.026	49.56	7.17	0.111
	Sextet 2, [B]	0.376	-0.212	51.31	44.95	0.241
	Sextet 2, [B_1]	0.351	-0.098	45.91	32.51	0.102
	Doublet	0.355	0.416	---	15.37	0.351

*Isomer shift values are relative to α-Fe metal foil (δ = 0.0 mm/s), (): tetrahedral, []: octahedral

In general, a system of magnetic nanoparticles becomes single-domain below a critical size. In the single-domain state, these nanoparticles become superparamagnetic with a blocking temperature (T_B). Below T_B, the magnetization of such superparamagnetic nanoparticles fluctuates spontaneously with a relaxation time $(\tau) \leq 10^{-9}$ sec. As a result, in the Mössbauer spectrum, magnetic splitting disappears resulting in a superparamagnetic doublet, as observed for 'as synthesized' $Ni_{0.5-x}Mn_xZn_{0.5}Fe_2O_4$ ($x = 0.0$-0.5) ferrites [218-219]. In nanoferrites, the H_{hf} values for both tetrahedral (A) and octahedral $[B$ and $B_1]$ sites are close to each other at higher Mn substitution ($x = 0.5$). This is because, the tetrahedral (A) and octahedral $[B$ and $B_1]$ sub-lattices are magnetically coupled and hence the spins at these sites fluctuate in unison [220]. But, the H_{hf} values at the octahedral $[B_1]$ sites are much lower as compared to tetrahedral (A) at lower Mn substitution ($x \leq 0.4$), which is due to a much faster relaxation process. The isomer shift 'δ' values for all the ferrites in the range 0.254 mm/s to 0.375 mm/s for tetrahedral (A), 0.281 mm/s to 0.376 mm/s for octahedral $[B]$ and 0.317 mm/s to 0.397 mm/s for octahedral $[B_1]$ with respect to α-Fe metal foil ($\delta = 0.00$ mm/s) were observed. It indicates that, iron is in Fe^{3+} high spin ionic state [221]. The observed values of isomer shift are comparatively less than the expected value of 0.8 mm/s for the Fe^{2+} ion, which indicates that the formation of Fe^{2+} ion do not occurs during ferritization [222-224]. Hence, the sample maintains stiochiometry during their formations. The isomer shift 'δ' value of sextet A and sextet B increases with Mn substitution (Fig. 4.10a). This shows that bond length (Fe^{3+}-- O^{2-}) of tetrahedral and octahedral sites increases with Mn substitutions. Except for the supreparamagnetic (SP) doublets ($\Delta_D = 0.406$ mm/s to 0.455 mm/s, $\delta_D = 0.319$ mm/s to 0.355 mm/s and $R_A = 2.49$ % - 15.37 %), the quadrupole splitting 'Δ' values were nearly 0.0 mm/s [Table 4.8], suggesting that Fe^{3+} ions show cubic symmetry of polyhedron. The

variation in the quadrupole splitting 'Δ' with Mn substitution of different Fe^{3+} ion sites is

shown in Fig. 4.10b. The comparatively higher value of quadrupole splitting 'Δ' for doublet

was attributed to an increase in the asymmetry around the iron ions.The variation in relative

area 'R_A' with Mn substitution of different Fe^{3+} ion sites is shown in Fig. 4.10c.
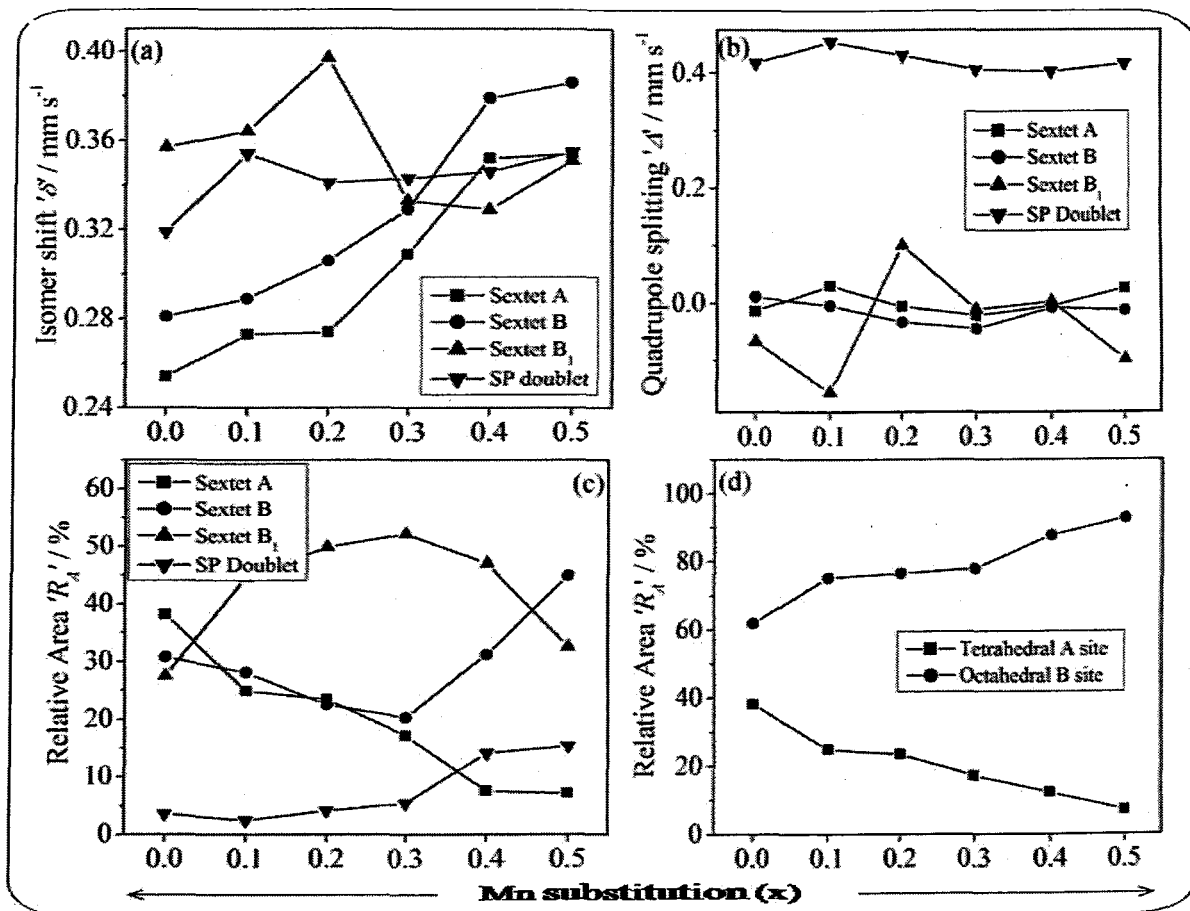
Fig.4.10. Variation of room temperature Mössbauer effect parameters a) isomer shift 'δ',

b) quadrupole splitting 'Δ', c) relative area 'R_A' (Sextet A, B, B_1 and SP doublet) and d)

relative area 'R_A' (tetrahedral 'A' and octahedral 'B' site) with Mn substitution (x) of 'as

synthesized' $Ni_{0.5-x}Mn_xZn_{0.5}Fe_2O_4$ (x = 0.0-0.5) ferrites

The relative area of sextet B_1 and SP doublet were found to increase whereas the

relative area of sextet A and sextet B decreases with Mn substitutions. The isomer shift 'δ'

values of SP doublet are between 0.319 mm/s to 0.355 mm/s. These values are consistent with iron ions in trivalent state (octahedral). The final relative area of tetrahedral (A) site (sextet A) and octahedral [B] site (sextet B + sextet B_1 + SP doublet) is shown in the Fig. 4.10 d. It is clear from the Fig. 4.10d, that the relative area of tetrahedral (A) site (R_A- A site) decreases (from 38.15 % - 7.17 %) whereas, the relative area of octahedral [B] site (R_A- B site) increases (from 61.85 % - 92.83%) with increasing Mn substitutions.

4.3. Solid state properties of 'as synthesized' $Ni_{0.5-x}Mn_xZn_{0.5}Fe_2O_4$ (x = 0.0-0.5) ferrites

The studies on the solid state properties such as dc resistivity, thermoemf, ac susceptibility, dielectric and magnetic properties were carried out to investigate the effect of Mn substitution on these properties of Ni-Zn ferrites.

4.3.1. DC resistivity measurement

The mechanism of electrical conduction in ferrites involves hopping of electrons between cations of same metal present in different oxidation states [225] discussed in detail in section 3.3.1 of chapter 3. It was also reported that besides electron hopping, other factors such as particle size, grain boundaries, nature and concentration of other substituents present are known to affect the conductivities of ferrites [227-228]. The conductivities of nanocrystalline ferrite materials were also found to be affected by moisture content which results from their high porosity and low green density. The temperature dependence of the dc resistivity (log ρ) for all 'as synthesized' $Ni_{0.5-x}Mn_xZn_{0.5}Fe_2O_4$ (x = 0.0-0.5) ferrite nanoparticles is shown in Fig. 4.11. The plot displays two distinct regions of conductivity. In the first region from room temperature to 393 K to 403 K resistivities of the order of ~10^6

198

Ωcm to 10^9 Ωcm was observed depending upon the composition of the nanosize ferrites. With increase in temperature in this region, the resistivity increases and reaches maximum in the temperature range of ~ 373 K to 388 K. This behavior is attributed to the presence of open porosity, loose agglomeration and entrapped moisture inside the pores of the powders [229-230].
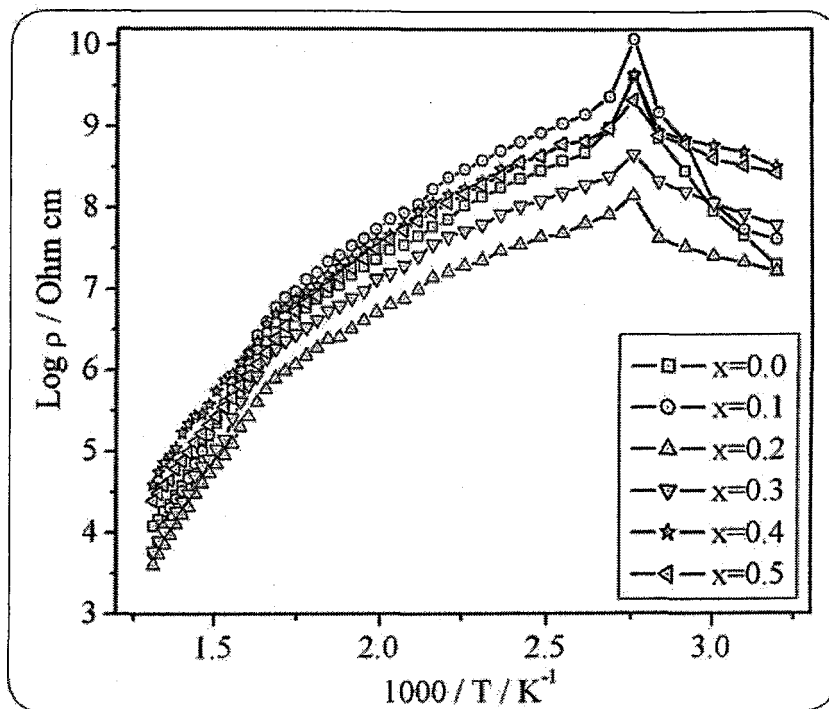
Fig.4.11. Plot of log resistivity against 10^3 / T of 'as synthesized' $Ni_{0.5-x}Mn_xZn_{0.5}Fe_2O_4$ (x = 0.0-0.6) ferrites

The heating from room temperature upto ~383K causes total evaporation of moisture from the samples and therefore, maximum resistivities (ρ = 10^8 Ωcm to 10^9 Ωcm) were observed in the temperature region 373 K to 388 K. The low resistivity behavior at room temperature is resultant of protonic conductivity due to entrapped moisture [231-232]. In the second region above 393 K (Fig. 4.11), the samples exhibits typical negative temperature

coefficient of resistance (NTC) behaviour of ferrites [233] and linear plots were obtained. The plots were straight lines of two different slopes indicating that the samples change their magnetic behaviour at Curie temperature (T_c). The resistivity-temperature behavior obeys the equation 2.28 given in the section 2.3.11 of chapter 2. The activation energy of each sample was determined from the slope of the linear plots using the equation number 2.29 describe in section 2.3.11 of chapter 2. In low temperature (ferrimagnetic) region the activation energies in the range 0.305 eV to 0.418 eV were observed while in the high temperature (paramagnetic) region the activation energies were found to be in the range 0.471 eV to 0.731 eV [Table 4.9].

Table 4.9. Activation energies and Curie temperatures of 'as synthesized' $Ni_{0.5-x}Mn_xZn_{0.5}$ Fe_2O_4 ($x = 0.0-0.5$) ferrites

| x | Activation energy (E_a) / eV | | Curie temperature |
	Low temperature region / E_f	High temperature region / E_p	(T_c) / K
0.0	0.418	0.731	633
0.1	0.341	0.714	621
0.2	0.305	0.658	612
0.3	0.336	0.536	599
0.4	0.313	0.489	581
0.5	0.358	0.471	568

In mixed ferrite system like Ni-Mn-Zn ferrites, the activation energy is decided by the hopping probability of electrons and holes among $Fe^{3+} \leftrightarrow Fe^{2+}$, $Mn^{3+} \leftrightarrow Mn^{2+}$ and $Ni^{3+} \leftrightarrow Ni^{2+}$ pairs. The activation energy required for conduction due to electron hopping in ferrites is found to be of the order of 0.4 eV [234]. For hole hopping on the other hand still much energy is needed as compared to electron hopping. The observed values of activation energy suggests, the electronic conduction in the ferromagnetic region, while the conduction in paramagnetic region is due to polaron hoping as it requires higher activation energies (> 0.4 eV). The effect of Mn substitution on room temperature dc resistivity is not clearly seen for 'as synthesized' ferrites indicating that the effect of particle size, porosity and moisture content is more predominant on the resistivity than Mn substitution. The low resistivity at room temperature (10^6 Ωcm to 10^8 Ωcm) suggests that the effect of particle size, porosity and moisture content is more predominant on the resistivity than the effect of Mn substitution.

4.3.2. Thermoemf / Seebeck coefficient measurements

The thermoemf measurements were carried out on 'as synthesized' $Ni_{0.5-x}Mn_xZn_{0.5}Fe_2O_4$ (x = 0.0-0.5) ferrites from 313 K to 723 K. The Seebeck coefficient was calculated using equation 2.30 given in the section 2.3.12 of chapter 2. The variation of the Seebeck coefficient as a function of temperature for some representative 'as synthesized' $Ni_{0.5-x}Mn_xZn_{0.5}Fe_2O_4$ (x = 0.0, 0.1 and 0.5) ferrites is shown in Fig. 4.12. It is clear from Fig. 4.12 that all the samples are degenerate semi conductors [236]. All the samples show a p-type to n-type transition in the temperature region 373 K to 413 K suggesting the change in the conduction mechanism. The values of Seebeck coefficient obtained for 'as synthesized'

$Ni_{0.5-x}Mn_xZn_{0.5}Fe_2O_4$ (x = 0.0-0.5) ferrites are much greater than 100 μV K^{-1}, indicating polaron hopping type of conduction [236].
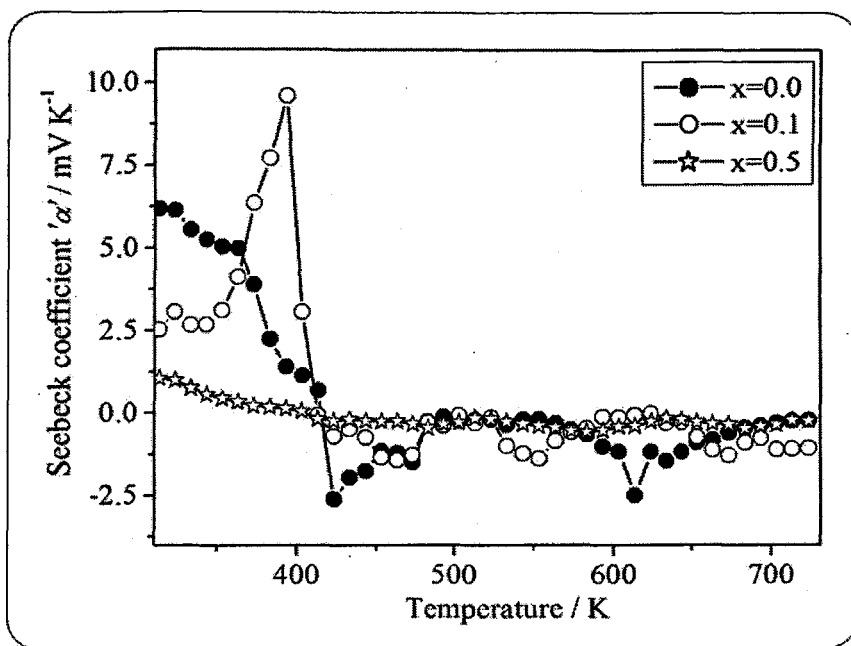
Fig.4.12. Variation of Seebeck coefficient against temperature of some representative 'as synthesized' $Ni_{0.5-x}Mn_xZn_{0.5}Fe_2O_4$ (x = 0.0, 0.1 and 0.5) ferrites

The change in the conduction mechanism in the temperature range 373 K to 413 K may be due to the protonic conductivity at lower temperature which is also observed in the dc resistivity plots.

4.3.3. Dielectric measurements

The dielectric properties of 'as synthesized' $Ni_{0.5-x}Mn_xZn_{0.5}Fe_2O_4$ (x = 0.0-0.5) ferrites were studied in a frequency range from 100 Hz to 10 MHz at room temperature as well as at higher temperatures upto 250°C. The dielectric constant, complex dielectric constant and

dielectric loss tangent were calculated using equation number 2.31, 2.32 and 2.33 respectively, given in the section 2.3.15 of chapter 2.

4.3.3.1. Frequency variation of dielectric properties

The frequency variation of dielectric constant (ε') and complex dielectric constant (ε'') at room temperature, of 'as synthesized' $Ni_{0.5-x}Mn_xZn_{0.5}Fe_2O_4$ (x = 0.0-0.5) ferrites in the frequency range 100 Hz to 10 MHz is presented in Fig. 4.13 (a-b). The dielectric constant of any material, in general, is due to dipolar, electronic, ionic and interfacial polarizations [238]. In a lower frequency region, surface polarization contributes predominantly than electronic or ionic polarization in determining the dielectric properties of ferrite materials [239]. The dispersion in dielectric constant observed in lower frequency region is due to Maxwell-Wagner interfacial type of polarization [239,240] which is well in agreement with Koop's phenomenological theory of dielectrics [29]. According to this model, the dielectric structure is assumed to be composed of two layers; the first layer is composed of well conducting grains separated by thin layer which is composed of relatively poor conducting grain boundaries. This creates inhomogeniety in the dielectric material which results in local accumulation of charge under the influence of an electric field. The electrons reach the grain boundary through hopping and if the grain boundary resistance is high enough, the electrons pile up at the grain boundaries and produce polarization. However, as the frequency of the applied field is increased, the electrons reverse their direction of motion more often. This decreases the probability of electrons reaching the grain boundary and as a result the polarization decreases. Therefore, the dielectric constant decreases with increasing frequency of the applied field. The dielectric constant values are quite low and are in the range of 0.04 to

29.4 at room temperature [Table 4.10] which is about 10^4 times lower than those reported for samples prepared using conventional ceramic method [29,241]. These low dielectric constant values are attributed to homogeneity, better symmetry and small grain size [242]. Small grains have large surface boundaries which act as scattering centres for the flow of electrons thus reducing the interfacial polarization [89].
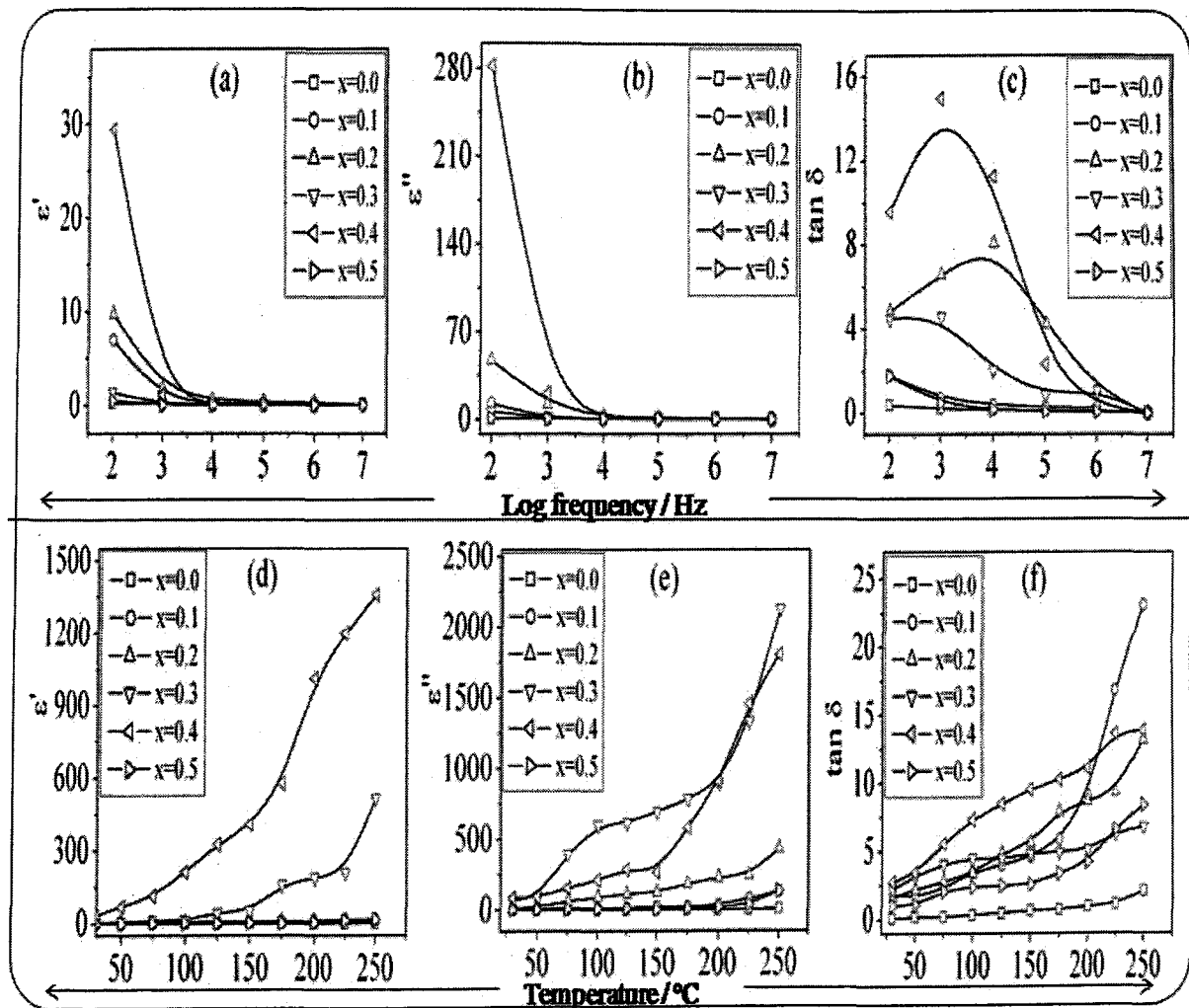
Fig.4.13. Frequency variation of a) dielectric constant (ε'), b) complex dielectric constant (ε"), c) dielectric loss tangent (tan δ) at room temperature and temperature variation of d) dielectric constant (ε') d) complex dielectric constant (ε"), f) dielectric loss tangent (tan δ) at 100 Hz of 'as synthesized' $Ni_{0.5-x}Mn_xZn_{0.5}Fe_2O_4$ (x = 0.0-0.5) ferrites

Table 4.10. Room temperature dielectric characteristics of 'as synthesized' $Ni_{0.5-x}Mn_x$ $Zn_{0.5}Fe_2O_4$ ($x = 0.0$-0.5) ferrites

Dielectric characteristics		x					
		0.0	0.1	0.2	0.3	0.4	0.5
Dielectric	100Hz	1.194	6.97	9.72	1.36	29.4	1.51
constant ($\acute{\epsilon}$)	1kHz	0.135	0.798	1.82	0.16	1.14	0.070
	10kHz	0.104	0.208	0.588	0.080	0.107	0.063
	1MHz	0.075	0.071	0.32	0.041	0.054	0.052
Complex	100Hz	0.072	12.51	47.0	6.11	281.7	0.889
dielectric	1kHz	0.028	0.576	11.94	0.734	20.48	0.033
constant (ϵ'')	10kHz	0.015	0.081	1.71	0.163	1.21	0.011
	1MHz	0.007	0.017	0.35	0.043	0.018	0.002
Dielectric loss	100Hz	0.369	1.80	4.84	4.49	9.57	1.76
tangent	1kHz	0.21	0.723	6.57	4.59	14.9	0.468
(tan δ)	10kHz	0.146	0.386	8.081	2.053	11.26	0.168
	1MHz	0.093	0.244	1.086	1.053	0.338	0.034

The variation of dielectric loss tangent (tan δ) with frequency is depicted in the Fig. 4.13 (c). It was observed that dielectric loss tangent increases initially with frequency for $x = 0.2$ to $x = 0.4$ followed by an decrease resulting in the resonance peak between 5 kHz to 50 kHz, while rest of the ferrites shows decrease in dielectric loss tangent with frequency. The dielectric loss in ferrite materials depend on a number of factors such as stoichiometry, Fe^{2+} concentration and structural homogeneity which in turn depend on the composition and

method of preparation. The dielectric loss gives the loss of energy from the applied field into the sample. This is caused by domain wall resonance. At higher frequencies, the losses are found to be low, since domain wall motion is inhibited and magnetization is forced to change rotation. The initial decreased can be understood from Koop's phenomenological model [29].

The appearance of a resonance peak (Debye relaxation peaks) for the compositions $x =$ 0.2, 0.3 and 0.4 can be explained on the basis of the position exchange of ions, where the ions have more than one equilibrium positions of the same potential energy separated by a potential barrier. If the natural frequency of ion exchange between positions of equal potential is the same as the frequency of the externally applied alternating field, then maximum energy is transferred to the oscillating ions and the loss tangent shoots up, thereby resulting in a resonance [89]. Further, the position of the resonance peak shifted towards the lower frequency as the Mn concentration was increased. In the present work the loss tangent peak, for the composition, $x = 0.2$, 0.3 and 0.4 at room temperature was observed at frequencies below 50 kHz.

4.3.3.2. Temperature variation of dielectric properties

The temperature variation of dielectric constant (ε') and complex dielectric constant (ε'') of 'as synthesized' $Ni_{0.5-x}Mn_xZn_{0.5}Fe_2O_4$ ($x = 0.0\text{-}0.5$) ferrites in the frequency range from 100 Hz to 10 MHz was studied and a representative study at 100 Hz is shown in Fig. 4.13 (d-e). The dielectric constant (ε') and complex dielectric constant (ε'') increases with temperature at all frequencies. It was observed in the present study that the increase in dielectric constant is rapid at lower frequencies than at higher frequencies. The dielectric constant of ferrite materials is due to the contribution of four types of polarizations, namely,

interfacial, dipolar, electronic and ionic [239]. At lower frequencies, the dipolar and interfacial polarizations are known to play the dominant role. Both these polarizations are strongly temperature dependent. The interfacial polarization increases with temperature due to creation of crystal defects, while dipolar polarization decreases with increase in temperature. The rapid increase in the dielectric constant with increase in temperature at low frequencies suggests that the effect of temperature is more pronounced on the interfacial than on the dipolar polarization [243]. At high frequencies, electronic and ionic polarizations are the main contributor and their temperature dependence is insignificant. Hence, it results in constant value of dielectric constant at higher frequencies.

The temperature variation studies of the dielectric loss tangent of 'as synthesized' $Ni_{0.5-x}Mn_xZn_{0.5}Fe_2O_4$ (x = 0.0-0.5) ferrites at 100 Hz (Fig. 4.13f) shows increase with temperature at all frequencies. The energy losses in the dielectric materials are due to the electric conductivity of the materials and the relaxation effect related to the dipole orientation. With increase in temperature, losses due to dipole orientations decreases, while those due to electric conductivity increases [239]. The increase in the dielectric loss with temperature observed for 'as synthesized' $Ni_{0.5-x}Mn_xZn_{0.5}Fe_2O_4$ (x = 0.0-0.5) ferrites suggests that the losses due to electrical conductivity dominate over those due to relaxation effects. The effect of Mn substitution on the dielectric properties do not follows any regular trend suggesting that the effect of factors such as particle size, porosity and density is predominant on dielectric properties than Mn substitution.

4.3.4. Magnetic measurements

The magnetic measurements of 'as synthesized' $Ni_{0.5-x}Mn_xZn_{0.5}Fe_2O_4$ (x = 0.0-0.5) ferrites were carried out at room temperature using vibrating sample magnetometer (VSM) with field upto 2 tesla.

4.3.4.1. Magnetization

The magnetic hysteresis loops of 'as synthesized' $Ni_{0.5-x}Mn_xZn_{0.5}Fe_2O_4$ (x = 0.0-0.5) ferrite samples are presented in the Fig. 4.14 and values of various hysteresis parameters are listed in the Table 4.11. The compositional variation of saturation magnetization and coercivity is given in the Fig. 4.15. The saturation magnetization values increases upto concentration, x = 0.2 and then decrease with increase in Mn content. Similar variations of saturation magnetization were also observed by other authors [107,244]. The increasing trend suggests that the variation in saturation magnetization can be explained on the basis of Neel two sublattice model [245]. The decreasing trend is due to the nonzero Yafet-Kittel (Y-K) angles in the sample which cannot be explained on the basis of Neel theory sublattices. Thus, for the samples (x > 0.2) the Y-K angles are nonzero which suggests triangular type spin arrangements on B sites that weakens the A-B interactions. In the spinel system containing mixed Ni-Zn ferrites and Mn-Zn ferrites, the Fe^{3+} ions and Mn^{2+} ions exist at both tetrahedral (A) and octahedral [B] sites, although Mn^{2+} ions prefer tetrahedral (A) sites than Fe^{3+} ions, while for octahedral [B] sites, Fe^{3+} ions have more preference than Mn^{2+} ions. The Zn^{2+} ions on the other hand have strong preference for the tetrahedral (A) sites while, the Ni^{2+} ions strongly prefers the octahedral [B] sites. When Mn^{2+} ions are introduced at the cost of Ni^{2+} ions, some of the Fe^{3+} ions migrate from tetrahedral (A) sites to the octahedral [B] sites. This

will increase the concentration of Fe^{3+} ion at octahedral $[B]$ sites, which results in increase of magnetic moment of B sub-lattice and hence the increase in total magnetization for lower Mn^{2+} ions content upto $x = 0.2$ [Table 4.11].
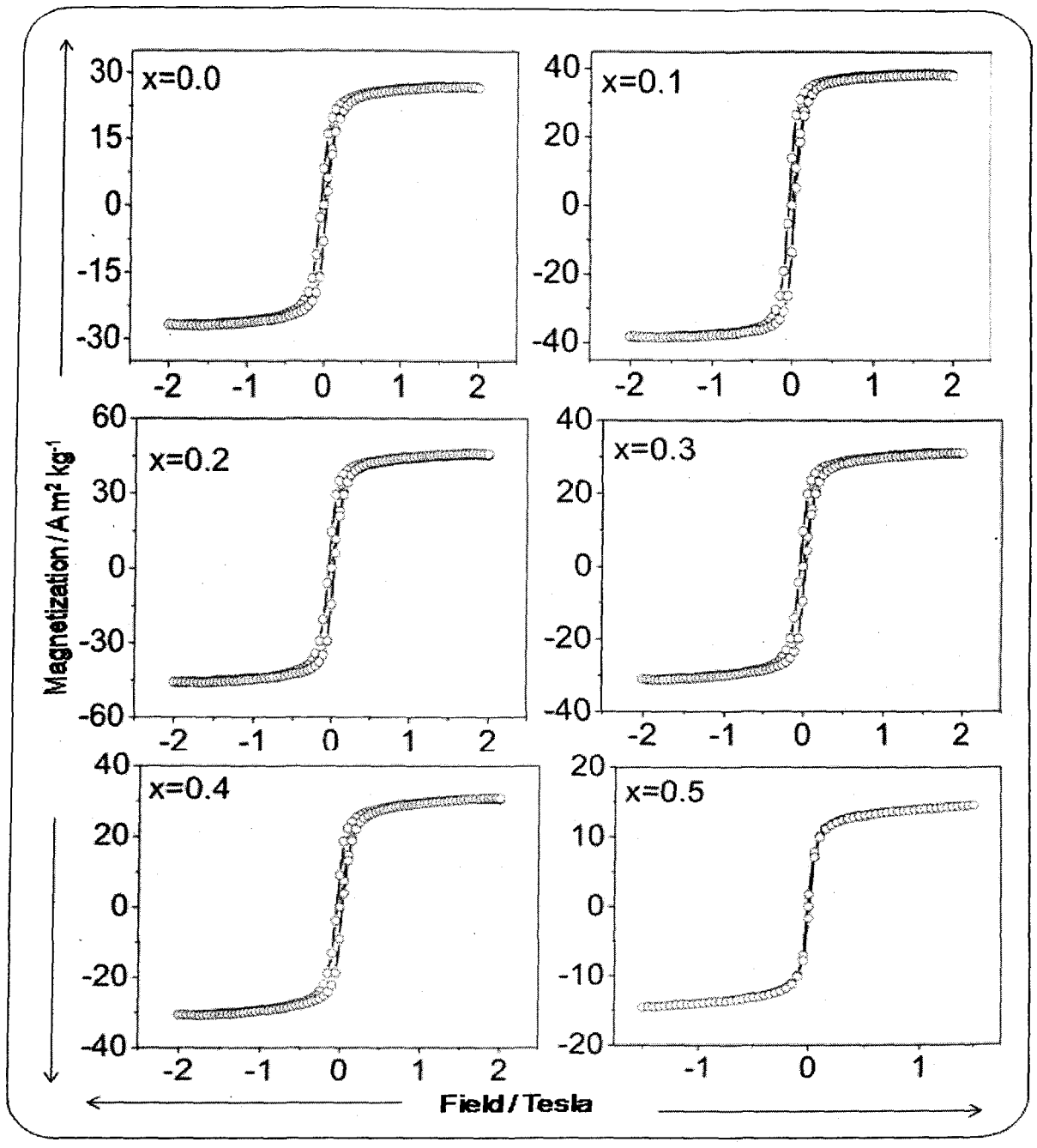
Fig.4.14. Hysteresis loops of a) $x = 0.0$, b) $x = 0.1$, c) $x = 0.2$, d) $x = 0.3$, e) $x = 0.4$ and

f) $x = 0.5$, of 'as synthesized' $Ni_{0.5-x}Mn_xZn_{0.5}Fe_2O_4$ $(x = 0.0-0.5)$ ferrites

Table 4.11. Hysteresis parameters of 'as synthesized' $Ni_{0.5-x}Mn_xZn_{0.5}Fe_2O_4$ (x = 0.0-0.5) ferrites

x	M_s / A m^2 kg^{-1}	M_r / A m^2 kg^{-1}	H_c x 10^{-3} / Tesla	Curie temp. 'T_c' / K
0.0	40.1	13.70	392.6	621
0.1	53.3	15.96	381.7	613
0.2	64.98	20.37	363.9	598
0.3	53.91	16.54	348.1	590
0.4	33.78	11.38	351.4	582
0.5	14.5	1.74	99.09	562

However, as Mn^{2+} ions concentration increases further, the Fe^{3+} ions left at tetrahedral (A) sites being small in number, the A-B sublattice interaction experienced by octahedral [B] site Fe^{3+} ions decreases. Also, the increase of Fe^{3+} ions concentration at octahedral [B] site increases the B-B interaction, which results in the canting of spins [246] and hence, the magnetization of B sublattice decreases. Although the magnetic moment of Mn^{2+} ions and Fe^{3+} ions is same (5 μB), the exchange interaction between Mn^{2+} ions and Fe^{3+} ions at tetrahedral (A) sites being small, there will be canting of spins at the tetrahedral (A) site. The increase in the Mn concentration in the ferrite therefore decreases the magnetic moment of the A sublattice and hence the overall decrease (Fig. 4.15). The low values of magnetization observed for 'as synthesized' $Ni_{0.5-x}Mn_xZn_{0.5}Fe_2O_4$ (x = 0.0-0.5) nanocrystalline ferrites as compared with the bulk may be due to the surface disorder and modified cationic distribution [247-249]. In addition, formation of dead layer on the surface, existence of random canting of

particle's surface spins, non-saturation effects due to random distribution of cations, have been reported for the reduction in magnetic properties of ferrite nanoparticles [250].

4.3.4.2. Coercivity (Hc)

The coercivity is the most fundamental hysteresis loop parameter which affects the shape of hysteresis loop. The coercivity is influenced by factors such as magnetocrystalline anisotropy, micro-strain, magnetic particle morphology, size distribution, shape anisotropy and magnetic domain size. Fig. 4.15 shows the variation of coercivity (Hc) with Mn substitution.
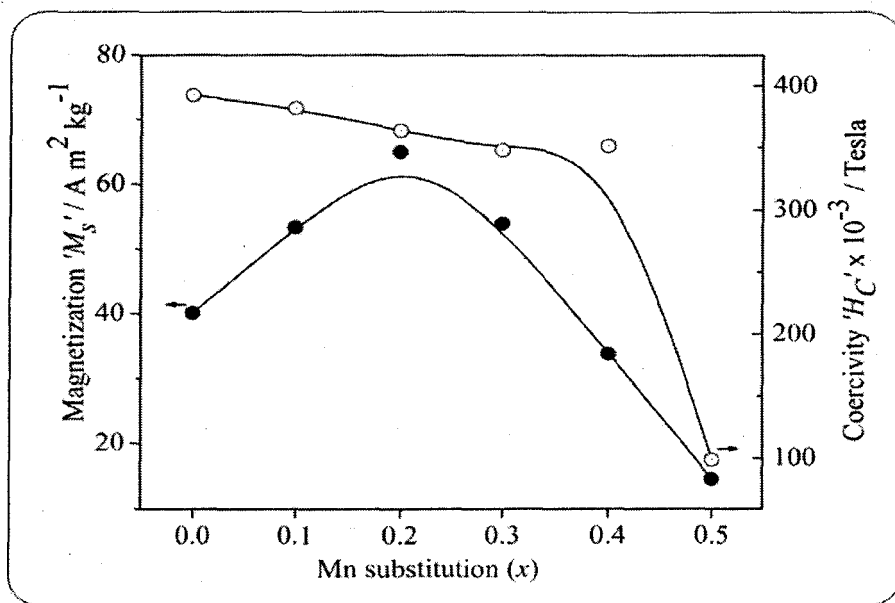
Fig.4.15. Variation of saturation magnetization and coercivity with Mn substitution (x) of 'as synthesized' $Ni_{0.5-x}Mn_xZn_{0.5}Fe_2O_4$ (x = 0.0-0.5) ferrites

The magnitude of coercivity decreases with increase in Mn content. It is known that the coercivity has a direct relation with the anisotropy constant of the sample. The anisotropy constant of Ni-Zn ferrites is greater than the Mn-Zn ferrites and hence the decrease in

coercivity can be related to the decreasing concentration of Ni^{2+} ions [251]. This means that the anisotropy constant decreases with increase in Mn^{2+} ions content and consequently, the magnitude of coercivity also decreases. The very high values of coercivity observed for the compositions, $x = 0.0, 0.1, 0.2, 0.3$ and 0.4 [Table 4.11] are due to the significant percentage of single domain particles, while for composition $x = 0.5$, relatively low values of coercivity may be due to the higher concentration of superparamagnetic particles which was also observed in the Mössbauer spectrum of this composition.

4.3.5. AC susceptibility studies

The a.c. susceptibility measurements can be used to determine the types of particles responsible for magnetic properties. The plot of normalized a.c. susceptibility (χ_T / χ_{RT}) with temperature can give an idea about the Curie temperature and domain structure. Below the Curie temperature ferrites have ferrimagnetic nature and above Curie temperature they are paramagnetic in nature. According to Bean [254], the susceptibility is inversely proportional to the coercive force. The existence of a coercive force clearly indicates that the 'as synthesized' $Ni_{0.5-x}Mn_xZn_{0.5}Fe_2O_4$ ($x = 0.0-0.5$) ferrite samples contain clusters of different sizes. For single domain particles, coercive force is large whereas it tends towards zero for superparamagnetic particles [254]. The variation of normalized ac susceptibility against temperature of all the 'as synthesized' ferrites is shown in Fig. 4.16 (a). These graphs show normal ferrimagnetic behavior and the susceptibility suddenly drops to zero at certain temperature, this temperature is called Curie temperature (T_c). The nature of plots indicates that, the sample contains clusters of both single domain and superparamagnetic particles and the superparamagnetic character increases with increase in Mn^{2+} ions substitution. The Curie

temperature of these ferrites obtained by this study are listed in Table 4.11. The variation of Curie temperature with composition is shown in the Fig. 4.16 (b) which can be correlated with the Mn^{2+} ions concentration and A-B interactions. The decrease in Curie temperature with increasing Mn content can be attributed to the decreasing A-B interaction resulting from replacement of Fe^{3+} ions by Mn^{2+} ions on tetrahedral (A) sites.
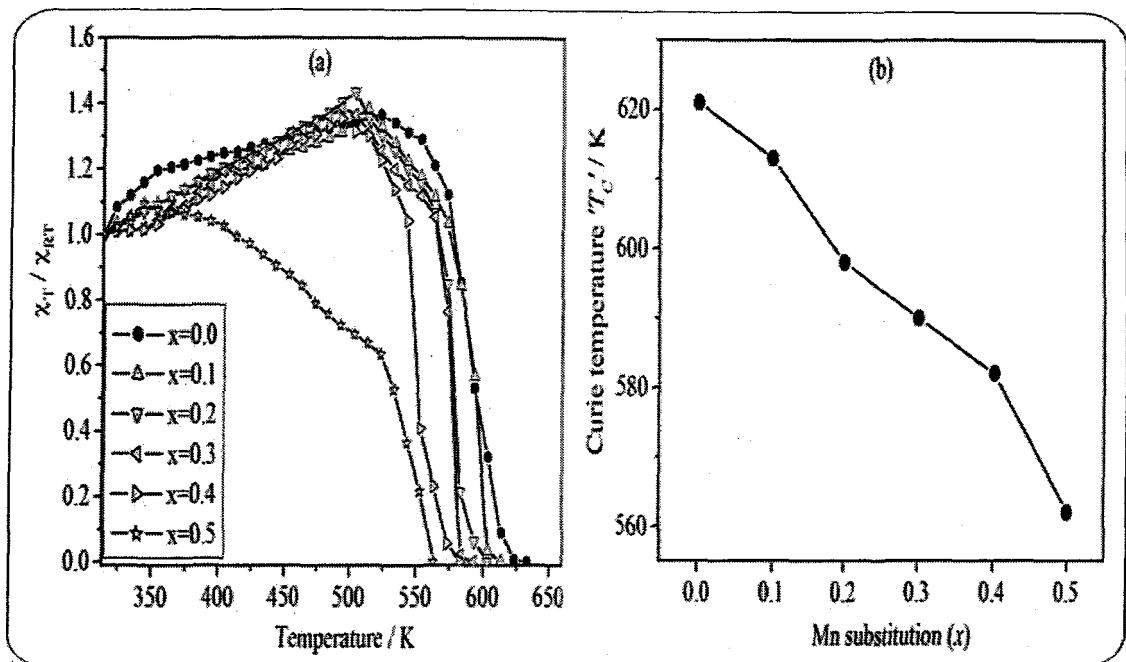
Fig.4.16. The plots of a) normalized a.c. susceptibility 'χ_T/χ_{RT}' against temperature, b) variation of Curie temperature 'T_c' with Mn substitution (x) of 'as synthesized' $Ni_{0.5-x}Mn_xZn_{0.5}Fe_2O_4$ ($x = 0.0-0.5$) ferrites

4.4. Gas sensing studies of 'as synthesized' $Ni_{0.5-x}Mn_xZn_{0.5}Fe_2O_4$ ($x = 0.0-0.5$) ferrites

Gas sensing studies were carried out using the thick films resistors prepared from 'as synthesized' $Ni_{0.5-x}Mn_xZn_{0.5}Fe_2O_4$ ($x = 0.0-0.5$) ferrite nanopowders. The details of gas sensing set up used are discussed in section 2.3.9 of chapter 2. Also, the detailed characterization of 'as synthesized' $Ni_{0.5-x}Mn_xZn_{0.5}Fe_2O_4$ ($x = 0.0-0.5$) ferrite nanopowders is

213

covered in section 4.2.1 to 4.2.5 of chapter 4. The sensor response of the thick films was studied for various gases like, NH_3, CO_2, H_2S, Cl_2, LPG and ethanol from room temperature to 450°C. All the samples of above composition showed very good response and selectivity for H_2S in the temperature region from 100°C to 450°C. The highest response was observed for thick film prepared from composition, $x = 0.2$ at around 350°C for H_2S concentration of 200 ppm. The sensor response of the thick films was found to be very low for other gases like NH_3, CO_2, Cl_2, LPG and ethanol even at the higher concentration of 1000 ppm. The Fig. 4.17 depicts the variation of gas response for H_2S (200 ppm) with operating temperature of the 'as synthesized' ferrites.
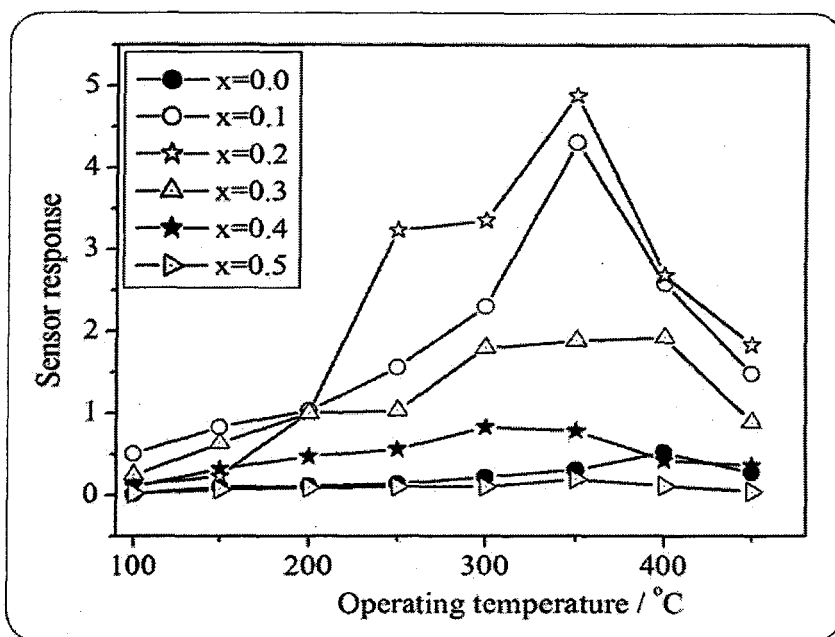
Fig.4.17. Variation of sensor response for 200 ppm H_2S gas with operating temperature for $Ni_{0.5-x}Mn_xZn_{0.5}Fe_2O_4$ ($x = 0.0$-0.5) ferrite thick films

At lower temperatures (RT to 100°C) the response was found to be very low, as the temperature was increased the response increases upto 350°C and then decreases with further

increase in temperature. The highest response was observed to be 4.88 at 350°C for composition, $x = 0.2$. The H_2S response at 350°C is expected to be monitored by adsorption-desorption of oxygen species on the surface of the film. The H_2S gas upon exposure gets oxidized after interaction with the adsorbed oxygen species on the surface of the film. This would decrease the film resistance, giving a response at 350°C. Below 350°C, the H_2S gas gets oxidized weakly giving lower response. When temperature is raised above 350°C, the gas exposed to the surface of the film, may get oxidized before reaching the surface of the film or the film surface chemistry was may not be favorable to sense the gas at such a high temperature and hence the response decreases after 350°C.

The selectivity of the thick films sensor for H_2S (200 ppm) gas at 350°C is depicted in the Fig. 4.18. The sensor showed high selectivity to H_2S against LPG, NH_3 CO_2, ethanol and Cl_2 gases. The selective response to H_2S gas (200 ppm) among other gases may be attributed to the high surface reactivity for adsorption and desorption of the H_2S gas on the surface of the thick film.
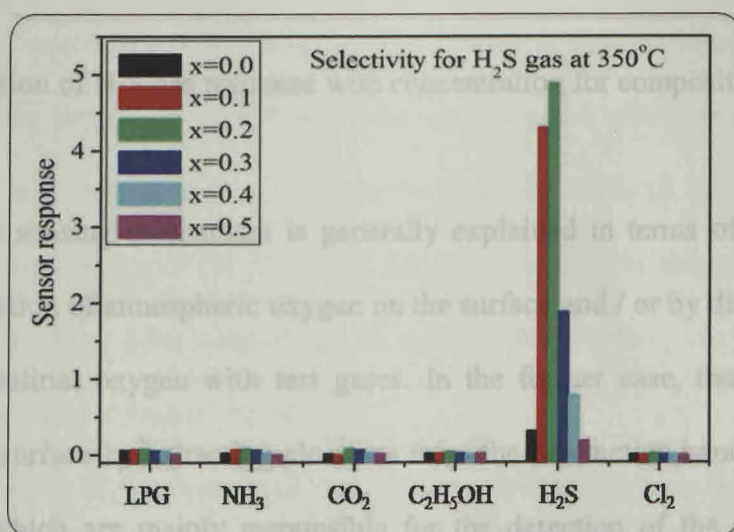
Fig.4.18. Selectivity for 200 ppm of H_2S gas at 350°C from mixture of gases of $Ni_{0.5-x}Mn_xZn_{0.5}Fe_2O_4$ ($x = 0.0$-0.5) ferrite thick films

The variation of gas response of the composition, $x = 0.2$ with H_2S gas concentration is presented in the Fig. 4.19. The sensor response with increasing concentration at $350^\circ C$ was studied by exposing the films to varying concentrations of H_2S gas from 100 ppm to 1200 ppm. The sensor showed sharp increase in the response at lower concentration upto 200 ppm and gradual rise in the response was observed for higher concentration (< 200 ppm) Thus, the active region of the sensor would be up to 200 ppm.
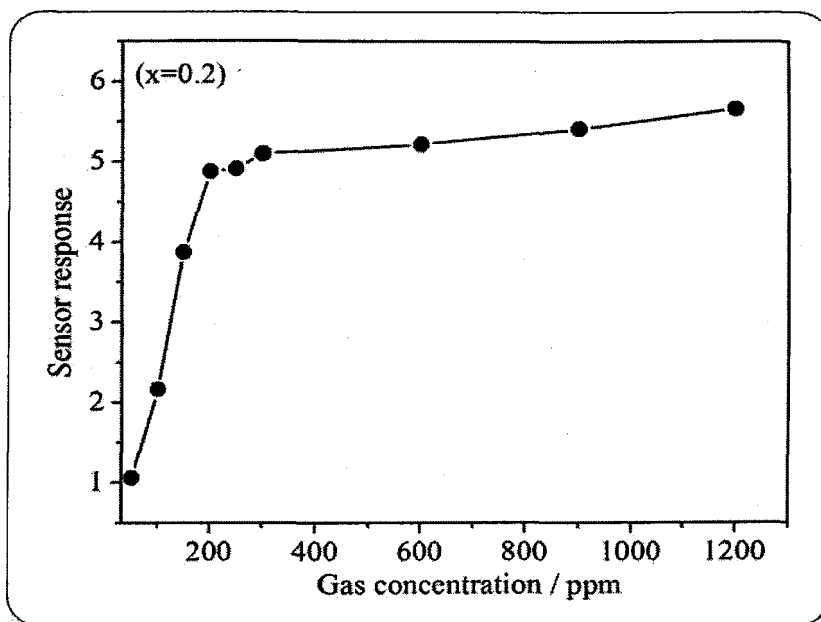
Fig.4.19. Variation of H_2S gas response with concentration for composition, $x = 0.2$ at $350^\circ C$

The gas sensing mechanism is generally explained in terms of conductance change either by adsorption of atmospheric oxygen on the surface and / or by direct reaction of lattice oxygen or interstitial oxygen with test gases. In the former case, the atmospheric oxygen adsorbs on the surface by extracting electrons from the conduction band to form superoxides or peroxides, which are mainly responsible for the detection of the test gases. At higher

temperature, the atmospheric oxygen O_2 adsorbs on the surface of the thick film. It captures the electrons from the conduction band as shown in the following equation 2.37.

$$O_{2(air)} + 2e^- \rightarrow 2O^-_{(film\ surface)} \qquad \text{-----------------} \{2.37\}$$
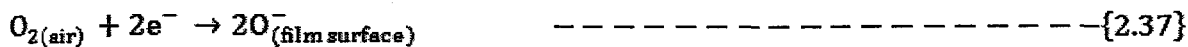
This would result in decreasing conductivity of the film. The H_2S gas when expose over the sensor film containing oxygen species during heating, the following reaction takes place (equation 2.38), ultimately converting the H_2S to water molecules and oxides of sulfur in vapour form.

$$nH_2S_{(gas)} + 3nO^-_{(film\ surface)} \rightarrow nH_2O_{(gas)} + nSO_{2(gas)} + 3ne^-_{(cond.band)} \qquad \text{----} \{2.38\}$$
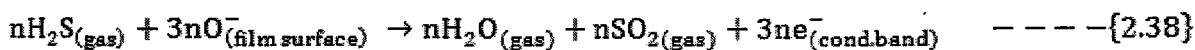
This shows the n-type conduction mechanism. For complete combustion, 1 mol of H_2S requires three times the amount of oxygen and will produce same number of water molecules. The entire surface of the sensor material is covered with chemisorbed oxygen ions O_2, O_2^-, O^- and O^{2-} depending on temperature as shown equation 2.39.

$$O_{2(RT)} \xrightarrow{\text{upto } 150^0 C} O_2^- \xrightarrow{\text{upto } 450^0 C} 2O^- \xrightarrow{\text{above } 450^0 C} O^{2-} \qquad \text{------------} \{2.39\}$$
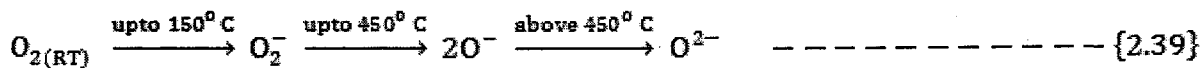
In this case, O^- ions take part in the reaction to sense the H_2S gas at 350°C. The adsorbed O^- species create space-charge region near the film surface at high temperature by extracting the electrons from the material. The H_2S is a reducing gas which reacts with adsorbed O^- species on the surface and re-injects the electrons back to the material (equation 2.38), thereby increasing the conductance of the film. The fast response may be due to the fast oxidation of H_2S into H_2O and SO_2. After evaporation of water molecules from the film surface, the film recovers to its original chemical status.

The selective H_2S response of the sensor at 350°C can be explained by the surface reaction processes (Fig. 4.20).
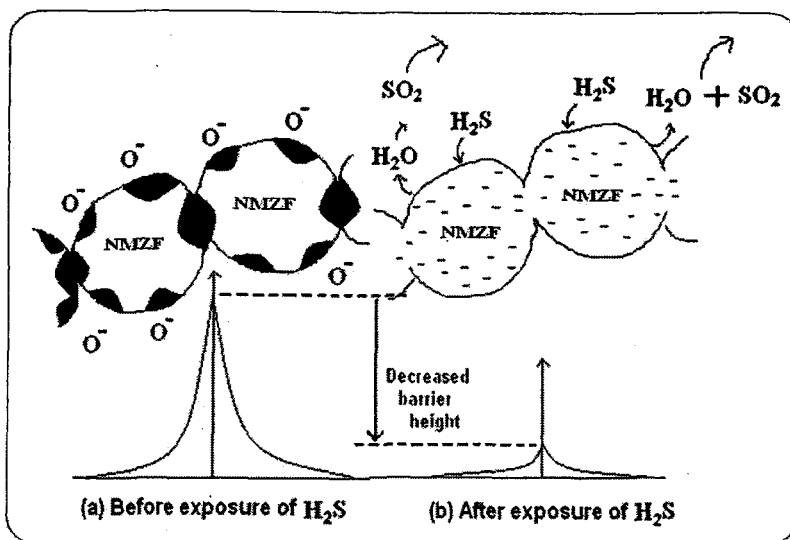
Fig.4.20. H$_2$S gas sensing mechanism of the sensors at 350°C

The atmospheric oxygen adsorbed on the surface which extracts electrons from the conduction band and form superoxides or peroxides. These superoxides or peroxides are mainly responsible for the increase in the resistance of the thick film sensor. Upon exposure to H$_2$S, a remarkable decrease in the resistance of the sensor was observed, which may be due to the surface reaction of H$_2$S with physisorbed superoxides or peroxides, which results in generation of electrons (equation 2.38) leading to the increase in conductivity. This would decrease the barrier height among the Ni$_{0.5-x}$Mn$_x$Zn$_{0.5}$Fe$_2$O$_4$ (NMZF) ferrite grains. Moisture and oxides of sulfur produced during the surface reaction are gaseous in nature. The high volatility of byproducts from the surface explains the quick response and fast recovery of the sensor.

4.5. Characterization of sintered Ni$_{0.5-x}$Mn$_x$Zn$_{0.5}$Fe$_2$O$_4$ (x = 0.0-0.5) ferrites

The details of sintering have been already discussed in the section 2.24-2.27 of chapter 2. The samples were sintered at four different temperatures starting from 1100°C to 1250°C

218

in air at constant time of 1h and furnace cooled to room temperature. The sintering temperature of 1100°C was fixed by carrying out optimization of sintering temperature (as discuss in the section 3.5.1) for complete phase formation using X-ray diffraction technique. The sintered samples were then characterized by XRD, FTIR, SEM and Mössbauer spectroscopy.

4.5.1. X-ray diffraction studies

The phase analysis of sintered $Ni_{0.5-x}Mn_xZn_{0.5}Fe_2O_4$ (x = 0.0-0.5) ferrites were carried out using X-ray diffraction technique. The X-ray diffraction patterns of ferrites sintered at 1100°C, 1150°C, 1200°C and 1250°C for 1h are shown in the Fig. 4.21. The X-ray diffraction patterns (Fig. 4.21) for all the sintered compositions (except for composition x = 0.5 sintered at 1100°C and 1150°C / 1h) clearly indicate the formation of single phase spinel type structure. For composition, x = 0.5 single phase formation was observed at 1200°C and above. Hence, the XRD pattern of composition, x = 0.5, is not included in the Fig. 4.21 (a-b). The complete analysis of XRD patterns revealed that the 2θ positions of the peaks are in agreement with the reported values [107]. The measured lattice parameter, density and porosity of sintered ferrites sintered at different temperature are given in the Table 4.12. It was observed that lattice parameter increases with increasing Mn substitution. The increase of the lattice parameter with increasing Mn content can be explained in terms of ionic radii [175] wherein a larger ion replaces the smaller one in the lattice, as already discussed in the section 3.2.1. It was observed that density decreases with increasing Mn substitution (Fig. 4.22). This behaviour is explained considering the replacement of heavier nickel ions (58.69 amu) by lighter manganese (54.94 amu) [256].
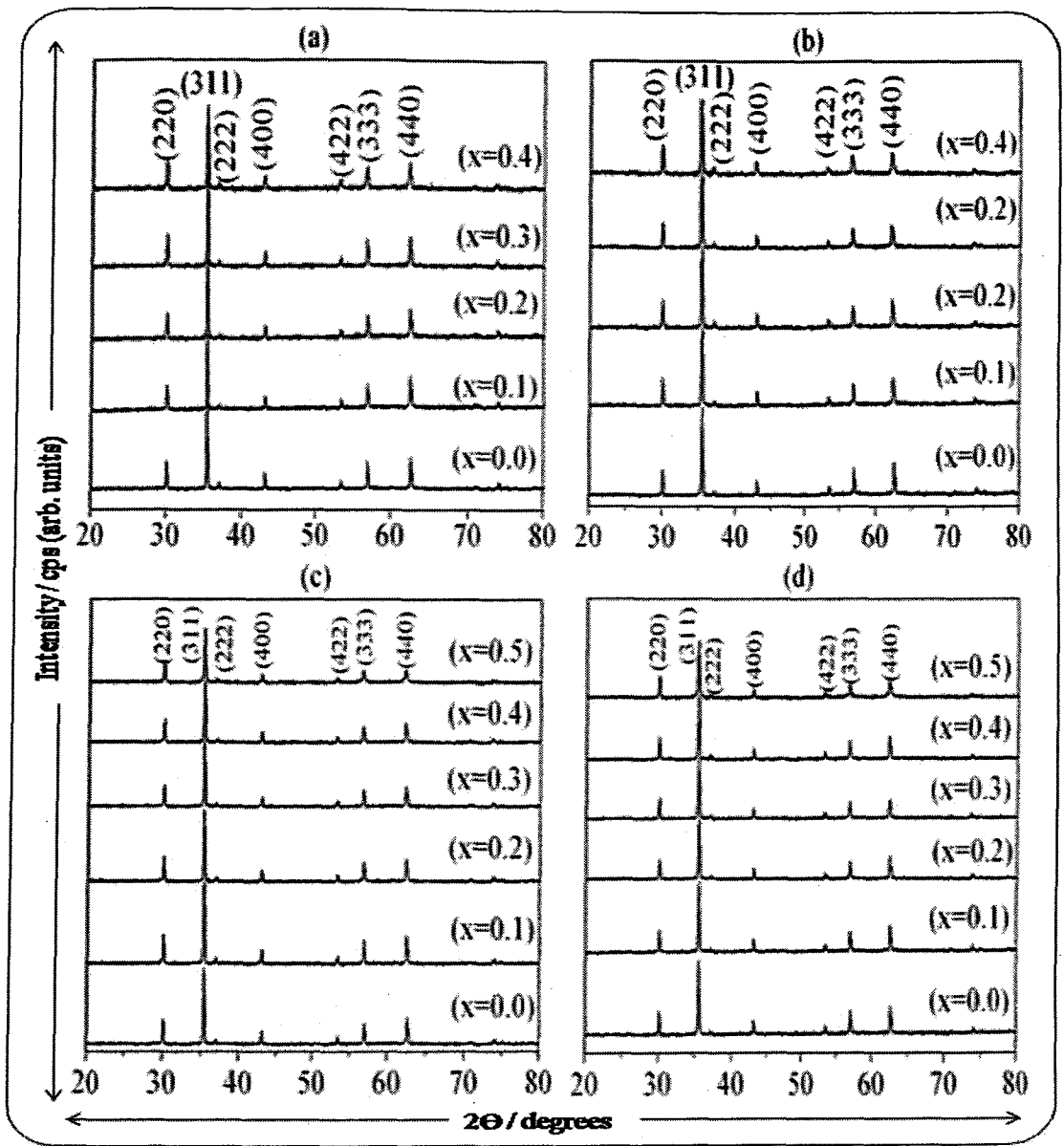
Fig.4.21. XRD patterns of $Ni_{0.5-x}Mn_xZn_{0.5}Fe_2O_4$ ($x = 0.0-0.5$) ferrites sintered at

a) $1100^\circ C$ / 1h, b) $1150^\circ C$ / 1h, c) $1200^\circ C$ / 1h and d) $1250^\circ C$ /1h

With increasing sintering temperature hardly any variation in the lattice parameter was observed. The variation of bulk density and porosity with sintering temperature of sintered ferrites is represented in Fig. 4.22.

220

Table 4.12. Lattice constant (a), density (d), porosity (P) and grain diameter of sintered $Ni_{0.5-x}Mn_xZn_{0.5}Fe_2O_4$ (x = 0.0-0.5) ferrites

Property	Sintering temp. / °C	x					
		0.0	0.1	0.2	0.3	0.4	0.5
Lattice Parameter 'a' / A°	1100°C / 1h	8.3859	8.3930	8.3994	8.4116	8.4223	---
	1150°C / 1h	8.3879	8.3973	8.4097	8.4178	8.4260	---
	1200°C / 1h	8.3859	8.3965	8.4099	8.4187	8.4262	8.4371
	1250°C / 1h	8.3865	8.3943	8.4081	8.4173	8.4235	8.4379
Density 'd' (X-ray / Exp) / gcc⁻¹	1100°C / 1h	5.35 / 4.21	5.33 / 4.20	5.31 / 4.14	5.28 / 4.10	5.25 /3.99	---
	1150°C / 1h	5.35 /4.53	5.32 / 4.45	5.29 / 4.38	5.27 / 4.30	5.24 / 4.21	---
	1200°C / 1h	5.35 / 4.87	5.33 / 4.79	5.29 / 4.63	5.27 / 4.59	5.24 / 4.48	5.22 / 4.34
	1250°C / 1h	5.35 / 5.01	5.33 / 4.95	5.30 / 4.87	5.27 /4.73	5.25 / 4.64	5.21 / 4.59
Porosity 'P' / %	1100°C / 1h	21.31	21.20	22.04	22.35	24.0	---
	1150°C / 1h	15.33	16.35	17.20	18.41	19.66	---
	1200°C / 1h	8.97	10.13	12.48	12.90	14.50	16.86
	1250°C / 1h	6.35	7.13	8.11	10.24	11.62	11.90

It was observed that the density of the sinterd ferrites increases, when sintering temperature was from 1100°C to 1250°C, while the porosity decreases [Table 4.12]. The increase of density with increasing temperature is expected because during sintering process, the thermal energy generates the force that drives the grain boundaries to grow over pores thereby decreasing the pore volume.
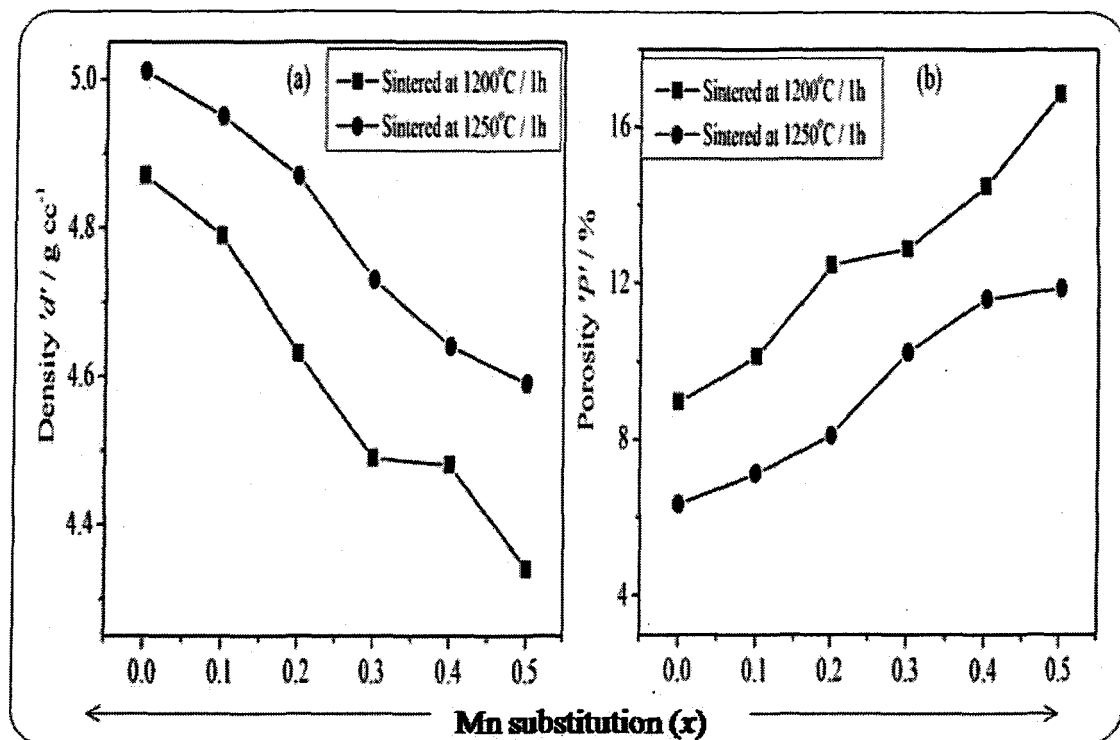
Fig.4.22. Variation of bulk density and porosity against composition (x) of sintered $Ni_{0.5-x}Mn_xZn_{0.5}Fe_2O_4$ ($x = 0.0$-0.5) ferrites

4.5.2. FTIR spectral studies

The FTIR spectra of $Ni_{0.5-x}Mn_xZn_{0.5}Fe_2O_4$ ($x = 0.0$-0.5) ferrites sintered at different temperatures are shown in the Fig. 4.23 and the absorption frequency values are given in the Table 4.13.
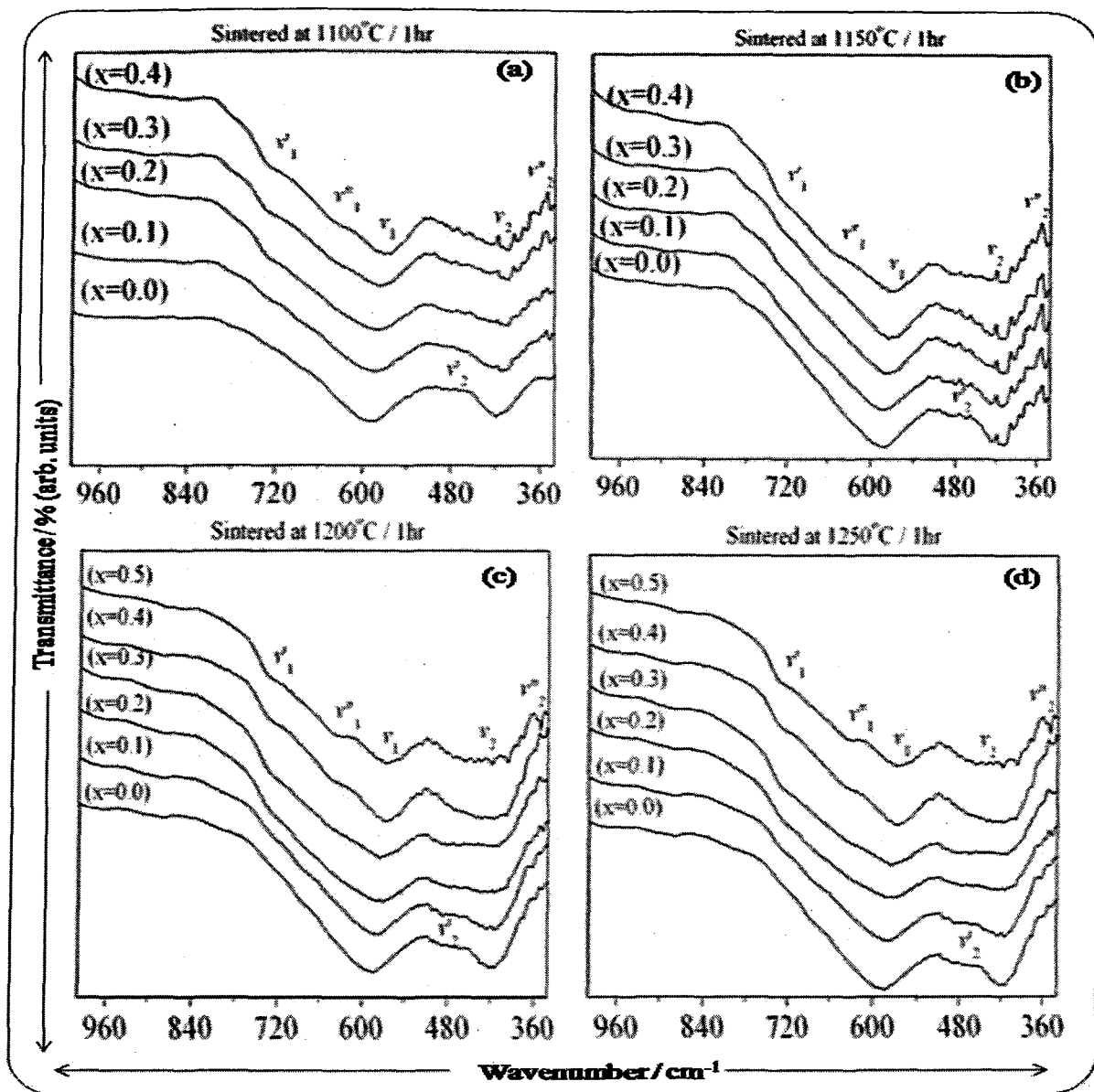
Fig.4.23. FTIR spectra of $Ni_{0.5-x}Mn_xZn_{0.5}Fe_2O_4$ (x = 0.0-0.5) ferrites sintered at

a) 1100°C / 1h, b) 1150°C / 1h, c) 1200°C / 1h and d) 1250°C / 1h

The spectra show two principal absorption bands in the frequency range 750 cm^{-1} to 340 cm^{-1}. The high frequency (v_1) band was observed in the range 590 cm^{-1} to 564 cm^{-1} and the lower frequency (v_2) band was observed in the range 421 cm^{-1} to 404 cm^{-1}.

Table 4.13 Position of absorption bands of FTIR spectra of sintered $Ni_{0.5-x}Mn_xZn_{0.5}Fe_2O_4$ ($x = 0.0\text{-}0.5$) ferrites

FTIR bands	Sintering temp. / °C	x					
		0.0	0.1	0.2	0.3	0.4	0.5
v_1 / v_2	1100°C / 1h	590 / 421	581 / 414	579 / 406	576 / 405	572 / 404	---
	1150°C / 1h	585 / 407	581 / 413	578 / 409	573 / 406	570 / 406	---
	1200°C / 1h	585 / 416	580 / 415	575 / 415	575 / 411	575 / 419	564 / 419
	1250°C / 1h	583 / 419	578 / 416	575 / 415	575 / 411	567 / 418	566 / 419
v'_1 / v'_2	1100°C / 1h	--- / 468	--- / 461	728 / 462	728 / 468	728 / 462	---
	1150°C / 1h	--- / 462	--- / 463	--- / 463	--- / 461	728 / 466	---
	1200°C / 1h	--- / 462	--- / 462	733 / 462	730 / 463	730 / 460	730 / ---
	1250°C / 1h	--- / 463	--- / 462	--- / 462	731 / 462	733 / 462	733 / ---
v''_1 / v''_2	1100°C / 1h	--- / 351	--- / 347	--- / 345	--- / 348	631 / 348	---
	1150°C / 1h	--- / 346	--- / 346	--- / 348	631 / 346	631 / 345	---
	1200°C / 1h	--- / 349	--- / 350	--- / 347	630 / 343	633 / 347	634 / 351
	1250°C / 1h	--- / 348	--- / 349	--- / 347	--- / 343	630 / 347	631 / 351

The high frequency (v_1) band is related to the intrinsic vibrations of Fe^{3+}---O^{2-} bond in tetrahedral sites, while the lower frequency (v_2) band is due to the stretching vibrations of Fe^{3+}---O^{2-} groups occupying octahedral sites [166-167]. Besides these main absorption bands, few weak bands were also observed in the FTIR spectra which were assigned considering the site preference of metal ions present for tetrahedral and octahedral sites in the mixed $Ni_{0.5-x}Mn_xZn_{0.5}Fe_2O_4$ (x = 0.0-0.5) ferrite system. The relatively weak shoulder (v'_1) which appears with increasing Mn content in the region ~ 730 cm^{-1} has been attributed to the stretching vibration of Mn^{2+}--O^{2-} in tetrahedral sites which is also reported in the literature [202]. Another weak shoulder (v''_1) observed in the range 634 cm^{-1} to 630 cm^{-1} with increasing Mn concentration which has been assigned to stretching vibration of tetrahedral Zn^{2+}--O^{2-} bond and very weak band (v'_2) in the region 468 cm^{-1} to 460 cm^{-1} observed for all the composition (except x = 0.5) have been assigned to the stretching vibrations of Ni^{2+}-- O^{2-} bond in octahedral sites [107]. The IR peak (v''_2) observed in the region 351 cm^{-1} to 343 cm^{-1} can be assigned to Zn^{2+}--O^{2-} stretching vibrations [107]. The appearance of these weak absorption bands in the FTIR spectra is discussed in details in section 3.2.2.

4.5.3. SEM microstructures of sintered $Ni_{0.5-x}Mn_xZn_{0.5}Fe_2O_4$ (x = 0.0-0.5) ferrites

The SEM microstructures of $Ni_{0.5-x}Mn_xZn_{0.5}Fe_2O_4$ (x = 0.0-0.5) ferrite compositions sintered at different temperatures from 1100°C to 1250°C are presented in the Fig. 4.24 (a-b) and 4.25 (a-b). The average grain size (grain diameter) of the ferrites were determined from optical micrographs by linear intercept method [257] and are compiled in the Table 4.14. From the micrographs, it was observed that the grain size significantly depends on the Mn concentration in Ni-Zn ferrite. In general, the average grain size increases with increasing Mn content which is also reported in the literature

[258]. This is due to the lower melting point of Mn as compared to Ni [104]. This increase in grain diameter is very small at lower Mn content (x < 0.2) but at higher Mn content the grain size increases to greater extent.
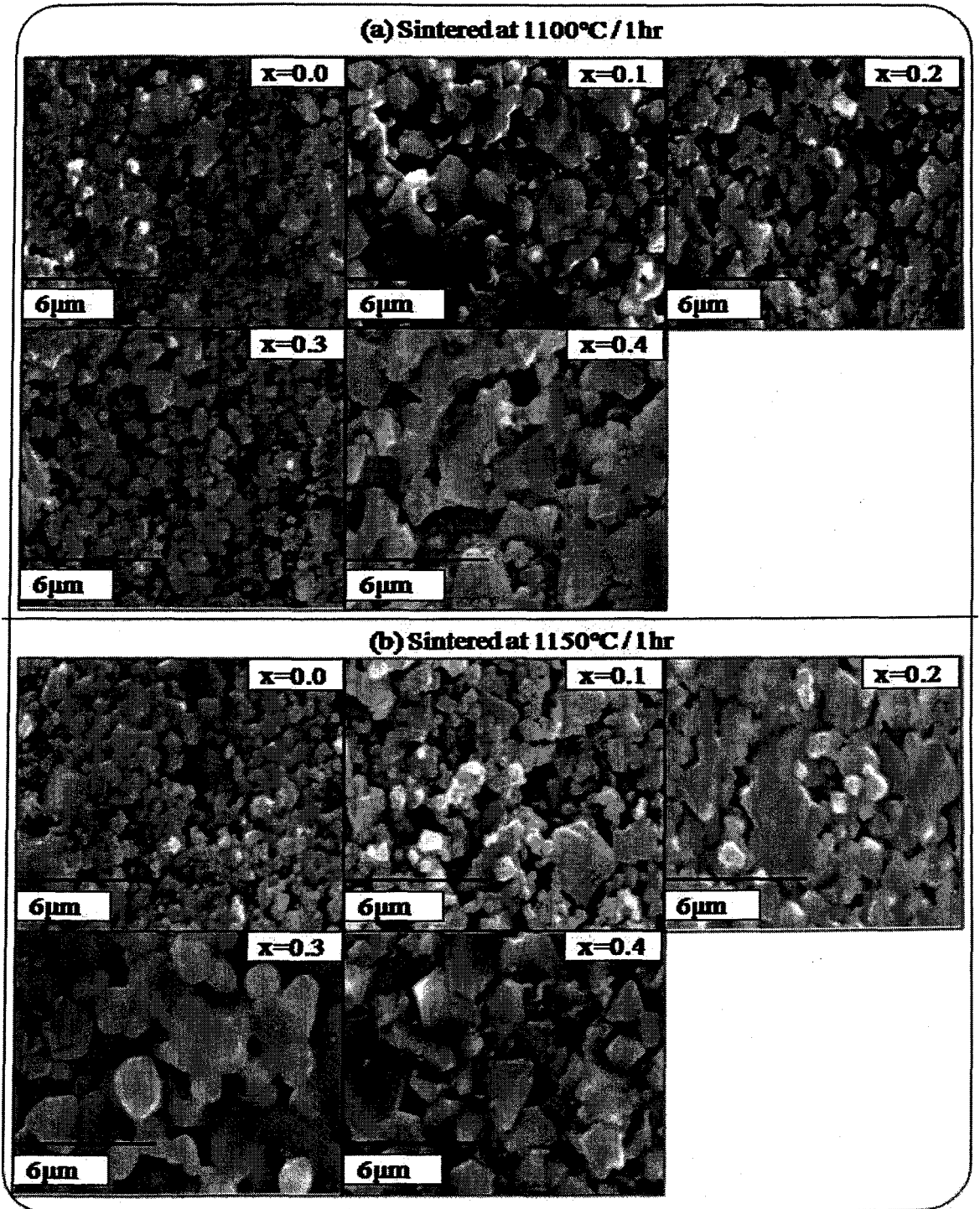
Fig.4.24. SEM of $Ni_{0.5-x}Mn_xZn_{0.5}Fe_2O_4$ ($x = 0.0$-0.5) ferrites sintered at a) $1100^{\circ}C$ / 1h and b) $1150^{\circ}C$ / 1h

The samples sintered at 1100°C and 1150°C reveal porous microstructure (Fig. 4.24 a-b) with fine grains less than 2.3 μm in diameter [Table 4.14]. The samples sintered at 1200°C and 1250°C presented a homogeneous microstructure with narrow grain distribution and average grain diameter in the range 0.76 μm to 1.86 μm.
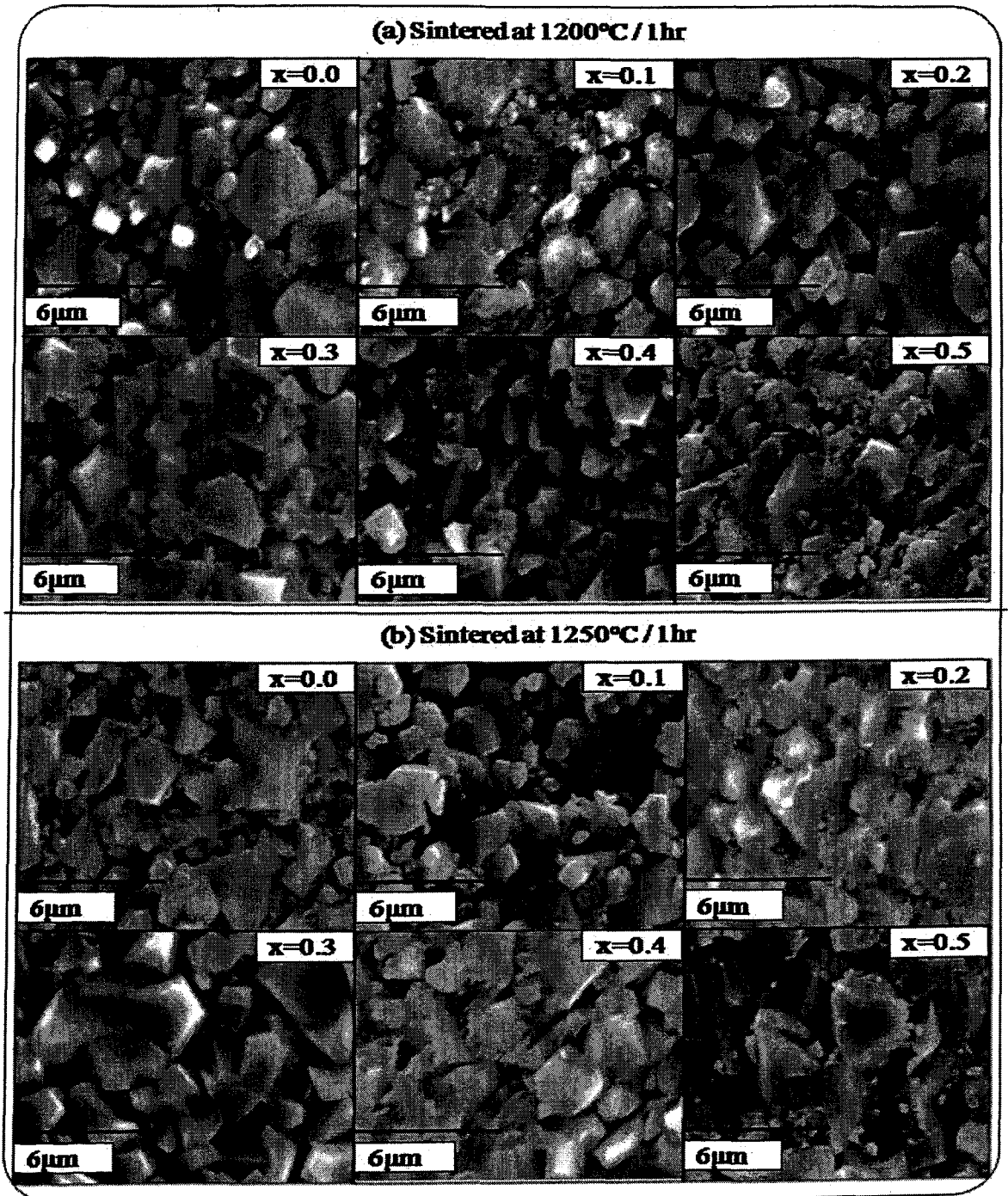
Fig.4.25. SEM of $Ni_{0.5-x}Mn_xZn_{0.5}Fe_2O_4$ ($x = 0.0$-0.5) ferrites sintered at a) 1200°C / 1h and b) 1250°C / 1h

Table 4.14. Average grain diameter and diameter range of sintered $Ni_{0.5-x}Mn_xZn_{0.5}Fe_2O_4$ (x = 0.0-0.5) ferrites

x	Average grain diameter (diameter range) / μm			
	1100°C / 1h	1150°C / 1h	1200°C / 1h	1250°C / 1h
0.0	0.59	0.62	0.93	1.30
	(0.27-0.91)	(0.27-1.09)	(0.27-2.82)	(0.27-3.64)
0.1	0.64	0.63	1.06	0.92
	(0.27-1.64)	(0.27-2.18)	(0.27-2.27)	(0.36-2.27)
0.2	0.68	0.89	0.90	1.04
	(0.27-1.46)	(0.27-2.27)	(0.27-2.27)	(0.35-2.73)
0.3	0.56	1.21	1.14	1.42
	(0.36-0.82)	(0.46-2.18)	(0.46-2.36)	(0.64-3.91)
0.4	1.21	1.30	1.13	1.09
	(0.64-1.91)	(0.46-2.18)	(0.46-2.73)	(0.36-3.18)
0.5	--	---	0.76	1.86
			(0.27-1.91)	(0.46-2.82)

The intragranular porosity was found to be very low in all the sintered compositions. The average grain diameter increases and largest particle diameter of 3.91 μm was observed for composition, x = 0.3 [Table 4.14], sintered at 1250°C which is much lower than reported for sintered ferrites prepared by conventional method [82,259].

4.5.4. Mössbauer spectral studies

The Mössbauer spectra of mixed Ni-Mn-Zn ferrites, $Ni_{0.5-x}Mn_xZn_{0.5}Fe_2O_4$ (x = 0.0-0.5) ferrite sintered at 1200°C / 1h recorded at room temperature are displayed in Fig.

4.26. For ferrite samples with compositions upto $x = 0.2$, the Mössbauer spectra exhibits a superposition of two Zeeman sextets, one sextet corrosponding to a higher magnetic field was attributed to Fe^{3+} ions on the B site and the other sextet corrosponding to lower magnetic field was attributed to Fe^{3+} ions on A site. While, for the compositions, $x = 0.3$ and 0.4, the Mössbauer spectra exhibits a superposition of two Zeeman sextets and a doublet and for the composition, $x = 0.5$ the spectrum consists of one sextet and single quadrupole doublet. For samples with composition, $x > 0.2$ their spectra indicate that the samples has ferromagnetic and paramagnetic natures simultaneously. The central doublet can be attributed to the magnetically isolated Fe^{3+} ions which do not participate in the long range magnetic ordering due to a large number of nonmagnetic nearest neighbors.
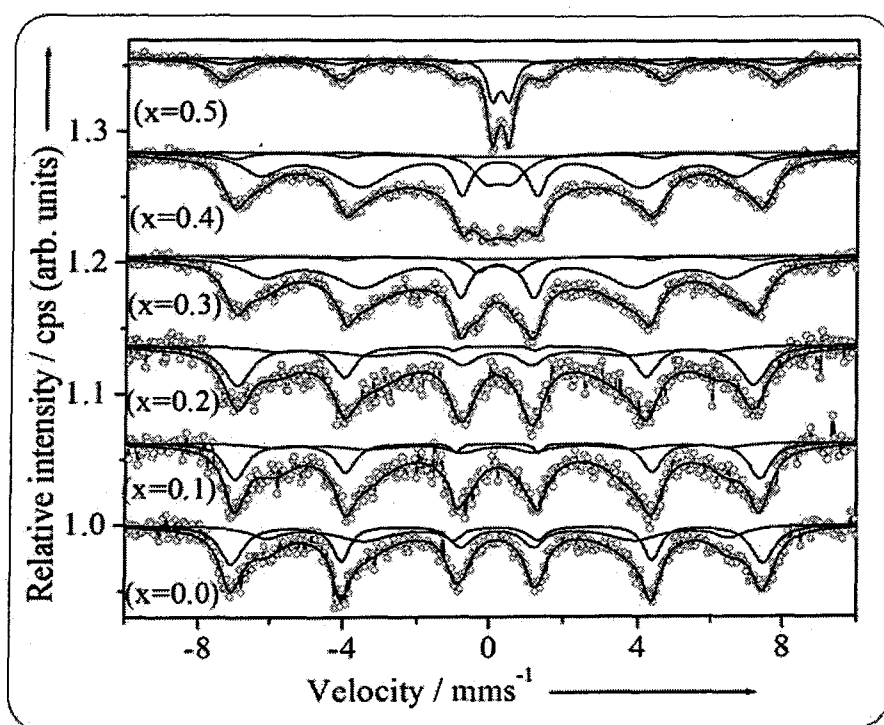
Fig. 4.26. Mössbuauer spectra of $Ni_{0.5-x}Mn_xZn_{0.5}Fe_2O_4$ $(x = 0.0-0.5)$ ferrites sintered at 1200°C /1h

The refined values of the hyperfine parameters computed from the Mössbauer spectra are listed in Table 4.15. In the mixed Ni-Mn-Zn ferrites system, with increasing

Mn substitution, it was observed that the values of isomer shift 'δ' of tetrahedral (A) sites increases indicating that Mn^{2+} ions predominatly occupy A sites in spinel lattice [197].

Table 4.15. Room temperature Mössbauer effect parameters: isomer shift 'δ', quadrupole splitting 'Δ', hyperfine field 'H_{hf}', relative Area 'R_A' and inner line width 'Γ' of $Ni_{0.5-x}Mn_xZn_{0.5}Fe_2O_4$ ($x = 0.0$-0.5) ferrites sintered at 1200°C / 1h

Sample	Site	*δ / mms^{-1}	Δ / mms^{-1}	H_{hf} / Tesla	R_A / %	Γ / mms^{-1}
0.0	Sextet 1, (A)	0.283	0.035	45.06	49.37	0.620
	Sextet 2, [B]	0.317	0.008	39.41	50.63	0.712
0.1	Sextet 1, (A)	0.306	-0.011	44.45	37.94	0.316
	Sextet 2, [B]	0.365	0.064	38.32	62.07	1.018
0.2	Sextet 1, (A)	0.224	0.019	43.72	35.25	0.329
	Sextet 2, [B]	0.275	0.044	36.85	64.75	0.862
0.3	Sextet 1, (A)	0.271	-0.022	39.29	51.90	0.561
	Sextet 2, [B]	0.261	-0.022	44.08	45.20	4.443
	Doublet	0.309	1.095	---	2.90	0.665
0.4	Sextet 1, (A)	0.315	-0.028	40.34	38.78	0.572
	Sextet 2, [B]	0.316	0.0028	44.76	54.54	4.40
	Doublet	0.333	0.692	---	6.68	0.933
0.5	Sextet 1, [B]	0.331	-0.013	47.03	78.15	0.787
	Doublet	0.354	0.452	-----	21.85	0.385

*Isomer shift values are relative to α-Fe metal foil ($\delta = 0.0$ mm/s), (): tetrahedral, []: octahedral

The isomer shift at room temperature for A and B site were found to be in the range 0.224 mm/s to 0.315 mm/s and 0.261 mm/s to 0.365 mm/s, respectively, relative to

the α-Fe metal foil which are consistent with the high spin Fe^{3+} ionic state [221]. Furthermore, the observed isomer shift values are significantly lower than the expected value, 0.8 mm/s for Fe^{2+} ions, hence the formation of Fe^{2+} ions in the present ferrite system during sintering is ruled out [222-224]. Except for the paramagnetic doublet for composition, $x = 0.6$ ($\Delta = 0.452$ mm/s to 1.095 mm/s, $\delta = 0.309$ mm/s to 0.354 mm/s and $R_A = 2.90$ % to 21.85 %), the quadrupole splitting 'Δ' values were nearly 0.0 mm/s, suggesting that Fe^{3+} ions show cubic symmetry of polyhedron.

4.6. Studies on solid state properties of sintered $Ni_{0.5-x}Mn_xZn_{0.5}Fe_2O_4$ ($x = 0.0-0.5$) ferrites

The sintered $Ni_{0.5-x}Mn_xZn_{0.5}Fe_2O_4$ ($x = 0.0-0.5$) ferrites were analyzed for their solid state properties such as d.c. resistivity, dielectric properties, a.c. susceptibility, hysteresis characteristics and magnetic permeability measurements.

4.6.1. DC resistivity studies on sintered $Ni_{0.5-x}Mn_xZn_{0.5}Fe_2O_4$ ($x = 0.0-0.5$) ferrites

The d.c. resistivity measurements were carried out on the silver coated pellets of sintered ferrite samples using two probe method. The details of resistivity measurement are discussed in the section 2.3.11. of chapter 2. The resistivity values were calculated using expression 2.27 given in the same section.

4.6.1.1. Thermal variation of d.c. resistivity

The thermal variation of log resistivity 'log ρ' of sintered $Ni_{0.5-x}Mn_xZn_{0.5}Fe_2O_4$ ($x = 0.0-0.5$) ferrites is represented in the Fig. 4.27, while the room temperature resistivity and activation energy values are given in the Table 4.16. The sintered $Ni_{0.5-x}Mn_xZn_{0.5}Fe_2O_4$ ($x = 0.0-0.5$) ferrites shows decrease in the resistivity with increasing

temperature displaying a typical semiconducting (NTC) behavior. The log ρ versus 10^3 / T (K^{-1}) graph of each ferrite can be divided into three linear regions. The first region extends upto 390 K where change in the slope was observed. This region was found to be almost independent of Mn substitution and hence the conduction in this region can be attributed to the impurities as reported [260-262]. The second region of slope change was found to depend on the Mn content and hence, the transition in this region can be attributed to the magnetic phase changes from ferrimagnetic to paramagnetic state and the temperature at which this transition takes place is the Curie temperature. The third region represents the conductivity in paramagnetic region.
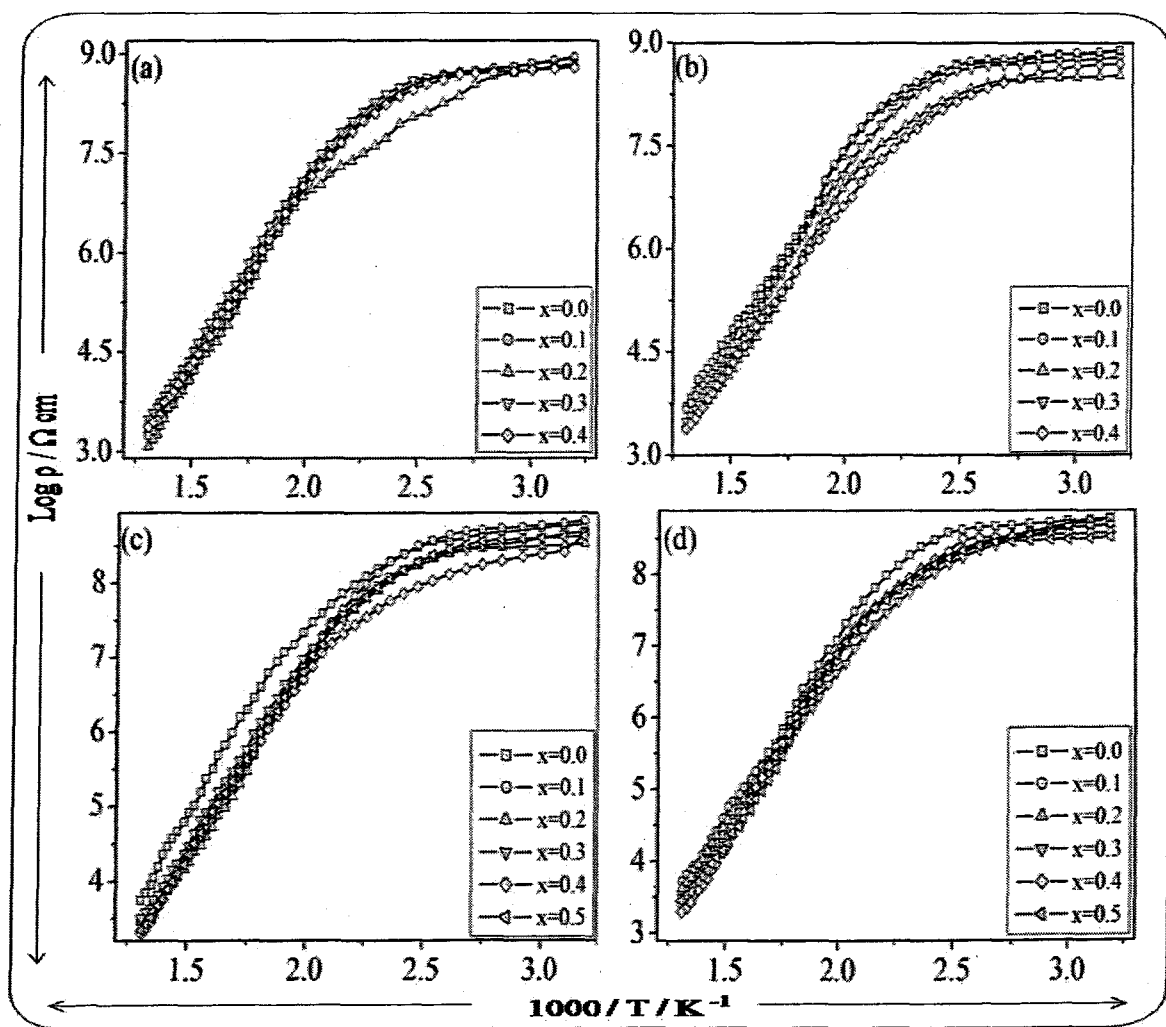
Fig.4.27. Variation of log of d.c. resistivity with 10^3 / T of $Ni_{0.5-x}Mn_xZn_{0.5}Fe_2O_4$ (x = 0.0-0.5) ferrites sintered at a) 1100°C / 1h, b) 1150°C / 1h, c) 1200°C / 1h and d) 1250°C / 1h

The activation energy 'E_a' corresponding to ferrimagnetic and paramagnetic region of all ferrites was calculated using the formula 2.28 given in the section 2.311. The activation energy values for sintered ferrites are given in the Table 4.16. In the low temperature (ferrimagnetic) region the activation energies were observed in the range 0.258 eV to 0.491 eV. At higher temperatures, the concentration of Fe^{2+} and Mn^{3+} is known to increase by the process [263]:

$$Ni^{2+} + Fe^{3+} \leftrightarrow Ni^{3+} + Fe^{2+} \qquad ----------------\{2.40\}$$

$$Fe^{3+} + Mn^{2+} \leftrightarrow Fe^{2+} + Mn^{3+} \qquad ----------------\{2.41\}$$
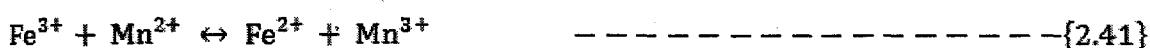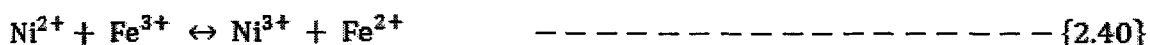
The increased concentration of Fe^{2+} and Mn^{3+} ions increases the hopping and thereby increases the conductivity at higher temperatures. It has been reported that [178,264] the activation energy associated with the above processes is in the range of 0.3 eV to 0.5 eV. The observed values in the range 0.349 eV to 0.612 eV for sintered $Ni_{0.5-x}Mn_xZn_{0.5}Fe_2O_4$ ($x = 0.0$-0.5) ferrites suggest the polaron hopping conduction mechanism.

4.6.1.2. Compositional variation of d.c. resistivity

The d.c. resistivity values of sintered ferrites at room temperature are given in Table 4.16. The resistivity values were found to be in the range 10^8 to 10^7 Ωcm. In general, the the resistivity decreases with increasing Mn substitution. The observed variation in the resistivity can be explained considering the distribution of cations in tetrahedral (A) and octahedral [B] sites in spinel lattice. It is well known fact that iron exists in ferrite systems primarily as Fe^{3+}, while manganese exists primarily as Mn^{2+}. There is also a small probability of finding Fe and Mn in +2 and +3 states, respectively. The introduction of any small amount of Mn^{3+} at the cost of Ni^{2+} creates charge imbalance in the lattice. ions.

Table 4.16. Room temperature d.c. resistivity and activation energy data of the sintered $Ni_{0.5-x}Mn_xZn_{0.5}Fe_2O_4$ ($x = 0.0$-0.5) ferrites

x	RT dc resisitivity 'ρ' x 10^7/ Ω cm				Activation energy 'Ea' / eV							
					1100°C		1150°C		1200°C		1250°C	
	1100°C	1150°C	1200°C	1250°C	E_f	E_p	E_f	E_p	E_f	E_p	E_f	E_p
0.0	67	61	26	10	0.306	0.396	0.306	0.376	0.296	0.354	0.258	0.349
0.1	78	66	55	50	0.491	0.570	0.465	0.478	0.434	0.462	0.318	0.400
0.2	73	64	53	34	0.488	0.612	0.461	0.556	0.428	0.544	0.367	0.532
0.3	71	62	49	29	0.436	0.556	0.393	0.546	0.347	0.538	0.334	0.521
0.4	68	60	45	24	0.428	0.523	0.422	0.463	0.405	0.482	0.349	0.463
0.5	---	---	43	39	---	---	---	---	0.376	0.508	0.299	0.475

In order to maintain charge neutrality, Fe^{3+} ions get converted to Fe^{2+} and as a result the conductivity increases due to increase in hopping between Mn^{3+} and Mn^{2+} and between Fe^{2+} and Fe^{3+}

4.6.1.3. Effect of sintering temperature on d.c. resistivity

The d.c. resistivity values of the sintered $Ni_{0.5-x}Mn_xZn_{0.5}Fe_2O_4$ (x = 0.0-0.5) ferrites have been summarised in the Table 4.16. These values are much higher than the reported [178,265-266]. It was observed that the resistivity decreases with increase in sintering temperature. During sintering the grains coalesce to reduce total surface energy of the system. The grain size therefore, increases with increase in sintering temperature. The average grain sizes of the sintered ferrites are presented in Table no. 4.14. The average grain sizes increases from 0.56 μm to 1.86 μm with increasing sintering temperature from 1100°C to 1250°C. The decrease in resistivity with increase in sintering temperature can be attributed to increase in average grain size. The resistivity of polycrystalline materials, in general, increases with decrease in grain size [267] because smaller grains has a larger number of grain boundaries which acts as scattering centres to the flow of electrons thereby increasing the grain boundary resistance and also the resistivity. Also, with small grain size the oxidation of Fe^{2+} advances faster due to larger surface to volume ratio [268]. Therefore, in smaller grains re-conversion of any Fe^{2+} formed during the sintering process, back to Fe^{3+} takes place readily. At lower sintering temperature (≤ 1200°C) the probability of the existence of Fe^{2+} ions is relatively low. And, also the conduction in ferrites being primarily due to hopping of electrons between ions of the same element but of different valencies present at equivalent sites [225], one can assume that the samples sintered at lower temperature (≤ 1200°C) will have high resistivity. The relatively lower values of resistivity of the samples sintered at 1250°C [Table 4.16] are due to the fact that at higher

235

sintering temperatures there is bound to be some Zn loss by increased volatilization [269]. This Zn loss causes unsaturated oxygen bonds which tend to saturate by bonding with the surrounding Fe^{3+} ions, at least in part, reducing latter to Fe^{2+}, which increases the Fe^{2+} ion concentration, resulting in increased hopping. Non-uniform grain sizes obtained for samples sintered at 1250°C may also contribute to their lower resistivity.

4.6.2. Thermoemf / Seebeck coefficient measurements

The plots of Seebeck coefficient 'α' with temperature of some representative $Ni_{0.5-x}Mn_xZn_{0.5}Fe_2O_4$ (x = 0.0-0.5) ferrites sintered at 1200°C and 1250°C are represented in the Fig. 4.28. Similar plots were observed for sample sintered at 1100°C and 1150°C. The values of Seebeck coefficient 'α' were found to be negative throughout the temperature range from 393 K to 720 K. The negative value of Seebeck coefficient 'α' indicates that the samples are n-type semiconductors with electron as dominant charge carriers.
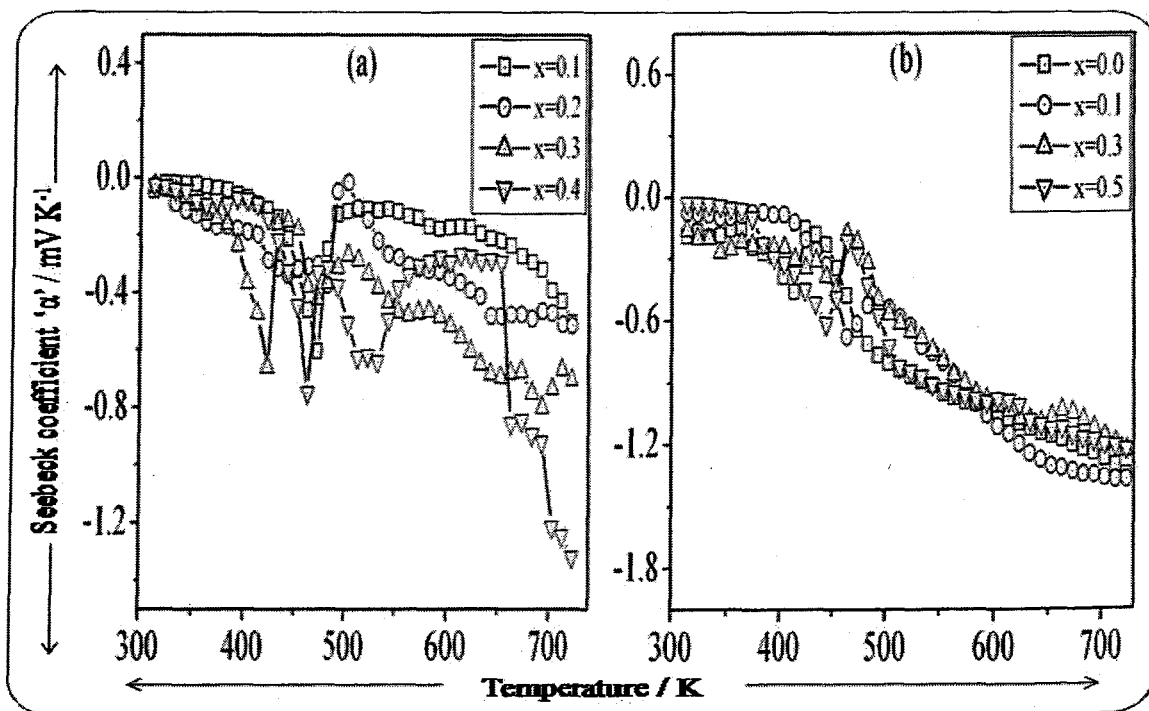
Fig.4.28. Variation of Seebeck coefficient 'α' with temperature of some representative $Ni_{0.5-x}Mn_xZn_{0.5}Fe_2O_4$ (x = 0.0-0.5) ferrites sintered at a) 1200°C / 1h and b) 1250°C / 1h

From the thermal variation of ferrites sintered at 1200°C / 1h, it was observed that

the absolute value of Seebeck coefficient 'α' in the paramagnetic (after Curie temperature)

region is greater than ferrimagnetic (before Curie temperature) region which can be

interpreted in terms of spin polaron formation where after Curie temperature the moving

electron will tend to polarise the ion spins near to it, in ferromagnetic sense. Hence, if the

band is sufficiently narrow the electron will be trapped in the ferromagnetic spin cluster

[270]. Therefore the number of electron in the conduction process reduces and hence, the

absolute value of thermoelectric power increases [271]. Thus, these results support polaron

hopping conduction mechanism.

4.6.3. Dielectric properties of sintered $Ni_{0.5-x}Mn_xZn_{0.5}Fe_2O_4$ (x = 0.0-0.5) ferrites

The frequency variation of dielectric constant and dielectric loss in the range from

100 Hz to 10 MHz were studied at room temperature as well as higher temperature upto

250°C of all the sintered $Ni_{0.5-x}Mn_xZn_{0.5}Fe_2O_4$ (x = 0.0-0.5) ferrites.

4.6.3.1. Frequency variation of dielectric constant and dielectric loss

The frequency variation of the dielectric constant of the ferrites has been studied

from room temperature to 250°C. Each sintered $Ni_{0.5-x}Mn_xZn_{0.5}Fe_2O_4$ (x = 0.0-0.5) ferrites

exhibits normal dielectric behavior wherein the dielectric constant decreases rapidly up to

1 kHz, followed by a slow decrease from 1 kHz to 100 kHz, and was nearly independent

of frequency above 100 kHz. The frequency variation of dielectric constant and dielectric

loss of ferrites is depicted in the Fig. 4.29 (a-d). As observed in Fig. 4.29, the dielectric

constant values are quite low at room temperature, which is also observed by other group

who prepared the similar ferrites series by citrate method [87]. However, the groups

[29,241] who prepared the similar ferrites by ceramic method reported about 10^3 times

higher values. The lower values of dielectric constant is due to the fact that wet chemical methods like precursor method forms homogeneous ferrites with low Zn losses unlike ferrite prepared by ceramic method which are generally inhomogeneous with higher Zn losses and hence higher dielectric constant values.
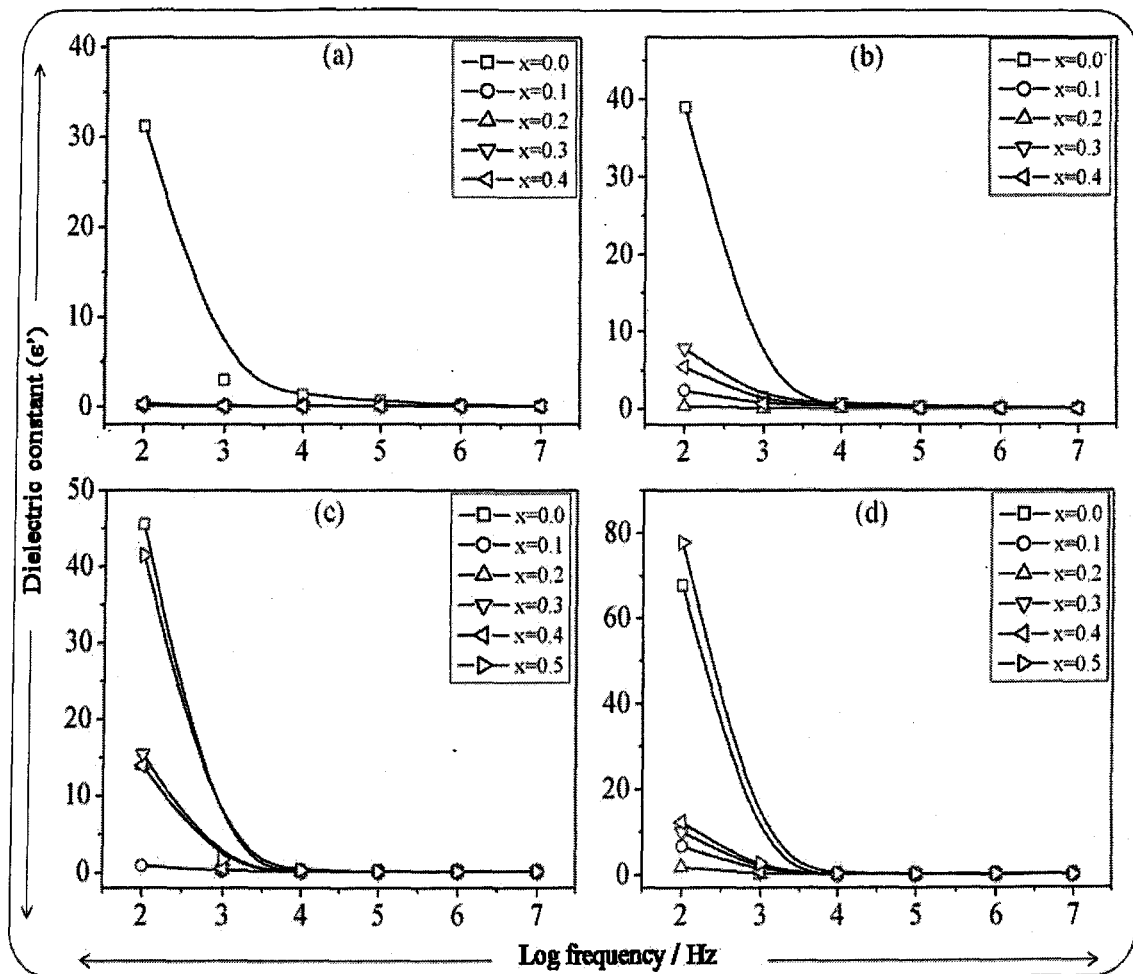
Fig.4.29. Room temperature frequency variation of dielectric constant of $Ni_{0.5-x}Mn_xZn_{0.5}Fe_2O_4$ (x = 0.0-0.5) ferrites sintered at a) 1100°C / 1h, b) 1150°C / 1h, c) 1200°C / 1h and d) 1250°C / 1h

The observed results of dielectric constant versus variable frequency can be explained on the basis of space charge polarization which is a result of the presence of higher conductivity phases (grains) in the insulating matrix (grain boundaries) of

238

dielectrics, causing localized accumulation of charge under the influence of an electric field [29]. The electrons reach the grain boundaries through hopping and if the resistance of the grain boundary is high enough, electrons pile up at the grain boundaries and produce polarization. However, as the frequency of the applied field is increased, there is phase lag between the moving electrons and applied field making the electrons to reverse the direction of motion. This decreases the probability of electron reaching the grain boundaries and as a result, the polarization decreases. Therefore, the dielectric constant decreases with an increasing frequency of the applied field [29]. The frequency variation of dielectric loss tangent 'tan δ' is represented in the Fig. 4.30. The loss tangent decreases initially with increasing frequency, followed by the appearance of a resonance peak in the frequency range from 100 kHz to 1MHz in ferrites sintered at $1100^{\circ}C$ and $1150^{\circ}C$. The value of the loss tangent obtained for all the sintered ferrites are in the range 10^{-2} to 13 in a frequency range from a 100 Hz to 1 MHz. These values of the loss tangent are lower than those reported for ferrites prepared by the conventional ceramic method [29,241,272]. The initial decrease of loss tangent with an increase in frequency is explained on the basis of Koops' theory [29] while, the appearance of a resonance peak is due to the matching of the time period of the applied electric field with that of the corresponding relaxation phenomena and the resonance is due to the jump of ion between more than one of its equilibrium positions. If an ion has more than one equilibrium position, say two positions X and Y of equal potential energies, separated by the potential barrier, the probabilities of jumping of ions from X to Y and from Y to X are the same. Depending upon this probability, the ion exchanges position between the two states with some frequency, called the natural frequency of jump between the two positions. When an external alternating electric field of same frequency is applied, maximum electrical energy is transferred to the oscillating ions and power loss shoots up, thereby resulting in resonance. Since Mn^{2+} $(r =$

0.82 A°) ion has higher ionic radius than that of Zn^{2+} (r = 0.75 A°) ion, the Mn^{2+} ion pushes the neighbouring ions and that results in the separation between the equilibrium positions of the next neighbouring ions. Consequently, the jump probability between the two next neighbouring positions increases. This results in an increase in the jump frequency and therefore a shift in the resonance peak towards higher frequency. This behavior is also observed by Singh *et al.* [87].
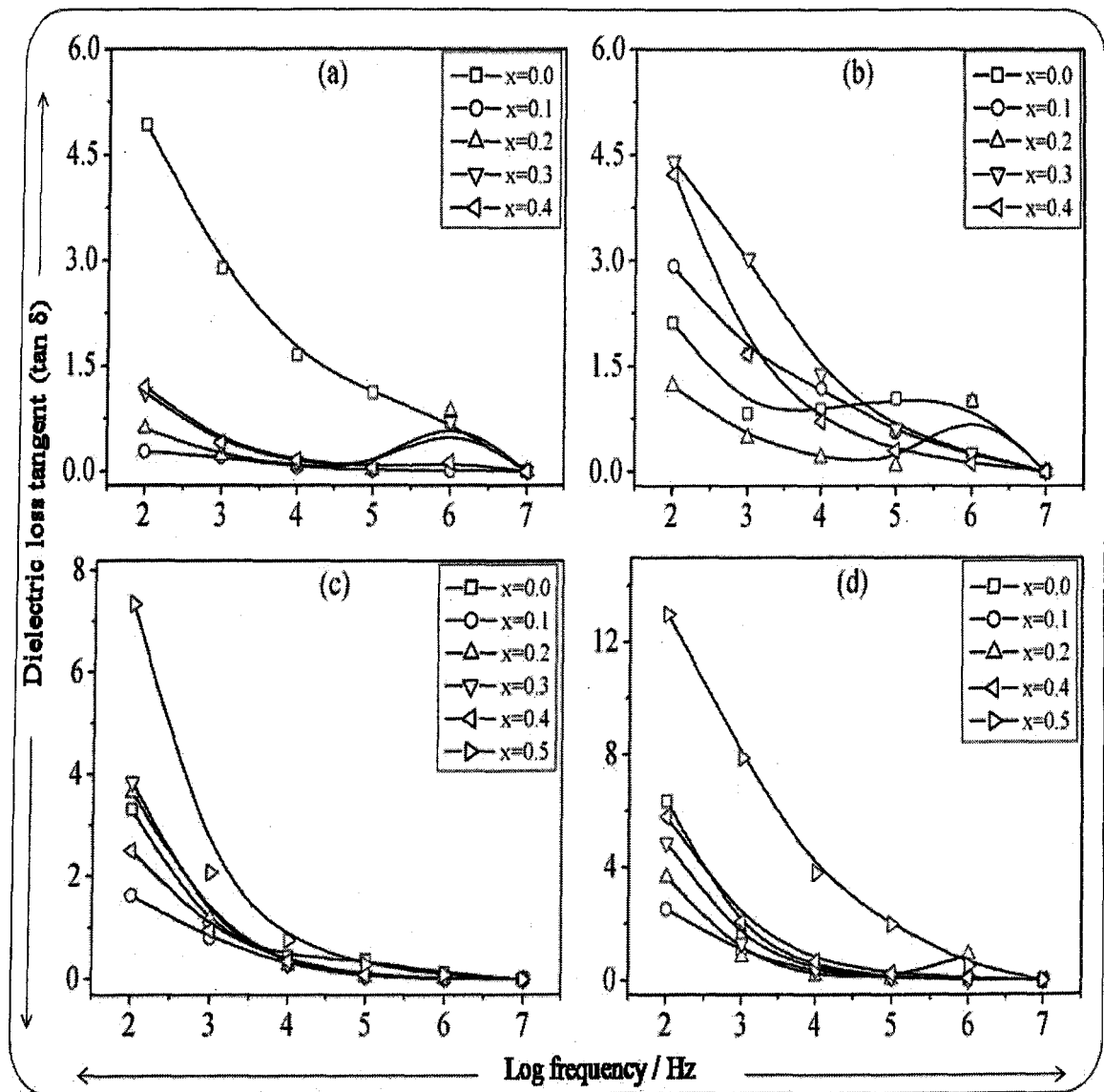
Fig.4.30. Room temperature frequency variation of dielectric loss tangent of

$Ni_{0.5-x}Mn_xZn_{0.5}Fe_2O_4$ (x = 0.0-0.5) ferrites sintered at a) 1100°C / 1h, b) 1150°C / 1h,

c) 1200°C / 1h and d) 1250°C / 1h

4.6.3.2. Temperature variation of dielectric constant and dielectric loss

The temperature variation of dielectric constant at 100 Hz of all ferrites is shown in the Fig. 4.31. The dielectric constant increases with temperature at all the frequencies. The increase in the value of the dielectric constant is very large at lower frequencies (100 Hz), while at higher frequencies (10 MHz) the increase is very small. The dielectric constant of any material, in general, is due to dipolar, electronic, ionic and interfacial polarizations [238]. At low frequencies, dipolar and interfacial polarizations are known to play the most important role.
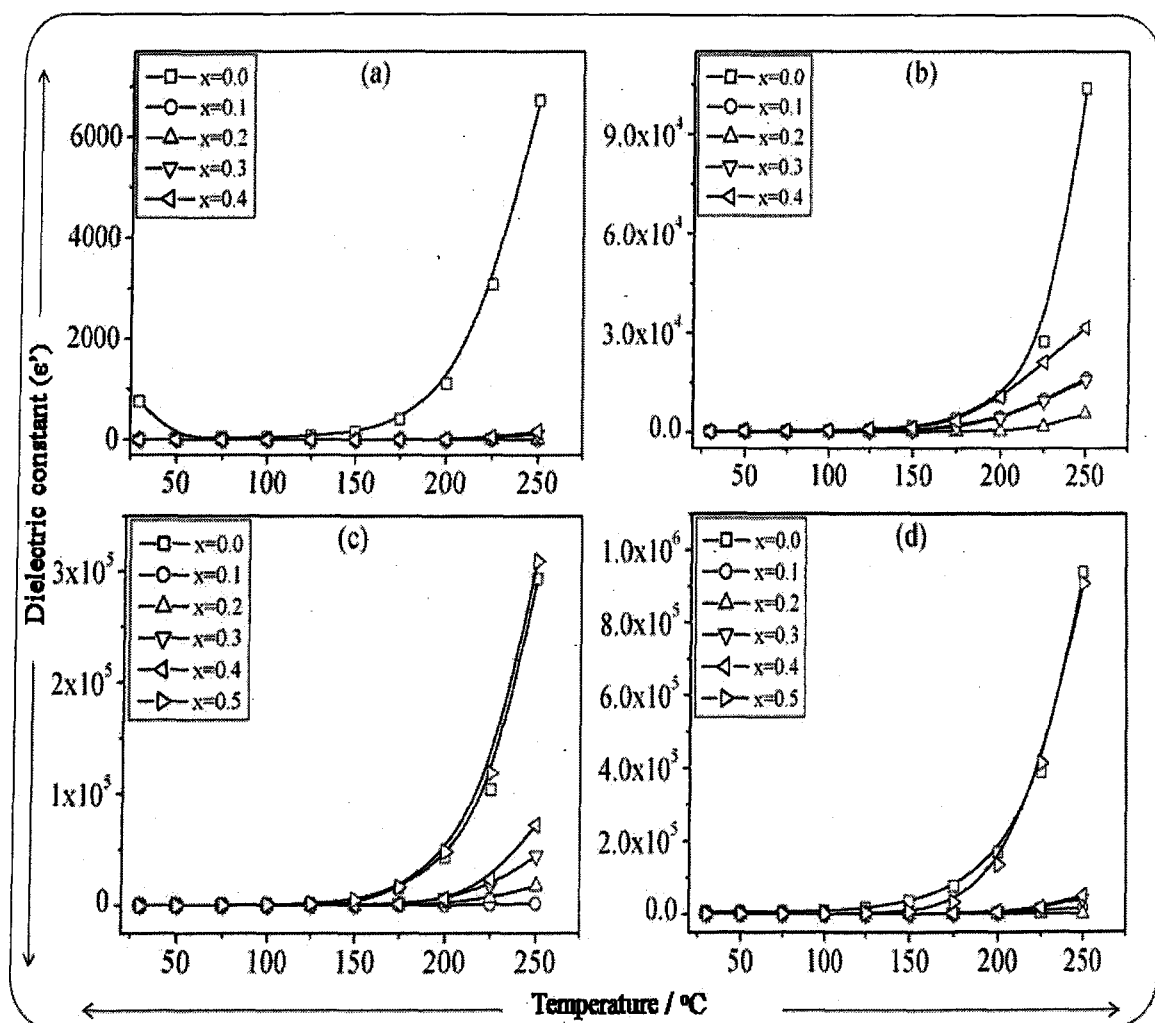
Fig.4.31. Temperature variation of dielectric constant of $Ni_{0.5-x}Mn_xZn_{0.5}Fe_2O_4$ (x = 0.0-0.5) ferrites sintered at (a) 1100°C / 1h, (b) 1150°C / 1h, (c) 1200°C / 1h and (d) 1250°C / 1h

Both these polarizations are strongly temperature dependent. Whereas, the interfacial polarization increases with temperature due to creation of crystal defects, dipolar polarization decreases with an increase in the temperature. The rapid increase in the dielectric constant with an increase in the temperature at low frequencies suggests that the effect of temperature is more pronounced on the interfacial than on the dipolar polarization. At higher frequencies, electronic and ionic polarizations are the main contributors [238] and their temperature dependence is insignificant therefore it results in a constant and low value of the dielectric constant at higher frequencies. The temperature variation of dielectric loss at frequency of 100 Hz is represented in the Fig. 4.32.
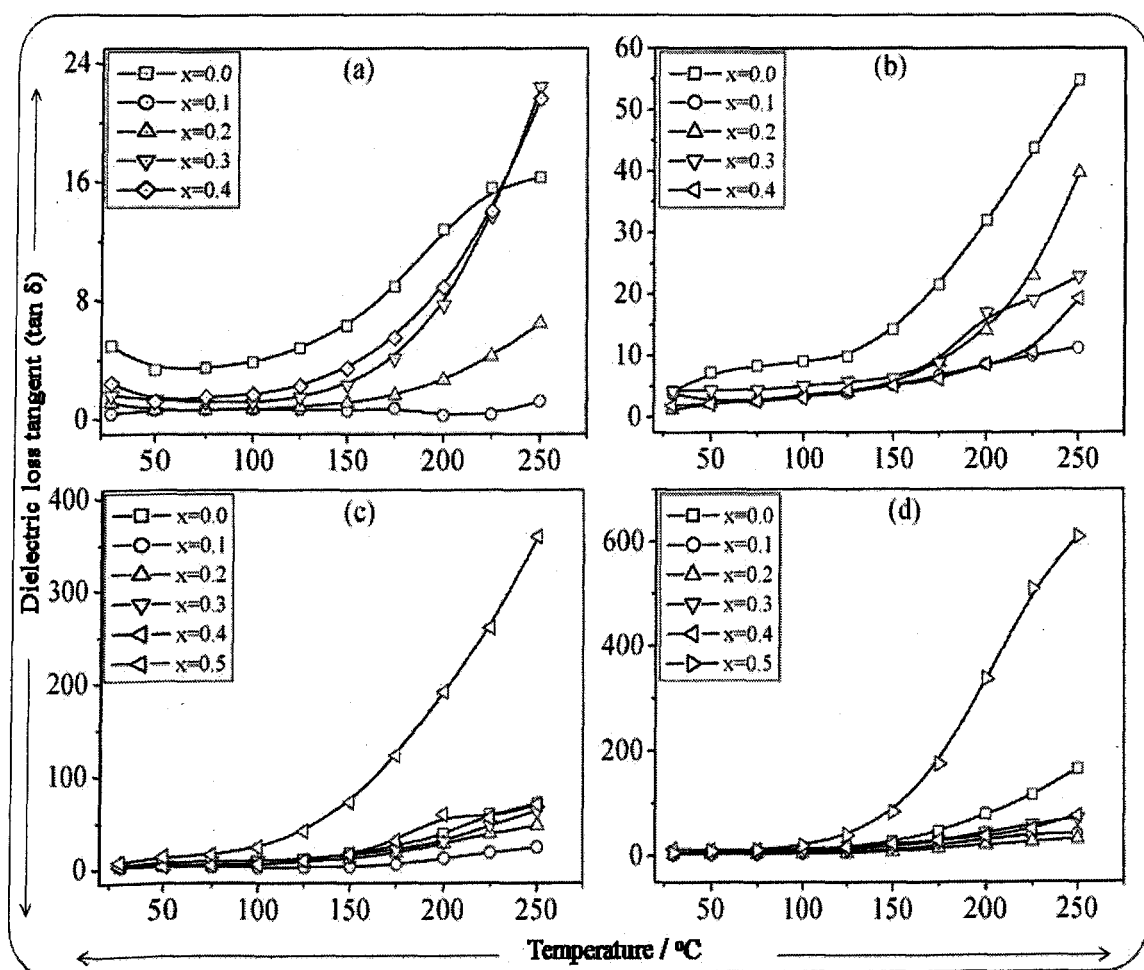
Fig.4.32. Temperature variation of dielectric loss tangent of $Ni_{0.5-x}Mn_xZn_{0.5}Fe_2O_4$

($x = 0.0$-0.5) ferrites sintered at a) $1100°C$ / 1h, b) $1150°C$ / 1h, c) $1200°C$ / 1h

and d) $1250°C$ / 1h

4.6.3.3. Compositional variation of dielectric constant

The room temperature values of dielectric constant (ε) and dielectric loss (tan δ) at 1 kHz for all the sintered ferrites are given in the Table 4.17. It was observed that the dielectric constant increases with an increase in Mn concentration except for composition, $x = 0.3$, where it shows a sudden rise. The exceptional behavior for composition, $x = 0.3$ is also reported by others [87, 265]. In mixed spinel system such as Mn-Ni-Zn ferrites, Zn and Ni ions occupy tetrahedral (A) and octahedral [B] sites, respectively [178,273]. The Mn^{2+} and Fe^{3+} ions are known to exist at both A and B sites [273-274]. When Mn^{2+} is added in place of Ni^{2+}, going as Mn^{3+} in the system will reduce some of the Fe^{3+} to Fe^{2+} so as to maintain the charge balance. This increased concentration of Fe^{2+} will increase the hopping between Fe^{3+} and Fe^{2+} ions, thereby decreasing the resistance of the grain as a result the probability of the electrons reaching the grain boundary increases causing increase in polarization and hence the increase in dielectric constant as observed.

4.6.3.4. Effect of sintering temperature on dielectric properties

The dielectric constant in few compositions i.e. $x = 0.1$, 0.3 and 0.4, initially increases upto 1150°C then decreases at 1200°C and finally increases at 1250°C, in compositions $x = 0.2$ and 0.5, dielectric constant increases with sintering temperature while in composition $x = 0.0$, it decreases upto 1200°C and then increases drastically at 1250°C. The dielectric loss also shows mixed trend wherein composition from $x = 0.0$ to $x = 0.3$ shows initial increase and then decrease while, in composition, $x = 0.4$, it decreases upto 1150°C. The $x = 0.5$ composition shows increase with increasing sintering temperature. The sintering of the ferrites at higher temperatures can results in the loss of Zn due to volatilization [268]. As a result of Zn loss, the associated oxygen bonds become

unsaturated. These unsaturated bonds get associated with the neighboring Fe^{3+} ions and convert later to Fe^{2+} ions.

Table 4.17. Dielectric constant and dielectric loss of sintered $Ni_{0.5-x}Mn_xZn_{0.5}Fe_2O_4$ ($x = 0.0-0.5$) ferrites

x	Dielectric constant (έ) / dielectric loss (tan δ) at 1kHz frequency							
	1100°C / 1h		1150°C / 1h		1200°C / 1h		1250°C / 1h	
	έ	tan δ	έ	tan δ	έ	tan δ	έ	tan δ
0.0	2.978	2.881	1.55	0.826	0.538	0.896	11.70	0.891
0.1	0.057	0.206	0.595	1.68	0.255	0.805	3.03	0.674
0.2	0.068	0.224	0.114	0.481	0.381	1.181	3.38	1.011
0.3	0.075	0.381	1.05	3.034	0.456	1.053	21.1	0.864
0.4	0.091	0.408	0.741	1.671	0.553	1.954	4.21	2.93
0.5	---	---	---	---	1.72	2.087	55.31	2.658

The Zn loss increases with the increase in sintering temperature and as a result, the Fe^{2+} concentration increases. Since, the Fe^{2+} ions are easily polarizable as compared to Fe^{3+} ions, the dielectric constant increases with the increasing sintering temperature. The lower values of dielectric constant and dielectric loss suggest the better homogeneity and lower Zn losses in the samples prepared by fumarato hydrazinate precursor method.

4.6.4. Magnetization studies

The magnetic properties such as saturation magnetization, coercivity, remanence were studied at room temperature for sintered $Ni_{0.5-x}Mn_xZn_{0.5}Fe_2O_4$ ($x = 0.0-0.5$) ferrites.

4.6.4.1. Compositional variation of magnetic properties

The magnetic hysteresis loops of $Ni_{0.5-x}Mn_xZn_{0.5}Fe_2O_4$ (x = 0.0-0.5) ferrites sintered at $1200°C$ / 1h are shown in the Fig. 4.33 and the values of various magnetic parameters are listed in the Table 4.18. The observed variations can be explained on the basis of cation distributions and exchange interaction between Fe^{3+} and Mn^{2+} ions at tetrahedral (A) and octahedral [B] sites. It is known [178] that Zn^{2+} and Ni^{2+} ions occupy A and B sites, respectively. Although Fe^{3+} and Mn^{2+} ions exist at both A and B sites, they have preference for the B and the A sites, respectively [178]. In ferrites, the saturation magnetization is the difference between the magnetization of B and A sublattices. The effect of composition on the saturation magnetization can be due to the redistribution of ions in A and B sites which can directly affect the net magnetization. When Mn^{2+} ions are substituted for Ni^{2+} ions, some of the Fe^{3+} ions migrate from A to the B sites in view of their site preference. This increases the Fe^{3+} ion concentration at B sites. As a result, the magnetic moment of B sub-lattice increases for small Mn^{2+} concentrations (upto, x =0.2) as explained on the basis of Neel two sublattice model [245]. However, as Mn^{2+} concentration increases (x > 0.2), the Fe^{3+} ions left at A site being small in number, the A-B interaction experienced by B site Fe^{3+} ions decreases. Also, the increased number of Fe^{3+} ions at the B site increases the B-B interaction, resulting in spin canting [247-249,275]. Consequently, the magnetizations of B sublattice decreases. Similar variations of saturation magnetization are also reported in the literature [15,107]. The observed values of saturation magnetization are higher than those reported for sintered $Ni_{0.5-x}Mn_xZn_{0.5}Fe_2O_4$ (x = 0.0-0.5) ferrites system [86]. The coercivity was found to increase upto x = 0.1, then decreases at x = 0.2. At x = 0.3 it increases again but decreases at x = 0.4 and at x = 0.5 it is high again. This trend was found to be same at all sintering

temperatures. Since, the coercivity is affected by grain size, porosity and anisotropy constant the observed zig-zag trend is due to the combined effect of all three factors.
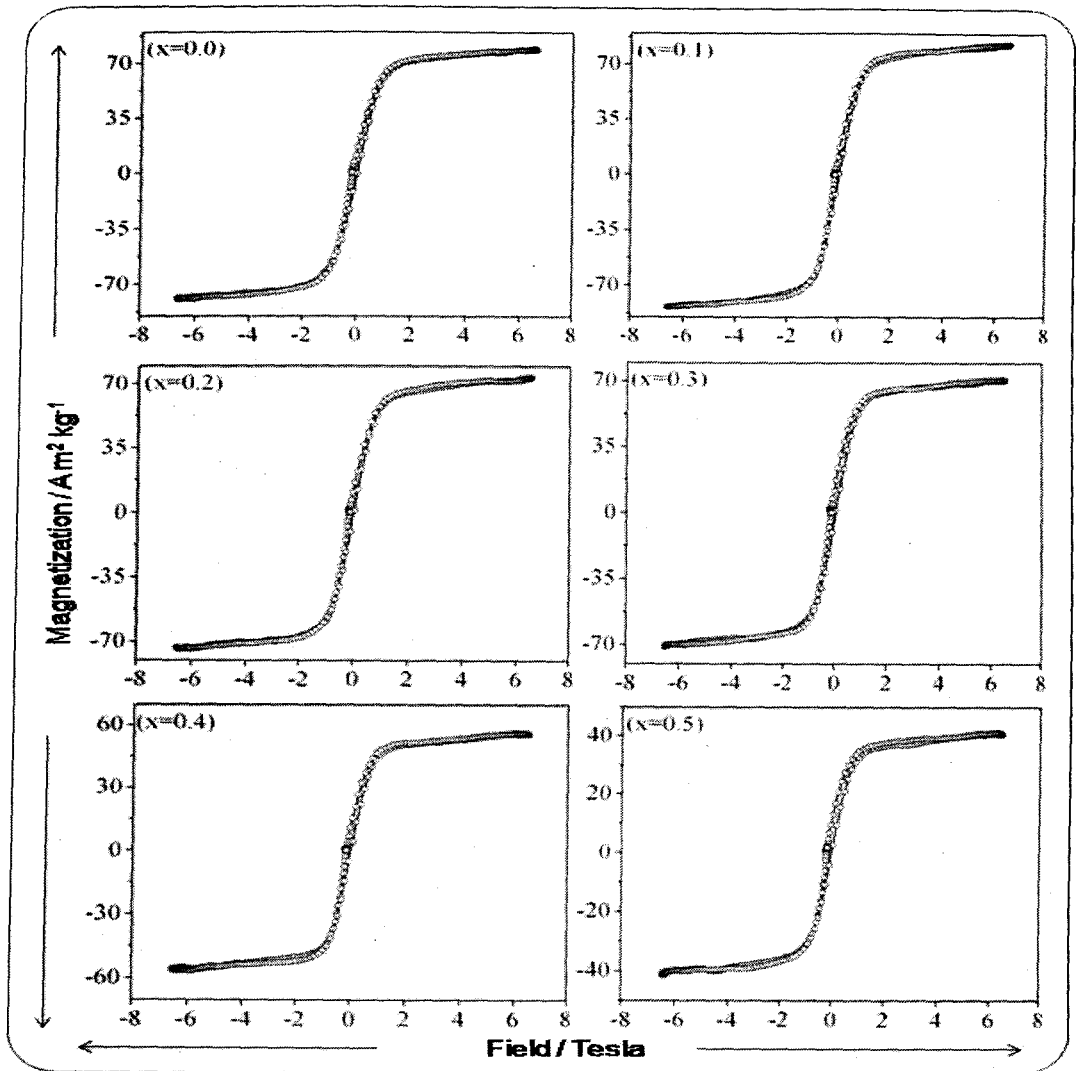
Fig.4.33. Hysteresis loops of $Ni_{0.5-x}Mn_xZn_{0.5}Fe_2O_4$ (x = 0.0-0.5) ferrites sintered at 1200°C / 1h

4.6.4.2. Effect of sintering temperature on magnetic properties

The saturation magnetization values of sintered $Ni_{0.5-x}Mn_xZn_{0.5}Fe_2O_4$ (x = 0.0-0.5) ferrites are listed in the Table 4.18. It was observed that the saturation magnetization increases with increase in the sintering temperature upto 1200°C.

Table 4.18. Magnetic hysteresis data of the sintered $Ni_{0.5-x}Mn_xZn_{0.5}Fe_2O_4$ ($x = 0.0$-0.5) ferrites

Property	Sintering temp. / °C	x					
		0.0	0.1	0.2	0.3	0.4	0.5
Saturation magnetisation (M_s) / A m² kg⁻¹	1100°C / 1h	69.4	73.1	63.8	61.0	46.5	---
	1150°C / 1h	73.4	76.9	70.8	62.4	50.4	---
	1200°C / 1h	75.6	79.3	74.2	63.7	55.4	41.3
	1250°C / 1h	74.6	78.5	73.0	62.5	54.3	40.6
Remanent magnetization (M_r) / A m² kg⁻¹	1100°C / 1h	5.19	3.96	9.83	13.11	14.9	---
	1150°C / 1h	3.33	3.45	4.65	8.27	9.32	---
	1200°C / 1h	2.35	2.78	2.12	5.07	6.10	2.11
	1250°C / 1h	1.08	1.12	1.50	1.78	2.11	2.75
Coercivity (H_c) x 10⁻³ / Tesla	1100°C / 1h	81.6	91.2	69.3	86.4	78.2	---
	1150°C / 1h	79.6	89.2	68.6	83.2	76.8	---
	1200°C / 1h	76.2	85.3	60.8	78.0	72.9	98.4
	1250°C / 1h	70.6	82.0	55.6	71.7	66.0	81.6

The increase in saturation magnetization is expected, since the saturation magnetization is directly related to the density and grain size [276-277] which increases with increasing sintering temperature and inversely to the magnetocrystalline anisotropy which decreases with increasing Mn substitution. The decrease in the saturation magnetization in the samples sintered at 1250°C may be due to the zinc loss due to volatilization at higher temperatures (>1200°C) which reduces Fe^{3+} ions to Fe^{2+} ions to maintained charge neutrality. This results in an increase in anisotropy [268] and decrease in the magnetic moment thereby decreasing the magnetization. This behavior was also observed by Verma *et al.* [94] for Zn substituted Mn-Ni ferrites. The overall trend of remanent magnetization observed in the present study is that it increases with Mn substitution upto $x = 0.4$ while, it decreases with sintering temperature as observed by others [292] in undoped Ni-Zn ferrites system.

4.6.5. Initial permeability measurements

The magnetic permeability may be considered to be measure of efficiency of magnetic materials. The inductance and measurements were carried out on toroidal core of 50 turns as function of frequency (100 Hz to 10 MHz) as well as temperature from room temperature to 723 K. The initial permeability was calculated using relation 2.35 given in the section 2.3.16 of chapter 2.

4.6.5.1. Frequency variation of initial permeability 'μ_i' and tan δ

The observed initial permeability 'μ_i' as a function of frequency at room temperature for sintered $Ni_{0.5-x}Mn_xZn_{0.5}Fe_2O_4$ ($x = 0.0-0.5$) ferrites is shown in Fig. 4.34. It was observed that initial permeability decreases very slowly with frequency up to about 6 MHz and then shows an increase at higher frequencies upto 10 MHz, the frequency limit

upto which the measurements carried out. This increase is attributed to the onset of resonance which is also reported in the literature [94,279-280]. Initial permeability in ferrites is due to domain wall displacement. The decrease in initial permeability with frequency is due to phase lag between the applied field and the domain wall displacement. In general, the resonance peak in ferrites is observed due to domain wall oscillations [280-281] at lower frequencies (1MHz to100 MHz) and another at higher frequencies (~1 GHz) due to Larmor precession of electron spins [279].
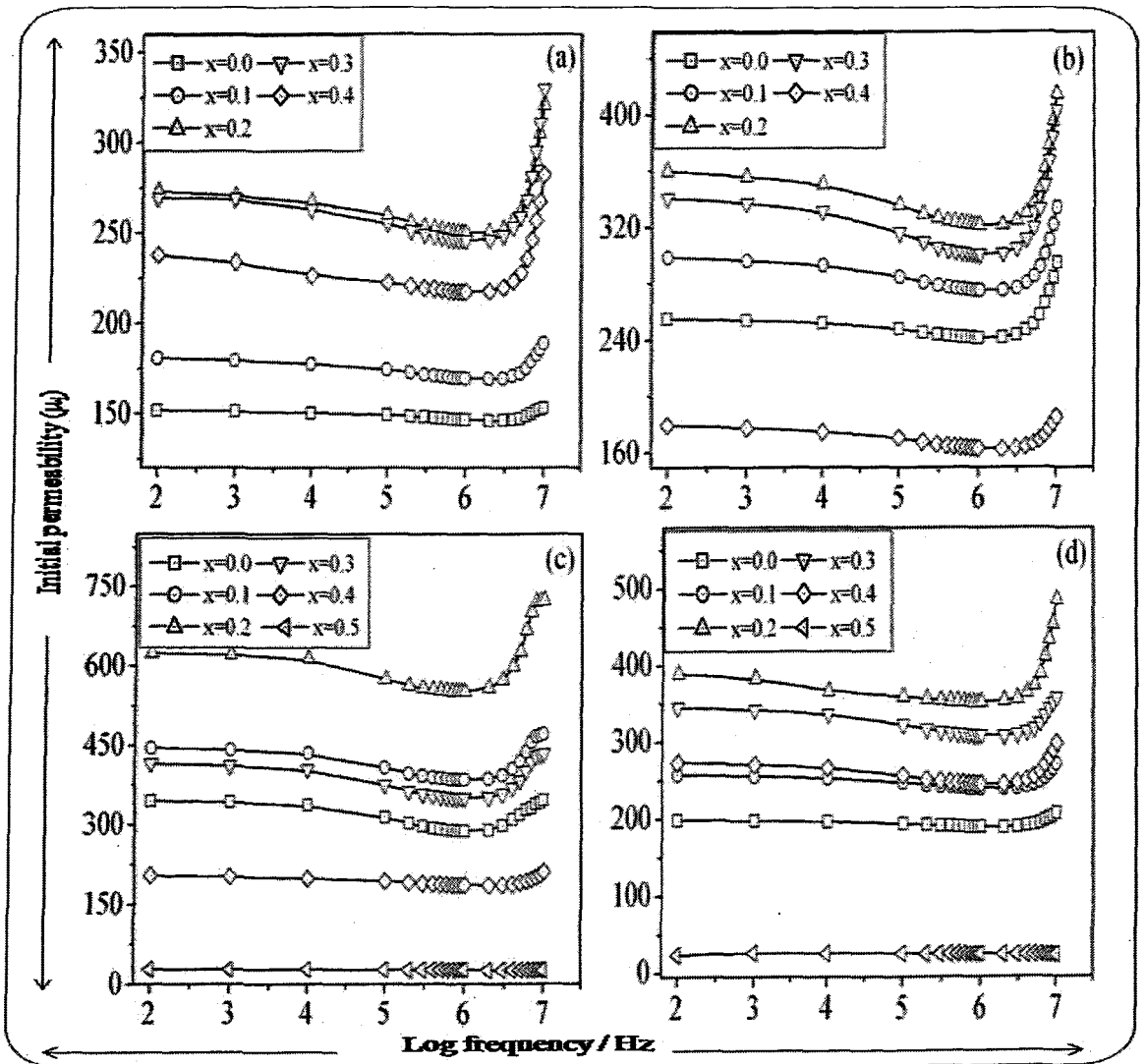
Fig.4.34. Room temperature frequency variation of initial permeability 'μ_i' of

$Ni_{0.5-x}Mn_xZn_{0.5}Fe_2O_4$ ($x = 0.0$-0.5) ferrites sintered at a) 1100°C / 1h, b) 1150°C / 1h,

c) 1200°C / 1h and d) 1250°C / 1h

The initial permeability values at 1 kHz are found to be in the range 26 to 621 [Table 4.19] for all sintered $Ni_{0.5-x}Mn_xZn_{0.5}Fe_2O_4$ (x = 0.0-0.5) ferrites. These values are higher than those reported in the literature [97]. The variation of tan δ with frequency for all ferrites sintered at different temperatures has been studied from 100 Hz to 10 MHz and the plots are shown in Fig. 4.35. The tan δ values are found to be in the range of 100 to 10^{-3} in the frequency range 100 Hz to 10 MHz. These values are low as compare to those reported for ferrites by other workers [178,280-281]. The loss is due to lag of motion of domain walls with respect to the applied alternating magnetic field and is attributed to imperfections in the lattice [282].
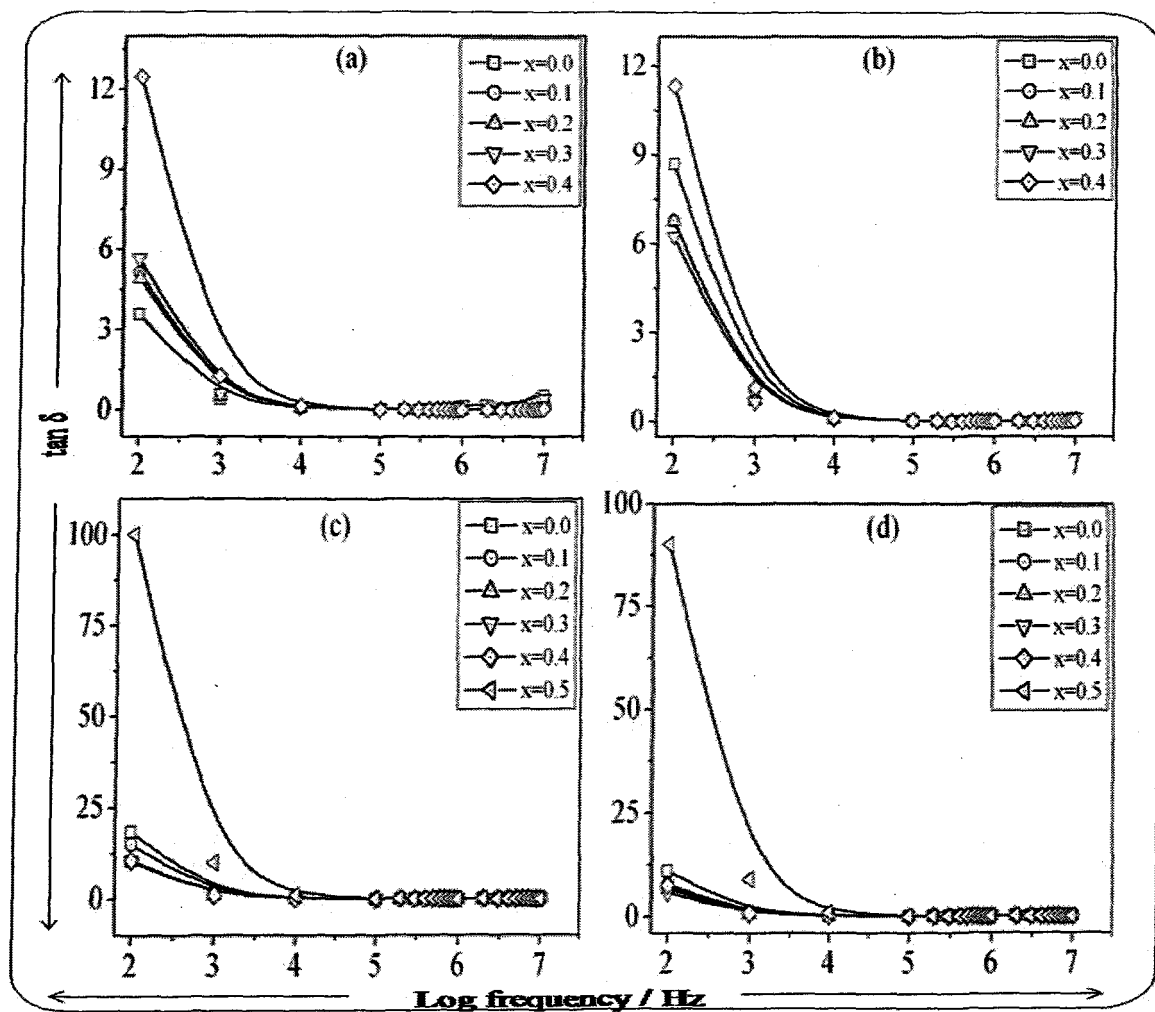
Fig.4.35. Room temperature frequency variation of tan δ of $Ni_{0.5-x}Mn_xZn_{0.5}Fe_2O_4$ (x = 0.0-0.5) ferrites sintered at a) 1100°C / 1h, b) 1150°C / 1h, c) 1200°C / 1h and d) 1250°C / 1h

4.6.5.2. Temperature variation of initial permeability 'μ_i' and tan δ

In order to study the temperature dependence of initial permeability 'μ_i', the permeability was determined and plotted as a function of temperature. The initial permeability-temperature 'μ_i - T' curves for all the sintered ferrite compositions as depicted in Fig. 4.36 show increase in initial permeability with temperature and rise to the peak value near Curie temperature, then drops sharply at Curie temperature, T_c.
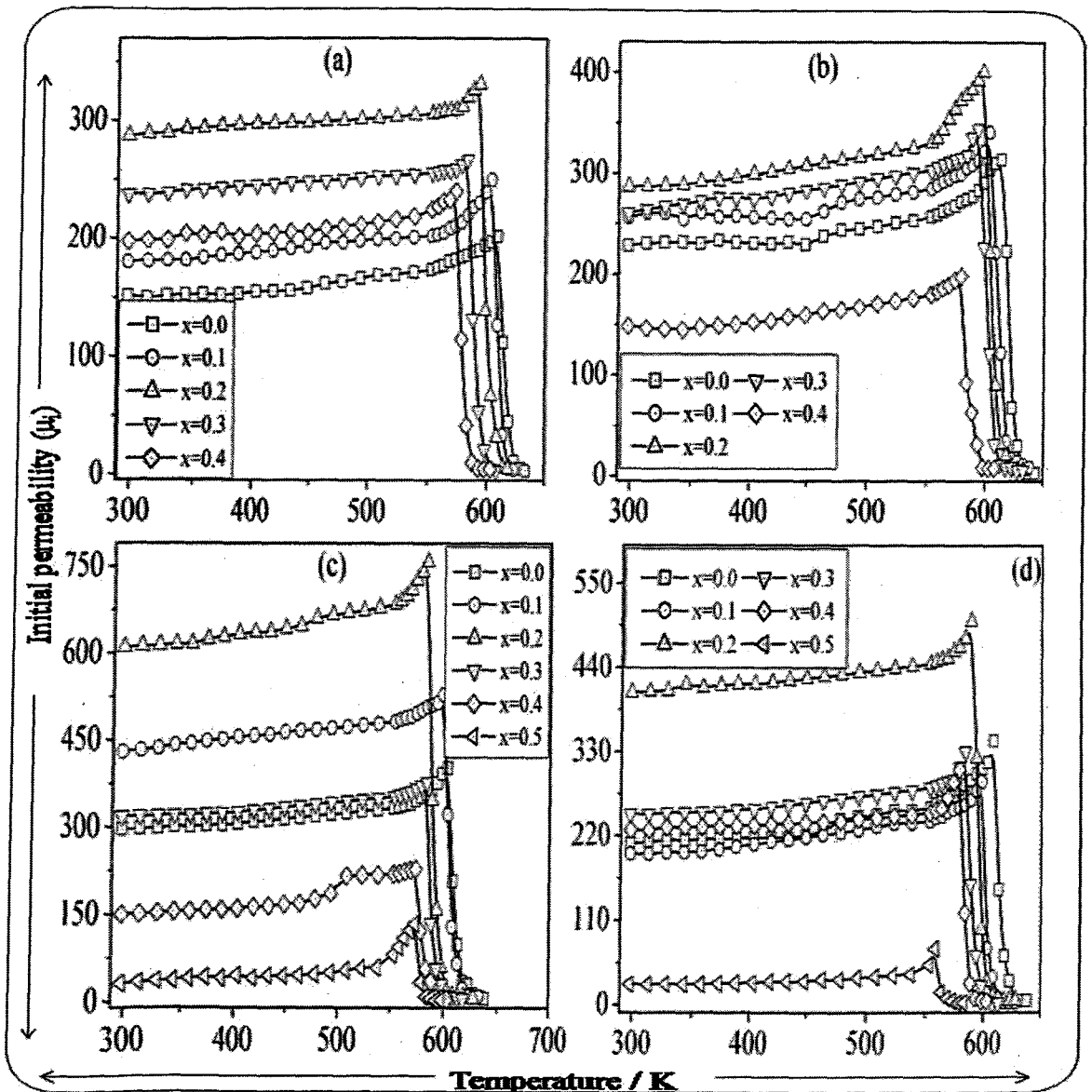
Fig.4.36. Temperature variation of initial permeability 'μ_i' at 100 Hz of $Ni_{0.5-x}Mn_xZn_{0.5}Fe_2O_4$ (x = 0.0-0.5) ferrites sintered at a) 1100°C / 1h, b) 1150°C / 1h, c) 1200°C / 1h and d) 1250°C / 1h

251

This sharp drop in initial permeability 'μ_i' supports the single phase formation and the homogeneity of the samples [283]. The Curie temperatures were determined by drawing tangent to the μ_i -T plots at a point of sharp fall in initial permeability. The profiles also shows a Hopkinson's peak near the Curie temperature which is a typical behavior exhibited by cubic structures [284].

Table 4.19. Initial permeability 'μ_i' and tan δ of $Ni_{0.5-x}Mn_xZn_{0.5}Fe_2O_4$ (x = 0.0-0.5) ferrites sintered at different temperatures and measured at 1 kHz.

x	Initial permeability (μ_i) / tan δ at 1 kHz							
	1100°C / 1h		1150°C / 1h		1200°C / 1h		1250°C / 1h	
	μ_i	tan δ	μ_i	tan δ	μ_i	tan δ	μ_i	tan δ
0.0	151.2	0.394	254.6	0.888	342.4	1.83	197.3	1.12
0.1	179.6	0.557	297.1	0.703	441.3	1.53	255.4	0.812
0.2	270.5	0.541	356.8	0.708	621.3	1.05	383.1	0.705
0.3	269.1	0.614	338	0.661	411.5	1.08	341.6	0.614
0.4	233.9	1.28	178.2	1.36	202.3	1.10	270.7	0.781
0.5	---	---	---	---	28.1	9.98	25.7	9.01

The variation of tan δ with temperature is shown in the Fig. 4.37. The tan δ is almost constant in the temperature range from room temperature to near Curie temperature, while above Curie temperature it increases exponentially.

4.6.5.3. *Compositional variation of initial permeability* 'μ_i'

The initial permeability and loss factor values of the sintered $Ni_{0.5-x}Mn_xZn_{0.5}Fe_2O_4$ (x = 0.0-0.5) ferrites at room temperature and 1 kHz frequency are listed in the Table 4.19 It is

clear from the Table 4.19 that initial permeability is increased upto $x = 0.2$ and then decreases. The initial permeability is dependent on many parameters such as stoichiometry, grain structure, composition, impurity contents, crystal anisotropy, and porosity. The value of initial permeability increases with the increase in grain size and stoichiometry [280,285] and decreases with the increase in porosity and decrease in the magnetocrystalline anisotropy [280, 286-287].
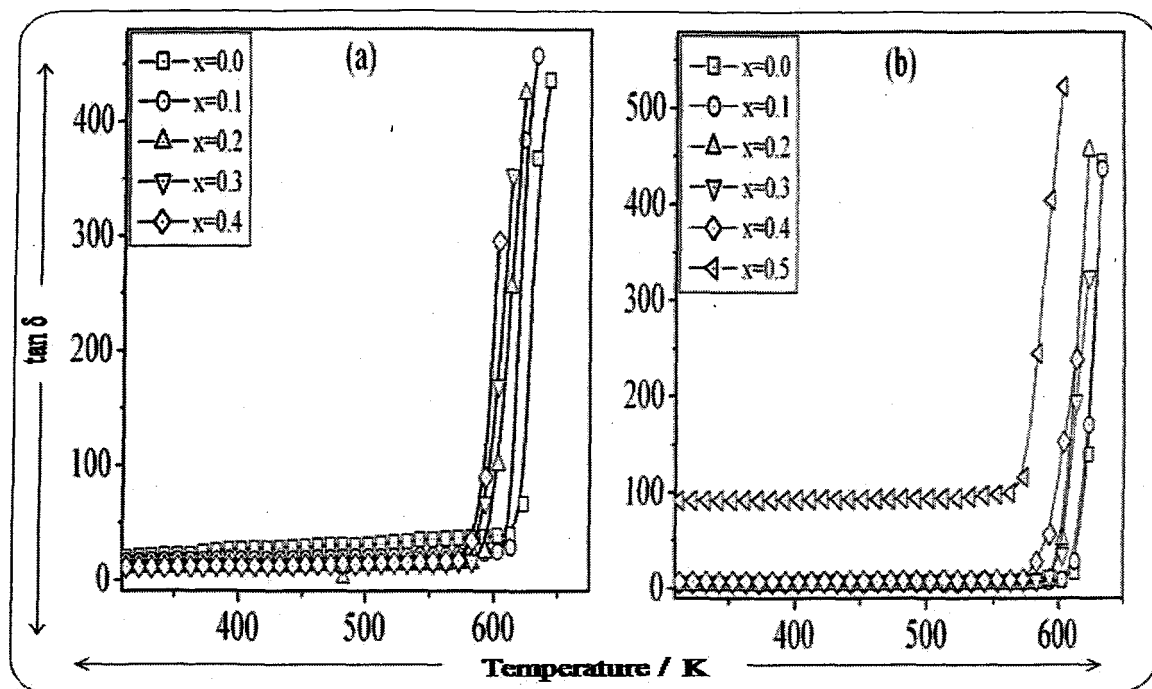
Fig.4.37. Temperature variation of tan δ at 100 Hz of $Ni_{0.5-x}Mn_xZn_{0.5}Fe_2O_4$ ($x = 0.0-0.5$) ferrites sintered at a) 1100°C / 1h and b) 1200°C / 1h

It has a major contribution from domain wall motion, but a smaller effect due to spin rotation [280]. The initial increase in initial permeability suggests that the effect of stoichiometry and magnetocrystalline anisotropy play a dominant role at lower Mn substitution ($x \leq 0.2$). This means that as the Mn concentration increases, the anisotropy constant (K_1) decreases, and thus the initial permeability increases at lower Mn substitution.

Table 4.20. Curie temperatures determined from d.c. resistivity, a.c. susceptibility and initial permeability studies of $Ni_{0.5-x}Mn_xZn_{0.5}Fe_2O_4$ (x = 0.0-0.5) sintered at different temperatures

Curie Temperature / K	Sintering temp. / °C	x					
		0.0	0.1	0.2	0.3	0.4	0.5
Dc resistivity	1100°C / 1h	628	614	595	583	578	--
$(\log \rho - 10^3 / T)$	1150°C / 1h	626	616	603	590	571	--
plots	1200°C / 1h	645	631	600	591	574	556
	1250°C / 1h	641	633	597	586	560	551
Ac susceptibility	1100°C / 1h	623	615	612	594	585	
$(\chi_T / \chi_{RT} - T)$	1150°C / 1h	626	616	610	597	587	
plot	1200°C / 1h	629	618	611	598	588	580
	1250°C / 1h	624	619	610	593	589	576
Initial permeability	1100°C / 1h	628	619	611	599	589	
$(\mu_i - T)$ plot	1150°C / 1h	632	624	615	601	592	
	1200°C / 1h	635	622	617	603	591	585
	1250°C / 1h	627	618	606	598	589	580

254

As the particle size increases and porosity decreases with the increase in Mn substitution. It therefore follows that the effect of particle size and porosity would increase the value of initial permeability for compositions, $x \leq 0.2$. Since saturation magnetization and permeability being interdependent, their variations with Mn substitution are self consistent. The Curie temperature (Table 4.20) has been observed to decrease with the increase in the Mn substitution at all the sintering temperatures of ferrites. The variation of Curie temperature can be explained on the basis of strength of the exchange interactions. In the case of $Ni_{0.5-x}Mn_xZn_{0.5}Fe_2O_4$ ($x = 0.0\text{-}0.5$) ferrites, the ferromagnetic Fe^{3+} ions are replaced by the diamagnetic Mn^{2+} ions with every step of substitution. Therefore, a decrease in the density of magnetic ions and the magnetic moment of the sublattices is expected. This weakens the A-B exchange interactions. Also an increase in the Mn concentration causes an increase in the lattice parameter. This means that the distances between the ions increases, which leads the different A-B interactions to decrease. Since, the Curie temperature is determined by an overall strength of the A-B exchange interactions, the weakening of the $Fe^{3+}_{(A)}\text{-}O^{2-}$ - $Fe^{3+}_{(B)}$ interaction results in a decrease in the Curie temperature, when the concentration of Mn increases. Also, exchange integral 'J' between Fe^{3+} ions and Ni^{2+} ions (J = -24 K) is greater than that between Fe^{3+} ions and Mn^{2+} ions (J = -19.1 K) which causes the decrease in A-B interactions [288] and hence the Curie temperature.

4.6.5.4. Effect of sintering temperature on initial permeability 'μ_i' and tan δ

It has been observed that initial permeability increases with the increase in sintering temperature upto $1200^{\circ}C$ (except $x = 0.4$) but decreases with further increase in sintering temperature [Table 4.19]. This increase in initial permeability can be attributed to the increase

255

in density and grain size, which increases with sintering temperature [289]. Increase in grain size results in an increase in the number of domain walls in each grain. As the movement of walls determines the initial permeability, any increase in the number of domain walls would result in an increase in initial permeability. At higher sintering temperatures (>1200°C) there is increase in the intragranular pores that are trapped in the grains. These pores act as pinning centers for the domain wall movement. Consequently, domain wall movement is restricted and this limits the rate of growth of initial permeability. Further, magnetocrystalline anisotropy decreases with the increase in sintering temperature [290] and therefore enhances the initial permeability. The tan δ was also observed to increase with increase in sintering temperature upto 1200°C and then decreases at 1250°C. The increase in the sintering temperature results in Zn loss in the samples thereby creating defects in the lattice which gives rise to magnetic loss.

4.6.6. AC susceptibility studies

The plots of normalized a.c. susceptibility against temperature for all the sintered ferrites are shown in the Fig. 4.38. The sintered samples exhibit normal ferromagnetic behavior. The Curie temperature determined from the ac susceptibility measurement is given in the Table 4.20. According to Neel's model [245] the A-B interaction is most dominant in ferrites and therefore the Curie temperatures are determined from the overall strength of A-B interaction. The strength of A-B interaction is a function of number of Fe^{3+}_A - O^{2-} -Fe^{3+}_B linkage [291] which in turn depend upon the number of Fe^{3+} ions in the formula unit and their distribution amongst tetrahedral (*A*) and octahedral [*B*] sites. The observed variation of Curie temperature with Mn substitution can be explained considering the distribution of Mn^{2+} ions

in tetrahedral (*A*) and octahedral [*B*] sites. The decrease in Curie temperature with increasing

Mn substitution results from weakening of A-B interaction and canting of spins due to excess

Fe^{3+} ions in octahedral [*B*] sites.
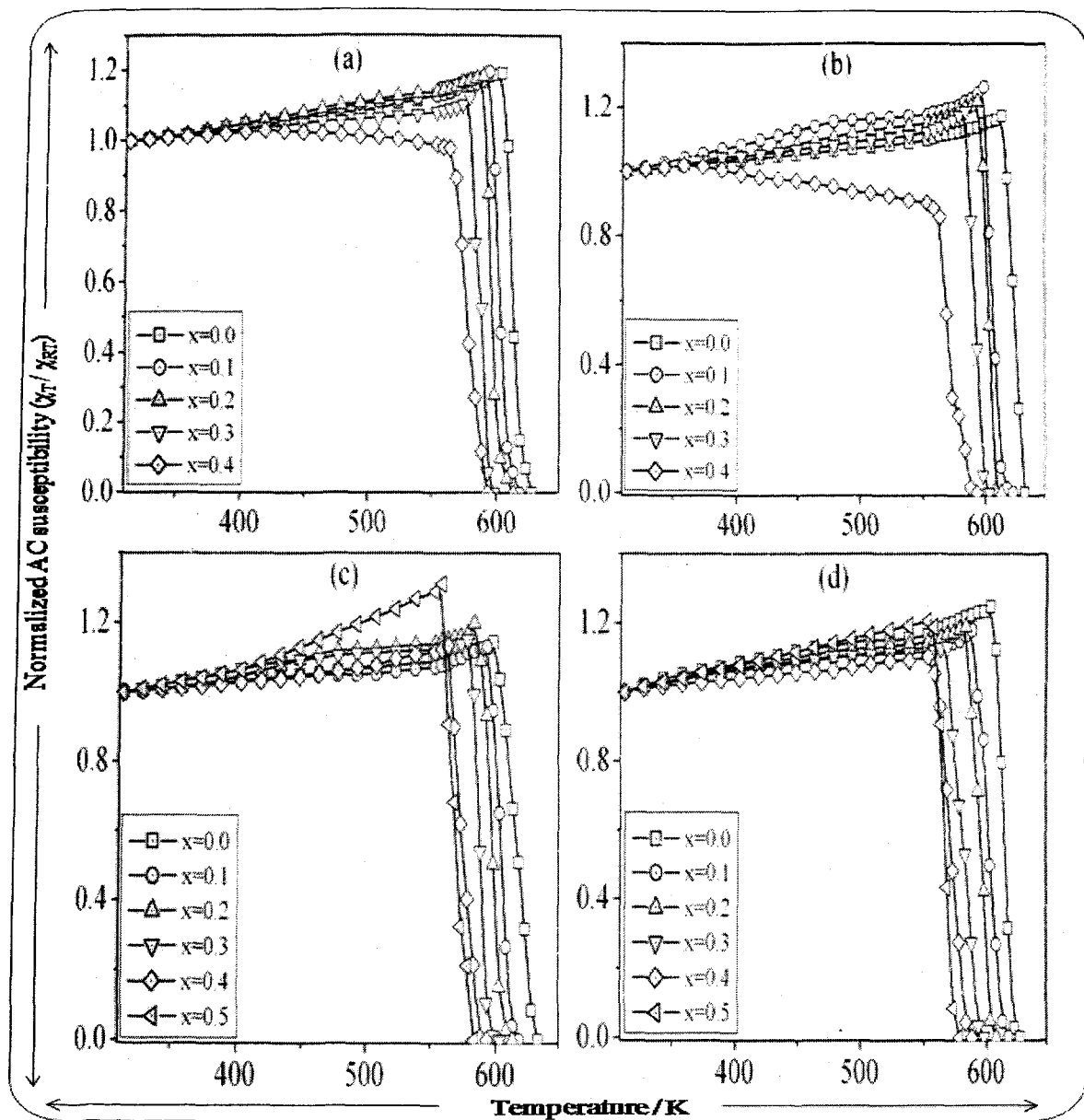
Fig.4.38. The plot of normalized a.c. susceptibility against temperature of

$Ni_{0.5-x}Mn_xZn_{0.5}Fe_2O_4$ (*x* = 0.0-0.5) ferrites sintered at a) 1100°C / 1h, b) 1150°C / 1h, c)

1200°C / 1h and d) 1250°C / 1h

4.7. Summary

In this chapter the synthesis and characterization of the $Ni_{0.5-x}Mn_xZn_{0.5}Fe_2O_4$ ($x = 0.0$-0.5) ferrite compositions have been discussed. The spinel ferrites, $Ni_{0.5-x}Mn_xZn_{0.5}Fe_2O_4$ ($x = 0.0$-0.5) were synthesized by low temperature self propagating autocatalytic decomposition of hydrazinated mixed metal fumarate precursors, $Ni_{0.5-x}Mn_xZn_{0.5}Fe_2(C_4H_2O_4)_3 \cdot 6N_2H_4$ ($x = 0.0$-0.5). These precursors were characterized by chemical analysis, total mass loss, FTIR and thermal studies. The nanosize nature of 'as synthesized' $Ni_{0.5-x}Mn_xZn_{0.5}Fe_2O_4$ ($x = 0.0$-0.5) ferrites was confirmed from XRD peaks broadening and by TEM. The lattice parameter was found to increase while X-ray as well as bulk density decrease with increase in Mn concentration. The shift in the absorption frequency of high frequency (ν_1) band towards lower frequency in FTIR spectra of $Ni_{0.5-x}Mn_xZn_{0.5}Fe_2O_4$ ($x = 0.0$-0.5) ferrites is indicative of the transfer of Fe^{3+} ions from tetrahedral to octahedral sites in spinel lattice. The Mössbauer studies of 'as synthesized' $Ni_{0.5-x}Mn_xZn_{0.5}Fe_2O_4$ ($x = 0.0$-0.5) ferrites indicated their superparamagnetic and ferromagnetic nature while, the sintered $Ni_{0.5-x}Mn_xZn_{0.5}Fe_2O_4$ ($x = 0.0$-0.5) ferrites showed ferromagnetic nature for lower Mn substitution (upto $x = 0.2$) and both paramagnetic and ferromagnetic nature for higher Mn contents. The ac susceptibility studies reveals presence of clusters of both superparamagnetic and single domain particles in 'as synthesized' $Ni_{0.5-x}Mn_xZn_{0.5}Fe_2O_4$ ($x = 0.0$-0.5) ferrites. The saturation magnetization shows initial increase followed by decrease with increasing Mn substitution attributed to the Fe^{3+} ions transfer leading to spin canting. The reduction of magnetic moment of nanocrystalline $Ni_{0.5-x}Mn_xZn_{0.5}Fe_2O_4$ ($x = 0.0$-0.5) ferrites was attributed to both the anisotropy constant and canted spin structure at the surface of the particles and the high value of coercivity to strong interparticle interactions. The lattice parameter and average grain size was found to increase

with increasing Mn substitution in Ni-Zn ferrites sintered at (a) 1100°C / 1h, (b) 1150°C / 1h, (c) 1200°C / 1h and (d) 1250°C / 1h. The microstructural studies show that the grain size increases with sintering temperature. The d.c. resistivity was found to decrease with Mn substitution (x = 0.1-0.4) and sintering temperature. The Seebeck coefficient measurement shows negative values indicating n-type conduction and high values of Seebeck coefficient suggests polaron hopping mechanism. The dielectric constant and dielectric loss were found to be comparatively low and were found to increase with sintering temperature. The dispersion observed in the dielectric constant is explained on the basis of the double layer dielectric structure and the relaxation peaks observed in the variation of dielectric loss tangent is due to the matching of hopping frequency of electrons with that of the electric field. The frequency variation of initial permeability of ferrites at different sintering temperatures indicates that the resonance peak due to domain wall oscillation is at a frequency above 10MHz. The sharp decrease in the initial permeability at Curie temperature indicates high homogeneity in all sintered ferrites. The initial permeability as well as saturation magnetization was found to increase with increase in Mn content upto x = 0.2, followed by decrease. The saturation magnetization and initial permeability increases with increasing sintering temperature upto 1200°C and shows decrease thereafter. The Curie temperature of the samples determined by initial permeability studies, dc resistivity measurements and those obtained from ac susceptibilty studies matches closely. All the three methods used for Curie temperature determination shows decrease in Curie temperature with increasing Mn substitution. The gas sensing studies carried out on the thick films of 'as synthesized' $Ni_{0.5-x}Mn_xZn_{0.5}Fe_2O_4$ (x = 0.0-0.5) ferrite samples indicated high sensitivity towards H_2S among

the six different test gases. All the samples showed good gas sensing activity at 350°C and at low gas concentration of 200 ppm H_2S with highest response shown by composition, $x = 0.2$.

Chapter 5

Summary and conclusions

Chapter 5

Summary and conclusions

5.1. Summary

The research work incorporated in thesis consists of the preparation of mixed metal fumarate hydrazinates precursors along with their detail characterization involving the characterization techniques such as chemical analysis, FTIR, TG and DSC / DTA, total mass loss and isothermal mass loss studies. The hydrazine display bidentate bridging coordination and fumarate dianion shows monodentate linkage to the metal in all the synthesized precursors. The Mn substituted Ni-Zn ferrite compositions i.e. $Ni_{0.6-x}Mn_xZn_{0.4}Fe_2O_4$ (x = 0.0-0.6) and $Ni_{0.5-x}Mn_xZn_{0.5}Fe_2O_4$ (x = 0.0-0.5) were obtained from the low temperature thermal decompositions of their respective precursors i.e. $Ni_{0.6-x}Mn_xZn_{0.4}Fe_2(C_4H_2O_4)_3.6N_2H_4$ (x = 0.0-0.6) and $Ni_{0.5-x}Mn_xZn_{0.5}Fe_2(C_4H_2O_4)_3.6N_2H_4$ (x = 0.0-0.5). All the fumarate hydrazinate precursors exhibit self propagating autocatalytic decomposition behaviour to form 'as synthesized' nanosize ferrite. The single phase formation of 'as synthesized' $Ni_{0.6-x}Mn_xZn_{0.4}Fe_2O_4$ (x = 0.0-0.6) and $Ni_{0.5-x}Mn_xZn_{0.5}Fe_2O_4$ (x = 0.0-0.5) ferrites were confirmed by the XRD measurements wherein all the XRD peaks characteristics of cubic spinel ferrite were observed. The lattice parameters of all ferrites were found to increase gradually with increasing Mn substitution. The peak broadening observed for these 'as synthesized' ferrites indicates their nanocrystalline nature. With Mn subtitution the absorption band v_1 in the FTIR spectra of both, the 'as synthesized' and sintered ferrites of both the series, shifts to lower frequency side and is narrowed which is due to the trasfer of Fe^{3+} ions from tetrahedral 'A' sites to octahedral 'B' sites. The TEM observations shows that the 'as synthesized' ferrites consists of loose agglomerates of primary particles and their diameter lies in the range of 10

261

nm to 50 nm. The XPS studies indicated the proper valence of the metal ions in 'as synthesized' ferrites and also supports the cation distribution deduced from XRD measurements. The Mn substitution was found to affect the bond length at both, tetrahedral and octahedral sites. The Mössbauer effect studies on 'as synthesized' ferrites indicated the existence of both ferromagnetic and superparamagnetic particles. The isomer shift values are consistent with the trivalent iron and quadrupole values indicates the cubic symmetry of polyhedra. The decrease in the relative area of tetrahedral 'A' site confirms the transfer of Fe^{3+} ions from tetrahedral 'A' sites to octahedral 'B' sites, with increase in Mn content.

The Mn substitution has sigificant influence on the electromagnetic properties such as d.c. resistivity, dielectric constant, dielectric loss tangent, saturation magnetization, coercivity etc. The lower d.c. resistivity values in the range 10^5 Ωcm to 10^7 Ωcm observed for 'as synthesized' $Ni_{0.6-x}Mn_xZn_{0.4}Fe_2O_4$ (x = 0.0-0.6) ferrites at room temperature suggest the protonic conductivity due to moisture trapped inside the pores, which is also responsible for hysteresis observed in d.c. plots during first heating and first cooling cycle. The positive values of Seebeck coefficient in the lower temperature region of both the 'as synthesized' ferrite series was also due to the protonic conduction while, the negative values of Seebeck coefficient indicates that the electrons are majority charge carriers at higher temperatures. The activation energies of conduction in both ordered and disordered states suggests the polaron hopping conduction mechanism. The dielectric constant and dielectric loss tangent was found to be low. The saturation magnetization shows initial increase followed by decrease with increasing Mn content which was attributed to the Fe^{3+} ions transfer from A to B sites leading to spin canting in spinel ferrite lattice. The reduction of magnetic moment of nanocrystalline 'as synthesized' ferrites was attributed to both the anisotropy constant and canted spin

262

structure at the surface of the particles while, the high value of coercivity to strong interparticle interactions. The a.c. susceptibility studies reveal the presence of clusters of both, superparamagnetic and single domain particles in 'as synthesized' ferrites.

The optimization of sintering temperature studies revealed the complete single phase formation at sintering temperature of 1100°C for 1h for all ferrites except for ferrites with zero nickel content. The lattice parameter increases with Mn substitution in the sintered $Ni_{0.6-x}Mn_xZn_{0.4}Fe_2O_4$ ($x = 0.0-0.6$) and $Ni_{0.5-x}Mn_xZn_{0.5}Fe_2O_4$ ($x = 0.0-0.5$) ferrite compositions. The effect of sintering temperature is not pronounced on the lattice parameter. The bulk density increases with sintering temperature while no change in the X-ray density was observed. The sintering temperature of 1100°C was not sufficient to complete the densification process resulting in small grain size and open porosity while, the sintering temperature of 1200°C produces a homogeneous microstructure with an average grain size of about 2μm. The higher sintering temperature (>1200°C) results in to abnormal grain growth and greater trapped porosity may be due to zinc loss. The Mössbauer spectra represents two Zeeman sextet pattern for all sintered $Ni_{0.6-x}Mn_xZn_{0.4}Fe_2O_4$ ($x = 0.0-0.6$) compositions (except $x = 0.6$, which in addition shows a single quadrupole doublet) which indicates their ferromagnetic character while, the Mössbauer effect studies on $Ni_{0.5-x}Mn_xZn_{0.5}Fe_2O_4$ ($x = 0.0-0.5$) ferrites showed the ferromagnetic nature for composition, $x \leq 0.2$, and simultaneous ferromagnetic and paramagnetic character for composition, $x > 0.2$. The central doublet was attributed to the magnetically isolated Fe^{3+} ions which do not participate in the long range magnetic ordering due to a large number of nonmagnetic nearest neighbours. The d.c. resistivity at room temperature was found to vary from 10^8 Ωcm to 10^7 Ωcm with increasing sintering temperature of $Ni_{0.6-x}Mn_xZn_{0.4}Fe_2O_4$ ($x = 0.0-0.6$) series. The activation energies of

263

conduction in both ordered and disordered states more or less decreases with Mn substitution as well as increasing sintering temperatures in this series. The negative values of Seebeck coefficient in both the sintered ferrite series indicate electrons as majority charge carriers while higher values may be due to the polaron hopping conduction. The dielectric constant and dielectric loss was found to be low at room temperature for both the sintered ferrite series. The dielectric constant and dielectric loss increases with sintering temperature in $Ni_{0.6-x}Mn_xZn_{0.4}Fe_2O_4$ ($x = 0.0$-0.6) series. The saturation magnetization shows initial increase upto $x = 0.1$ and then decreases with increasing Mn substitution, while it increases with increasing sintering temperature (except at 1250°C) in both the sintered ferrite series. The sintered $Ni_{0.6-x}Mn_xZn_{0.4}Fe_2O_4$ ($x = 0.0$-0.6) and $Ni_{0.5-x}Mn_xZn_{0.5}Fe_2O_4$ ($x = 0.0$-0.5) ferrite compositions exhibit high initial permeability with low permeability losses. The very high values of initial permeability were observed for the ferrites sintered at 1200°C. With exception of composition, $x = 0.1$ of $Ni_{0.6-x}Mn_xZn_{0.4}Fe_2O_4$ ferrites, the Curie temperature decreases gradually with increasing Mn substitution in both the ferrite series. The Curie temperature of both the series (sintered at different temperatures) determined by initial permeability, d.c. resistivity and a.c. susceptibility studies were found to match closely. The sharp fall in the normalized a.c. susceptibility near Curie temperature indicates the very high purity and homogeneity of both the sintered ferrite series. The gas sensing studies carried out on nanocrystalline 'as synthesized' $Ni_{0.6-x}Mn_xZn_{0.4}Fe_2O_4$ ($x = 0.0$-0.6) and $Ni_{0.5-x}Mn_xZn_{0.5}Fe_2O_4$ ($x = 0.0$-0.5) ferrite compositions indicated a very high response for NH_3 gas at room temperature for composition, $x = 0.3$ of 'as synthesized' $Ni_{0.6-x}Mn_xZn_{0.4}Fe_2O_4$ ($x = 0.0$-0.6) ferrites while, the composition $x = 0.2$ of 'as synthesized' $Ni_{0.5-x}Mn_xZn_{0.5}Fe_2O_4$ ($x = 0.0$-0.5) ferrites, showed good sensing response for H_2S gas at 350°C.

5.2. Conclusions

The present investigation was focused on the effect of Mn substitution as well as sintering temperature on the electromagnetic properties of Ni-Zn ferrites. $Ni_{0.6-x}Mn_xZn_{0.4}Fe_2O_4$ ($x = 0.0$-0.6) and $Ni_{0.5-x}Mn_xZn_{0.5}Fe_2O_4$ ($x = 0.0$-0.5) ferrite series were used to study the doping effect of Mn on electric, dielectric and magnetic properties. These studies were carried out on both, the nanocrystalline (as synthesized) and bulk ferrite compositions.

The significant findings of this investigation are as follows:

1. Nanocrystalline $Ni_{0.6-x}Mn_xZn_{0.4}Fe_2O_4$ ($x = 0.0$-0.6) and $Ni_{0.5-x}Mn_xZn_{0.5}Fe_2O_4$ ($x = 0.0$-0.5) ferrites were successfully prepared using fumarate-hydrazinate precursor technique at relatively lower temperature. The temperature and time of preparation were reduced as compared to the conventional solid state process.

2. The self propagating autocatalytic decomposition of these mixed Ni-Mn-Zn-Fe fumarate hydrazinates resulted in the nanosize (9 nm – 50 nm), highly reactive (specific surface area - 28.6 m^2/gm – 61.0 m^2/gm) and crystalline spinel ferrites.

3. The obtained 'as synthesized' ferrite powder requires low sintering temperature for forming sufficiently dense but fine grained microstructured ferrites which are of interest for high frequency applications.

4. The gas sensing studies carried out on the thick films of 'as synthesized' ferrite samples indicates their potential as gas sensor for toxic gases such as H_2S and NH_3 at very low concentration.

5. The average grain size (1.86 μm) observed for sintered ferrites at highest sintering temperature of 1250°C was comparative smaller than those reported for samples prepared by ceramic method.

6. The d.c. resistivity values observed at room temperature for sintered ferrites were found to be three order of magnitude greater than those ferrites prepared by ceramic method.

7. The dielectric constant and dielectric loss tangent values are appreciably lower than those reported for samples prepared by ceramic method.

8. The high initial permeability and low permeability losses of samples sintered at 1200°C can make these mixed ferrite compositions suitable for multilayer chip inductors (MLCI) and high frequency applications.

9. The saturation magnetization values observed for mixed Ni-Mn-Zn ferrite compositions were found to be higher than those reported for same compositions prepared using ceramic method.

10. The increase in saturation magnetization and initial permeability without appreciable reduction in the resistivity makes these mixed Ni-Mn-Zn ferrite compositions practically useful over wider range of frequency than Ni-Zn and Mn-Zn ferrties.

Finally, from the overall results observed in the present study it can be concluded that with fumarate-hydrazinate precursor route it is possible to process the ferrite at relatively lower temperatures and in much shorter time duration than that require in the conventional solid state technique with advantages such as saving energy, zero contamination by the container, high homogeneity, small grain size, high electrical resistivity, relatively higher initial permeability and saturation magnetization, low losses and increase in the utility zone to higher frequency.

References:

1. D.S. Mathew and R.S. Juang. Chem. Eng. J., 129 (2007) 51.

2. I. Safarik, M. Safarikova, H. Hofmann, Z. Rahman and U. Schubert (Eds.), Nanostructured Materials, Springer, Vienna. 2002: pp. 1-23.

3. A.S. Albuquerque, J.D. Ardisson, W.A.A. Macedo and M.C.M. Alves, J. Appl. Phys., 87 (2000) 4352.

4. P.J. Van der Zaag, P.J. Van der Valk and M.T. Rekveldt, Appl. Phys. Lett., 69 (1996) 2927.

5. P.C. Fannin, S.W. Charles and J.L. Dormann, J. Magn. Magn. Mater., 201 (1999) 98.

6. S. Komarneni, E. Fregeau, E. Breval and R. Roy, J. Am. Ceram. Soc., 71 (1) (1988) C-26.

7. N.S. Chen, X.J. Yang, E.S. Liu and J.L. Huang, Sens. Actuators B, 66 (2000) 178.

8. C.V.G. Reddy, S.V. Manorama and V.J. Rao, Sens. Actuators B, 55 (1999) 90.

9. Y. Shimizu and M. Egashira, MRS Bull., 24 (1999) 18.

10. C. Xu, T. Jun, N. Miura and N. Yamazoe, Chem. Lett., 3 (1990) 441.

11. E. Traversa, Sens. Actuators B, 23 (1995) 135.

12. B. Viswanathan and V.R.K. Murthy, Ferrite Materials, Springer Verlag, Berlin, 1990.

13. A. Goldman, Modern Technology, 2ndedn. John Wiley New York, 1990.

14. B.V. Bhise, M.B. Dongare, S.A. Patil and S.R. Sawant, J. Mater. Sci. Lett., 10 (1991) 922.

15. A.K. Singh, T.C. Goel and R.G. Mendirattaa, J. Appl. Phys., 92 (71) (2002) 3872.

16. C. Venkataraju, G. Sathishkumar and K. Sivakumar, J. Magn. Magn. Mater., 322 (2010) 230.

17. Magnetism Fundamentals, Edited by E. du Tremolet, de Lacheisserie, D. Gignoux and M. Schlenker, Springer International ed. 2006, pp.3-11.

18. Benjamin Lax and Kenneth J Button, Microwave ferrites and ferrimagnets, MeGraw-Hill Book Co. New York, 1962, pp.-442

19. Carter C. Barry and Norton M. Grant, Ceramic Materials and Engineering, Springer Science and Business Media, LLC, 2007

20. A.R. West, Solid State Chemistry and its Applications, Wiley-India, 2003,

21. H.V. Keer, Principles of the Solid State Chemistry, 2nd ed., New Age International Publishers Ltd., India, 1993.

22. S. Sun, H. Zeng, D.B. Robinson, S. Raoux, P.M. Rice, S.X. Wang and G. Li, J. Am. Chem. Soc., 126 (2004) 273.

23. L. Neel, Ann. Phys., (1948) 137.

24. P. Weiss, J. de Phys., 6 (4) (1907) 661.

25. D. Dunlop and O. Ozdemir, Rock Magnetism: Fundamentals and Frontiers, Cambridge University Press, Cambridge, UK, 1997, pp.-573.

26. C.M. Sorensen, Nanoscale Materials in Chemistry, John-Wiley and Sons Inc. New York, 2001, pp.-169.

27. L.G. Van Uitert, Proc. IRE, 44 (1956) 1294.

28. W.D. Kingeri, Ceramic Fabrication Processes, M.I.T Technical Press, John Wiley, New York, 1958.

29. C.G. Koops, Phys. Rev., 83 (1951) 121.

30. X.Q. Liu, Z.L. Xu and Y.S. Shen, J. Yunnan Univ., 19 (1997) 147.

31. N. Rezlescu, C. Doroftei, E. Rezlescu and P.D. Popa, Sens. Actuators B, 115 (2006) 589.

32. Y. Li, Q. Li, M. Wen, Y. Jhang, Y. Jhai, Z. Xie, F. Xu and S. Wei, J. Electr. Spectrosc. Relat. Phenom. 160 (2007) 1.

33. P.Y. Lee, K. Ishizaka, H. Suematsu, W. Jiang and K. Yatsui, J. Nanopart. Res., 8 (2006) 29.

34. M. Tada, T. Kanemaru, T. Hara, T. Nakagawa, H. Handa and M. Abe, J. Magn. Magn. Mater., 321 (2009) 1414.

35. G. Zhang, C. Li, F. Cheng and J. Chen., Sens. Actuators B, 120 (2007) 403.

36. C. Xiangfeng, J. Dongli and Z. Chenmou, Sens. Actuators B, 123 (2007) 793.

37. R.B. Kamble and V.L. Mathe, Sens. Actuators B, 131 (2008) 205.

38. H. Zhu, X. Gu, D. Zuo, Z. Wang, N. Wang and K. Yao, Nanotechnology, 19 (2008) 405503.

39. Y. Wang, Y. Liu, C. Ciobanu and B.R. Patton, J. Am. Ceram. Soc., 83 (2000) 2219.

40. R. Rella, P. Siciliano, S. Capone, M. Epifani, L. Vasanelli and A. Liciulli, Sens. Actuators B, 58 (1999) 283.

41. M. Ferroni, D. Boscarino, E. Comini, D. Gnani, G. Martinelli, P. Nelli, V. Rigato and G. Sberveglieri, Sens. Actuators B, 58 (1999) 289.

42. R. Martins, E. Fortunato, P. Nunes, I. Fereira and A. Marques, J. Appl. Phys., 96 (2004) 1398.

43. N. Rezlescu, N. Iftimie, E. Rezlescu, C. Doroftei and P.D. Popa, Sens. Actuators B, 114 (2006) 427.

44. A. Gurlo, N. Barsan and U. Weimar, in: The 16th European Conference on Solid-State Transducers, Prague, Czech. Republic, 15–18 September, 2002, pp. 970.

45. T.G.G. Maffeis, G.T. Owen, M.W. Penny, T.K.H. Starke, S.A. Clark, H. Ferkel and S. P. Wilks, Surf. Sci., 520 (2002) 29.

46. E. Comini, M. Ferroni, V. Guidi, G. Fagila, G. Martinelli and G. Sberverglieri, Sens. Actuators B, 84 (2002) 26.

47. N. Rezlescu, C. Doroftei, E. Rezlescu and P.D. Popa, Phys. Stat. Sol. A, 203 (2006) 306.

48. D.R. Patil, L.A. Patil, G.H. Jain, M.S. Wagh and S.A. Patil, Sens. Transducers J., 74 (2006) 874.

49. Z. Jin, H.J. Zhou, Z.L. Jin, R.F. Savinell and C.C. Liu, Sens. Actuators B, 52 (1998) 188.

50. I. Ferreira, R. Igreja, E. Fortunato and R. Martins, Sens. Actuators B, 103 (2004) 344.

51. J.E. Fagan and V.R.W. Amarakoon, Am. Ceram. Soc. Bull., 27 (1993) 119.

52. K. Sun, Z. Lan, Z. Yu, L. Li, J. Huang and X. Zhao, J. Phys. D: Appl. Phys., 41 (2008) 235002.

53. J. Slama, E. Usak, M. Soka, A. Gruskova, M. Usakova and V. Jancarik, IEEE Trans. Magnetics, 46 (2) (2010) 447.

54. M.K. El-Nimr, B.M. Moharram, S.A. Saafan and S.T. Assar, J. Magn. Magn. Mater., 322 (2010) 2108.

55. M.H. Abdullah and A.N. Yusoff, Pertanika J. Sci. Tech., 6 (2) (1998) 95.

56. E. Rezlescu, N. Rezlescu, C. Pasnicu and M.L. Craus, J. Magn. Magn. Mater., 157 (1996) 487.

57. A.C.F.M. Costa, M.A.R.R. Morelli and R.H.G.A. Kiminami, J. Mater. Sci., 39 (2004) 1773.

58. T.J. Shinde, A.B. Gadkari and P.N. Vasambekar, J Mater Sci: Mater Electron., 21 (2010) 120.

59. S.E. Jacobo, S. Duhalde and H.R. Bertorello, J. Magn. Magn. Mater., 272 (2004) 2253.

60. K. Vijaya Kumar, D. Ravinder, Mater. Lett., 52 (2002) 166.

61. K. Vijaya Kumar, A. Chandra Shekhar Reddy and D. Ravinder, J. Magn. Magn. Mater., 263 (2003) 121.

62. X. Fu, H. Geb, Q. Xinga and Z. Peng, Mater. Sci. Eng. B, 176 (2011) 926.

63. X. Shen, Y. Wang, X. Yang, L. Lu and L. Huang, J. Mater. Sci: Mater. Electron., 21 (2010) 630.

64. J.S. Ghodake, R.C. Kambale, S.V. Salvi, S.R. Sawant and S.S. Suryavanshi, J. Alloys Compds., 486 (2009) 830.

65. J.S. Ghodake, R.C. Kambale, S.D. Kulkarni, S.R. Sawant and S.S. Suryavanshi, Smart Mater. Struct. 18 (2009) 125009.

66. T.T. Ahmed, I.Z. Rahman and M.A. Rahman, J. Mater. Proces. Tech. 153 (2004) 797.

67. M. K. Dimri, A. Verma, S. C. Kashyap, D. C. Dube, O. P. Thakur and Chandra Prakash, Mater. Sci. Eng. B, 133 (2006) 42.

68. J. Hu, M. Yan and W. Luo, Physica B, 368 (2005) 251.

69. S.B. Waje, M. Hashim, W. Daud. W. Yusoff and Z. Abbas, Austra. J. Basic Appl. Sci., 3 (3) (2009) 2716.

70. D. L. Zhao, Q. Li and Z.M. Shen, J. Alloys Compds., 480 (2) (2009) 634.

71. A.M. Kumar, M.C. Varma, G.S.V.R.K. Choudary, K.S. Rao, K.H. Rao and G. Gopalkrishna, J. Optelect. Adv. Mater., 12 (12) (2010) 2386.

72. K.M. Batoo and M.S. Ansari, Nanoscale Res. Lett.,7 (2012) 112.

73. A. Verma, O.P. Thakur, C. Prakash, T.C. Goel and R.G. Mendiratta, Mater. Sci. Eng. B, 60 (1999) 156.

74. A.C.F.M. Costa, E. Tortella, M.R. Morelli and R.H.G.A. Kiminami, J. Magn. Magn. Mater., 256 (2003) 174.

75. N. Kikukawa, M. Takemori, Y. Nagano, M. Sugasawa, S. Kobayashi, J. Magn. Magn. Mater., 284 (2004) 206.

76. A. Verma, O.P. Thakur, C. Prakash, T.C. Goel and R.G. Mendiratta, Mater. Sci. Eng. B 116 (2005) 1.

77. R.C. Kambale, N.R. Adhate, B.K. Chougule and Y.D. Kolekar, J. Alloys Compds., 491 (2010) 372.

78. X. Li and G. Wang, J. Magn. Magn. Mater., 321 (2009) 1276.

79. A. Kumar, A. Singh, M.S. Yadav, M. Arora and R.P. Pant, Thin Solid Films, 519 (2010) 1056.

80. H. Goto, I. Maeda, U. Kihara and M. Torii, IEEE Trans. Magnetics, 19 (3) (1983) 1463

81. J. J. Bara, B. F. Bogacz and M. I. Danilkieicz, Hyperfine Interactions, 28 (1986) 663.

82. G.F. Dionne and R.G. West, J. Appl. Phys., 61 (8) (1987) 3868.

83. V.K. Babbar and R.K. Puri, IEEE Trans. Magnetics, 28 (1) (1992) 21

84. B.V. Bhise, A.K. Ghatage, B.M. Kulkarni, S.D. Lotke and S.A. Patil, Bull. Mater. Sci., 19 (3) (1996) 527.

85. E. Rezlescu, L. Sachelarie, P.D. Popa, and N. Rezlescu, IEEE Trans. Magnetics, 36 (6) (2000) 3962.

86. A.K. Singh, O.P. Thakur, C. Prakash, T.C. Goel and R.G, Mendiratta, 'In 'Inorganic Materials: Recent Advances'(Eds. Dhirendra Bahadur, Satish Vitta and Om praksh) Narosa Publishing House New Delhi, 2004, pp.-125.

87. A.K. Singh, T.C. Goel, R.G. Mendiratta, O.P. Thakur and Chandra Prakash, J. Appl. Phys., 91 (2002) 6626.

88. A.K. Singh, A. Verma, O.P. Thakur, Chandra Prakash, T.C. Goel and R.G. Mendiratta, Jpn. J. Appl. Phys., 41 (2002) 5142.

89. A.K. Singh, A. Verma, O.P. Thakur, Chandra Prakash, T.C. Goel and R.G. Mendiratta, Mater. Lett., 57 (2003) 1040

90. A.K. Singh, Abhishek K. Singh, T.C. Goel and R.G. Mendiratta, J. Magn. Magn. Mater., 281 (2004) 276.

91. A.K. Singh, T.C. Goel and R.G. Mendiratta, Phy. Stat. Sol. A, 201 (7) (2004) 1453.

92. A.K. Singh, T.C. Goel and R.G. Mendiratta, Jpn. J. Appl. Phys., 42 (2003) 2690.

93. A.K. Singh, T.C. Goel and R.G. Mendiratta, Sol. State Commun., 125 (2003) 121.

94. A. Verma and R. Chatterjee, J. Magn. Magn. Mater., 306 (2006) 313.

95. H. Zhong and H. Zhang, J. Magn. Magn. Mater., 283 (2004) 247.

96. A.A. Sattar, H.M. El-Sayed, K.M. El-Shokrofy and M.M. El-Tabey, J. Appl. Sci., 5 (2005) 162.

97. A.A. Sattar, H.M. El-Sayed, K.M. El-Shokrofy and M.M. El-Tabey, J. Mater. Eng. Perf., 14 (2005) 99.

98. A.A. Sattar, H.M. El-Sayed, K.M. El-Shokrofy and M.M. El-Tabey, J. Mater. Sci., 42 (2007) 149.

99. A.R. Bueno, M.L. Gregori and M.C.S. Nobrega, Mater. Chem. Phys., 105 (2007) 229.

100. A.R. Bueno, M.L. Gregori and M.C.S. Nobrega, J. Magn. Magn. Mater., 320 (2008) 864.

101. K. Sun, Z. Lan, Z. Yu, L. Li, H. Ji and Z. Xu, Mater. Chem. Phys., 113 (2009) 797.

102. K Sun, Z. Lan, Z. Yu, L. Li, X. Nie and Z. Xu, J. Alloys Compds., 468 (2009) 315.

103. P. Mathur, A. Thakur and M. Singh, Int. J. Moder. Phys. B, 23 (11) (2009) 2523.

104. A.K.M. Akther Hossain, T.S. Biswas, S.T. Mahmud, T. Yanagida, H. Tanaka and T. Kawai, J. Magn. Magn. Mater., 321 (1) (2009) 81.

105. C. Venkataraju, G. Sathishkumar, K. Sivakumar, J. Alloys Compds., 498 (2) (2010) 203.

106. D.R. Mane, D.D. Birajdar, S.E. Shirsat, R.A. Telugu and R.H. Kadam, Phys. Stat. Sol. A, 207 (10) (2010) 2355.

107. S.E. Shirsath, B.G. Toksha, R.H. Kadam, S.M. Patange, D.R. Mane, G.S. Jangam and A. Ghasemi , J. Phys. Chem. Solids, 71 (2010) 1669.

108. D.R. Mane, D.D. Birajdar, S.E. Shirsat and R.H. Kadam, NIST-Nanotech., (1) (2010) 539.

109. S. Hua, Z. Huai-Wu, T. Xiao-Li and J. Yu-Lan, Trans. Nonferrous Met. Soc. China, 21(2011) 109.

110. D. Gajapathy and K.C. Patil, Mater. Chem. Phys., 9 (1983) 423.

111. D. Gajapathy, S. Govindarajan K.C. Patil and H. Manohar, Polyhedron, 2 (1983) 865.

112. P. Ravindranathan and K.C. Patil, Thermochim. Acta, 71 (1983) 53.

113. P. Ravindranathan and K.C. Patil, Proc. Ind. Acad. Sci., 95 (1985) 345.

114. P. Ravindranathan, G.V. Mahesh and K.C. Patil, J. Solid State Chem., 66 (1987) 20.

115. P. Ravindranathan and K.C. Patil, J. Mater. Sci., 22 (1987) 3261.

116. G.V. Mahesh and K.C. Patil, Thermochim. Acta, 99 (1986) 153.

117. K.C. Patil, Proc. Ind. Acad Sci., 96 (1986) 459.

118. S. Sundar Manoharan and K.C. Patil, Proc. Ind. Acad. Sci., 101 (1989) 377.

119. V. Moye, K.S. Rane and V.N. Kamat Dalal, J. Mater. Sci.: Mater. Elect., 1 (1990) 212.

120. V. Borker, K.S. Rane and V.N. Kamat Dalal, J. Mater. Sci.: Mater. Elect., 4 (1993) 241.

121. M.M.A. Sekar and K.C. Patil, Mater. Res. Bull., 28(5) (1993) 485.

122. B.N. Sivasankar and S. Govindarajan, Synth. React. Inorg. Met.-Org. Chem., 24 (9) (1994) 1573.

123. B.N. Sivasankar, J. Therm. Anal. Cal., 86 (2006) 385.

124. B.N. Sivasankar and J.R. Sharmila, J. Therm. Anal. Cal., 73 (2003) 271.

125. B.N. Sivasankar and S. Govindarajan, J. Therm. Anal., 46 (1996) 117.

126. B.N. Sivasankar and S. Govindarajan, Mater. Res. Bull., 31 (1996) 47.

127. E.R. Jiji and K.K. Aravindakshan, J. Therm. Anal., 44 (1995) 65.

128. K. Kuppusamy, B.N. Sivasankar and S. Govindarajan, Thermochim. Acta, 274 (1996) 125.

129. K. Kuppusamy and S. Govindarajan, Synth. React. Inorg. Met.-Org. Chem., 26 (1996) 225.

130. S. Yasodhai, T. Sivakumar and S. Govindarajan, Thermochim. Acta, 338 (1999) 57.

131. S. Yasodhai and S. Govindarajan, Synth. React. Inorg. Met.-Org. Chem., 30 (2000) 745.

132. S. Yasodhai and S. Govindarajan, J. Therm. Anal. Cal., 62 (2000) 737.

133. S. Yasodhai and S. Govindarajan, J. Therm. Anal. Cal., 67 (2002) 679.

134. K.S. Rane, V.M.S. Verenkar, R.M. Pednekar and P.Y. Sawant, J. Mater. Sci.: Mater. Elect., 10 (1999) 121.

135. K.S. Rane, V.M.S. Verenkar and P.Y. Sawant, J. Mater. Sci.: Mater. Elect.,10 (1999)133.

136. T. Premkumar and S. Govindarajan, J. Therm. Anal. Cal., 79 (2005) 115.

137. T. Premkumar and S. Govindarajan, J. Therm. Anal. Cal., 84 (2006) 395.

138. S. Vairam, T. Premkumar and S. Govindarajan, J. Therm. Anal. Calorim., 101 (2010) 979.

139. L. Vikram and B.N. Sivasankar, Thermochimica Acta, 452 (2007) 20.

140. L. Vikram and B.N Sivasankar, Ind. J. Chem., 46A (2007) 568.

141. K.S. Rane, H. Uskaikar, R.M. Pednekar and R. Mhalsikar, J. Therm. Anal. Calorim., 90 (2007) 627.

142. B. Raju and B.N. Sivasankar, J. Therm. Anal. Calorim., 94 (2008) 289.

143. B. Raju and B.N. Sivasankar, J. Therm. Anal. Calorim., 98 (2009) 371.

144. V.M.S. Verenkar and K.S. Rane, 'In: P.V. Ravindran, M. Sudersanan, N.L. Misra and V. Venugopal, editors. Proceedings of the 12th National Symposium on Thermal Analysis, Thermans 2000. Gorakhpur, India: Indian Thermal Analysis Society; pp.-194.

145. V.M.S. Verenkar, R.A. Porob and K.R. Kannan, 'In: C.G.S. Pillai, K.L. Ramakumar, P.V. Ravindran and V. Venugopal, editors. Proceedings of the 13th National Symposium on Thermal Analysis', Thermans 2002, Mumbai, India: Indian Thermal Analysis Society; pp.-154.

146. V.M.S. Verenkar, S.Y. Sawant and K.R. Kannan, 'In: K.D. Mudher Singh, S. Bharadwaj, P.V. Ravindran, S.K. Sali and V. Venugopal, editors. Proceedings of the 14th National Symposium on Thermal Analysis', Thermans 2004, Vadodara, India: Indian Thermal Analysis Society; pp- 335.

147. R.A. Porob, S.Z. Khan, S.C. Mojumdar and V.M.S. Verenkar, J. Therm. Anal. Calorim., 86 (2006) 605.

148. S.Y. Sawant, V.M.S. Verenkar and S.C. Mojumdar, J. Therm. Anal. Calorim., 90 (2007) 669.

149. A. More, V.M.S. Verenkar and S.C. Mojumdar, J. Therm. Anal. Calorim., 94 (2008) 63.

150. L.R. Gonsalves, V.M.S. Verenkar and S.C. Mojumdar, J. Therm. Anal. Calorim., 96 (2009) 53.

151. L.R. Gonsalves, S.C. Mojumdar and V.M.S. Verenkar, J. Therm. Anal. Calorim., 100 (2010) 789.

152. L.R. Gonsalves, S.C. Mojumdar and V.M.S. Verenkar, J. Therm. Anal. Calorim., 104 (2011) 869.

153. L.R. Gonsalves and V.M.S. Verenkar, J. Therm. Anal. Calorim., 108 (2012) 871.

154. L.R. Gonsalves, S.C. Mojumdar and V.M.S. Verenkar, J. Therm. Anal. Calorim., 108 (2012) 859.

155. H. Parmar, R. Desai and R.V. Upadhyay, Appl. Phys. A, 104 (2011) 229.

156. C. Kim, J. Lee, S. Kato, R. Murakami and M. Yoshimura, Mater. Res. Bull., 36 (2001) 2241.

157. S. Thakur, S.C. Katyal and M. Singh, J. Magn. Magn. Mater., 321 (2009) 1.

158. P.B. Pandya, H.H. Joshi and R.G. Kulkarni, J. Mater. Sci., 26 (1991) 5509.

159. R. Arulmurugan, B. Jeyadevan, G. Vaidyanathan and S. Sendhilnathan, J. Magn. Magn. Mater., 288 (2005) 470.

160. W. Bayoumi, J. Mater. Sci., 42 (2007) 8254.

161. A.S. Prakash, A.M.A. Khadar, K.C. Patil and M.S. Hegde, J. Mater. Synth. Process., 10 (3) (2002) 135.

162. M.H. Yousefi, S. Manouchehri, A. Arab, M. Mozaffari, G.R. Amiri and J. Amighian, Mater. Res. Bull., 45 (2010) 1792.

163. P. Pramanik and A. Pathak , Bull. Mater. Sci., 17 (1994) 967.

164. P.P. Sarangi, B.D. Naik and N.N. Ghosh, J. Am. Ceram. Soc., 91 (2008) 4145.

165. Vogel's, Text book of quantitative inorganic analysis (Revised by G.H. Jeffery, Bassett, J. Mendham and R.C. Denney), 5th edn. Longman, UK; 1989, pp. 402.

166. K. Mohan and Y.C. Venudhar, J. Mater. Sci. Lett.,18 (1999) 13.

167. R.D. Waldron, Phys. Rev., B 99 (6) (1955) 1727.

168. B.D. Cullity, Elements of X-ray Diffractions, Addison Wesley Pub. Co. Inc. 1956.

169. M.U. Islam, Z. Ahmad and T. Abbas, Proc. 6th International Symposium on Advanced Materials, 1999, p-155.

170. A.M.M. Farea, S. Kumar, K.M. Batoo, A. Yousef, C.G. Lee and Alimuddin, J. Alloy Compd., 464 (2008) 361.

171. H.P. Klug and L.E. Alexander, X-ray Diffraction Procedures, Wiley Inter Science, New York, 1954, p-504.

172. P.V. Reddy and T.S. Rao, J. Less-Common Metals, 75 (1980) 255.

173. M. Pascard, A. Globus and V. Cabon, J. Physique 38,C1 (1977) 163.

174. R.D. Shanon and C.T. Prewitt, Acta Crystalogr. B, 26 (1970) 1046.

175. M.A. Amer and M.E. Hiti, J. Magn. Magn. Mater., 234 (2001) 118.

176. O. Ravinder, J. Appl. Phys., 75 (1994) 6121.

177. S.A. Mazen, M.H. Abdallah, B.A. Sabrah and H.A.M. Hashem, Phys. Stat. Sol.(a), 134 (1992) 263.

178. J. Smit and H.P.J Wijn, in: Ferrites, Philips Technical Library, Eindhoven, 1959, pp -149.

179. C. Arean, J. Blanco, J. Gonzles and M. Fernandez, J. Math. Psychol. 9, (1990) 229.

180. T. Abbas, Y. Khan, M. Ahmad and S. Anwar, Solid State Commun., 82 (1992) 701.

181. D.K. Chakrabarty and B. Viswanathan, Heterogeneous Catalysis, New Age Int. Publishers, India (2008).

182. R.S. Dhaka, A.K. Shukla, M. Maniraj, S.W. D'Souza, J. Nayak and S.R. Barman, Rev. Sci. Instrum., 81 (2010) 043907.

183. E. Fluck, W. Kerler and W. Neuwirth, Angew. Chem., 75 (1963) 461.

184. L.A. Patil and D.R. Patil, Sens. Actuators B, 120 (2006) 316.

185. M.S. Wagh, G.H. Jain, D.R. Patil, S.A. Patil and L.A. Patil, Sens. Actuators B, 115 (2006) 128.

186. B. Lorentz and D. Ihle, Phys. Stat. Sol. B, 69 (1975) 451.

187. M.G. Patil, V.C. Mahajan, B.V. Bhise, A.K. Ghatage, S.D. Lotke and S.A. Patil, Bull. Mater. Sci., 17 (4) (1994) 399.

188. C. Romeijn, Philips Res. Rep., 8 (1953) 316.

189. S. D. Likhite and C. Radhakrishnamurthy, Curr. Sci., 35 (1966) 534.

190. B.K. Bammannavar and L.R. Naik, J. Magn. Magn. Mater., 324 (2012) 944.

191. D. Ravinder and K. Vijaya Kumar, Bull. Mater. Sci., 24 (5) (2001) 505.

192. A. Verma, T.C. Geol, R.G. Mendiratta and P. Kishon, J. Magn. Magn. Mater., 208 (2000) 13.

193. A. Braibanti, F. Dallavalle, M.A. Pellinghelli and E. Leporati, Inorg. Chem.,7 (1968) 1430.

194. R. Tsuchiya, M. Yonemura, A. Uehera and E. Kyuno, Bull. Chem. Soc. Jap., 47 (3) (1974) 660.

195. K. Nakamoto, Infrared and Raman Spectra of Inorganic and Coordination Compounds Part B, 6th ed., John Wiley, New York, 1978, pp.-153.

196. L. Vegard, Zeitschrift für Physik, 5 (1921) 17.

197. F. Petil and M. Lenglet, Solid State Comm., 86 (1993) 67.

198. T.J. Daou, G. Pourroy, S. Begin-Colin, J.M. Greneche, C. Ulhaq-Bouïllet, P. Legare, P. Bernhardt, C. Leuvrey and G. Rogez, Chem. Mater., 18 (2006) 4399.

199. G. Fagherazzi and F. Garbassi, J. App. Crystallograph., 5 (1972) 18.

200. C.O. Orean, E.G. Diaz, J.M. R. Gonzalez and M.A.V. Garcia, J. Solid State Chem., 77 (1988) 275.

201. P.P. Hankare, R.P. Patil, K.M. Garadkar, R. Sasikala and B.K. Chougule, Mater. Res. Bull. 46 (2011) 447.

202. Q.M Wei, J.B Li and Y-J Chen, J. Mater. Sci., 36 (2001) 5115.

203. K.A. Mohammed, A.D. Al-Rawas , A.M. Gismelseed, A. Sellai, H.M. Widatallah, A. Yousif, M.E. Elzain and M. Shongwe, Physica B, 407 (2012) 795.

204. N.M. Deraz, J. Anal. Appl. Pyrol., 91 (2011) 48.

205. T.T. Srinivasan, C.M. Srivastava, N. Venkatramani and M.J. Patni, Bull. Mater. Sci., 6 (1984) 1063.

206. O.S. Josyulu and J. Sobhanadri, Phys. Stat. Sol. A, 65 (1981) 479.

207. A.M. Shaikh, S.A. Jadhav, S.C. Watawe and B.K. Chougule, Mater. Lett., 44 (2000) 192.

208. A. Alarifi, N.M. Deraz and S. Shaban, J. Alloys Compd., 486 (2009) 501.

209. G. Chandrasekaran, S. Selvandan and K. Manivannane, J. Mate. Sci.: Mater. Elec., 15 (2004) 15.

210. V.K. Mittal, P. Chandramohan, S. Bera, M.P. Srinivasan, S. Velmurugan and S.V. Narasimhan, Solid State Comm., 137 (2006) 6.

211. P. Gao, E.V. Rebrov, M.W.G.M. Verhoeven, J.C. Schouten, R. Kleismit, G. Kozlowski J. Cetnar, Z. Turgut and G. Subramanyam, J. App. Phy., 107 (2010) 044317-1.

212. C.V. Ramana, M. Massot and C.M. Julien, Surf. Interface Anal. 37 (2005) 412.

213. Y. Zhang and D. Wen, Mater Chem Phys., 131 (2012) 575.

214. G. Bonsdorfa, K. Schaferb, K. Teskea, H. Langbeina, H.Ullmanna, Solid State Ionics, 110 (1998) 73.

215. J. Hu, M. C. L. Irene and G. H. Chen, Langmuir, 21 (2005) 11173.

216. V.K. Mittal, S. Bera, R. Nithya, M.P. Srinivasan, S.Velmurugan and S.V. Narasimhan, J. Nucl. Mater., 335 (2004) 302.

217. S. Yan, W. Ling and E. Zhou, J. Cryst. Growth, 273 (2004) 226.

218. K. Mandal, S. Pan Mandal, P. Agudo and M. Pal, Appl. Surf. Sci., 182 (2001) 386.

219. R. Ghosh, L. Pradhan, Y.P. Devi, S.S. Meena, R. Tewari, A. Kumar, S. Sharma, N. S. Gajbhiye, R.K. Vatsa, B.N. Pandey and R.S. Ningthoujam, J. Mater. Chem., 21 (2011) 13388

220. R. Shukla, R.S. Ningthoujam, S.S. Umare, S. J. Sharma, S. Kurian, R.K. Vatsa, A.K. Tyagi and N.S. Gajbhiye, Hyperfine Interact., 184 (2008) 217.

221. S.S. Shinde, S.S. Meena, S.M. Yusuf and K.Y. Rajpure, J. Phys. Chem. C, 115 (2011) 3731.

222. K. Sharma, S.S. Meena, S. Saxena, S.M. Yusuf, A. Srinivasan and G.P. Kothiyal, Mater. Chem. Phys., 133 (2012) 144.

223. K. Sharma, S.S. Meena, C.L. Prajapat, S. Bhattacharya, Jagannath, M.R. Singh, S.M. Yusuf and G.P. Kothiyal, J. Magn. Magn. Mater. 321 (2009) 3821.

224. K. Sharma, A. Dixit, S. Singh, Jagannath, S. Bhattacharya, C.L. Prajapat, P.K. Sharma, S.M. Yusuf, A.K. Tyagi and G.P. Kothiyal, Mater. Sci. Eng. C, 29 (2009) 2226.

225. E.J.W. Verwey and J.M. De Boer, Rec. Trav. Chim. Phys. Bas, 55 (1936) 531.

226. D. Kothari, S. Phanjoubam and J.S. Baijal, J. Mater. Sci., 25 (1990) 5142.

227. L.R. Devi, S. Phanjoubam, H.N.K. Sarma and C. Prakash, Mater. Lett., 44 (2000) 65.

228. R. Satyanarayan, S.R. Murthy and T.S. Rao, J. Less Common Met., 86 (1982) 115.

229. N. Rezelescu, E. Rezelescu, C. Doroftei and P.D. Popa, J. Phys. Conf. Ser., 15 (2005) 296.

230. C. Cantalini, M. Faccio, G. Ferri and M. Pelino, Sens. Actuators B, 18 (1994) 437.

231. S. A. Saafan, T. M. Meaz, E. H. El-Ghazzawy, M. K. El-Nimr, M. M. Ayad and M. Bakr, J. Magn. Magn. Mater. 322 (2010) 2369.

232. P. P. Sarangi, S.R. Vadera, M.K. Patra and N.N. Ghosh, Powder Tech., 203 (2010) 348.

233. A. Verma, T.C. Goel, R.G. Mendiratta and R.G. Gupta, J. Magn. Magn. Mater., 192 (1999) 271.

234. A.M. Abdeen, J. Magn. Magn. Mater. 192 (1999) 121.

235. B.V. Bhise, A.K. Ghatage and S.A. Patil, Indian J. Pure Appl. Phys., 33 (1995) 459.

236. D. Ravinder, G.R. Kumar and Y.C. Venudhar, J. Alloys Compounds, 363 (2004) 6.

237. J. B. Goodenough, Prog. Solid State Chem. 5 (1971) 145.

238. L.L. Hench and J.K. West, Principles of Electronic Ceramics, John-Wiley, NewYork, 1990, p. 205.

239. J.C. Maxwell, Electric and Magnetism, Oxford University Press, London,1973, p.328

240. K.W. Wagner, Ann. Phys, 40 (1973) 817.

241. L. Radhapiyari, S. Phanjoubam, H.N.K. Sarma and C. Prakash, Mater. Lett., 44 (2000) 65.

242. P. Mathur, A. Thakur and M. Singh, Physica Scripta, 77 (2008) 025701.

243. K. Iwachi and Y. Ikeda, Phys. Stat. Sol. A, 93 (1986) 309.

244. S.I. Patil and R.V. Dabhade, IEEE Trans. Magnetics, 30 (1994) 4915.

245. L Nèel, Comptes-Rendus Acad. Sci. Paris 230 (1950) 375.

246. S.V. Kakatkar, S.S. Kakatkar, R.S. Patil, A.M. Sankpal, S.S. Suryawanshi, D.N. Bhosale and S.R. Sawant, Phys. Stat. Sol. B, 198 (1996) 853.

247. I. Nowik, J. Appl. Phys., 40 (1969) 872.

248. C.E. Patton, C.A. Edmonson and Y.H. Liu, J. Appl. Phys. 53 (1982) 2431.

249. G.F. Dionne, J. Appl. Phys., 61(1987) 3865.

250. B. Parvatheeswara Rao, O. Caltun, W.S. Cho, C.O. Kim and C.G. Kim, J. Magn. Magn. Mater., 310 (2007) e812.

251. R.C. Kambale, P.A. Shaikh, C.H. Bhosale, K.Y. Rajpure and Y.D. Kolekar, Smart Mater. Struct. 18 (2009) 115028.

252. V.R.K. Murthy, J. Geo. Soc. Ind., 26 (1985) 640.

253. G.J. Baldha and R.G. Kulkarni, Solid State Comm., 53 (1985) 11.

254. C.P. Bean, J. Appl. Phys., 26 (1955) 1981.

255. G.S. Trivikrama Rao and D. Tarakarama Rao, Sens. Actuators B, 55(1999)166.

256. C. Kittle, Introduction to Solis State Physics, 7th ed. Wiley, Singapore, 1996.

257. M.I. Mendelson, J. Am. Ceram. Soc., 52 (1967) 443.

258. M.F. Yan and D. Johnson, J. Am. Ceram. Soc., 61 (1978) 342.

259. M. Drofenik and S. Besenicar, Am. Ceram. Soc. Bull., 65 (1986) 656.

260. M.G. Patil, V.C. Mahajan, S.D. Lotke, B.V. Bhise and S.A. Patil, Solid State Commun., 91 (1994) 667.

261. B.L. Patil, S.R. Sawant, S.A. Patil and R.N. Patil, J. Mater. Sci., 29 (1994) 175.

262. B.V. Bhise, S.D. Lotke and S.A. Patil, Phys. Stat. Sol. A, 157 (1996) 411.

263. M. Kosenberg, M. Vencesu, J. Phys. Soc. Jpn., 28 (1970) 264.

264. L. Radhapiyari, S. Phanjoubam, H.N.K. Sarma and C. Prakash, J. Phys. D 32 (1999) 2151.

265. K.H. Rao, S.B. Raju, K. Aggarval and R.G. Mendiratta, J. Appl. Phys., 52 (1980) 1376.

266. B.P. Rao and K.H. Rao, J. Appl. Phys. 80 (1996) 6804.

267. W.D. Kingery, H.K. Bowen and P.R. Uhlmann, Introduction to Ceramics, Wiley, New Work, 1975 pp.-904.

268. K. Iwauchi, Jpn. J. Appl. Phys. 10 (1971) 1520.

269. J.M. Brownlow, J. Appl. Phys., 29 (1958) 373.

270. I.G. Austin and N.F. Mott, Adv. Phys., 18 (1969) 41.

271. G.C. Jain and W.B. Berry, Transport properties of solids and solid state energy conversion, Tata McGraw-Hill, C-98, South Extension II, New Delhi, 1972, pp.-37.

272. D.R. Secrist and H. L. Turk, J. Am. Ceram. Soc., 53 (1970) 683.

273. R.G. Gupta and R. G. Mendiratta, J. Appl. Phys., 48 (1977) 2998.

274. K.H. Rao, S.B. Raju, K. Aggarval and R.G. Mendiratta, Solid State Commun., 36 (1980) 777.

275. O. Caltun, G.S.N. Rao, K.H. Rao, B. Parvatheeswara Rao, I. Dumitru, C.O. Kim and C.G. Kim, J. Magn. Magn. Mater., 316 (2007) e618.

276. X.H. Wang, T.L. Ren, L.Y. Li and L.S. Zhang, J. Magn. Magn. Mater., 184 (1998) 95.

277. W.C. Kim, S.L. Park, S.J. Kim, S.W. Lee and C.S. Kim, J. Appl. Phys., 87 (2000) 6241.

278. P.D. Baba, J. Am. Ceram., 48 (1968) 305.

279. G.T. Rado, R.W. Wright, W.H. Emerson and A. Terris, Phys. Rev., 88 (1952) 909.

280. S.H. Kang and H.I. Yoo, J. Appl. Phys., 88 (2000) 4754.

281. O.F. Caltun and L. Spinu, IEEE Trans. Magnetics, 37 (2001) 2353.

282. B.S. Chauhan, R. Kumar, K.M. Jadhav and M. Singh, J. Magn. Magn. Mater., 283 (2004) 71.

283. A.A. Sattar, A.H. Wafik, K.M. El-Shokrofy and M.M. El-Tabey, Phys. Stat. Sol. A, 171 (1999) 563.

284. S. Chikazumi, Physics of Ferromagnetism, Clarendon Press, Oxford, 1977, pp.- 486.

285. P.S. Anilkumar, J.J. Shotri, C.E. Deshpande and S.K. Date, J. Appl. Phys., 81 (1997) 4788.

286. G.T. Rado, Rev. Mod. Phys., 17 (1953) 81.

287. J.H. Nam, W.H. Hur and J.H. Oh, J. Appl. Phys., 81 (1997) 4794.

288. C.M. Srivastava, G. Srinivasan and N.G. Nanadikar, Phys. Rev. B: Condens. Mater., 19 (1979) 499.

289. T. Nakamura and Y. Okaro, J. Appl. Phys. 79 (1996) 7129.

290. D. Polder, Inst. Eletron Eng. Part II (1950) 246.

291. M.A. Gilleo, J. Phys. Chem. Solids, 13 (1960) 33.

292. A. Verma, T.C. Goel, R.G. Mendiratta and P. Kishan, J. Magn. Magn. Mater., 208 (2000) 13.

APPENDIX – I

PUBLICATIONS (Peer Reviewed Journals)

1. **U.B. Gawas,** V.M.S. Verenkar, "Synthesis, thermal and infrared spectroscopic studies of hydrazinated mixed metal fumarates", J Therm Anal Calorim, 2013, In press (DOI 10.1007/s10973-013-3250-9)

2. **U.B. Gawas,** V.M.S. Verenkar, "Synthesis, thermo-analytical and IR spectral studies of hydrazinated mixed metal carboxylates: A single source precursor to nanosize mixed metal oxides", Thermochim. Acta 556 (2013) 41-46

3. **U.B. Gawas,** V.M.S. Verenkar, S.R. Barman, S.S. Meena, Pramod Bhatt, "Synthesis of nanosize and sintered $Mn_{0.3}Ni_{0.3}Zn_{0.4}Fe_2O_4$ ferrite and their structural and dielectric studies" J. Alloys Compds., 555 (2013) 225-231.

4. **U.B. Gawas,** V.M.S. Verenkar and S.C. Mojumdar, "Nano-crystalline $Mn_{0.3}Ni_{0.3}Zn_{0.4}Fe_2O_4$ obtained by novel fumarato-hydrazinate precursor method, Synthesis, Characterization and studies of magnetic and electrical properties". J Therm Anal Calorim, 2012; 108(3) 865-870.

5. **U. B. GAWAS,** V. M. S. VERENKAR and D. R. PATIL, "Nanostructured Ferrite Based Electronic Nose Sensitive to Ammonia at Room Temperature" Sensors & Transducers Journal,134(11)(2011)45-55.

6. **U.B. Gawas,** V.M.S. Verenkar and S.C. Mojumdar, "Synthesis and characterization of $Ni_{0.6}Zn_{0.4}Fe_2O_4$ nano-particles obtained by auto catalytic thermal decomposition of carboxylato-hydrazinate complex". J Therm Anal Calorim. 2011; 104 (3): 879-83.

7. **U.B. Gawas,** V.M.S. Verenkar and S.C. Mojumdar. "Synthesis, characterization, infrared studies, and thermal analysis of $Mn_{0.6}Zn_{0.4}Fe_2(C_4H_2O_4)_3 \cdot 6N_2H_4$ and its decomposition product $Mn_{0.6}Zn_{0.4}Fe_2O_4$". J Therm Anal Calorim. 2010; 100 (3): 867-71.

8. **U.B. Gawas,** V.M.S. Verenkar and S.C. Mojumdar. "$Ni_{0.5}Mn_{0.1}Zn_{0.4}Fe_2(C_4H_2O_4)_3 \cdot 6N_2H_4$ precursor $Ni_{0.5}Mn_{0.1}Zn_{0.4}Fe_2O_4$ nanoparticles preparation, IR spectral, XRD, SEM-EDS and thermal analysis". J Therm Anal Calorim. 2009; 96(1):49-52.

APPENDIX –II

PUBLICATIONS (Conference)

1. Thermal and Infra-red spectral characteristics of mixed metal carboxylato hydrazinate complex and its decomposition product

   U.B. Gawas and V.M.S. Verenkar

   In 18th Annual Symposium /Workshop on Thermal Analysis, Thermans 2012, held at Department of Chemistry, BARC, Mumbai, January-2012.

2. Synthesis, characterization, Thermal and Infrared spectral studies of manganese doped nickel zinc ferrous fumarato hydrazinate complex

   U.B. Gawas and V.M.S. Verenkar

   In 16th Annual Symposium /Workshop on Thermal Analysis, Thermans 2010, held at Department of Chemistry, Kuruksheshtra University, Kuruksheshtra, Haryana, March-2011.

3. Nanocrystalline Mn substituted Ni-Zn Ferrite Thick Film Resistors as Room Temperature H_2 and O_2 Gas Sensor

   U.B. Gawas, V.M.S. Verenkar and D.R. Patil

   In DAE-BRNS 3rd International Symposium on Material Chemistry, organized by Department of Chemistry BARC, Mumbai, December-2010.

4. Synthesis, characterization, magnetic and electrical studies on $Ni_{0.6}Zn_{0.4}Fe_2O_4$ nanoparticles obtained by self propagating auto-combustion of novel fumarato hydrazinate precursor

   U.B. Gawas and V.M.S. Verenkar

In International Conference on Nanoscience and Nanotechnology in Chemistry, Health, Enviroment and Energy, organized by Department of Chemistry, Dayalbagh Educational Institute, Agra, January-2010.

5. Combustion synthesis of $Mn_{0.3}Ni_{0.3}Zn_{0.4}Fe_2O_4$ nanoparticles using a novel fumarato hydrazinate precursor

U.B. Gawas and V.M.S. Verenkar

In Indo-Russian workshop on self propagating High Temperature Synthesis, organized by Department of Material Science, Indian Institute of Science Bangalore, November-2008.

6. Synthesis and characterization of $Ni_{0.6}Zn_{0.4}Fe_2O_4$ obtained by self propagating auto-combustion of novel precursor

U.B. Gawas, S. Bhattacharyya, A. More and V.M.S. Verenkar

In International Conference on Advanced Materials and Applications, organized by Department of Physics, Shivaji University, Kolhapur, November-2007.

T- 604